

## DOCTOR OF PHILOSOPHY

### Modelling and simulation studies on near-field beamforming based through wall imaging system

Shankpal, Preetham

*Award date:*  
2014

*Awarding institution:*  
Coventry University  
M S Ramaiah University of Applied Sciences

[Link to publication](#)

#### General rights

Copyright and moral rights for the publications made accessible in the public portal are retained by the authors and/or other copyright owners and it is a condition of accessing publications that users recognise and abide by the legal requirements associated with these rights.

- Users may download and print one copy of this thesis for personal non-commercial research or study
- This thesis cannot be reproduced or quoted extensively from without first obtaining permission from the copyright holder(s)
- You may not further distribute the material or use it for any profit-making activity or commercial gain
- You may freely distribute the URL identifying the publication in the public portal

#### Take down policy

If you believe that this document breaches copyright please contact us providing details, and we will remove access to the work immediately and investigate your claim.

# MODELLING AND SIMULATION STUDIES ON NEAR-FIELD BEAMFORMING BASED THROUGH WALL IMAGING SYSTEM

By

**Preetham Shankpal**

**February - 2014**

**A thesis submitted in partial fulfilment of the University's requirements  
for the Degree of Doctor of Philosophy**

**Coventry University**

**in collaboration with**

**M. S. Ramaiah School of Advanced Studies**



## *CERTIFICATE*

*This is to certify that the Doctoral Dissertation titled “Modelling and Simulation Studies on Near-Field Beamforming based Through Wall Imaging System” is a bonafide record of the work carried out by Ms. Preetham Shankpal in partial fulfilment of requirements for the award of Doctor of Philosophy Degree of Coventry University*

*February - 2014*

*Dr. Govind R. Kadambi  
Diretor of Studies  
M.S.Ramaiah School of Advanced Studies, Bangalore*

*Dr. James Shuttleworth  
Supervisor  
Coventry University, UK*

## **Acknowledgements**

Firstly, I would like to thank my Guru, Dr.Govind R.Kadambi for his constant supervision, timely advice, patience and kindness. I also would like to thank Dr. James Shuttleworth for his timely supervision and guidance.

I thank my parents, Dr. S.R.Shankapal and Leelavathi, and my brother, Punith, for being the inspiration that they are to me.

I thank my husband Supreeth J. Burji for his love, support and encouragement which means a lot to me. A special thanks to my parents in law Jagadish B. Burji and Vijayalakshmi for their support.

I thank my best friends Varun V. Arur and Sreekrishna R. for being there for me all the time and for all the fun we have. Special regards to Varun for all the help during simulations and paper writing.

I would love to dedicate this work to my lovely son Shivansh, the most precious thing happened in my life.

Above all, I thank God for being my hope and my strength and for bringing all these people together at the right time and right place in order to jointly make this endeavor a success.

Preetham Shankpal

## Contents

Acknowledgements .....	iii
List of Tables.. .....	vii
List of Figures.....	viii
Nomenclature... ..	xiii
Abstract.....	xv
<b>Chapter 1: Introduction .....</b>	<b>1</b>
1.1 Introduction.....	1
1.2 Research Motivation and Problem Formulation .....	2
1.3 Objectives .....	4
1.4 Original Research Contributions of the Thesis .....	6
1.5 Thesis Organization .....	6
<b>Chapter 2: Introduction to Through Wall Imaging and Beamforming Techniques.....</b>	<b>8</b>
2.1 Introduction.....	8
2.2 Through Wall Imaging (TWI) System.....	9
2.3 Waveform Generation.....	10
2.3.1 Sine Wave Technique .....	11
2.3.2 Impulse Technique .....	14
2.4 Beamforming .....	16
2.4.1 Far-field Beamforming .....	18
2.4.2 Near-Field Beamforming .....	22
2.5 Analysis of Far Field Radiation Pattern of Aperture Antennas: .....	25
2.5.1 Circular Aperture .....	26
2.5.2 Rectangular Aperture .....	48
2.6 Image processing .....	31
2.7 Summary .....	33
<b>Chapter 3: Literature Review.....</b>	<b>35</b>
3.1 Introduction.....	35
3.2 Synthetic Aperture Radar (SAR) and its limitations.....	36
3.3 Beamformer for Through-The-Wall Imaging.....	43
3.4 Wave Propagation in Layered Medium .....	44

3.5 Inverse Synthetic Aperture, Stepped Frequency Radar and its Limitations .....	46
3.6 Stepped Frequency Imaging Radar .....	49
3.7 Summary .....	54
<b>Chapter 4: An Approach for Computation of Near Field Radiation Pattern of an Antenna .....</b>	<b>58</b>
4.1 Introduction.....	58
4.2 Generalized Analytical Formulation for Near Field Radiation Pattern of antenna .....	60
4.3 Simulation Results: .....	67
4.3.1 Aperture Current Distribution.....	67
4.3.2 Near-field and far-field radiation patterns .....	70
4.4 Conclusions .....	88
<b>Chapter 5: A Novel Approach For Near Field Beamforming .....</b>	<b>91</b>
5.1 Introduction.....	91
5.2 Near Field and Far Field Beamforming .....	92
5.3 Simulation Results of Near Field and Far Field Beamforming .....	97
5.3.1 Near Field Beamforming with Linear and Planar Arrays:.....	97
5.3.2 Influence of Near field radial distance of observation on beamwidth of Near field Beamformer .....	108
5.3.3 Response of Near Field Beamforming Linear array with change in Frequency.....	115
5.3.4 Effect of Beamsteering angle on the beamwidth of near field beamformer .....	111
5.3.5 Comparison of Near Field and Far Field Beamforming Arrays .....	113
5.3.6 Two dimensional Beamsteering :.....	116
5.3.7 Minimum Distance for Desired Near Field Beamforming: .....	118
5.4 Conclusions.....	120
<b>Chapter 6: Analysis of Near-Field Beamforming Based TWI System.....</b>	<b>122</b>
6.1 Introduction.....	122
6.2 Through Wall Imaging System:.....	122
6.3 Wall and Object Modelling.....	126
6.3.1 Modelling of Wall.....	127
6.3.2 Modelling of Objects (Targets):.....	129
6.4 Wave Propagation in Medium .....	131

6.4.1 Computation of Incident Field on the Outer surface of the Wall .....	133
6.4.2 Wave Propagation through the Wall:.....	135
6.4.3 Computation of Field incident on the Target.....	139
6.4.4 Refraction of the Field Reflected by the Target.....	168
6.4.5 Computation of the Field at the Receiver Array.....	169
6.5 Image Processing .....	148
6.5.1 DFT Image Registration .....	149
6.5.2 Image Fusion.....	150
6.6 Simulation Results of TWI System.....	153
6.6.1 Model of Free Space .....	153
6.6.2 Reconstruction Images of Targets Modelled with different Material.....	153
6.6.3 Image Reconstruction with Fusion and Translation .....	156
6.6.4 Stepped Frequency in TWI.....	157
6.6.5 Comparative Analysis of Results of Proposed TWI and (Aftanas M.,2009).....	160
6.6.6 Imaging of Curved Body .....	163
6.7 Conclusions:.....	167
<b>Chapter 7: Conclusion and Future Work.....</b>	<b>169</b>
7.1 Summary .....	169
7.2 Conclusions.....	171
7.2.1 Near Field Analysis of Antennas .....	171
7.2.2 Near Field Beamforming Analysis .....	172
7.2.3 Mathematical Modelling of TWI.....	173
7.3 Recommendation for Future Work: .....	174
<b>References.....</b>	<b>176</b>
APPENDIX -1.....	182
APPENDIX - 2.....	191
APPENDIX - 3.....	195
APPENDIX - 4.....	196

## **List of Tables**

Table 2. 1: Fusion Techniques and their Performance Parameters.....	33
Table 6. 1: Material Properties.....	128
Table 6. 2: Image Reconstruction of Objects made of Different Materials.....	156
Table 6. 3: Image Reconstruction using Image Fusion and combination of Fusion and Translation methods.....	157
Table 6. 4: MSE and PSNR of images obtained from X-Band Frequencies .....	160



## List of Figures

Figure 2.1:Functional Block Diagram of a Beamforming Based TWI system .....	9
Figure 2.2: Block diagram For Generation of Sine Waveform (Kucukkilic T., 2006).....	11
Figure 2. 3:Sine Wave Technique Based Radar Data Processing (Kucukkilic T.,2006).....	12
Figure 2. 4: Imaging of Six Point scatterers (Kucukkilic T., 2006).....	13
Figure 2. 5: Block diagram of M-Sequence technique (Kmec <i>et al</i> , 2006) .....	15
Figure 2. 6: Block diagram of 8 element linear array beamformer(Montebugnoli <i>et al</i> ,2004) ....	17
Figure 2. 7: Far-field Beamforming.....	19
Figure 2. 8: BeamForming with Planar Array .....	21
Figure 2. 9: Near-field Beamforming .....	22
Figure 2. 10: Coordinate System for Radiation Pattern Analysis of circular Waveguide .....	26
Figure 2.11: Radiation Pattern of a Cylindrical Circular Waveguide.....	29
Figure 2. 12: Conical Horn Antenna.....	29
Figure 2. 13: Rectangular Waveguide .....	30
Figure 2. 14: Radiation Pattern of a Rectangular Waveguide .....	31
Figure 3.1: Radar Beam of SAR (Schlutz M., 2009).....	36
Figure 3. 2: Wall Modelling and Compensation (Aftanas M., 2009) .....	41
Figure 3.3: Image Reconstruction of a building scene (a) Imaging Scene; (b) and (c) reconstructed scene (Aftanas M., 2009). .....	42
Figure 3. 4: Schematic configuration of the layered medium model (Lu et al, 2010).....	45
Figure 3. 5: Imaging Scenario and Reconstruction of Images( Amin et al, 2005) .....	53
Figure 4. 1: Coordinate System for Near Field Analysis of Circular Waveguide .....	60
Figure 4. 2: Conical Horn Antenna.....	68
Figure 4. 3: Current Distribution Over Aperture of Circular Waveguide.....	69
Figure 4. 4: Current Distribution Over Aperture of Conical Horn .....	69
Figure 4. 5(a): Comparison of Far Field Radiation Patterns of Circular Waveguide obtained from (Balanis C.A., 2005) and proposed Near-field method .....	71

Figure 4. 5(b): Comparison of Far Field Radiation Patterns of Circular Waveguide obtained from (Silver S., 1949) and proposed Near-field method .....	71
Figure 4. 6 (a): Amplitude Pattern Patterns of a Circular Waveguide at $r=0.75\lambda$ .....	72
Figure 4. 6 (b): Phase Pattern of a Circular Waveguide at $r=0.75\lambda$ .....	78
Figure 4. 7: Radiation Pattern of Circular Waveguide at a distance of $D^2/\lambda$ .....	73
Figure 4. 8: Comparison Far Field (FF) and Near Field (NF) pattern of Circular Waveguide at $r=D^2/\lambda$ .....	73
Figure 4. 9: Amplitude Radiation Patterns of Circular Waveguide. (a) $r=D^2/\lambda$ ; (b) $r=2D^2/\lambda$ .....	74
Figure 4. 10: Phase Radiation Pattern of Circular Waveguide. (a) $r=D^2/\lambda$ ; (b) $r=2D^2/\lambda$ .....	74
Figure 4. 11: Near Field Radiation pattern of Circular Waveguide at $r=0.2\lambda$ (0.64 cm).....	75
Figure 4. 12: Radiation Pattern of Circular Waveguide at $r=0.3\lambda$ (0.96 cm) .....	76
Figure 4. 13: Radiation Pattern of Circular Waveguide at $r=0.4\lambda$ (1.28 cm) .....	77
Figure 4. 14: Radiation Pattern of Circular Waveguide at $r=0.5\lambda$ (1.6 cm) .....	78
Figure 4. 15(a): Radiation Pattern of Circular Waveguide at a distance $r=0.75\lambda$ .....	78
Figure 4. 15(b): Phase Pattern of Circular Waveguide at a distance $r=0.75\lambda$ .....	85
Figure 4. 16: Comparison of Far Field Radiation Patterns of Conical Horn Antenna obtained from (Balanis C.A., 2005) and proposed Near-Field method.....	80
Figure 4. 17: Near Field Radiation Pattern of Conical Horn at $r=D^2/\lambda$ .....	81
Figure 4. 18: Comparison of Near-field and Far field Radiation Patterns of Conical Horn; ( radius= 4.1 cm; semi-flare angle $\alpha_o = 21.09^\circ$ ) .....	81
Figure 4. 19: Comparison of Amplitude Radiation Pattern of Conical Horn: (a) $r=D^2/\lambda$ (b) $r=2D^2/\lambda$ .....	82
Figure 4. 20: Comparison of Phase Radiation Pattern of Conical Horn: (a) $r=D^2/\lambda$ (b) $r=2D^2/\lambda$ .....	82
Figure 4. 21(a): Near Field Radiation pattern of Conical Horn at a distance $r=1\lambda$ (3.2cm) .....	83
Figure 4. 21(b): Near Field Phase pattern of Conical Horn at a distance $r=1\lambda$ (3.2cm).....	90
Figure 4. 22(a): Near Field Radiation pattern of Conical Horn at $r=2\lambda$ (6.4cm) .....	85
Figure 4.22(b): Near Field Radiation pattern of Conical Horn at $r=2\lambda$ (6.4cm).....	92
Figure 4. 23 (a): Near Field Radiation pattern of Conical Horn at a distance $r=3\lambda$ (9.6cm) .....	86
Figure 4. 23(b): Near Field Phase pattern of Conical Horn at a distance $r=3\lambda$ (9.6cm).....	93
Figure 4. 24(a): Radiation pattern of Conical Horn at $r=10\lambda$ (32cm).....	87

Figure 4. 24(b): Radiation pattern of Conical Horn at $r= 10 \lambda$ (32cm).....	94
Figure 5. 1: Near Field Beamforming Linear Array .....	93
Figure 5. 2: Near Field Beamforming Planar Array .....	94
Figure 5. 3: Far Field beamforming at $(\varphi_0 = 00, \theta_0=00)$ with (5x1) Linear Array .....	98
Figure 5. 4: Far Field Beamforming at $(\varphi_0 = 00, \theta_0=00)$ with (5x5) Planar Array.....	98
Figure 5. 5: Far Field Beamforming at $(\varphi_0 = 00, \theta_0=100)$ with (5x1) Linear Array .....	99
Figure 5. 6: Far Field beamforming at $(\varphi_0 = 00, \theta_0=100)$ with (5x5) Planar Array .....	100
Figure 5. 7(a): Amplitude Pattern of Near-field Beamforming with Linear Array of 5 Elements; $R_{NF} = 3\lambda$ ; $(\varphi_0=00, \theta_0=50)$ .....	101
Figure 5. 7 (b): Phase Pattern of Near-Field Beamforming with Linear Array of 5 Elements; $R_{NF}$ $= 3\lambda$ ; $(\varphi_0=00, \theta_0=50)$ .....	101
Figure 5. 8(a): Amplitude Pattern of Near-Field Beamforming with Linear Array of 7 Elements; $R_{NF} = 3\lambda$ ; $(\varphi_0=00, \theta_0=100)$ .....	102
Figure 5. 8 (b): Phase Pattern of Near-Field Beamforming with Linear Array of 7 Elements; $R_{NF}$ $= 3\lambda$ ; $(\varphi_0=0^0, \theta_0=10^0)$ .....	109
Figure 5. 9(a): Amplitude Pattern of Near-Field Beamforming with Planar Array of 5x5 elements; $R_{NF} = 3\lambda$ ; $(\varphi_0=00, \theta_0=100)$ .....	103
Figure 5. 9(b): Phase Pattern of Near-Field Beamforming with Planar Array of 5x5 elements; $R_{NF} = 3\lambda$ ; $(\varphi_0=0^0, \theta_0=10^0)$ .....	110
Figure 5. 10(a): Amplitude Pattern of Near-Field Beamforming with Planar Array of 5x5 Elements; $R_{NF} = 3\lambda$ ; $(\varphi_0 = 00, \theta_0 = -100)$ .....	104
Figure 5. 10(b): Phase Pattern of Near-Field Beamforming with Planar Array of 5x5 Elements; $R_{NF} = 3\lambda$ ; $(\varphi_0 = 0^0, \theta_0 = -10^0)$ .....	111
Figure 5. 11: Far-Field Beamforming with Linear Array of 5 Elements at $R_{NF} = 100 \lambda$ ; .....	106
Figure 5. 12(a): Comparison of Amplitude Pattern of Near-Field Beamformer with (5x1) Linear Array and Planar Array (5 x 5 elements) at $R_{NF}=3 \lambda$ ; $(\varphi_0=00, \theta_0=100)$ .....	107
Figure 5. 12(b): Comparison of Phase Pattern of Near-Field Beamformer with (5x1) Linear Array and Planar Array (5 x 5 elements) at $R_{NF}=3 \lambda$ ; $(\varphi_0=00, \theta_0=100)$ .....	113
Figure 5. 13: Variation in Beamwidth of Near Field Beamformer (5x1 linear array) .....	108
Figure 5. 14: Variation in Beamwidth of Near field Beamformer (5x5 linear array) .....	109
Figure 5. 15: Effect of Change in Frequency on the Radiation Pattern of Near-field Beamformer with (7x1) Linear array ; $R_{NF}=3 \lambda$ ; $(\varphi_0=00, \theta_0=00)$ .....	110

Figure 5. 16: C – Band Near Field Beamformer with 5 Linear Array (5x1 element) at ( $\phi_0=00, \theta_0=00$ ) ; RNF = $3\lambda$ ; 3 dB; Beamwidth = $140^\circ$ .....	110
Figure 5. 17: Near Field Beamformer with 5 Linear Array (5x1 element) at ( $\phi_0=00, \theta_0=00$ ) ; RNF = $3\lambda$ ; 3 dB Beamwidth= $140^\circ$ .....	111
Figure 5. 18: Near Field Beamformer with 5 Linear Array (5x1 element) at ( $\phi_0=00, \theta_0=100$ ) ; RNF = $3\lambda$ ; 3 dB Beamwidth= $140^\circ$ .....	112
Figure 5. 19: Near Field Beamformer with 5 linear Array (5x1 element) at .....	112
Figure 5. 20: Near Field Beamformer with 5 Linear Array (5x1 element) at ( $\phi_0=00, \theta_0=00$ ) ; RNF = $3\lambda$ ; 3 dB; Beamwidth = $140^\circ$ .....	113
Figure 5. 21: Comparison of Near and Far Field Amplitude Patterns of Beamformer .....	114
Figure 5. 22: Comparison of Near and Far Field Phase Patterns of Beamformer with (5x1) Linear Array; ( $\phi_0=00, \theta_0=100$ ) (a) RNF= $3\lambda$ (b) RNF = $100\lambda$ .....	114
Figure 5. 23: Comparison of Near and Far Field Amplitude Patterns of Beamformer .....	115
Figure 5. 24: Comparison of Near and Far Field Phase Patterns of Beamformer with .....	115
Figure 5. 25 Comparison of Amplitude Patterns $E_\theta$ Component of Beamformer with (5x5) Planar array ( $\phi_0=450, \theta_0=100$ ) at (a)RNF= $3\lambda$ ; (b) RNF= $100\lambda$ ;.....	116
Figure 5. 26: Comparison of Amplitude Patterns $E_\phi$ Component of Beamformer with (5x5) Planar array ( $\phi_0=450, \theta_0=100$ ) at (a)RNF= $3\lambda$ ; (b) RNF= $100\lambda$ ;.....	116
Figure 5. 27: Comparison of Phase Patterns of $E_\theta$ Component of Beamformer with (5x5) Planar array ( $\phi_0=450, \theta_0=100$ ) at (a)RNF= $3\lambda$ ; (b) RNF= $100\lambda$ ;.....	117
Figure 5. 28: Comparison of Phase Patterns $E_\phi$ Component of Beamformer with (5x5) Planar array ( $\phi_0=450, \theta_0=100$ ) at (a) RNF= $3\lambda$ ; (b) RNF= $100\lambda$ ; .....	117
Figure 5. 29: Variation in Radiation Pattern of near field Beamformer with (5x1) Linear array: (a) $0.3\lambda$ (b) $0.5\lambda$ (c) $1\lambda$ (d) $2\lambda$ at ( $\phi_0=00, \theta_0=100$ ) .....	118
Figure 5. 30: Variation in Radiation Pattern of near field Beamformer with (5x5) Planar array: (a) $0.3\lambda$ (b) $0.5\lambda$ (c) $1\lambda$ (d) $2\lambda$ at ( $\phi_0=00, \theta_0=100$ ).....	119
Figure 6. 1: Conventional Block Diagram of TWI System .....	123
Figure 6. 2: Test scenario of SAR (Aftanas M.,2009) .....	125
Figure 6. 3: Proposed Block Diagram of TWI System.....	126
Figure 6. 4:Shapes and dimension of 2D flat plate Objects.....	129
Figure 6. 5 Half Cylinder Models. (a) Concave (b) Convex .....	130
Figure 6. 6: Signal transmission losses in TWI Systems .....	131

Figure 6. 7: TWI Scenario .....	132
Figure 6. 8: Wave incident on the outer surface of Wall .....	134
Figure 6. 9: Wave propagation through the wall .....	136
Figure 6. 10: Field incident on the target.....	140
Figure 6. 11: Field reflected from the target to the inner surface of the wall .....	142
Figure 6. 12: Wave refracted through the wall .....	145
Figure 6. 13: Field incident on the receiver .....	146
Figure 6. 14: Laplacian Pyramid Image Fusion technique (Fernández E. C., 2002).....	151
Figure 6. 15: Laplacian Pyramid Image Fusion flowchart .....	152
Figure 6. 16: Reconstructed images obtained through proposed near-field beamforming TWI system .....	154
Figure 6. 17: Reconstructed Images obtained through proposed near-field beamforming TWI system using Image Fusion only.....	155
Figure 6. 18: Stepped Frequency in Image Reconstruction.....	159
Figure 6. 19: Fused Stepped Frequency Images .....	159
Figure 6. 20: Comparison of Results of Imaging with (Aftanas, 2010) .....	162
Figure 6. 21: Comparison of Image reconstruction of Aquarium.....	163
Figure 6. 22: Comparison of an illumination of a flat and curved body from TWI perspective	164
Figure 6. 23: Half Cylinder Models ; (a) Concave ; (b) Convex .....	165
Figure 6. 24: Reconstructed image of Half Cylinder Models.....	166
Figure 6. 25: Reconstructed lit region 3D map of Half Cylinder Models .....	167

## Nomenclature

### Abbreviations

DAC	Digital to Analog Converter
DBF	Digital BeamForming
DFT	Discrete Fourier Transform
DSP	Digital Signal Processor
EM	ElectroMagnetic
EPDEH	Electric Point Dipole E and H Fields
FF	Far Field
FFT	Fast Fourier Transform
GFRP	Glass Fibre Reinforced Polymer
GHz / MHz	Giga / Mega Hertz
HRR	High Resolution Range
IFFT	Inverse Fast Fourier Transform
ISAR	Inverse Synthetic Aperture Radar
LOS	Light Of Sight
NF	Near Field
PRF	Pulse Repetition Frequency
RCS	Radar Cross Section
RX	Receiver
SAR	Synthetic Aperture Radar
SF	Stepped Frequency
SFWF	Stepped Frequency Wave Form
SOM	Subspace – based Optimization Method
TDOA	Time Difference Of Arrival
TOA	Time Of Arrival
TWI	Through Wall Imaging
TX	Transmitter
UWB	Ultra Wide Band

## **Symbols**

$\rho$	Rho
$\sigma$	Sigma, conductivity
$\varepsilon, \varepsilon_r$	Permeability, relative permeability
$\mu, \mu_r$	Permittivity, relative permittivity
$\theta$	Elevation angle
$\lambda$	Lambda, wavelength
$\varphi$	Azimuth angle
$E$	Electric field
$H$	Magnetic field
$J$	Magnetic current distribution
$M$	Electric current distribution
$K$	Wave number

## **Abstract**

This thesis presents a simulation model of Stepped Frequency (SF) and Near Field BeamForming (NF BF) based stationary Through Wall Imaging (TWI) system to scan an object behind the wall for the reconstruction of 2D/3D image of it. The developed simulation model of TWI system requires neither the movement of the antenna array nor the object to reconstruct the image of the object behind the wall, thus overcoming the limitation of SAR/ISAR based TWI system. The simulation model of TWI system arrived at in this thesis facilitates the scan of the desired scenario in both azimuth and elevation to maximize the information available for more effective reconstruction of the Image of object behind the wall. The reconstruction of the image has been realized through conventional image processing algorithms which are devoid of inversion techniques to minimize the computational burden as well as the overall execution time of the TWI system. Contrary to the present TWI systems, the proposed simulation model has the capability for the reconstruction of the shape and contour of the object. In addition, the formulated simulation model of the TWI system overcomes the previously imposed constraints on the distances of separation between the object and the wall as well as the wall and the target. The simulation model of TWI of this thesis can handle arbitrary distances (far field or near field) between the antenna array and the wall as well as the wall and the object, which is not the case with the existing TWI systems.

The thesis provides wave propagation analysis from the transmitting antenna array through the wall and the obstacle behind it and back to the receiver. Subsystems of TWI system like beamforming antenna arrays, wall and obstacles have been modeled individually. The thesis proposes a novel near field beamforming method that overcomes the usual requirement of 3D or volumetric near field radiation patterns of the beamforming array. Typical simulation results of NF BF with linear and planar arrays reveal the beam formation at a distance of one wavelength from the aperture of the array and which corresponds to the ratio of observation distance to aperture of array to be 0.2334. As a supplement to the presented NF BF a generic and versatile procedure to compute near field radiation patterns of antennas with prior knowledge of its either field or current distribution over the radiating aperture is also proposed. Examples of reconstruction of images of typical 2D and 3D objects are also illustrated in the thesis.



# **Chapter 1: Introduction**

## **1.1 Introduction**

Knowing the unknown is what interests the scientific community and it is a fascinating process. On the same lines, there are situations when people want to see things beyond opaque structures like walls of a room, which is not possible through naked eyes. The need or want for knowing the scenario behind the walls may arise during a rescue mission at times of earthquakes, fire or any other hazardous environments. The information that can be available beyond the walls during such conditions may be the ground plan of the room, positions of big or small objects and obviously presence of any person.

Through Wall Imaging (TWI) is one such emerging technology since the late 90's that aims to see things behind visually opaque structures like the walls. TWI can be used to detect buried people after natural disasters such as earthquake. It allows the fire rescue team to detect and locate people in case of a fire breakout in factories, apartments or office buildings. TWI can also be used by homeland security teams during a situation where identifying the number of hostages, hostage-takers and weapons are the main criteria and concern.

TWI uses Electromagnetic transmission and reception to acquire vision of scenes behind opaque structures. The scenes are usually non-accessible physically, optically, acoustically, or thermally. Many researchers and scientists are working on developing an efficient TWI system which can reconstruct behind the wall scenario accurately. However approaches and methodologies widely differ. Some experiments involve different methods of signal transmission and some see innovation in reception and scene reconstruction. A few techniques (Aftanas M., 2009; Leong K. M., 2000) for reconstruction of scene require prior information or marginal prior knowledge on scene statistics. A vast majority of existing TWI techniques involve motion of the system along the wall for its operation. In addition, the existing methods are unable to estimate or predict the shape of the object behind the scenario. This thesis provides the design and development of a novel simulation model of a TWI system which uses Stepped Frequency and Near Field - BeamForming (NF-BF) techniques to scan a through the wall scene and reconstruct 2D image of it. The reconstruction of the image of the object behind the wall has been realized through conventional digital image processing techniques which are devoid of inversion techniques and

would facilitate to identify the shape and contour of the object behind the wall. Unlike the existing TWI systems reported in the literature, the simulation model of TWI system of this thesis can handle any distance of separation (far field or near field) between the antenna array and the wall as well as the wall and the object.

## **1.2 Research Motivation and Problem Formulation**

The idea of TWI systems grew from Ground Penetrating Radar (GPR) systems (Baranoski, 2008). A GPR is a system that uses radar pulses to image the sub layers of the ground and identifies the presence of objects like mines, objects of archeological importance, changes in material, voids and cracks (Daniels, 2004). TWI is a cross-disciplinary area which involves research in electromagnetic propagation, antenna and waveform design, beamforming, wall compensation and image processing (Baranoski, 2008) among others. Since the late 1990s significant amount of research is being carried out on TWI systems and also have been increasingly published in the literature illustrating its ability to sense beyond a single wall from near-range (Frazier, 1996).

The TWI system ideally transmits ElectroMagnetic (EM) Waves/Microwaves through an antenna system that penetrates through the wall and it must be reflected/scattered by the targets behind. The reflected wave must again penetrate through the wall and must be received at the receive antenna system. One of the usual assumptions in TWI is that the wall cannot be too thick and preferably it should not itself constitute a severe attenuating device in the required frequency band of operation, to allow electromagnetic wave to travel through the wall and back. The EM waves undergo the optical phenomena of reflection, refraction, diffraction and absorption/attenuation every time the wave passes from one media to the other along with variation in velocity of the EM wave itself. Especially in a through wall scenario, multiple reflections between antennas, walls, and all the objects in the scanned area arise. The optical properties give rise to a very complex signal, full of noise and clutters, which is very difficult to interpret. Efficient signal processing algorithms have to be used or developed to decode the signals and predict the scanned environment and represent this information for the end users in an effective way.

The TWI approaches are generally borrowed from traditional optical, radar, and sonar image processing techniques (Baranoski, 2008). Imaging of structural features and contents of buildings requires systems which can scan a 3D space and provide 2D/3D images. But such systems cannot rely on Doppler processing alone for separation of desired features. Hence multilateration has been

the most common approach. Multilateration (Multilateration Executive Reference Guide, 2011) is the process of locating an object by accurately computing the Time Difference of Arrival (TDOA) of a signal emitted from that object to three or more receivers. It may also imply locating a receiver by measuring the TDOA of a signal transmitted from three or more synchronized transmitters. The general idea behind multilateration is to correlate range measurements from multiple sensors to specific points in the image. With sufficient spatial diversity from a large set of transmit/receive combinations, specific reflection points will start to integrate above the background interference (Baranoski, 2008). However, ambiguities will arise as the number of reflection points increases.

There are many efficient multilateration approaches like the Synthetic Aperture Radar (SAR) (Aftanas, 2009) and the Inverse Synthetic Aperture Radar (ISAR) (Leong K.M., 2000). But they have their own merits and limitations which are discussed in detail in Chapter 2 of the thesis. One of the few commercial available TWI systems is the CAMERO (Gassler J., 2008) which works with SAR technique. To image behind the wall scenario, the CAMERO must require a relative motion between the target and the radiating system; if both are stationary image is not formed. The system is not very compact and has to be carried around. To get high resolution images, one requires high band width data and hence the target scene must be illuminated at a higher Pulse Repetition Frequency (PRF). Existing methods use Sine, Impulse and M Sequence techniques which do not have high bandwidth leading to large errors and low resolution. If the system transmits data at high PRF, the received signal should be converted at a faster rate demanding a high computing ADC which makes the system very expensive. A relatively new technique called the Stepped Frequency (SF) is preferred for transmission and reception of signals with high bandwidth overcoming the need for high performance ADCs (Leong K.M., 2000). Present systems scan only in azimuth plane making it possible for reconstruction of the scene as a single or multiple blobs depending on the number of targets behind the wall.

Therefore there is a need for the formulation of a new approach for the development of TWI system overcoming the limitations of SAR as well as ISAR based TWI systems. The developed TWI system shall not require movement of the antenna array or the objects to reconstruct the image of the object behind the wall. In addition, the new formulation shall facilitate the scan of the desired scenario in both azimuth and elevation planes to maximize the information available for more effective reconstruction of the Image of object behind the wall. It is also desirable that the

developed TWI system must have the capability to handle any arbitrary distance of separation (far field or near field) between the antenna array and the wall as well as the wall and the object. It is also desirable that the reconstruction of the image of the object behind the wall be realized through conventional digital image processing techniques which are devoid of inversion techniques to minimize the computational burden and the overall execution time of the TWI system to realize the reconstruction of high resolution Image of the object behind the wall. From the above discussions, it is suffice to say a multidisciplinary approach involving the principles of antennas, wave-propagation, beamforming, signal and image processing is a necessity address the above cited needs and desirable features of TWI system. Formulation of an analytical/mathematical approach for the development of a simulation model of a TWI system which addresses the scheme to incorporate the above stated needs and desirable features constitute the core theme of this thesis. From research perspective, the proposed thesis answers the following questions.

### **1.3 Objectives**

As already stated each of the multilateration techniques and associated technology required for high resolution imaging are unique in their own way. Each aspect requires and demands tremendous research and development efforts, whether it is the technique to transmit signal or receive and process the data. Persistent and continued studies have been carried out in understanding and developing mathematical models for TWI systems involving the electromagnetic propagation, antenna and waveform design, beamforming, wall and target modeling, wall compensation and image processing.

This thesis aims to develop a mathematical model of Stepped Frequency based TWI Systems supported with Near Field Beamforming and wave propagation studies in multilayered mediums. The culminating objective of the proposed study is to reconstruct high resolution images of behind the wall scenarios irrespective of material mediums of the walls and targets. The developed simulation model would also identify and reconstruct the shape of the identified targets.

From the research perspectives, this thesis addresses the following questions.

- (1) Given an existing model of SAR based non stationary TWI system, what are the modifications necessary to make it stationary TWI system so as to overcome the

- requirement of relative motion between the radar antenna and the object behind the wall?
- (2) Can the developed model of stationary TWI system be used to image a stationary object/target behind the wall?
  - (3) Given such a model of a stationary TWI system, can the developed model be imparted the capability to handle the reconstruction of high resolution 2D Images along with the identification of shape and contour of the object to be imaged?

This thesis is structured to address the answers to the above listed research questions through the realization of the following objectives,

- 1. To review literature on UWB Radars, Through Wall Imaging concepts, Stepped Frequency waveform generation, Wall and Scatterer modeling, electromagnetic wave propagation through any given media, Digital Beamforming and ISAR imaging techniques including techniques to compensate for wall, clutter, phase, velocity, motion and reflection.
- 2. To arrive at an appropriate functional block diagram for Through Wall Imaging using Stepped Frequency Waveforms and Digital Beamforming
- 3. To design and simulate
  - 1. 2D Ultra Wide Band (UWB) Antenna array with beam steering to scan a 3D space and obtain the radiation pattern
  - 2. To carry out Near-field Beamforming Simulations
  - 3. To model the input Stepped Frequency waveforms, Wall and the Scatterers (stationary) behind the wall
- 4. To obtain and analyze electromagnetic field patterns along the path of transmitter-wall and back to the receiver through the wall
- 5. To develop high resolution images of behind the wall scenarios using the received signals and incorporate motion, velocity and phase compensations for accurate results

6. To simulate the Through Wall Imaging system for various test conditions and validate the results

#### **1.4 Original Research Contributions of the Thesis**

This thesis is associated with the following original contributions encompassing the multi-disciplinary topics of near field analysis of antennas, near field beamforming technique and Electromagnetic wave propagation study in multilayer material medium and Image Processing in the development of a simulation model of a stationary TWI system devoid of rotation of radar and target.

- Mathematical and simulation model of near field beamforming based stationary TWI system with Two Dimensional beam steering capability to reconstruct the image of the object including its shape and contour
- Novel near field Beamforming method that overcomes the prevalent requirement of 3D or volumetric near field radiation patterns of the beamforming array
- New imaging methodology involving fusion and translation methods to develop high resolution images of behind the wall scenarios with the amplitude of received signals
- Generic and versatile new procedure to compute near field radiation patterns of antennas with prior knowledge of its either field or current distribution over the radiating aperture
- Novel scheme which employs the hybrid combination of Geometrical Optics (Ray Technique) and Physical Optics techniques to reduce the computational burden in the wave propagation studies involved in the development of simulation model of TWI system

#### **1.5 Thesis Organization**

A brief description of the organization of the chapters of the thesis is as follows. The Thesis is organized into seven Chapters.

**Chapter 1** provides a brief introduction of TWI systems, problem formulation and the objectives of research.

**Chapter 2** has been structured to facilitate an introduction to the broad technology of TWI in general but with particular emphasis on Beamforming Techniques (including Antenna Array) as well as on important Algorithms in Digital Image Processing (DIP) relevant to TWI applications.

**Chapter 3** provides a discussion on research theses and papers pertaining to multilateration techniques like SAR, ISAR, Stepped Frequency in imaging, beamforming, wave propagation in multilayered media and image processing along with their contributions towards development of efficient TWI systems. This chapter also includes discussion on advancements in SAR and ISAR based TWI system. In addition, the short comings/limitations in the current research on TWI and the potential scope for original contributions towards development of an efficient TWI system have been appropriately identified.

**Chapter 4** discusses generalized new approach in the form of a detailed analytical formulation which would facilitate the determination of near field and far field radiation pattern of an antenna of given geometrical configuration including aperture and planar. It forms the foundation for the development of simulation model of a TWI system.

**Chapter 5** presents a novel approach to carry out near-field beamforming which sees an apt application in TWI Systems. This chapter discusses the mathematical formulation involved in carrying out both the near-field and far-field beamforming. In this chapter, a technique to achieve near-field/far-field beamforming is proposed which circumvents the earlier stated requirement of 3D near-field radiation pattern measurement

**Chapter 6** discusses formulation and analysis involved in wall modelling, object modelling, and the methodology to use near-field beamforming to image objects behind the wall. It gives a new and easier imaging methodology to visualize 2D and 3D objects behind the wall. It also provides an analysis and discussion of results obtained on subjecting the developed TWI model to different scenarios and test conditions. The chapter also presents the total system simulation results obtained from stepped frequency generation and discusses its effectiveness in generating high resolution images of behind the wall scenarios

**Chapter 7** presents a brief recapitulation of summary, inferences and technical conclusions derived out of the undertaken research study of this thesis. Potential scope and academic avenues for further research which emerge as logical extensions of the analytical formulations and simulations of this thesis are also highlighted

## **Chapter 2: Introduction to Through Wall Imaging and Beamforming Techniques**

### **2.1 Introduction**

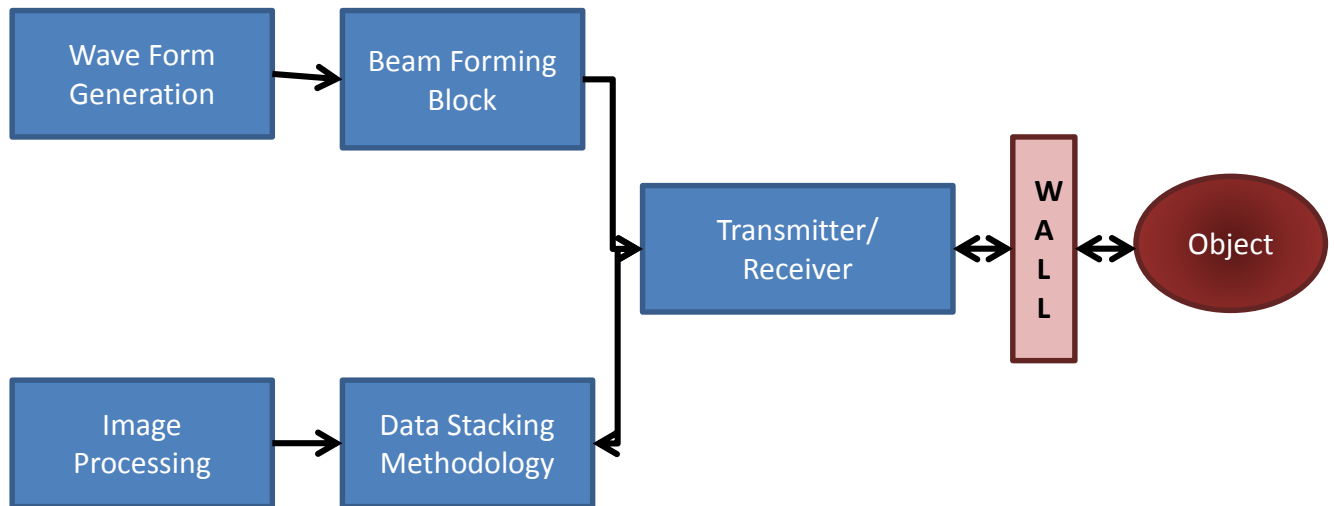
High resolution imaging of objects behind the walls, doors and other visually opaque structures using Electromagnetic/Microwave signals is gaining utmost importance for commercial and non-commercial applications. Through Wall Imaging (TWI) systems are Microwave imaging systems that provide high resolution visualization of behind the wall scenarios. They come handy during rescue missions in case of fire, earth quake, avalanche or hostile activity. It can also be used for surveillance and reconnaissance. TWI is a cross-disciplinary topic which involves research in electromagnetic propagation, antenna, antenna array design, beamforming, Signal and Image processing among others (Baranoski, 2008). The idea of TWI system evolved through Ground Penetration Radar (GPR). The working principles of TWI are similar to GPR except that the images are behind the wall rather than the ground (Baranoski, 2008). GPR uses electromagnetic radiation to detect objects of archaeological importance, changes in material, voids and cracks (Daniel D.J., 2004). GPR and TWI systems generally use Multilateration techniques like Synthetic Aperture Radar (SAR) and Inverse. Synthetic Aperture Radar (ISAR) to scan a given area. Multilateration is a process of locating an object by accurately computing the Time Difference Of Arrival (TDOA) of a signal emitted from that object to multiple receivers (sensors). The general idea behind Multilateration is to correlate range measurements from multiple sensors to specific points in the image (Neven W.H.L. *et al*, 2005). SAR and ISAR have their own limitations or pre-requisites for imaging – A relative motion between target and radar is a must; consequently stationary objects cannot be imaged. Since the late 1990s significant research is being carried out on TWI systems. TWI systems have been proved to work even beyond a single wall from near-range (Frazier L.M., 1998). Existing TWI systems are moved in small steps in horizontal directions to cover a certain azimuthal angular sector. Data obtained in this way shows loss in elevation. One has to carryout scanning in vertical directions to limit the loss but the process is too tedious and time consuming. In addition, for the formation of image using such systems, there is a requirement of relative motion between the radar and the target behind the wall. Hence it is appropriate to propose a TWI system which is stationary and yet can perform Two Dimensional Scan (Both Azimuth and elevation angles) of a given imaging scenario overcoming requirement of the relative



motion between radar and target. It will be of significant interest and importance to explore the feasibility of incorporating the Stepped Frequency method into the system in conjunction with the Beamforming technique to improve the resolution of the image and also formation of images at faster pace. This chapter has been structured to facilitate an introduction to the broad technology of TWI in general but with particular emphasis on Beamforming Techniques(including Antenna Array) as well as on important Algorithms in Digital Image Processing (DIP) relevant to TWI applications.

## 2.2 Through Wall Imaging (TWI) System

An example of a functional block diagram for imaging an object behind the wall scenario utilising the Beamforming technique and the Imaging principles is shown in Figure 2.1.



**Figure 2.1: Functional Block Diagram of a Beamforming Based TWI system**

The way in which the waveforms are generated and the power associated with them differs with every generation technique, such as, sine wave type or impulse type. The sine wave technique has many advantages over the impulse technique but its limitation is that it cannot be put on a monolithic integrated circuit. It can be preferred over other methods because of the: Ease in modeling of the waveforms, achievable bandwidth, Stability and appreciable Signal to Noise Ratio (SNR) (Sachs J., 2003). The waveform generation block is connected to the beamforming block. It in turn is connected to the antenna block which illuminates the wall. Beamforming methodologies differ with the choice of scanning techniques. The scanning can be carried out by

SAR or ISAR methods. Any scanning technique however requires an antenna that functions in both in transmit and receive modes. The antenna can be a single element or an array of elements. There can be a single transmitter and single receiver or a single transmitter and multiple receivers or multiple transmitters and multiple receivers. The choice of antenna configuration, its size as well as its performance parameters like the radiation pattern, beam width and frequency of operation play a vital role. The transmitted beams propagate and impinge on the target undergoing optical phenomena like reflection, scattering, diffraction and refraction. This in addition to re-radiated field by the target propagated again through the wall and captured at the receiver would lead to loss in the signal strength of the received field and thereby loss/distortion of data. A detailed discussion on mathematical modeling and analytical formulation of wave propagation through material medium and free space is presented in Chapter 6.

The received fields will be processed using one of the several migration methods like the back projection, back propagation or ISAR imaging methods involving forward and inverse Fourier transforms or one can even use 3D Fourier transforms. The received (scanned) data will be stacked first and will be further processed to generate an image with an acceptable resolution. The image processing methods can involve edge detection, Joint Time Frequency Transform (JTFT), background subtraction or even the fusion techniques (Aftanas M., 2009). The image processing methods can involve edge detection, JTFT, background subtraction or even the fusion techniques. The subsequent sections to follow explain the methodologies involved in each of the sub-blocks in detail.

### **2.3 Waveform Generation**

There are many methods for generation of waveform which involve either constant or continuous frequencies. The sine wave, impulse techniques and its variants are however the classical methods used for decades. These techniques are widely accommodated in GPR systems and they help in both transmission and reception of the electromagnetic waves which will be further processed to obtain an image of the given scenario. In this chapter the theory behind the various waveform generation techniques and technology behind its transmission, reception and data processing are provided. A detailed discussion on the generation of different types of waveforms is presented in Appendix – 1. The thesis adopts only the methodology of sine wave waveform generation method and not the technique behind its transmission and reception.

### 2.3.1 Sine wave technique

The sine wave technique is one of the most sensible and easy to model techniques having high signal bandwidth where a sweep or stepped frequency EM wave stimulates a given target. The signals generated through Sine Wave Technique have high SNR, excellent noise rejection and require ADC with low sampling rates. Vector network analyzers and stepped frequency radars typically apply or use the sine wave approach.

Figure 2.2 illustrates the general block diagram of sine wave technique based imaging radar. It consists of step-frequency synthesizer and an additional up-conversion and down-conversion circuitry. The frequency synthesizer allows the pulse to- pulse variation in the frequency of the signal. The transmitted signal is characterized by frequencies which are actually sum of components from a local oscillator and the frequency synthesizer. The mixers up convert the signal to RF and the resulting signal are power amplified and transmitted to illuminate the target. Each pulse of the modeled pulse train (a sequence of pulse, each varying in frequency) is transmitted for a time  $T/2$  and received at stored at time remaining  $T/2$ ,  $T$  is the pulse time period.

This item has been removed due to third party copyright. The unabridged version of the thesis can be viewed at the Lanchester Library, Coventry University.

**Figure 2.2: Block Diagram for Generation of Sine Waveform (Kucukkilic T., 2006)**

On the receive side, the returned signal is down converted to IF frequency and further brought down to baseband by mixing it with the output of the frequency synthesizer. To retain both the amplitude and phase information, the output of the Phase (Quadrature) detector is in the form of in phase (I) and quadrature (Q) components. The detector eliminates blind phases, improves signal-to-noise ratio by 3 dB and discriminates the positive from negative of the received Doppler signal frequencies. The typical sampling rate is one complex sample per pulse width. Each sample is termed a range bin R, as it represents the signal from a range window of length  $c\tau/2$ . The detector output for all range bins of interest due to all N pulses in a burst is collected prior to performing any processing. The signal transmission, signal reception, data storage and one of the many methods for image processing are depicted in Figure 2.3.

This item has been removed due to third party copyright. The unabridged version of the thesis can be viewed at the Lanchester Library, Coventry University.

### **Figure 2. 3: Sine Wave Technique Based Radar Data Processing (Kucukkilic T., 2006)**

For each pulse of width ' $\tau$ ' in the pulse train of varying frequencies, the received signal of duration ' $T$ ' is stored as a complex value consisting of amplitude and phase information. The data is stored in form of a matrix for multiple pulse trains and with varying frequencies. To this data, Inverse Discrete Fourier Transform (IDFT) is applied column-wise and later subjected to DFT. The

magnitude of elements of the derived complex matrix is computed to obtain an image. The image usually consists of spots of high intensity in the presence of structures or obstacles in imaging scenario. An example where six scattering objects are illuminated and imaged is depicted in Figure 2.4. The image is labeled as cross range along x -axis and slant range along y -axis. The slant range refers to distance measured along the radar line of sight and cross range is the one perpendicular to it.

This item has been removed due to third party copyright. The unabridged version of the thesis can be viewed at the Lanchester Library, Coventry University.

**Figure 2. 4: Imaging of Six Point Scatterers (Kucukkilic T., 2006)**

Stepped frequency techniques provide instantaneous spectrum but has a limitation that it requires a data collection time to observe response for a desired bandwidth. The observation time  $T_{Obs}$  can be calculated for moving or stationary targets as (Sachs J., 2003)

$$4 T_{Obs} |v_{\max}| = \frac{c}{B} \quad \dots (2.1)$$

Where,  $v_{\max}$  is the maximum velocity of a scatterer appearing in the imaging scenario,  $c$  is the speed of light and  $B$  is frequency bandwidth. It implies that the technique can be easily restricted in its applicability if multiple receivers are employed to image any scenario. One other demerit of the complex stepped frequency/ sine wave technique being used for imaging is that it is difficult to process in form of a semiconductor chip.

### 2.3.2 Impulse Technique

Like sine wave, the impulse technique is also a classical method to generate waveforms of large bandwidth. However, this method involves generation of short pulses of sufficient energy to stimulate any imaging scenario. The reflected echo signals obtained from repetitive illumination of target scene are under-sampled and captured on the Display. Data is stored at one sample per pulse. Similar to sine wave technique, the measurement time  $T_{Obs}$  will be high. Still it is accepted in many applications as the propagation speed of the transmitting waves is significantly higher than the typical speed of a target. (Sachs J., 2003) states that impulse technique has an advantage in handling signals having a large instantaneous bandwidth compared to sine wave technique due to the settling of the measurement system, low power consumption and low manufacturing costs of measurement device.

The impulse technique is known to handle high amplitude signals and control the sampling but to gain an acceptable SNR, an adequate amount of the energy must be concentrated in the short duration pulses illuminating the target. The impulse technique suffers while handling a larger bandwidth and the sampling time control is performed by a threshold triggering. Generally a linear ramp is generated synchronously to the transmitting signal and its duration is identical to the recording time. On setting a threshold and moving it over the ramp, the sampling point of the signals is shifted. Any inadequacy of the ramp and the threshold voltage will corrupt the data because of jitter, time drift and non-equidistant sampling. Noise removal requires complex hardware, signal processing and added control loops complicating the usability of device (Sachs J., 2003).

Another technique closely related to the impulse technique is the M-Sequence technique which has an additional advantage of stability compared to the sine wave method. The M-Sequence like the impulse technique involves transmitting signals of higher band width and under sampling the received echoes. The M- (Maximum Binary length) sequence method varies from the impulse technique in two aspects; one being the way the data is transmitted and the other is the sampling control. Figure 2.5 demonstrates the M-Sequence approach where a digital shift register generates the M-sequence of higher bandwidth (up to a few GHz) which is transmitted through a transmitter and the received signal will be under sampled and stored. The M-Sequence technique has large power requirements to generate signals of relatively low amplitudes and maintain a certain SNR.

The only advantage of M-sequence technique over the sine wave method is that it can easily be put in form of a monolithic integrated circuit chip.

This item has been removed due to third party copyright. The unabridged version of the thesis can be viewed at the Lanchester Library, Coventry University.

**Figure 2. 5: Block Diagram of M-Sequence Technique (Kmec *et al*, 2006)**

The sampling control of M-Sequence technique involves a binary divider which suppresses drift, jitter and non-linear sampling unlike the impulse method. The sampling rate is chosen to be higher than the processing throughput to suppress random noise by synchronous averaging. M-Sequence differs from the impulse technique in notably two aspects; one being that the sequence of transmitted signals is random but periodic and the other being the logic behind the received signal. M-Sequence technique receives signal using the binary divider which releases a sampling event after it has run completely through all its internal states. This sampling method accelerates the process of data acquisition to meet the needs of a measurement task. For high speed applications long binary dividers are used. The only limiting factor is the complex signal processing involved in processing the data captured. Most of the GPRs like DEMINE (Belgium), DEMAND (Italy) and a project from QinetiQ (UK) work on the principles of M-Sequence (Sachs J., 2003).

As stated earlier, this thesis considers only the transmission aspect of the discussed waveform generation techniques and not the reception and processing methods implying that the proposed thesis adopts only the waveform generation methodology and not the technique involved in its transmission or reception. The primary aim of this thesis is the development of a mathematical model of TWI application by combining various techniques to obtain high resolution images of behind the wall scenario. All the issues pertaining to the technique and technology to realize the TWI application on the monolithic integrated circuit chip are secondary from the perspective of

the core theme of the proposed thesis. The sine wave technique is chosen over the M-Sequence technique in the thesis because of the ease in modelling the waveforms, the achievable higher bandwidth and stability, and higher signal to noise ratio.

The following section discusses beamforming technique which performs directional transmission of signals that are generated by the waveform generation block. The beamforming unit can control both the phase and amplitude of generated signals and lies prior to the array of antenna elements.

## **2.4 Beamforming**

Beamforming is a signal processing technology that is used to control the directionality of signal transmission or reception. Beamforming has been in use for many years in the fields of communication, surveillance, radio and acoustic radars. In Beamforming, both amplitude and phase shift (weights) at each element in the antenna array control the directionality of the transmitted or received beam without physical motion of the antenna array. While phase shifts control the directionality of the beam, the amplitude values control the side lobes and null steering for rejection of radio interference. This thesis however explains only the transmit beamforming.

The principles of Beamforming involves the knowledge of a few basic terminology of antenna like the radiation pattern, directional antenna, antenna array, and electronically steered arrays. Beamforming is being used for many years and is known to be achieved in either analog or digital domains. Analog methods are known to be sensitive to component tolerance and drifts and hence digital methods are preferred. Digital Beamforming generally produces directional beams by introducing either time shifts or phase shifts. Time shift approaches allow forming and steering of beams by introducing delays which are independent of the operating frequency and bandwidth of the antenna elements. Time shift approaches are generally applicable to systems involving large bandwidths.

Phase shift approaches introduce a phase instead of true time delays in the antenna elements. Though this approach is simpler it can only be used for systems with small bandwidth. The choice of using time shift or phase shift approach is determined by the acceptable loss of gain when beam is steered (Montebugnoli *et al*,2004). Gain depends on the bandwidth  $B$  and time delay  $\Delta t$  (different time of arrival of signal at the elements due to physical dimension of the array) as given in the equation (2.2)



$$G = \frac{\sin(\pi B \Delta t)}{\pi B \Delta t} \quad \dots(2.2)$$

It is easier to understand the basic beamforming implementation through a linearly spaced array and Figure 2.6 shows an 8 element linear array on which plane is incident at different intervals of time depending on the incident angle  $\theta$ . Hence the required time delay for every antenna element in the array is given by Equation (2.3)

$$\Delta t = \frac{(n-1)d \sin \theta}{c} \quad \dots(2.3)$$

where, d is the inter element spacing and c is the speed of light.

This item has been removed due to third party copyright. The unabridged version of the thesis can be viewed at the Lanchester Library, Coventry University.

**Figure 2. 6: Block Diagram of 8 Element Linear Array BeamFormer (Montebugnoli *et al*,2004)**

The notation 'n' in both Figure 2.6 and Equation (2.3) denotes the n<sup>th</sup> element of the array with n varying from 1 to N expressed as n=1,2, ..., N and 'N' denotes the total number of elements in the array. For the linear array shown in Figure 2.6, N=8.

As already mentioned, such a delay introduced to each element in the array can steer beam in any specified direction while the weights  $W_n$  allow to control the sidelobe levels. All these findings lead to consider the array as a Finite Impulse Response [FIR] filter in spatial domain and hence

the weights can be computed similar to the coefficients of a standard filter. Taking FFT of  $W_n$  (amplitude coefficients), the radiation pattern  $E(\theta)$  of a linear array is given by equation(2.4)

$$E(\theta) = \sum_{n=0}^{N-1} W_n e^{j(knd \sin \theta)} \quad \dots (2.4)$$

where,  $k=2\pi/\lambda$  The signal arriving at antenna element 1 is known to have a phase of  $0^0$  while the last element (n) in the array leads in phase as  $= knds \sin \theta$ . This leads to the definition of Array Propagation Vector  $v$  that contains the information of the direction of arrival of the signal given in equation (2.5) as

$$v = \begin{bmatrix} 1 & e^{jkd \sin \theta} & \dots & e^{jk(N-1)d \sin \theta} \end{bmatrix} \quad \dots (2.5)$$

and hence array factor is defined as in equation (2.6)

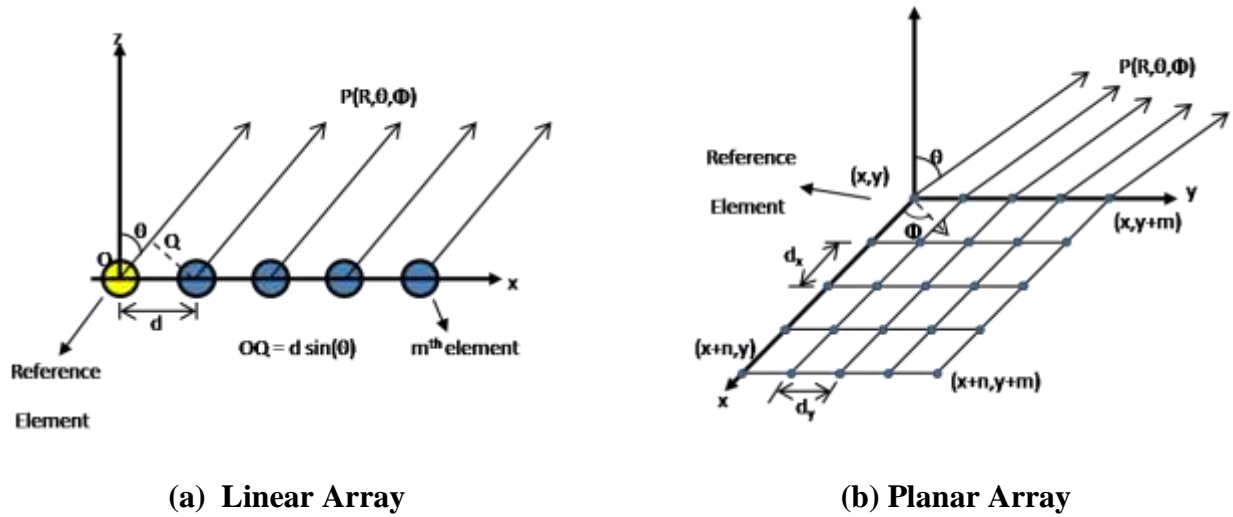
$$A(\lambda, \theta) = W^T v \quad \dots (2.6)$$

In vast majority of research on array beamforming, the observation point is assumed to be in the far-field of the array implying that the radiation pattern of the beamformer will be considered at a distance of at least  $R = 2D^2/\lambda$  from the array, where R is the distance from the array; D is largest dimension of the array; and  $\lambda$  is operating wavelength. When the observation point is located at a far field distance, the resulting incident wave-front on the test aperture of test antenna array is planar. The planarity of the incident wave-front on the aperture of test antenna simplifies the analyses of antenna as well as beamforming. In antenna engineering, analysis of radiation pattern of antenna at a distance of observation  $R < 2D^2/\lambda$  is called near-field radiation pattern. The following sub-sections discuss the far-field and near-field beamforming.

### 2.4.1 Far-field Beamforming

In far-field beamforming, it is assumed that the rays carrying electromagnetic field incident on or radiated from all the antenna elements are always parallel. Conventionally, the distance between the array elements and the observation (source) point is factored out in the determination of amplitude variation of the radiation pattern. However, progressive phase shift of the array elements relative to reference element is required. Figure 2.7 demonstrates the concept of far-field for both linear and planar (2D) arrays. As explained previously, to steer the beam electronically (without

physical movement of the antenna) at desired angles, a phase shift is introduced at every element. The phase shift depends on the elemental spacing (distance between individual elements of the array), angular coordinates where the main beam is to be directed and also the frequency of operation. The phase shift does not depend on the actual distance between the field (observation) point and the individual elements of the array.



**Figure 2. 7: Far-Field Beamforming**

For ease of understanding in both cases of the linear and planar array beamforming, the first or the center element is considered as the reference element. The reference element has zero phase and the subsequent elements in the array will have a progressive increase in phase. An easier way to achieve beamforming is to have the knowledge of radiation pattern of the individual elements of the array and convolute the phase information to it and achieve the directional pattern in desired angles. The phase information is provided in form of product of Array factor,  $A(\theta, \phi)$ , and phase factor,  $P(\theta, \phi)$ .

It is an implicit assumption that all the elements of the array are identical and are spaced equally; for a linear array let us consider that the radiation pattern in azimuth plane is  $E_\phi$  and  $E_\theta$  be the radiation pattern in the elevation plane. The equations for radiation patterns are provided and explained in detail in section 2.5.

In Figure 2.7,  $P(R, \theta, \phi)$  represents the observation point in Spherical Coordinate system,  $R$  is far-field distance measured from the reference element to the observation point  $P$ . The array factor

$A(\theta, \varphi)$  for a linear array can be represented as  $1 \times m$  matrix where  $m$  denotes the number of elements in the array. The array factor  $A(\theta, \varphi)$  for linear array is given by (Balanis C.A., 2005)

$$A_{(1,p)}(\theta, \varphi) = e^{-jk(p-1)d \sin \theta} \quad \dots(2.7)$$

$$p = 1, 2, 3, \dots, m$$

$d$  is the inter-element spacing

The beam steering phase factor  $P(\theta_0, \varphi_0)$  is given in Equation (2.8) as

$$P_{(1,p)}(\theta_0, \varphi_0) = e^{+jk(p-1)d \sin \theta_0 \cos(\varphi_0)} \quad \dots(2.8)$$

where  $(\theta_0, \varphi_0)$  are the desired azimuth and elevation angles along which the main beam of the beamforming array should point or along which the main beam of the array needs to be steered.  $(\theta_0, \varphi_0)$  are also termed as beam steering or beam pointing angles. Equations for radiation patterns of far-field beamforming linear array are given by Equations (2.9) and (2.10)

$$E_{\theta}^{FF}(R, \theta, \varphi, \theta_0, \varphi_0) = E_{\theta}^E(R, \theta, \varphi) \times \sum_q A_{(1,q)}(\theta, \varphi) \times P_{(1,q)}(\theta_0, \varphi_0) \quad \dots(2.9)$$

$$E_{\varphi}^{FF}(R, \theta, \varphi, \theta_0, \varphi_0) = E_{\varphi}^E(R, \theta, \varphi) \times \sum_q A_{(1,q)}(\theta, \varphi) \times P_{(1,q)}(\theta_0, \varphi_0) \quad \dots(2.10)$$

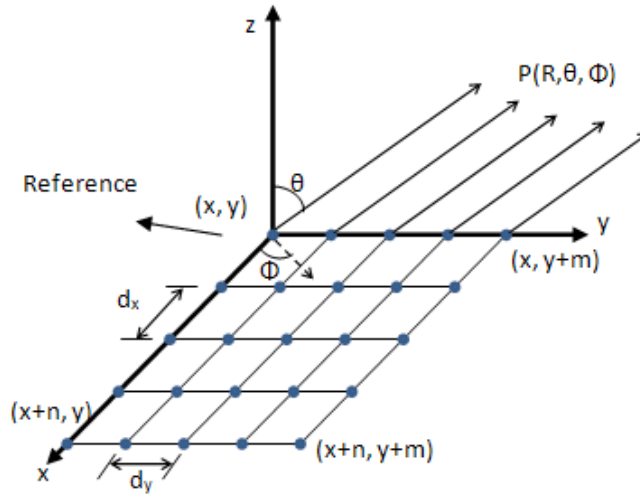
$$q = 1, 2, 3, \dots, n$$

Where  $E_{\theta}^{FF}(\dots)$  and  $E_{\varphi}^{FF}(\dots)$  are the elevation ( $\theta$ ) and azimuthal ( $\varphi$ ) components of radiation patterns of the beamforming linear array. Equation (2.9) is applicable if the antenna elements are placed conforming to horizontal polarization. Equation (2.10) is applicable for the linear array elements positioned for vertical polarization.

$E_{\theta}^E(\dots)$  and  $E_{\varphi}^E(\dots)$  are respectively the  $\theta$  and  $\varphi$  components of radiation patterns of individual elements of the array. They are also called the elemental radiation patterns of the array. From the expressions (Equations (2.9) and (2.10)) for the far-field radiation patterns of beam forming linear array, it is evident that the elemental radiation pattern of all the array elements is same and

therefore it is factored out of the summation operation involving the product of the array factor  $A(\theta, \varphi)$  and the beam steering phase factor  $P(\theta_o, \varphi_o)$ .

Unlike a linear array, the elements of a planar array are oriented in mutually perpendicular or orthogonal directions as shown in Figure 2.8. The mutually orthogonal placement of the elements of the planar array facilitates the provision for two dimensional beam steering implying that the beam can be steered for varying angles of both  $\theta_o$  and  $\varphi_o$  in 3D space.



**Figure 2. 8: Beam Forming with Planar Array**

For planar arrays, inter element spacing in x direction as well as in y directions have to be incorporated. Accordingly the array factor  $A_{(q,p)}(\theta, \varphi)$  and beam steering phase factor  $P_{(p,q)}(\theta_o, \varphi_o)$  for a far-field beamforming planar array are given by:

$$A_{(q,p)}(\theta, \varphi) = A_p(\theta, \varphi) \cdot A_q(\theta, \varphi) \quad \dots(2.11)$$

$$A_p(\theta, \varphi) = e^{-jk(x_{r1} + (p-1)d_x) \cdot \sin\theta \cos\varphi} \quad \dots(2.12)$$

$$A_q(\theta, \varphi) = e^{-jk(y_{r1} + (q-1)d_y) \cdot \sin\theta \sin\varphi} \quad \dots(2.13)$$

$$p = 1, 2, 3, \dots, m$$

$$q = 1, 2, 3, \dots, n$$

$m = \text{number of elements along } x\text{-axis}$

$n = \text{number of elements along } y\text{-axis}$

$(x_{r1}, y_{r1}) = x \text{ and } y \text{ coordinates of reference element } (p = q = 1)$

$dx = \text{spacing between elements along } x\text{-axis}$

$dy = \text{spacing between elements along } y\text{-axis}$

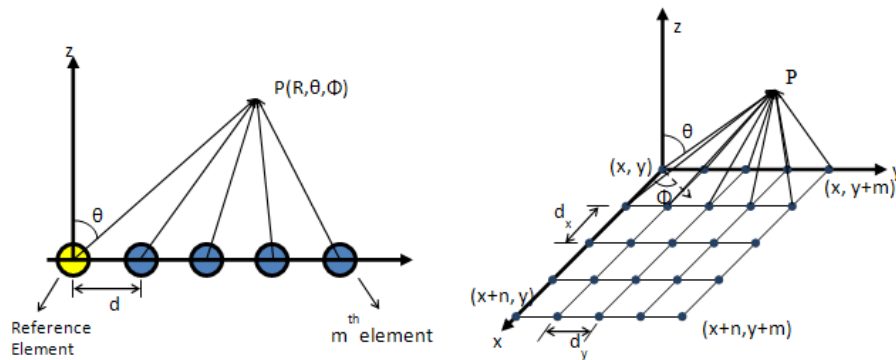
The resulting equations for far-field radiation pattern of beamforming planar array with beam pointing angular coordinates of  $\theta_o$  and  $\varphi_o$  are given by the following equations:

$$E_{\theta}^{FF}(R, \theta, \varphi, \theta_o, \varphi_o) = E_{\theta}^E(R, \theta, \varphi) \times \sum_{p=1}^m \sum_{q=1}^n A_{(p,q)}(\theta, \varphi) \cdot P_{(p,q)}(\theta_o, \varphi_o) \quad \dots(2.14)$$

$$E_{\varphi}^{FF}(R, \theta, \varphi, \theta_o, \varphi_o) = E_{\varphi}^E(R, \theta, \varphi) \times \sum_{p=1}^m \sum_{q=1}^n A_{(p,q)}(\theta, \varphi) \cdot P_{(p,q)}(\theta_o, \varphi_o) \quad \dots(2.15)$$

### 2.4.2 Near-Field Beamforming

Unlike far-field beamforming, in the near-field beamforming the electromagnetic rays impinging on the aperture of the array are not assumed to be parallel as the distance between source and receiver is small. Figure 2.9 demonstrates the near-field beamforming for both linear and planar arrays.



(a) Linear Array

(b) Planar Array

Figure 2. 9: Near-Field Beamforming

The significant contrasts between the far-field and near-field beamforming are :

- (i) In near-field beam forming, the rays incident on or radiated from all the elements of the array cannot be assumed to be parallel.
- (ii) Unlike in far-field beamforming, the elemental radiation patterns cannot be the same for a given observation point  $P(R, \theta, \phi)$  since the distance between the different array elements and the specified observation point is not constant.
- (iii) As a consequence of (ii), the spherical polar angles  $\theta$  and  $\phi$  of a point  $P$  subtended by various antenna elements will be different for each elements of the array. Therefore, the elemental radiation pattern of the individual array elements cannot be assumed to be same. Accordingly, the elemental radiation patterns cannot be factored out from the summation operation as in the case of far-field beamforming scenario.

There is an abundance of literature on far-field beamforming techniques. However, the reported research on near –field beamforming appears to be rather limited in open literature. Probably, this is in tune with heavy and continued emphasis in Antenna Engineering on the far-field characterization of the antenna radiating elements and arrays. The focus on near-field characterization of the antenna radiating elements is usually significantly low relative to that of far-field case. It is generally accepted that near-field analysis or characterization is more involved and tedious task than its far-field study.

There are no close form expressions available in literature for near-field beamforming.( Kennedy R.A. et al., 1998) from the Australian National University have carried out research on near-field beamforming. They have developed an analytical formulation for near field beamforming based on radial reciprocity transformation. The developed formulation invokes spherical harmonic solutions to wave equations. The given near-field radiation pattern specifications are mapped to an equivalent far-field radiation pattern specifications. This method requires volumetric measurements of antenna radiation patterns. Radial reciprocity transformations reconstruct far-fields only along the spherical surfaces concentric with the origin of the measured near-field system. The near-field beamforming using radial reciprocity transformation is performed in three steps as following (Kennedy R. et al, 1998):

1. Measurement of volumetric Near-field radiation patterns for  $\theta = 0 - 180$ ,  $\phi = 0 - 360$  for a specified near field distance ' $r_0$ '
2. Calculation of the Coefficients ( $\alpha_n, \beta_{nm}, \gamma_{nm}$ ) for the desired near-field radiation-pattern at  $r = r_0$  using equations (2.16 - 2.18)

$$\alpha_n = \frac{n + \frac{1}{2}}{2\pi r^{-\frac{1}{2}} H_{n+\frac{1}{2}}(kr)} \times \int_0^{2\pi} \int_0^\pi b_r(\theta, \phi; k) P_n(\cos \theta) \sin \theta d\theta d\phi \quad \dots(2.16)$$

$$\beta_{nm} = \frac{n + \frac{1}{2}}{2\pi r^{-\frac{1}{2}} H_{n+\frac{1}{2}}(kr)} \frac{(n-m)!}{(n+m)!} \times \int_0^{2\pi} \int_0^\pi b_r(\theta, \phi; k) P_n^m(\cos \theta) \sin \theta e^{-jm\phi} d\theta d\phi \quad \dots(2.17)$$

$$\gamma_{nm} = \frac{n + \frac{1}{2}}{2\pi r^{-\frac{1}{2}} H_{n+\frac{1}{2}}(kr)} \frac{(n-m)!}{(n+m)!} \times \int_0^{2\pi} \int_0^\pi b_r(\theta, \phi; k) P_n^m(\cos \theta) \sin \theta e^{jm\phi} d\theta d\phi. \quad \dots(2.18)$$

3. Computation of the Far-field pattern at  $r = r_\infty$  using equation(2.19)

$$b_r(\theta, \phi; k) = r^{-\frac{1}{2}} \left( \sum_{n=0}^{\infty} \alpha_n H_{n+\frac{1}{2}}^{(1)}(kr) P_n^m(\cos \theta) \times (\beta_{nm} e^{jm\phi} + \gamma_{nm} e^{-jm\phi}) \right) \quad \dots(2.19)$$

Where,  $P_n^m(\cdot)$  is Legendre's function

$H_n$  is Hankel function

$n$  is the order;  $m=0$

$\alpha$ ,  $\beta$  and  $\gamma$  are beam pattern co-efficients

$\theta$  and  $\phi$  are elevation and azimuth angles

To summarize, radial reciprocity described in (Kennedy R.A., et al. 1998) depends on far-field techniques. The radial reciprocity utilizes specifications of near-field radiation pattern and maps it to an equivalent far-field pattern specification. This method requires 3D or volumetric measurements of Near-field pattern of the array at a desired near-field distance. Spherical near-



field to far-field transformation is required in this analysis. Then the weights are computed for far-field beamforming and the computed weights also satisfy the near-field specification.

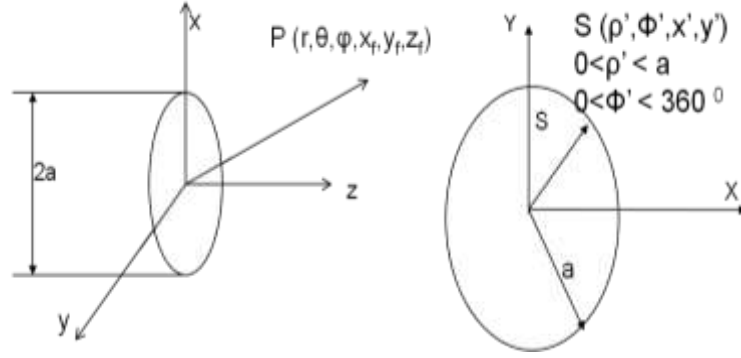
In Chapter 5 of this thesis, a technique to achieve near-field/far-field beamforming is proposed which circumvents the earlier stated requirement of 3D near-field radiation pattern measurement. Unlike in (Kennedy R.A. et. al, 1998), the weights for steering of the beam are computed directly for the near-field specification. The arrived formulations for the array factor  $A(\theta, \varphi)$  and beam steering phase factor  $P(\theta_o, \varphi_o)$  essential for beamforming and beam steering are uniformly valid for both near-field and far-field beamforming scenarios. The proposed near-field beamforming analysis is valid for both linear and planar array antenna configurations. The developed near-field beamforming analysis requires the determination of near-field radiation pattern of the antenna elements. A generalized procedure to compute the near-field radiation patterns of the antenna is also presented in chapter 4 of this thesis. The presented near-field radiation pattern analysis of the antenna requires prior knowledge of either the field distribution or the current distribution over its radiating aperture.

## **2.5 Analysis of Far Field Radiation Pattern of Aperture Antennas:**

In this section, analytical formulations for the computation of far field radiation patterns of aperture antennas such as wave guides and horn antennas are reviewed with succinct and relevant technical details. The characteristics of radiation pattern of aperture antenna such as waveguides and horn are significantly determined by the size and shape of radiating aperture, the choice of propagating mode, the distance of observation from the radiating aperture and the frequency of operation. A vast majority of aperture antennas most commonly used in antenna engineering is featured with either rectangular or circular radiating aperture. Most of the commercially available waveguide and horn antennas are usually designed for dominant mode of propagation. The term dominant mode implies the mode having lowest cut off frequency. The operating frequency band of aperture antenna is so chosen that the waveguide type of antennas is virtually a high pass filter. The upper operating frequency is chosen so as to be lower than the first higher mode of propagation. To orient this section to the specific antenna elements discussed elaborately in Chapters 4, 5 and 6, particular emphasis of this section will be devoted to circular cylindrical waveguide and conical horn. This section extends the formulations available in (Balanis C.A., 2005) to the circular waveguide.

### 2.5.1 Circular Aperture

A coordinate system for the computation of radiation pattern of a circular cylindrical waveguide is shown in Figure 2.10.



**Figure 2. 10: Coordinate System for Radiation Pattern Analysis of Circular Waveguide**

The circular waveguide antenna is assumed to support TE mode with  $m=1$  and  $n=1$ . The electric field distribution over the radiating aperture of the waveguide is given by (Narasimhan M.S. and Rao B.V., 1971):

$$E_{\rho}^{mnTE}(\rho', \phi') = \frac{m}{\rho'} J_m \left( \frac{x'_{mn}}{a} \rho' \right) e^{-jk\rho'} \sin(m\phi') \quad \dots(2.20)$$

$$E_{\phi}^{mnTE}(\rho', \phi') = \frac{x'_{mn} m}{a} J'_m \left( \frac{x'_{mn}}{a} \rho' \right) e^{-jk\rho'} \cos(m\phi') \quad \dots(2.21)$$

where,  $J_m$  is the cylindrical Bessel function of order  $m$

$J'_m$  is the derivative of cylindrical Bessel function of order  $m$

$$x'_{mn} = 1.841$$

Similarly, the magnetic fields  $H_{\rho}$  and  $H_{\phi}$  over the aperture are given by (Narasimhan M.S. and Rao B.V., 1971):

$$H_{\rho}(\rho', \phi') = \frac{E_{\rho}^{mnTE}(\rho', \phi')}{\frac{\omega\mu}{K_z^{TE}}} \quad \dots(2.22)$$

$$H_{\phi}(\rho', \phi') = \frac{E_{\phi}^{mnTE}(\rho', \phi')}{\frac{\omega\mu}{K_Z^{TE}}} \quad \dots(2.23)$$

$$K_Z^{TE} = \sqrt{k^2 - \left(\frac{x'_{mn}}{a}\right)^2} \quad \dots(2.24)$$

The electric ‘J’ and magnetic ‘M’ currents are computed with the relations given in (Balanis C.A., 2005):

$$J_{\rho}(\rho', \phi') = -H_{\phi}(\rho', \phi') \quad \dots(2.25)$$

$$J_{\phi}(\rho', \phi') = H_{\rho}(\rho', \phi') \quad \dots(2.26)$$

$$M_{\rho}(\rho', \phi') = E_{\phi}(\rho', \phi') \quad \dots(2.27)$$

$$M_{\phi}(\rho', \phi') = -E_{\rho}(\rho', \phi') \quad \dots(2.28)$$

$$J_x(x', y') = J_{\rho}(\rho', \phi') \cos \phi' - J_{\phi}(\rho', \phi') \sin \phi' \quad \dots(2.29)$$

$$J_y(x', y') = J_{\rho}(\rho', \phi') \sin \phi' + J_{\phi}(\rho', \phi') \cos \phi' \quad \dots(2.30)$$

$$M_x(x', y') = M_{\rho}(\rho', \phi') \cos \phi' - M_{\phi}(\rho', \phi') \sin \phi' \quad \dots(2.31)$$

$$J_y(x', y') = M_{\rho}(\rho', \phi') \sin \phi' + M_{\phi}(\rho', \phi') \cos \phi' \quad \dots(2.32)$$

The components of the far field radiation patterns of a circular cylindrical waveguide at an observation point P with coordinates (R,  $\theta$ ,  $\phi$ ) can be computed using the expressions given in (Balanis C.A., 2005):

$$E_{\theta}(\theta, \varphi) = -\frac{jke^{-jkR}}{4\pi R} [L_{\varphi}(\theta, \varphi) + \eta N_{\theta}(\theta, \varphi)] \quad \dots(2.33)$$

$$E_{\varphi}(\theta, \varphi) = \frac{jke^{-jkR}}{4\pi R} [L_{\theta}(\theta, \varphi) - \eta N_{\varphi}(\theta, \varphi)] \quad \dots(2.34)$$

$$N_{\theta}(\theta, \varphi) = \int_0^a \int_0^{2\pi} \left[ J_{\rho}(\rho', \varphi') \cos \theta \cos(\varphi - \varphi') + J_{\varphi}(\rho', \varphi') \cos \theta \sin(\varphi - \varphi') \right] e^{jk\rho' \sin \theta \cos(\varphi - \varphi')} \rho' d\rho' d\varphi' \quad \dots(2.35)$$

$$N_{\varphi}(\theta, \varphi) = \int_0^a \int_0^{2\pi} \left[ -J_{\rho}(\rho', \varphi') \sin(\varphi - \varphi') + J_{\varphi}(\rho', \varphi') \cos(\varphi - \varphi') \right] e^{jk\rho' \sin \theta \cos(\varphi - \varphi')} \rho' d\rho' d\varphi' \quad \dots(2.36)$$

$$L_{\theta}(\theta, \varphi) = \int_0^a \int_0^{2\pi} \left[ M_{\rho}(\rho', \varphi') \cos \theta \cos(\varphi - \varphi') + M_{\varphi}(\rho', \varphi') \cos \theta \sin(\varphi - \varphi') \right] e^{jk\rho' \sin \theta \cos(\varphi - \varphi')} \rho' d\rho' d\varphi' \quad \dots(2.37)$$

$$L_{\varphi}(\theta, \varphi) = \int_0^a \int_0^{2\pi} \left[ -M_{\rho}(\rho', \varphi') \sin(\varphi - \varphi') + M_{\varphi}(\rho', \varphi') \cos(\varphi - \varphi') \right] e^{jk\rho' \sin \theta \cos(\varphi - \varphi')} \rho' d\rho' d\varphi' \quad \dots(2.38)$$

where,  $\eta$  is the free space wave impedance.

As already mentioned the Equations (2.33) and (2.34) can be used to compute  $E_{\varphi}$  and  $E_{\theta}$  components of the far-field and they are not valid for determination of radiation patterns in near field.

A more compact expression for the radiation patterns of circular cylindrical waveguide designed for TE<sub>11</sub> mode of propagation are given in (Silver S., 1949) which are also valid only for the far field scenario. The compact closed form expressions for the circular waveguide given in (Silver S., 1949) are:

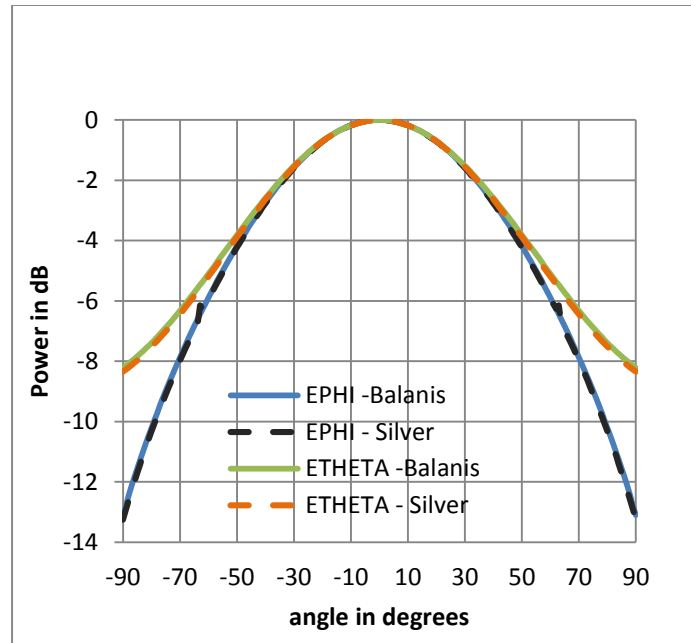
$$E_{\theta} = \frac{kam\omega\mu}{2R} \left( 1 + \frac{\beta_{11} \cos \theta}{k} \right) J_1(k_{11}a) \frac{J_1(ka \sin \theta)}{(ka \sin \theta)} \sin \varphi \quad \dots(2.39)$$

$$E_{\varphi} = \frac{ka\omega\mu}{2R} \left( \cos \theta + \frac{\beta_{11}}{k} \right) J_1(k_{11}a) \frac{J_1(ka \sin \theta)}{1 - \left( \frac{ka \sin \theta}{k_{11}} \right)^2} \cos \varphi \quad \dots(2.40)$$

$$\text{where } k_{11} = \frac{1.841}{a}$$

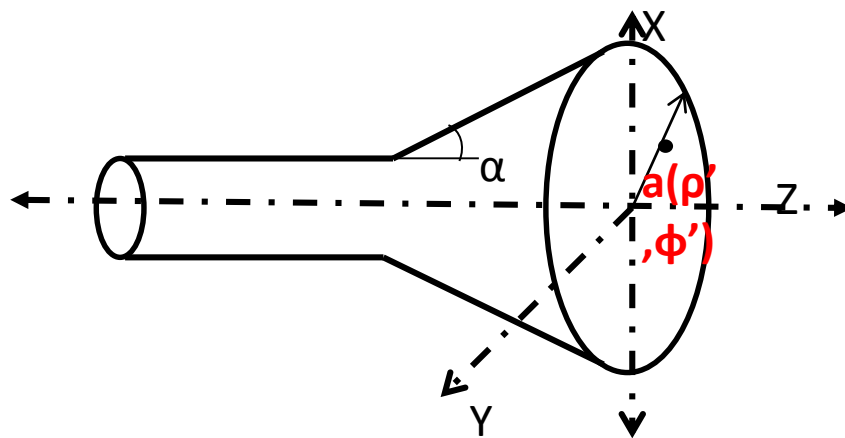
$$\beta_{11} = \sqrt{k^2 - k_{11}^2} \quad \dots(2.41)$$

Figure 2.11 shows the radiation pattern of a circular cylindrical waveguide obtained from formulations in (Balanis C.A., 2005) and (Silver S., 1949).



**Figure 2.11: Radiation Pattern of a Cylindrical Circular Waveguide**

**Conical Horn:** The analysis followed for the radiation pattern analysis of circular waveguide using the analytical formulation given in (Balanis C.A., 2005) can easily be extended to conical horn (Figure 2.12).



**Figure 2. 12: Conical Horn Antenna**

The aperture field distribution of a conical horn are given by (Narasihan .M.S and Rao B.V, 1971)

:

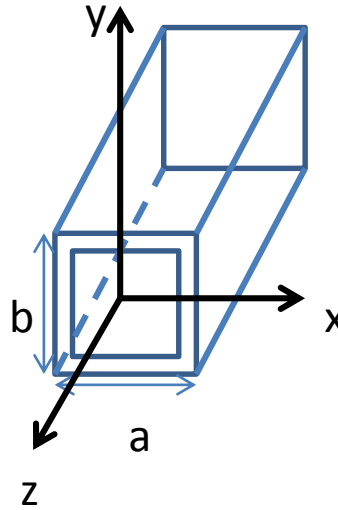
$$E_{\rho}^{mnTE}(\rho', \phi') = \frac{m}{\rho'} J_m \left( \frac{x'_{mn}}{a} \rho' \right) e^{-jk\sqrt{\rho'^2 + L^2}} \sin(m\phi') \quad \dots(2.42)$$

$$E_{\phi}^{mnTE}(\rho', \phi') = \left( \frac{x'_{mn}}{a} \right) J'_m \left( \frac{x'_{mn}}{a} \rho' \right) e^{-jk\sqrt{\rho'^2 + L^2}} \cos(m\phi') \quad \dots(2.43)$$

where, a is radius of radiating aperture of conical horn. For a conical horn designed for dominant TE<sub>11</sub> mode, m=1 n=1 with  $x'_{mn}=1.841$

### 2.5.2 Rectangular Aperture

While the circular waveguide is a classical example of an antenna with a circular aperture, open ended rectangular waveguide (Figure 2.13) is a most widely used antenna element with a rectangular aperture. The expressions for the radiation patterns of a rectangular waveguide supporting dominant TE<sub>10</sub> mode are given by (Silver S., 1949):



**Figure 2. 13: Rectangular Waveguide**

$$E_{\theta}(\theta, \varphi) = -\left(\frac{\mu}{\varepsilon}\right)^{1/2} \frac{\pi a^2 b}{2\lambda^2 R} \sin \varphi \left[1 + \frac{\beta_{10}}{k} \cos \theta\right] \Psi(\theta, \varphi) \quad \dots(2.44)$$

$$E_{\varphi}(\theta, \varphi) = -\left(\frac{\mu}{\varepsilon}\right)^{1/2} \frac{\pi a^2 b}{2\lambda^2 R} \cos \varphi \left[\cos \theta + \frac{\beta_{10}}{k}\right] \Psi(\theta, \varphi) \quad \dots(2.45)$$

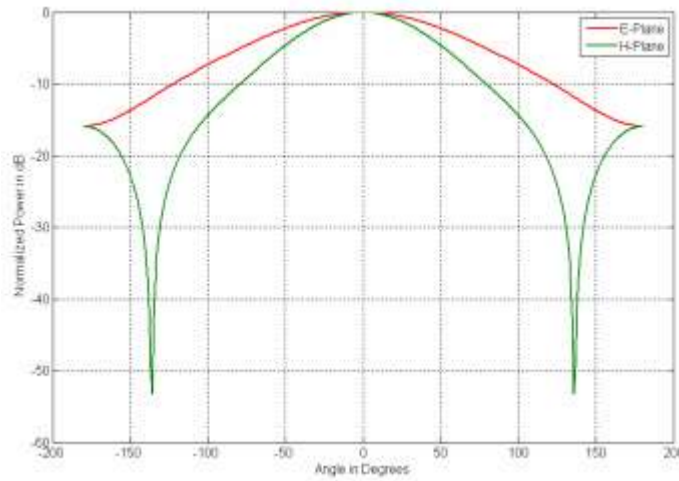
where

$$\Psi(\theta, \varphi) = \left[ \frac{\cos\left(\frac{\pi a}{\lambda} \sin \theta \cos \varphi\right)}{\left(\frac{\pi a}{\lambda} \sin \theta \cos \varphi\right)^2 - \left(\frac{\pi}{2}\right)^2} \right] \left[ \frac{\sin\left(\frac{\pi b}{\lambda} \sin \theta \sin \varphi\right)}{\left(\frac{\pi b}{\lambda} \sin \theta \sin \varphi\right)} \right] \quad \dots(2.46)$$

$$\beta_{10} = \sqrt{k^2 - k_{10}^2} \quad \dots(2.47)$$

$$k_{10} = \frac{\pi}{a} \quad \dots(2.48)$$

The E- Plane (E theta) and H- Plane (E Phi) radiation patterns of a dominant mode rectangular waveguide with  $a=2.32\text{cm}$  and  $b=1\text{cm}$  at  $9.375\text{GHz}$  are shown in Figure 2.14.



**Figure 2. 14: Radiation Pattern of a Rectangular Waveguide**

## 2.6 Image processing

In this section, Image registration and Fusion technique applicable to TWI applications are briefly reviewed. (Seng C.H., et al, 2010) and (Amin M., et al, 2008) suggest that data fusion along with

image registration methods provide composite images of behind the wall scenarios with relatively higher accuracy in terms of :

- Target identification
- Lower clutter noise in images
- Lower computation time

Some of the common fusion techniques that are used for remote sensing and similar to TWI applications are pixel-wise additive fusion, multiplicative fusion, Wavelet Transform fusion, Principal Component Analysis (PCA) fusion and fuzzy logic fusion. There are also methods that use the maximum operator for fusion (Seng C.H., et al, 2010).

Arithmetic fusion techniques like the additive and multiplicative methods are generally employed in TWI applications. For SAR based TWI systems where images are obtained at different standoff positions, the multiplicative methods are employed. It is known to provide improved detection and localization of indoor targets even when data is captured with co-polarization and cross-polarization.

Let us consider  $I_j(u, v)$  to be the  $j$ -th input image normalized to range  $[0, 1]$ . The arithmetic fusion methods produce the additive image  $I_A(u, v)$  and multiplicative image  $I_M(u, v)$  which are given as:

$$I_A(u, v) = \frac{1}{N} \sum_{j=1}^N I_j(u, v) \quad \dots(2.49)$$

$$I_M(u, v) = \frac{1}{N} \prod_{j=1}^N I_j(u, v) \quad \dots(2.50)$$

where  $N$  is the number of input images

$(u, v)$  is a point on the image

The other mentioned techniques are featured with demerits like tedious computations time and relatively more complex. Fusion is carried out on images that are subjected to normalization and registration. Performance measurement based on computational time and image quality is carried out in (Seng C.H., 2010) for different Image fusion techniques. Parameters like the Improvement Factor of the Target-to-Clutter Ratio (IF) and the Target Improvement Factor (TIF) are also computed and tabulated as in Table 2.1.



Method	IF (dB)	TIF (dB)	Time (ms)
Additive Fusion (A)	0.0	0.0	7.2
Multiplicative Fusion (M)	15.31	-9.62	3.2
Wavelet Transform Fusion (W)	-1.35	2.03	493.3
PCA Fusion(P)	-1.33	2.04	27.6
Two Step Fuzzy Fusion with (A & M)	26.76	3.38	13.7
Two Step Fuzzy Fusion with (W & P)	11.70	4.08	13.4

**Table 2. 1: Fusion Techniques and their Performance Parameters**

The Table 2.1 clearly indicates that multiplicative fusion method has significant advantage over other methods though the TIF is slightly lower. Hence multiplicative fusion technique can be adopted for imaging the behind the wall scenario. In this thesis, Laplacian pyramid based fusion with derivatives from multiplicative fusion and DFT based registration are adopted. The Chapter 6 of the thesis discusses the same in detail.

## 2.7 Summary

TWI technology is a cross-disciplinary area which involves research in electromagnetic propagation, antenna and waveform design, beamforming, wall compensation and image processing among others. The waveform could be of impulse or sine wave type but the sine wave technique has the only limitation that it cannot be put on a monolithic integrated circuit. It is chosen over other methods because of the ease in modelling of the waveforms, the high bandwidth that can be achieved, stability and appreciable signal to noise ratio. Beamforming is generally performed at far-field distances and it is assumed that the EM rays incident on / emitted from the antenna elements is always parallel as the distance between source and receiver is very large.

The analytical formulations on near-field beamforming techniques are limited in literature. The existing method based on radial reciprocity require volume metric measurement of array antenna at a given near field. This method uses spherical harmonic solutions to wave equations which take near-field beam pattern specifications and map it to equivalent far-field beam pattern specifications. Radial reciprocity transformations reconstruct far-fields only along the spherical surfaces concentric with the origin of the measured near-field system. The radial reciprocity

transformation however cannot directly be applied for the reconstruction of far-field pattern on flat surfaces. TWI applications usually involve flat wall surfaces.

For TWI applications the X-Band (3-10 GHz) radars are used in order to have high resolution imaging. Antenna design and radiation patterns of Conical Horn antennas and Circular waveguides are briefly reviewed through established mathematical models and results. Computation of radiation patterns from the electric and magnetic current distributions on the aperture of the antenna is a well-established method. This method can be applied to obtain the radiation pattern of the desired antenna models.

In order to reconstruct the image of the object behind the wall, sophisticated Image processing techniques are required to process the data received from scanning the desired area repeatedly differing beampointing angles. Based on the tabulation of performance parameters of images subjected to registration and normalization, fusion methods based on multiplicative technique are best suited for TWI based image processing to identify targets behind the wall. Hence Image fusion and image registration techniques have been chosen as the desirable image processing methods to realize high resolution images of TWI.

## **Chapter 3: Literature Review**

### **3.1 Introduction**

Significance and importance of TWI systems in search and rescue operations during scenarios of natural disasters like a fire or earth quake have been highlighted in chapter 2 of the thesis. The TWI systems use electromagnetic radiation to detect and identify presence of objects like mines, objects of archeological importance, change in material, voids and cracks (Daniels D.J., 2004). TWI is a cross-disciplinary domain which involves research in electromagnetic propagation, antenna and waveform design, beamforming, wall compensation and image processing (Baranoski E.J., 2008) among others. Since the late 1990s significant amount of research is being carried out on TWI systems and also have been increasingly reported in open literature showing its abilities to sense beyond a single wall from near-range (Frazier L.M., 1998).

The TWI and GPR approaches are generally a resultant of traditional optical, radar, and sonar image processing techniques. The working principles of TWI and GPR encompass the multiple domains of basic physics to developing matched filters for every point in the imaging target space (Baranoski E.J., 2008). Imaging of features of structure and structural blocks of buildings requires systems which can scan 3D space and provide 2D/3D images. But such systems cannot rely on Doppler processing alone for localizing and distinguishing the desired features. Therefore multilateration has been the most common approach for scanning space that needs to be imaged. Multilateration (Multilateration Executive Reference Guide, 2011) is the process of locating an object by accurately computing the Time Difference Of Arrival (TDOA) of a signal emitted from that object to three or more receivers. It also refers to the case of locating a receiver by measuring the TDOA of a signal transmitted from three or more synchronized transmitters. The general idea behind Multilateration is to correlate range measurements from multiple sensors to specific points in the image. However, multiple reflections occur during the wave propagation from the transmitter to the desired target and also when it traverses back to receiver. Reflections may be due to the media in which wave travels or the target alone. These specific reflection points will start to assimilate and introduce the background interference (Baranoski E.J., 2008). Imaging becomes difficult with increase in the number of reflection points contributing to the interference.

There are many efficient multilateration approaches like the Synthetic Aperture Radar (SAR) (Aftanas M., 2009) and the Inverse Synthetic Aperture Radar (ISAR) (Leong K.M., 2000). But

they both have their own merits and limitations which are discussed in detail in the subsequent sections. In this chapter research theses and papers pertaining to multilateration techniques like SAR, ISAR, Stepped Frequency in imaging, beamforming, wave propagation in multilayered media and image processing are discussed and reviewed for their contributions towards development of efficient TWI systems. This chapter also includes discussion on advancements in SAR and ISAR based TWI system. In addition, the short comings/limitations in the current research on TWI and the potential scope for original contributions towards development of an efficient TWI system have been appropriately identified.

### **3.2 Synthetic Aperture Radar (SAR) and its limitations**

SAR offers a higher resolution of image compared to the conventional radar imaging techniques without sophisticated post processing by utilizing the movement of the antenna with respect to the target. SAR systems usually have a small aperture and are generally of a length that could fit a side of a plane or a satellite. They produce a beam that is much wider when it scans a target at a long distance as shown in Figure 3.1. The wider the beam on the target, the more difficult it is to distinguish between reflections coming from the ground and target and thus locate the target.

This item has been removed due to third party copyright. The unabridged version of the thesis can be viewed at the Lanchester Library, Coventry University.

#### **Figure 3.1: Radar Beam of SAR (Schlutz M., 2009)**

A narrower beam on the target would improve the resolution of images and help distinguish targets without post processing but that would require a larger antenna. Having larger antenna does not indicate an efficient way of carrying out the scanning and imaging. If an antenna platform is moving with respect to the target, many beams can be sent from and received at the antenna as shown in Figure 3.1. The re-radiated field is later processed together by coherent combination using the Doppler processing algorithms to form an image with the resolution similar to that of a

system with a wider aperture. Systems using Doppler based methods reconstruct an image of the illuminated scene by correlating the received noisy raw SAR signal with template reflections from an ideal radar scattering (Schlutz M., 2009).

Generally SAR based systems are used for surveillance and satellite imagery like applications. One can extend its usage to Through Wall Imaging applications also to image behind the wall scenarios. In such cases the SAR systems have to transmit radiation through the walls and receive the reflected signals. But the wave when propagating through the wall will be at a different velocity as to that of the wave through free space (air). This is because of the different permittivity, permeability, and conductivity of the wall. Wave diffraction and refraction will therefore occur on air-wall and wall-air interfaces as well as direction of wave propagation will change. These parameters directly affect the TDOA of transmitted signals which eventually provide incorrect imaging results indicating inaccurate positions of objects present behind the wall. Hence there is a justifiable and inevitable requirement for wall compensation techniques to avoid such problems (Debes C., 2010).

The SAR which is a 2D imaging sensor also has another requirement of utmost importance namely the faster rate of collection of data at the receiver end of the system so that the data collected can be processed into an image. SAR systems scan a given area along horizontal directions in defined number of steps. If one increases the number of steps, the time consumed to scan a given area will be much higher. SAR systems operate at limited frequency bandwidth and hence do not contribute to improvement in image resolution. Also the size of the antenna, as already discussed previously plays an important role in SAR based imaging systems. Investigations on developing SAR based imaging systems suggest that the length of the antenna should be very small for reconstructing images of higher resolution (Leong K.M., 2000).

In order to achieve high resolution, primary necessity of the radar is to send pulses at a faster rate (Pulse Repetition Frequency-PRF) (Leong K.M., 2000). Consequently, there is a reduction in time between pulses to collect data in the receiving (range) direction. Unfortunately, only one pulse for a given radar frequency can be detected at a time. Otherwise, range ambiguity occurs, thereby negating two dimensional imaging. Increasing time between pulses may facilitate to obtain more information but it affects the image resolution as well. In addition, time taken for generation of image will also increase.

A study on the development of a SAR based TWI system that can facilitate the detection of moving targets inside a building is reported in (John E. Peabody et. al, 2012). The SAR based TWI system comprises an S- band FMCW radar with a spatial frequency range gate coupled to a time-division multiplexed MIMO array. This combination is aimed to rapidly acquire, process, and display radar imagery at a frame rate of 10.8 Hz. The thickness of the solid concrete wall considered for the study is 20 cm. The system uses a range gated FMCW radar that transmits LFM chirps from 2-4 GHz in 1 ms with peak transmit power of 1 watt at 50% duty cycle. The linear antenna array of the system with 44 elements has both Vivaldi and linear slot antennas with an inter element spacing of  $\lambda/2$ . The length of the antenna array is 2.25 m. The TWI system is able to identify the presence of moving targets through a wall which is 20 cm thick and made of solid concrete from a distance of 20 m. The TWI radar resolves targets by using RMA SAR imaging algorithm. The performance validation was carried out with the two humans behind different types of walls such as solid concrete walls and a cinder-block wall with thickness of 10 cm and 20 cm. The TWI system was also tested in free space. The radar was placed at a distance of 6m from the wall. The targets behind the wall were approximately 10 m from the radar. In summary, the TWI system developed by (John E. Peabody et. al, 2012) can locate moving human targets located behind the concrete and cinder block walls of varying thickness of 10 cm and 20cm. However the above TWI system cannot be used if the human targets are standing still or sitting. The detection is still in terms of blobs and has the limitations of SAR systems as mentioned in the previous chapters. The TWI system cannot realise the reconstruction of the Image of the Object behind the wall with clearly defined contours.

Due to the multipath propagation, the signal from the radar source or target appears to originate from diverse positions. In a conventional Algorithms like MUSIC (Schmidt R.O., 1986) for Direction of Arrival (DOA) estimation, the effect of multipath is not considered. Doppler processing is inherent in SAR. Due to the motion of radar platform, a stationary target is seen from different angles. This leads to a variation of the radial velocity between the radar and the target. The Doppler shift induced by the radial velocity exhibits an approximate linear variation with time (at least for narrow beam width systems). Therefore the received target response exhibits a Doppler bandwidth. SAR makes use of Doppler Frequency shift phenomenon to obtain angular resolution and/or scanning in azimuth. SAR achieves much finer resolution along track or azimuth than that

offered by its antenna beam-width. This is achieved by data processing of SAR that exploits the Doppler modulation due to the relative motion of the SAR and the target.

SAR systems have inherent limitation in the amount of data that can be acquired leading to limitation in overall performance of high resolution radar imaging (Aftanas M., 2009). Continued research and development efforts in the field of acquisition and processing of data for radar imaging applications are being carried out to acquire and process large amount of data with smaller computation time. Data collection and its processing form the important metrics for system evaluation. Noticeable technological advances in Radar design elements like the ground link, A to D converters, onboard recorders are being pursued. Most system designers look for ways of efficient usage of prevalent technologies and the already available resource. However the limitations associated with available resources influence data collection, image and signal processing and eventually the entire imaging process (Leong K.M., 2000).

(Aftanas M., 2009) in his thesis lays a strong foundation introducing techniques on imaging of the objects through opaque walls with Ultra Wide Band (UWB) radars. The frequency range of operation is 3.5-10 GHz. By providing the sound analytical/technical basis for studying new techniques for TWI, the thesis provides an extensive overview of state of the art technology of calibration, preprocessing and post processing steps required for TWI. The mathematical modeling of the TWI system along with wall compensation methodology has been discussed in the thesis. The modelling also involves methods to compensate clutter, crosstalks and also structures like a wall between the target and radar. Assumptions and suggestions for compensating multiple reflections that may occur from the walls or surroundings are also highlighted. The thesis emphasizes on using M-Sequence Radar for faster transmission and reception of data which is later stacked appropriately by data migrations or data fusion techniques for the development of 2D Radar image.

The key contributions of the thesis (Aftanas M., 2009) are as follows:

1. Development of a new, effective, and precise method for estimation of Time Of Arrival (TOA) through the wall required for precise data migration, with minimal computation complexity, that can be used for practical applications.

2. Development of the new, fast, precise, and easy to handle measurement method for estimation of the wall parameters required for precise TOA estimation. Because of its very low computational requirements it can be used in real time for practical applications.
3. Development of compensation techniques for motion, wall, clutter and crosstalk
4. Development of the image processing method for indicating presence and edge detection of walls and objects inside a structure like a building. The image processing technique aims to enhance the visibility of wall of a building scanned from outside.
5. Performance analysis of the developed methods on real measurements based on practical scenarios in comparison with conventional methods

Double ridged Horn antennas radiating between 0.5 -2.25 GHz and 9 GHz are used to illuminate a given wall of thickness ranging between 13-50 cm. Both mathematical models and results of real time measurement are explored by the author. The author states that conventional methods use constant velocity model which introduces errors in estimation of shape and position of object.

(Aftanas M., 2009) suggests a new method which transforms three layer wall model to an equivalent two layer (air-wall) model with reduced computational complexity and better precision. An iterative solution is provided with a few assumed initial conditions to further reduce the computational complexity. M Sequence Radar is used for faster signal transmission and collection of data. The M-Sequence radar transmits periodic binary coded signals and receives the reflected signal at a faster rate. The data is stacked appropriately using data migration techniques for image development. For the reconstruction of scenario behind the wall, data migration techniques like back projection algorithm, Stoltz, Kirchoffs, SAR and many others are explained in detail in (Aftanas M., 2009). The image reconstruction algorithms have been implemented on real time scenarios with and without wall compensation. Imaging has been carried out for objects behind brick, concrete and wooden walls. The results of simulations indicated that the frequency based Stoltz data migration technique is faster and yields minimal error.

Aftanas M. in his research study for the fast and efficient computation of TDOA has the following assumptions:

- Wall is homogeneous with constant permittivity and constant thickness
- Relative permittivity of the air in front of the wall and behind it is the same



- Co-ordinations of the antenna  $A[x_A; z_A]$  and the target  $T[x_T; z_T]$ , the permittivity of the wall  $\epsilon_w$ , the thickness of the wall  $D_w$ , and distance of the wall from antenna in Z direction  $W_{di}$  are known

The author assumes that the material inside the wall is homogeneous and hence the angles should be  $\varphi_1 = \varphi_4$  and  $\varphi_2 = \varphi_3$  as indicated in Figure 3.2. The actual distance between antenna and target is not equal to straight distance  $|AT|$  between them (Figure 3.2). It has to be computed as summation of distances namely  $d_{tot} = d_{a1} + d_w + d_{a2}$ . It is also assumed that the rear side of the wall is at the target position and hence the two layer model (air - wall) can be used.

This item has been removed due to third party copyright. The unabridged version of the thesis can be viewed at the Lanchester Library, Coventry University.

### **Figure 3. 2: Wall Modelling and Compensation (Aftanas M., 2009)**

The proposed methods in Aftanas' thesis for measurements of the wall parameters, estimation of TOA through the wall can be used to enhance precision of detection, localization, and tracking of moving objects behind the wall. However the author indicates that imaging stationary objects behind the wall is much more difficult in comparison with moving objects. Figure 3.3 indicates an image reconstructed from the scene behind the wall using the methods proposed in (Aftanas M., 2009). The typical building scene is shown in Figure 3.3a. The building is scanned from 3 sides in steps of 0.5 m. The M-Sequence radar transmits and receives the radio signals and data is appropriately processed to reconstruct the scene. The author has used back projection algorithms and edge detection methods to reconstruct the scene as shown in Figure 3.3 b and Figure 3.3 c.

This item has been removed due to third party copyright. The unabridged version of the thesis can be viewed at the Lanchester Library, Coventry University.

**Figure 3.3: Image Reconstruction of a Building Scene (a) Imaging Scene; (b) and (c) reconstructed scene (Aftanas M., 2009)**

With the relatively larger scan time and duration of data collection, the reconstructed image provides only partial information of behind the wall scenario. The scene shown in Figure 3.3(a) is homogenous or a two layered medium with just concrete wall and air and the technology developed appropriately highlights the contour of the walls. The image processing algorithms involved are complex and the associated computation time is high. The requirement of the SAR based TWI system to be in movement is itself a drawback. The investigation suggests that invoking beamforming methods would improve image quality and also provide better images of the scene behind the wall by overcoming the requirement of motion of radar. As highlighted by the author, the developed methodology has a few limitations like it does not include multilayer model approach for the measurements of the wall parameters. The developed model is also computationally very intensive. Effective computation of wall parameters would help to evaluate thickness, permittivity and conductivity for every layer of the wall such as plaster, air cavity; glass-wall. Investigations also suggest that the compensation for the beam propagating in different directions within the wall due to the material medium and its various optical characteristics should be taken into account. Multiple reflections between target and the radar have to be considered for

better imaging. The author also mentions that better compensation techniques for Motion, velocity and also hardware to acquire data at faster rates have to be looked into. Beamforming methodologies have to be explored to avoid long duration of scene scanning, data collection and processing.

### **3.3 Beamformer for Through-The-Wall Imaging**

In (Aftanas M., 2009), one of the elements in the  $(1 \times n)$  antenna array acted as the transmitter while all the others served as receivers. The signals from the receiver arrays are further subjected to appropriate post processing for the reconstruction of the images. It was also observed that the beam angle, signal refraction, material of wall and obstacles and also multiple reflections affect the image quality. Objects behind the wall can be stationary or moving and they also contribute to errors in imaging. It is also mentioned that the method in which that data is captured by the receiver can also improve image quality.

(Ahmad et al., 2003) have developed a simulation model of synthetic aperture beamformer which uses a hybrid sub-array post data acquisition processing. In sub-array post data acquisition method, the transmit and receive arrays are divided into sub-array pairs, where each sub-array consists of a single transmitter and one or more receivers. The developed model also incorporates the effects of the thickness of wall, refraction, change in velocity of wave propagation and attenuation. The developed method also intends to image stationary targets and thereby rendering it suitable for TWI applications. Data from the sub-arrays are used to form independent components of the image of the scene by post-data acquisition beamforming. These independent component images are then added coherently to obtain a composite intensity image with the desired spatial resolution.

The authors of (Ahmad et al., 2003) follow the basic modelling of a TWI as in (Aftanas M., 2009) but have incorporated the beamformer technique to negate the errors that may occur due to refractions, multiple reflections and the varying dielectric constants of the wall itself. The authors have simulated the TWI system considering a  $1 \times 8$  element linear antenna array in which 4 elements act as transmitters and 8 act as receivers. B-Scan (range vs. angle) images were obtained using the beamformer technique. An amplitude modulated rectangular pulse of 1 GHz bandwidth centered at 2 GHz was used for imaging. The thickness of concrete wall was 6 inches with  $\epsilon=9$ . The one-way attenuation through the wall was taken to be 6 dB for 6 inch thickness. The room contained stationary point target with a reflection coefficient of unity.

As already stated, the authors (Ahmad et al, 2003) presented a synthetic aperture beamformer with hybrid sub array-post data acquisition processing. Their design incorporates all the necessary parameters that replicate a practical TWI application and a proof of concept through simulation results is presented. The authors also have presented a least-squares performance measure for the beamformer under conditions of errors in wall parameters for a single target scenario.

### **3.4 Wave Propagation in Layered Medium**

High resolution images with exact locations of targets can be obtained by analysis of the electromagnetic wave propagation from the transmitting antenna elements through different mediums (air, wall, targets) and back to the receiving elements. Studies on analysis of electromagnetic wave propagation and field distribution can compensate for the errors occurring due to the varying media, multiple scattering, diffraction and refraction effects.

(Lu et al., 2010) have developed a simulation model for two-dimensional layered medium for the analysis of TWI. The developed mathematical model is integrated with the Subspace- based Optimization Method (SOM) for reconstructing the relative permittivity profile of structures behind the wall/ concealed in the wall in a fast and robust manner. Numerical results have shown that the concealed targets within walls can be reconstructed using the proposed model. However the shape or size of the targets is only partially available because of the attenuation of signal caused by the wall. The model has also been employed for studying the effect of the presence of walls on imaging.

The authors have considered a set up as shown in Figure 3.4. The developed method computes wave propagation in the multiple layers using Greens function. The technique uses a known source field distribution to compute the field at any observation point along the direction of wave propagation.

This item has been removed due to third party copyright. The unabridged version of the thesis can be viewed at the Lanchester Library, Coventry University.

### **Figure 3. 4: Schematic Configuration of the Layered Medium Model (Lu et al, 2010)**

Presence of extended scatterers interferes with the electric fields from the source and influences the resultant field at observation point. The electric field at the observation point is a summation of field due to source, primary scatterers and also a few secondary sources in the scatterers that have different electromagnetic properties. The radiation from the secondary sources contributes to the total electric fields at the observation points in the region of interest. This effect is called the multiple scattering. Among various ways of incorporating the mutual multiple scattering, the authors have used coupled dipole method.

The authors (Lu et al, 2010), provide a mathematical model to obtain the electric field distribution through multi layered walls. The model also includes a methodology to compensate multiple scattering which occurs within the multilayered wall. The investigations suggest SOM for reconstructing the relative permittivity profile in a fast and robust manner. Results obtained in the research indicate that signal recovered in this way can be used to reconstruct images of concealed targets of different profiles even in the presence of significant amount of noise and absence of full aperture for imaging. The authors have presented many examples to demonstrate the effectiveness of SOM in TWI. They indicate that at most 30 iterations of optimization are sufficient to reconstruct error free high resolution images. Frequency hopping provides good results on reconstruction of images. In conclusion it can be suggested that combination of the analytical model for layered medium and the SOM can be used to study the effect of the walls on the quality of image reconstruction.

(Asprone et al., 2010) have carried out numerical analyses and simulations to assess the electromagnetic disturbance that is caused by a barrier with a concrete base and Glass Fiber Reinforced Polymer (GFRP) fencing structure. The various comparisons on numerical and experimental results confirm that composites and in particular, GFRP results in low interference with electromagnetic fields. The main contribution to interference is generated by the concrete base only.

(Soutsos et al., 2001) in their study on “Dielectric properties of concrete and their influence on radar testing” indicate the need for reliable data to identify possible variations of dielectric properties of different concrete mixes and their condition on site. The results of this study provide extensive and comprehensive reference data relating to the electromagnetic parameters like electrical conductivity and permittivity and its influence in radar testing. They indicate the influence of relative permittivity and electrical conductivity of concrete mixtures and conditions likely to be encountered in practice. These data can be used for mathematical modeling of objects and structures.

### **3.5 Inverse Synthetic Aperture, Stepped Frequency Radar and its Limitations**

Inverse Synthetic Aperture Radar (ISAR) imaging technique is another way to achieve radar images of high resolution. Both SAR and ISAR have the same underlying theory [Leong K M, 2000]. The main difference between them lies in the design configuration. In SAR imaging, the radar is flying in the space, and the object is stationary, while in ISAR imaging, the object is moving and the radar is stationary. But only the relative movement between the object and the radar is important. So the ISAR imaging problem can be found to be equivalent to the SAR imaging problem [Leong K M, 2000]. The data collection limitation of SAR can be overcome in ISAR by using pulse compression techniques like the Impulse, Sine wave, and stepped frequency.

Conventional ISAR imaging method generally is based on 2D-Fourier transform based range-Doppler algorithms. However, the generated images often result in poor resolution; reason being the measurements are carried out at smaller frequency bandwidths and over limited azimuthal angles. Recent developments involve adoption of high resolution spectral estimation techniques like AutoRegressive (AR) model, Multiple Signal Classification (MUSIC), and Matrix Enhancement and Matrix Pencil MUSIC (MEMP-MUSIC) to develop high resolution ISAR images. Investigations in (Park J.I. and Kim K.T., 2010) show a critical review of the mentioned

methods in the development of high resolution ISAR images. Their study shows that the MEMP-MUSIC method provides the best results in terms of resolution and target identification. While MUSIC shows relatively reasonable results, the other two methods do not provide appreciable results in terms of target localization.

A polarimetric compact radar range operating at a center frequency of 100 GHz suitable for measurement of radar cross section, ISAR imagery and Doppler measurements of rotating objects has been reported in (Guy B. DeMartinis et. al, 2013). The compact range can also be used to generate high range resolution profiles of targets and imagery of objects behind the wall. The reported compact range can also facilitate scale model studies on much lower frequency bands such as C and S bands. The sweep rate of kHz range Doppler is a significant feature of the design. The transceiver of the system has dual transmit and dual receive blocks and they are associated with chain of frequency multipliers. The high gain parabolic reflector of the compact range with a diameter of 1.5 m replaces traditional array commonly used in ISAR system. The quiet zone of the compact range is 66 cm long with a diameter of 3 dB. The backscattered signal from the target is down converted through multi stages to a final IF of 50-kHz which constitutes an input to DSP Lockin amplifier to measure the amplitude and phase of the received signal. The system bandwidth of 16 GHz is utilised in sweep mode to cover several thousand frequency points to accomplish enhanced range resolution sufficient to cover the measurement chamber. In addition, this also imparts the capability for detection and identification of appropriate range bin of the target. The developed TWI system has also a provision for a software range gating.

The developed TWI system is based on the principles of ISAR. The measurement was performed on a cinder block wall with a thickness of 15.24 cm. The operating frequency was 4.17 GHz. The models of the wall with an object behind it consists of a scale-model cinder block wall (1:24). A variety of scale-model objects behind the walls are considered and all the scale modelled objects are mounted on a ground plane. The wall and the objects behind it were found to provide reasonably accurate modeling of the relevant materials at 100 GHz for the preliminary demonstration. The system was tested for its results of ISAR imaging of the 1:24 scale model cinder block wall with plexi-glass mounting plate on a ground plane. For this baseline or reference measurement, there were no objects mounted behind the wall. The developed scale model of ISAR based TWI system could detect the two drums and Trihedron placed behind the wall. This results confirmed the system's potential for scale-model of TWI. It has been stated that at various

azimuthal orientations of the measurement setup, the imaging of the objects behind the wall posed challenges and at times found difficult to image. The authors attributed the challenges and the difficulties to a combination of multi-bounce, the distortions of the wave-front of the signal caused by the cinder block wall and ground clutter. The suggestion for the future work involves refining and improving the approach by implementing various signal processing techniques such as background subtraction and filtering, and the potential use of Doppler information for moving targets.

The limitation of ISAR imaging of generating images of poor resolution due to the measurements carried out at small frequency bandwidths can be overcome by including Stepped-Frequency (SF) technique in conjunction with it (Karakassiliotis A.V., 2007). The SF technique as already discussed in Chapter 2 is known to achieve a wider bandwidth over several pulses instead of within a single pulse. However, its instantaneous bandwidth remains small thereby requiring a relatively simpler hardware for the receiver. The effective SF waveform bandwidth is the product of the number of coherently integrated pulses ' $N$ ' and the step size ' $\Delta f$ '. The returns of the  $N$  pulses at different carrier frequencies form the frequency spectrum of the reflectivity of target and are coherently integrated by the Inverse Fast Fourier Transforms (IFFT) to give the High Resolution Range (HRR) profile of return signal which has information about the target. The HRR profile does not give the absolute range position of the target but only gives the relative position of each scatterer within the conventional range bin.

The key advantage of the SF implementation as compared to other pulse compression techniques is its higher range resolution without compromising its instantaneous bandwidth, or target detection range (Ahmad F. *et al*, 2003). It is easily implemented by adding a frequency synthesizer to a conventional narrowband receiver and performing the necessary signal processing on the received signal.

There are two main limitations associated with the SF radar implementation (Leong K. M., 2000). One being that it cannot directly measure the velocity of targets based on Doppler shift (due to frequency shift in the carrier during transmission) and the other is that it requires additional time to transmit and receive  $N$  pulses.



An ISAR image consists of two main dimensions namely Slant Range (Down Range/Range) and the Cross Range. Slant Range refers to range measured along the radar Line Of Sight (LOS). Cross-Range is equidistance cross-Range lines lying perpendicular to the Range axis. Clarity of a two dimensional image depends on the resolution obtained in each dimension. Range Resolution could be controlled by the properties of transmitted signals (signal type, repetition frequency, processing methods) and it could vary between the tens of meters and a few centimeters.

ISAR systems image objects in the cross range dimension due to rotational motion. Both ISAR and SF WaveForm (SFWF) work on principle of Doppler shift. ISAR requires fixed frequency measurement of a non-stationary target and the SFWF requires a swept frequency measurement of a stationary target. Proper selection of the radar parameters such as operating frequency, downrange resolution, pulse width, frequency step size, and others yield optimum range resolutions in both slant and cross ranges for a particular target of interest (Leong K. M., 2000).

### **3.6 Stepped Frequency Imaging Radar**

Simulation model of a stepped frequency- ISAR imaging system has been extensively discussed in (Leong K.M., 2000). The objective of the thesis is to use two proven high resolution processing technologies, namely stepped frequency and ISAR processing, to image the simulated signal returns from multiple scatterers located on the surface of object. A wire model of an aircraft with multiple scatterers is modeled. The transmit and receive signals are simulated based on calculated radar parameters like the down range resolution, instantaneous and effective bandwidth and frequency step size. The target is considered to have only angular or radial motion. The transmit signal is modeled for 15 bursts of the SF radar and the received data was stacked accordingly. An FFT technique is developed to have an efficient and faster way to reconstruct high resolution images using the stacked data of receiver. Radar Cross Section is of primary interest and the resulting images can individually isolate scattering sources on the target.

The key contributions of the thesis by (Leong K.M., 2000) include development of an aircraft model with multiple scatterers. It also involves modeling radial and angular motion of the scatterers. The SF radar parameters for high resolution imaging are obtained and simulation of the stepped frequency radar for 15 bursts is carried out. Optimum radar and target geometries are considered to efficiently image target motion precisely. The main contribution however involves

development of an FFT technique for faster and efficient method to obtain down range and cross range profiles as well as the individual isolation of the scatterers using RCS information.

In (Leong K.M.,2000 ) it is assumed that the aircraft does not have any translational motion but only radial and angular motion. Even if the translational motion exists it is assumed to be compensated. All the radar parameters like the down range resolution, instantaneous and effective bandwidth and frequency step size are presented in (Leong K. M., 2000). The resolution in cross and down ranges are of utmost importance for obtaining high resolution images. They depend on the frequencies and bandwidth of transmit signal of SF radar. The optimal tracking window is another critical parameter modeled to track the scatterers. Scatterers outside the window will be wrapped around and displayed incorrectly on the image. The author presents simulated results for improper lengths and highlights of window that deteriorate the quality because of range spreading. All the simulations are carried out in MATLAB.

The work in (Leong K. M., 2000) employed both SF and ISAR processing techniques to generate high resolution images of targets. Radar parameters were studied and chosen appropriately and the concept of ‘tracking window’ was highlighted for precise detection of objects. Analysis of the RCS imaging is carried out and the results obtained indicate that closely placed scatterers can easily be distinguished. In the thesis, it is assumed that target has only radial and rotational motion. As a future work, the author indicates that motion compensation can be applied to each scatterer rather than the target as a whole because individual scatterer can have its own motion. The author recommends that Joint Time Frequency Analysis should replace the conventional Fourier transform technique to obtain high resolution images at faster rates.

(Karakasiliotis et al., 2008), also have investigated the 2D ISAR model and image reconstruction with stepped frequency-modulated signal. In their research study, an interesting case of a target moving along a rectilinear trajectory at constant speed, within the detection range of ISAR radar transmitting SF-modulated pulses, is examined. A mathematical model of the time-domain ISAR return signal for the case of SF modulation and 2-D ISAR geometry has been developed. The novelty of the proposed ISAR signal modeling approach lies in the process of coherent summation of the SF-modulated signals reflected from different point scatterers of the illuminated target. Additionally, they have described a mathematical model for an efficient ISAR image reconstruction process, which is independent of the trajectory parameters of target. The

mathematical model consists of a cross-correlation-based range compression algorithm and an FFT-based azimuth compression algorithm. Coarse range alignment is also part of the proposed ISAR image reconstruction process, and it is carried out automatically by registering the first SF pulse reflected from the nearest point scatterer in the first sample of the received ISAR signal.

Researchers from the AKELA Inc., USA, have developed a first generation ISAR – Stepped frequency based radar (Hunt A.R., 2004). The imaging system consisted of three major subsystems; a digitally controlled- stepped frequency radar operating over the band from 450 MHz to 2 GHz, an antenna array and a system for control, processing and computer display which provides images of behind the wall scenario. The results obtained on scanning a site of lecture hall proved that the physics and technology of TWI is reasonably well understood but also showed the limitations imposed by its particular implementation. With the scanned antenna array and existing radar, the time it took to assemble a single image is approximately 10 seconds (Hunt A.R., 2004). Since motion detection was accomplished through coherent scene subtraction, real time motion detection could not be demonstrated because of large amount of movements between image frames. Increasing the speed of operation would allow data collection at a rate sufficient to maintain coherence in the data from image to image improving the ability to detect motion by image subtraction techniques. Random motion of objects such as leaves blowing in the wind is averaged to be zero, while more directed motion is enhanced. The most notable issue from an imaging point of view was the presence of ghost images. This was related to the use of a linear array with a fixed distance between antenna elements. The investigators suggest that a well-designed radar carrier that helps move the antennas to arbitrary locations would allow images to be formed from different perspectives and reduce the number of ghost images. The resulting variable aperture improves the cross range resolution. Option to change the number of antenna elements would improve signal to noise ratio and, therefore, image quality. A second generation radar imaging system is chosen for development. Experiments demonstrated that the radar detects an individual at a range of 12 meters through three internal walls, at 40 meters through dense foliage, and forms images through reinforced concrete walls. SF-ISAR techniques have been tried, tested and are proven to be successful in imaging aerial objects (Hunt A.R., 2004). Nevertheless, the system is not compact. The quality of image and the realized accuracy in terms of location of objects behind the wall are not high to identify both stationary and moving objects. The presence

of ghost images would mislead the operators. Further studies on moving targets, clutter, multiple reflections and phase compensation should be considered for high resolution images.

The authors (Aftanas M., 2009, Hunt A.R., 2004) suggest that incorporating beamformers in the TWI models would improve imaging and isolating individual targets which may be moving or stationary. Inclusion of beamformers provides improved scanning in both azimuth and elevation planes which is generally not provided by available systems (Park J.I, and Kim K.T., 2010).

A beamforming approach to Stepped-Frequency Synthetic Aperture Radars (SF-SAR) for TWI is addressed in (Amin et al., 2005). SF approaches have their own merits and limitations over the M-sequence radars as mentioned in Chapter 2 of the thesis. The research group of Amin et al uses a quadratically constrained Capon beamformer and has incorporated various effects of the presence of the wall, such as refraction, change in speed of the propagating electromagnetic wave and attenuation in their design. The scheme developed by (Amin et al., 2005) divides transmit and receive arrays into sub-array pairs, where each sub-array consists of a single transmitter and one or more receivers. The sub-arrays will be used to illuminate the scene independently and to measure the returns. Unlike conventional SAR, this method overcomes the use of the independent serial use of various sub-arrays by simplifying it to requirement of one sub-array combined with a sub-array multiplexer. The authors use horn antennas as their antenna elements to transmit SF signals radiating between 1 to 12.4 GHz with a step size of 5 MHz. In the experiments carried out, a set of 101 CW frequencies are transmitted from a single array element and the returns of the signal are received at the same array location and this process is repeated for 57 array locations. The data is stored and processed with background subtraction method to reconstruct behind the wall scenario. The experimental setup consisted of a typical behind the wall scenario where a metallic sphere of 12 inch diameter is placed behind a 3 inch plywood wall and at a distance of 3.4 meters away from antenna array. Figure 3.5 indicates both the imaging scenario and the image reconstructed from the scene behind the wall using the Stepped-Frequency-Capon Beamforming method. The reconstructed image clearly indicates the presence of the object. This method clearly indicates that beamforming method is a good choice to undertake analytical and mathematical studies on imaging technology and interpretation of behind the wall scenario. The developed methodology is a proof of concept adapted in SAR based systems for TWI application to provide

images of superior quality of the imaging scene and objects in the scene. It serves the purpose of locating and identifying structures behind the wall.

The authors conclude by clearly stating that SF technique in conjunction beamforming methods form a superior methodology to obtain information of behind the wall scenarios. However the imaging technique is just a proof of concept; and is based on background subtraction which practically does not hold good in TWI applications where prior information of the imaging scene is not known. Also the presence or absence of desired objects is not known.

This item has been removed due to third party copyright. The unabridged version of the thesis can be viewed at the Lanchester Library, Coventry University.

### **Figure 3. 5: Imaging Scenario and Reconstruction of Images (Amin et al, 2005)**

All the beamforming applications simply assume that a target or object is at a far-field distance from the transmitting antenna array. The algorithm for TWI application fails when objects are well within near-field distances of the antenna array. There is an abundance of literature on far-field beamforming techniques. However, the reported research on near-field beamforming appears to be rather limited in open literature. Probably, this is in tune with the continued emphasis in Antenna Engineering on the far-field characterization of the antenna radiating elements and arrays. Near-field compensation (Khalil F., et al, 1994) is one of the common methods to achieve near-field beamforming in which a delay correction is used on each antenna array element (sensor) to account for the near-field wave fronts, which tend to be spherical. Near-field compensation is a first order correction over a limited range of angle. Curvature of the spherical wavefront (because of the near-field) is approximated by a quadratic surface over the array aperture and it ignores the variation of magnitude with distance and angle. It is preferred only for beamforming closer to broad side angle.

Another method to achieve near-field beamforming reported in literature is the near-field/far-field reciprocity (Kennedy R. A. 1998). Near-field/far-field reciprocity described in (Kennedy R. A. 1998) highly depends on far-field techniques to arrive at near-field problem formulation. The radial reciprocity described in (Kennedy R. A. 1998) utilizes near-field beam-pattern specification and maps it to an equivalent far-field beam-pattern specification. This method requires 3D or volumetric measurements of Near-field pattern at a desired near-field distance. Spherical near-field to far-field transformation is required in this analysis. Then the weights are computed for far-field beamforming which also satisfy the near-field specification. In the proposed thesis, a technique to achieve near-field/far-field beamforming which circumvents the earlier stated requirement of 3D near-field radiation pattern measurement is proposed and discussed in detail in Chapter 5.

### **3.7 Summary**

Each of the multilateration techniques and associated technology required for high resolution TWI are unique in their own way. There are a few identified aspects for efficient TWI system development which demands and requires advancement in both techniques and technologies through research and development. The identified aspects being data transmission, electromagnetic wave propagation through multi layered mediums, appropriate beamforming method for both transmission and reception of data, and finally computing systems for fast computation and processing of received data.

The conducted review of literature suggests that the general SAR approach demands the need for faster data acquisition methods as well as compensation techniques for wall, beam and clutter. The associated high percentage of error in imaging and identifying the structures and objects behind the wall is inevitable. SAR also demands the radar to always be in motion which is not effective and suitable for some system applications. Research carried out in understanding and developing mathematical models for TWI system include the topics such as electromagnetic propagation, antenna and waveform design, beamforming, wall compensation and image processing.

However, the past research also suggests that ISAR technique can replace the SAR technique as the data can be captured with stationary radar and at a faster rate combined with SF technique. Studies carried out on a combination of SF- ISAR approach where stationary radars illuminate a given imaging scenario and receive the reflected echoes of radio waves revealed the improvement

in imaging quality as well as its drawback in identifying stationary objects. ISAR imaging can image objects with translational or rotational motion. Some studies on ISAR based imaging systems which incorporated SF and beamformers for TWI formed a proof of concept solutions to tackle limitations of state of the art technology like low measurement bandwidth and smaller angular measurements. Such systems are supposed to provide images highlighting the contours of objects behind the walls. Investigations at present still involve carrying out measurements using linear arrays with SAR based beamformers for TWI applications, where the radar is moved in small steps in horizontal direction to cover a certain azimuthal angular coverage only and not considering coverage in elevation. Scanning imaging scene in both azimuth and elevation planes is too tedious and time consuming. Studies therefore can be extended to involve planar beamforming arrays for coverage of an area in both azimuth and elevation angles to facilitate formation of high resolution images of behind the wall scenarios.

Most studies like in (Amin et al, 2005) generally assume that objects behind the wall are in far-field distances which normally are not the case in practice. Measurements carried out with such assumption without knowing the imaging scene apriori might lead to incorrect data interpretation. Research on near-field beamforming appears to be rather limited in open literature and application of the same for TWI systems seems to have not been attempted. This emphasizes that there is a scope for pertinent technological opportunity and academic avenue to explore the feasibility of invoking Near Field Beamforming technique for the development of simulation model of TWI system to realize images highlighting contours of objects behind the wall.

There are a few commercial TWI radars. CAMERO (Gassler J, 2008) deployed in Israel is based on SAR and has many versions. For systems like CAMERO, relative motion between target and antenna is a must. If both are stationary, image cannot be formed. The system has to be carried around by the users to obtain high resolution image. Since high resolution imaging requires measurement of data at higher bandwidth, there is an utmost need to illuminate a target at a higher PRF. Though existing waveform generation methods provide signals with high bandwidth, the signal and imaging technologies associated with it lead to low resolution images as well as errors in target identification. Systems like CAMERO scan only in azimuth and do not consider data along elevation. Hence it is appropriate to propose a TWI system that electronically scans a given scenario overcoming requirement of the relative motion between radar and target. The proposed

TWI system should form a stationary scanning system overcoming the requirement of carrying the system around. The numerous research studies in open literature tend to suggest and substantiate that stepped frequency method provides signal with high bandwidth as well as SNR. It will be of significant interest and importance to explore the feasibility of incorporating the stepped Frequency method into the system in conjunction with the near field beamforming technique to effectively acquire data in both azimuth as well elevation planes to eventually improve imaging as well as its associated accuracy in target identification.

A study has to be carried out on the analysis of the electromagnetic propagation between the transmitter-wall-target and target-wall-receiver and how the electromagnetic propagation affects the image quality. Image processing algorithms like Doppler-range algorithms which further involve Fourier transforms and high resolution spectral estimation techniques like Auto regression, MUSIC, MEMP-MUSIC, JTFT, back propagation algorithms involved in present TWI systems are highly complex and time consuming. A technique which does not involve complex transformations and yet can process the image at faster rates has to be explored and developed.

Based on the literature review presented in this thesis pertaining to the TWI system and the associated main sub blocks of it as well as the proposed research questions to be addressed by this thesis, the distinguishing features and the potential advantages of the major objectives of the proposed thesis are listed as follows.

The principal aim of this thesis is the development of simulation model of Stepped Frequency (SF) and Near Field BeamForming (NF BF) based stationary TWI system to scan an object behind the wall for the reconstruction of 2D/3D image of it. The application of near field beamforming technique in the developed simulation model of TWI system requires the movement of neither the antenna array nor the object to reconstruct the image of the object behind the wall, thus overcoming the limitation of SAR/ISAR based TWI system. The proposed near field Beamforming technique with a planar array in the simulation model of TWI system facilitates the scan of the desired behind the object scenario in both azimuth and elevation to maximize the information available for more effective reconstruction of the Image of object behind the wall. The near field beamforming method proposed in the thesis is novel and overcomes the prevalent requirement of 3D or volumetric near field radiation patterns of the beamforming array.



The realized reconstruction of the image in the proposed TWI does not involve inversion techniques thereby minimising the computational burden as well as the overall execution time of the TWI system. Contrary to the present TWI systems, the proposed simulation model has the capability for the reconstruction of the shape and contour of the object. In addition, the formulated simulation model of the TWI system overcomes the previously imposed constraints on the distances of separation between the radar and the wall as well as the wall and the target. The simulation model of TWI of this thesis can handle arbitrary distances (far field or near field) between the antenna array and the wall as well as the wall and the object, which is not the case with the existing TWI systems.

This thesis aims to develop a mathematical simulation model of Stepped Frequency based Through Wall Imaging Systems supported with Near Field Digital Beamforming and wave Propagation studies in multilayered medium. The end objective of the study is to reconstruct high resolution images of behind the wall scenarios irrespective of material mediums of the walls and targets. The model also should identify contours and reconstruct the shape of the identified targets.

## **Chapter 4: An Approach for Computation of Near Field Radiation Pattern of an Antenna**

### **4.1 Introduction**

Modelling and simulation studies on near-field beamforming based TWI system form the core theme of this thesis. From research perspective, the essence of this thesis lies in addressing a novel approach for the near field beamforming technique which will then be used to illuminate the wall and the target behind the wall. However, the approach for novel near field beamforming proposed in chapter 5 requires the near field radiation patterns of individual antenna elements. In a conventional far field beamforming technique, there is an explicit assumption that the radiation patterns of individual antenna elements are assumed to be identical and one needs only a far field radiation pattern of the antenna. However, in a near field beamforming technique, the presumption of identical radiation patterns of the antenna element is not valid. At a given point of observation at which the near field beamforming is desired, the radiation patterns of individual antennas of the beamforming array exhibit differing radiation patterns in terms of both amplitude and phase. Therefore determination of the near field radiation patterns of antenna elements becomes an important step in the near field beamforming techniques. In open literature, there is an abundance of information on research pertaining to various analytical techniques for the analysis of far field radiation pattern of antennas. The techniques of Method Of Moment (MOM), Uniform Geometrical Theory of Diffraction (UGTD), Physical Optics (PO), and Geometrical Optics (GO) are just a few to mention the more commonly and routinely used methods for the determination of far field of antenna. In addition, analytical expressions in closed form are available for certain configurations of antenna elements such as Open Ended rectangular and circular cylindrical waveguide in [Silver S., 1949]. On a relative measure, the literature on techniques for the determination of near field patterns of antennas is rather limited. This can partly be attributed to the spherical wavefront of Electromagnetic radiation impinging on the aperture of the antenna under test in the receive mode or the spherical wavefront of the field radiated by the antenna under test in transmit mode.

The distinction between the near field and far field can be explained through the concepts of radiation condition and wave front. In the far field of an antenna, the radiated wave is an outward travelling plane wave (Harrington R.F., 1961). An outward travelling wave is characterised

through  $e^{-jkr}$  variation where  $r$  is the distance between the source and the field point. In the far field, the associated wave fronts are planar. As a result, the profile or envelope of the normalised radiation pattern measured at any far field distance is independent of distance of measurement. In the case of near field, the wave fronts cannot be assumed to be planar and in most practical cases, the near field radiation is assumed to be either spherical wave front characterised through  $e^{-jkr}/r$  variation or cylindrical wave front exhibiting a variation of  $e^{-jkr}/\sqrt{r}$ . The non-planar nature of wave front in near field leads to the important observation that, the profile or envelope of the normalised radiation pattern is dependent on the distance of the field point or the radial distance of near field measurement.

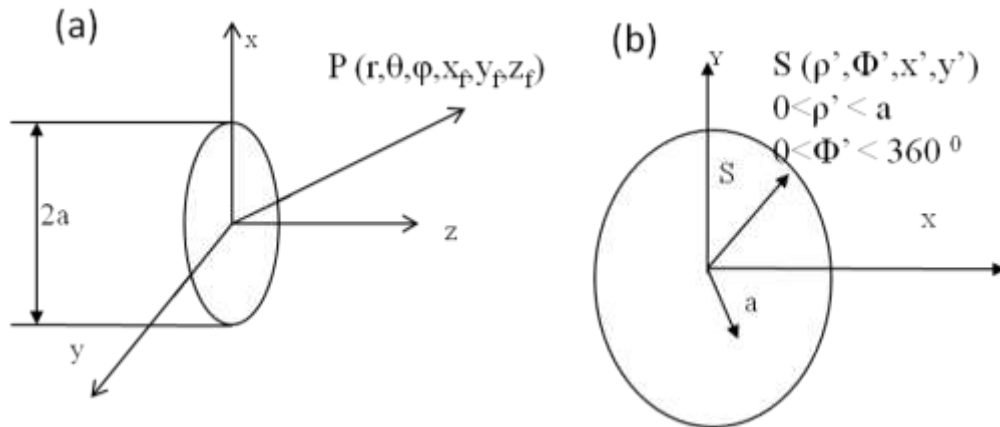
In the past, development of analytical formulation for the near field radiation pattern analysis has been a topic of research and invariably, the emphasis of various research publications is on very specific geometrical configuration of antennas. The near field radiation pattern of conical horn is addressed in [Narasimhan M.S. and Rao K.S., 1979 a; Narasimhan M.S. et. al, 1981]. The near field of pyramidal horn antenna is discussed in [Narasimhan M.S. and Rao K.S., 1979]. An analysis of near field of point dipoles required for near field synthesis is given in [Narasimhan M.S. and Bobby Philips, 1987 a,b]. The Cartesian components of near field radiation pattern of a point dipole are presented in [Narasimhan M.S. and Kumar B.P., 1990]. From the above succinct citation of various analytical formulations for the analysis of near field radiation pattern of antenna, it is obvious that each of the analytical formulations had been specifically developed keeping the geometric configuration of the antenna and they cannot be extended directly to treat near field analysis of other configurations of antennas implying the lack of generality in the derived analytical formulations. A generalized procedure in the form of a detailed analytical formulation which would facilitate the determination of near field radiation pattern of an antenna of given geometrical configuration including aperture and planar profiles constitutes the primary focus of this chapter. In addition, unlike some of the cited literature above, the proposed near field analysis is valid for the computation of near field radiation pattern in any arbitrarily defined plane of observation leading to the determination of 3D or volumetric radiation pattern which is a requirement in many applications involving antenna engineering. Particularly, for near field beamsteering or beamforming scenario covering both azimuthal and elevation angles, one needs the near field radiation patterns of antennas in arbitrarily defined planes of observation. In the

proposed analysis, the aperture of the antenna is replaced by an array of point electric and magnetic dipoles. As a consequence, application of this method requires the knowledge of either the current or field distribution over the radiating aperture of the antenna which for all practical purposes can be obtained with reasonable degree of accuracy and certainty.

#### 4.2 Generalized Analytical Formulation for Near Field Radiation Pattern of antenna

This section presents a generalized procedure for the computation of near field radiation pattern of an antenna. The method of determination of near field radiation pattern invokes the concepts of equivalent Electric current ‘J’, equivalent Magnetic Current “M” and the field radiated by the point electric and magnetic dipoles. In the proposed method, the radiating aperture of the antenna is assumed to be replaced by an array of point dipoles (electric/magnetic) whose current strength is determined by the field distribution (magnetic/electric) at the respective locations of dipole. The proposed method is versatile and generic enough to be applicable to any geometric configuration provided either the field distribution or the current distribution of the antenna is known. For the purpose of illustration, a circular waveguide designed and excited in dominant  $TE_{11}$  mode is considered for the analysis.

A conventional circular waveguide with the associated coordinate system for analysis of near field radiation pattern is shown in Figure 4.1(a). The radiating aperture of the circular waveguide is assumed to coincide with  $Z=0$  Plane or  $XY$  plane. Observation or field point of interest  $P$  is in the near field range of the antenna.



**Figure 4. 1: Coordinate System for Near Field Analysis of Circular Waveguide**

The electrical field distribution of the dominant TE<sub>11</sub> mode of a circular cylindrical wave guide over its aperture is given by [Narasimhan M.S. and Rao B.V., 1971]

$$E_{\rho}^{mnTE}(\rho', \phi') = \frac{m}{\rho'} J_m \left( \frac{x'_{mn}}{a} \rho' \right) e^{-jk\rho'} \sin(m\phi') \quad \dots(4.1)$$

$$E_{\phi}^{mnTE}(\rho', \phi') = \frac{x'_{mn} m}{a} J'_m \left( \frac{x'_{mn}}{a} \rho' \right) e^{-jk\rho'} \cos(m\phi') \quad \dots(4.2)$$

In equations (4.1) and (4.2), indices  $m = n = 1$  denote the dominant TE<sub>11</sub> mode of propagation. The radial distance  $\rho'$  and angle  $\phi'$  on the aperture of the waveguide are shown in Figure 4.1 (b). The radius of the circular cylindrical waveguide is denoted by 'a'. Further  $x'_{mn} = 1.841$  for  $m = n = 1$ . While  $J_m$  denote the cylindrical Bessel function of order m,  $J'_m$  refers to the derivative of the Bessel function  $J_m$ .

The corresponding aperture magnetic field distribution of the circular waveguide with TE<sub>11</sub> dominant mode propagation is represented as in [Narasimhan M.S. and Rao B.V., 1971]

$$H_{\rho}(\rho', \phi') = \frac{E_{\rho}^{mnTE}(\rho', \phi')}{\frac{\omega\mu}{K_Z^{TE}}} \quad \dots(4.3)$$

$$H_{\phi}(\rho', \phi') = \frac{E_{\phi}^{mnTE}(\rho', \phi')}{\frac{\omega\mu}{K_Z^{TE}}} \quad \dots(4.4)$$

$$K_Z^{TE} = \sqrt{k^2 - \left( \frac{x'_{mn}}{a} \right)^2} \quad \dots(4.5)$$

With the unit normal of the radiating aperture directed along the Z- axis (Figure 4.1a), the equivalent electric 'J' and magnetic 'M' currents on the aperture of the circular waveguide are computed from the equations (4.6) to (4.9).

$$J_{\rho}(\rho', \varphi') = -H_{\phi}(\rho', \varphi') \quad \dots(4.6)$$

$$J_{\phi}(\rho', \varphi') = H_{\rho}(\rho', \varphi') \quad \dots(4.7)$$

$$M_{\rho}(\rho', \varphi') = E_{\phi}(\rho', \varphi') \quad \dots(4.8)$$

$$M_{\phi}(\rho', \varphi') = -E_{\rho}(\rho', \varphi') \quad \dots(4.9)$$

The Cartesian components of the equivalent currents on the aperture of the waveguide can be written as:

$$J_x(x', y') = J_{\rho}(\rho', \varphi') \cos \varphi' - J_{\phi}(\rho', \varphi') \sin \varphi' \quad \dots(4.10)$$

$$J_y(x', y') = J_{\rho}(\rho', \varphi') \sin \varphi' + J_{\phi}(\rho', \varphi') \cos \varphi' \quad \dots(4.11)$$

$$M_x(x', y') = M_{\rho}(\rho', \varphi') \cos \varphi' - M_{\phi}(\rho', \varphi') \sin \varphi' \quad \dots(4.12)$$

$$M_y(x', y') = M_{\rho}(\rho', \varphi') \sin \varphi' + M_{\phi}(\rho', \varphi') \cos \varphi' \quad \dots(4.13)$$

In equations (4.10) to (4.13),  $x'$  and  $y'$  denote a point on the aperture of the waveguide (Figure 4.1b). The electric field and magnetic fields radiated by point electric dipole evaluated at an arbitrary field point P are dealt in [Narsimhan M.S. and Kumar B.P., 1990]. For a point electric dipole with  $x$  directed current ( $x$ - directed dipole), the co and cross polar components of the E- and H – fields at any arbitrary radial distance of observation are given by

$$E_{xx}^{ED}(x, y, z, r) = \left\{ \frac{\eta}{r^2} \left( 2 - 3 \frac{y^2 + z^2}{r^2} \right) - \left[ j \left( \frac{\omega u}{r} \left( \frac{y^2 + z^2}{r^2} \right) + \frac{\eta}{kr^3} \left( 2 - 3 \frac{y^2 + z^2}{r^2} \right) \right) \right] \right\} \frac{e^{-jkr}}{4\pi} \quad \dots(4.14)$$

$$E_{yx}^{ED}(x, y, z, r) = \left\{ \frac{3\eta}{r^2} + j \left( \frac{\omega u}{r} - \frac{3\eta}{kr^2} \right) \right\} \frac{yx}{r^2} \frac{e^{-jkr}}{4\pi} \quad \dots(4.15)$$

$$E_{zx}^{ED}(x, y, z, r) = \left\{ \frac{3\eta}{r^2} + j \left( \frac{\omega u}{r} - \frac{3\eta}{kr^2} \right) \right\} \frac{zx}{r^2} \frac{e^{-jkr}}{4\pi} \quad \dots(4.16)$$

$$H_{xx}^{ED}(x, y, z, r) = 0 \quad \dots(4.17)$$

$$H_{yx}^{ED}(x, y, z, r) = (1 + jk) \left( \frac{-z}{r^2} \right) \frac{e^{-jkr}}{4\pi} \quad \dots(4.18)$$

$$H_{zx}^{ED}(x, y, z, r) = (1 + jk) \left( \frac{y}{r^2} \right) \frac{e^{-jkr}}{4\pi} \quad \dots(4.19)$$

Where  $\eta$  = impedance of medium =  $120\pi$  (free-space),

$$x = x_f - x' \quad \dots(4.20)$$

$$y = y_f - y' \quad \dots(4.21)$$

$$z = z_f - z' \quad \dots(4.22)$$

$$r = \sqrt{x^2 + y^2 + z^2} \quad \dots(4.23)$$

$$x_f = r \sin \theta \cos \varphi \quad \dots(4.24)$$

$$y_f = r \sin \theta \sin \varphi \quad \dots(4.25)$$

$$z_f = r \cos \theta \quad \dots(4.26)$$

$(x', y', z')$  and  $(x_f, y_f, z_f)$  denote the coordinates of the source point and the observation point respectively.

In the expressions (4.14) to (4.19), superscript ED stands for electric dipole. The alphabets in the subscript of the expressions (4.14) to (4.19) are meant to identify or distinguish between the co polar and cross polar components of the field radiated by the point dipole associated with a designated direction of current. For example  $E_{yx}^{ED}$  denotes the y- component of Electric field due the x directed current in an electric dipole. The concept of duality between J and M, E and H, H and E,  $\eta$  (Harrington R.F., 1961) can be invoked to derive the near fields radiated by magnetic

dipole from the knowledge of the fields radiated by corresponding electric dipole. Accordingly, for a point Magnetic Dipole (MD) with x – directed magnetic current, the fields radiated by X-directed magnetic dipole are given by

$$E_{xx}^{MD}(x, y, z, r) = 0 \quad \dots(4.27)$$

$$E_{yx}^{MD}(x, y, z, r) = -(1 + jk) \left( \frac{-z}{r^2} \right) \frac{e^{-jkr}}{4\pi} \quad \dots(4.28)$$

$$E_{zx}^{MD}(x, y, z, r) = -(1 + jk) \left( \frac{y}{r^2} \right) \frac{e^{-jkr}}{4\pi} \quad \dots(4.29)$$

$$H_{xx}^{MD}(x, y, z, r) = \left\{ \begin{aligned} &\frac{1}{\eta r^2} \left( 2 - 3 \frac{y^2 + z^2}{r^2} \right) \\ &-j \left( \frac{\omega u}{r} \left( \frac{y^2 + z^2}{r^2} \right) + \frac{1}{\eta k r^3} \left( 2 - 3 \frac{y^2 + z^2}{r^2} \right) \right) \end{aligned} \right\} \frac{e^{-jkr}}{4\pi} \quad \dots(4.30)$$

$$H_{yx}^{MD}(x, y, z, r) = \left\{ \frac{3}{\eta r^2} + j \left( \frac{\omega u}{r} - \frac{3}{\eta k r^2} \right) \right\} \frac{yx}{r^2} \frac{e^{-jkr}}{4\pi} \quad \dots(4.31)$$

Similarly Electric and Magnetic fields for y-directed electric dipole are given as follows,

$$E_{yy}^{ED}(x, y, z, r) = \left\{ \begin{aligned} &\frac{\eta}{r^2} \left( 2 - 3 \frac{z^2 + x^2}{r^2} \right) \\ &-j \left( \frac{\omega u}{r} \left( \frac{z^2 + x^2}{r^2} \right) + \frac{\eta}{k r^3} \left( 2 - 3 \frac{z^2 + x^2}{r^2} \right) \right) \end{aligned} \right\} \frac{e^{-jkr}}{4\pi} \quad \dots(4.32)$$

$$E_{zy}^{ED}(x, y, z, r) = \left\{ \frac{3\eta}{r^2} + j \left( \frac{\omega u}{r} - \frac{3\eta}{k r^2} \right) \right\} \frac{zy}{r^2} \frac{e^{-jkr}}{4\pi} \quad \dots(4.33)$$

$$E_{xy}^{ED}(x, y, z, r) = \left\{ \frac{3\eta}{r^2} + j \left( \frac{\omega u}{r} - \frac{3\eta}{k r^2} \right) \right\} \frac{xy}{r^2} \frac{e^{-jkr}}{4\pi} \quad \dots(4.34)$$

$$H_{yy}^{ED}(x, y, z, r) = 0 \quad \dots(4.35)$$



$$H_{zy}^{ED}(x, y, z, r) = (1 + jk) \left( \frac{-x}{r^2} \right) \frac{e^{-jkr}}{4\pi} \quad \dots(4.36)$$

$$H_{xy}^{ED}(x, y, z, r) = (1 + jk) \left( \frac{z}{r^2} \right) \frac{e^{-jkr}}{4\pi} \quad \dots(4.37)$$

The electric and magnetic radiated by y- directed magnetic dipole are given by

$$E_{yy}^{MD}(x, y, z, r) = 0 \quad \dots(4.38)$$

$$E_{zy}^{MD}(x, y, z, r) = -(1 + jk) \left( \frac{-x}{r^2} \right) \frac{e^{-jkr}}{4\pi} \quad \dots(4.39)$$

$$E_{xy}^{MD}(x, y, z, r) = -(1 + jk) \left( \frac{z}{r^2} \right) \frac{e^{-jkr}}{4\pi} \quad \dots(4.40)$$

$$H_{yy}^{MD}(x, y, z, r) = \left\{ \frac{1}{\eta r^2} \left( 2 - 3 \frac{z^2 + x^2}{r^2} \right) - j \left( \frac{\omega u}{r} \left( \frac{z^2 + x^2}{r^2} \right) + \frac{1}{\eta k r^3} \left( 2 - 3 \frac{z^2 + x^2}{r^2} \right) \right) \right\} \frac{e^{-jkr}}{4\pi} \quad \dots(4.41)$$

$$H_{zy}^{MD}(x, y, z, r) = \left\{ \frac{3}{\eta r^2} + j \left( \frac{\omega u}{r} - \frac{3}{\eta k r^2} \right) \right\} \frac{zy}{r^2} \frac{e^{-jkr}}{4\pi} \quad \dots(4.42)$$

$$H_{xy}^{MD}(x, y, z, r) = \left\{ \frac{3}{\eta r^2} + j \left( \frac{\omega u}{r} - \frac{3}{\eta k r^2} \right) \right\} \frac{xy}{r^2} \frac{e^{-jkr}}{4\pi} \quad \dots(4.43)$$

For circular waveguide of Figure 4.1(a), since there is no equivalent electric or magnetic current directed along Z direction, the expressions for field radiated by Z directed electric and magnetic dipoles are not discussed.

At a given observation or field point  $P(x_f, y_f, z_f)$ , the Cartesian components of the electric and magnetic field due to electric and magnetic dipoles located at a point  $(x', y', z')$  on the radiating aperture of the waveguide can be written as

$$E_{xT}(x, y, z, r) = J_x(x', y')E_{xx}^{ED} + J_y(x', y')E_{xy}^{ED} + M_x(x', y')E_{xx}^{MD} + M_y(x', y')E_{xy}^{MD} \quad \dots(4.44)$$

$$E_{yT}(x, y, z, r) = J_x(x', y')E_{yx}^{ED} + J_y(x', y')E_{yy}^{ED} + M_x(x', y')E_{yx}^{MD} + M_y(x', y')E_{yy}^{MD} \quad \dots(4.45)$$

$$E_{zT}(x, y, z, r) = J_x(x', y')E_{zx}^{ED} + J_y(x', y')E_{zy}^{ED} + M_x(x', y')E_{zx}^{MD} + M_y(x', y')E_{zy}^{MD} \quad \dots(4.46)$$

$$H_{xT}(x, y, z, r) = J_x(x', y')H_{xx}^{ED} + J_y(x', y')H_{xy}^{ED} + M_x(x', y')H_{xx}^{MD} + M_y(x', y')H_{xy}^{MD} \quad \dots(4.47)$$

$$H_{yT}(x, y, z, r) = J_x(x', y')H_{yx}^{ED} + J_y(x', y')H_{yy}^{ED} + M_x(x', y')H_{yx}^{MD} + M_y(x', y')H_{yy}^{MD} \quad \dots(4.48)$$

$$H_{zT}(x, y, z, r) = J_x(x', y')H_{zx}^{ED} + J_y(x', y')H_{zy}^{ED} + M_x(x', y')H_{zx}^{MD} + M_y(x', y')H_{zy}^{MD} \quad \dots(4.49)$$

The Cartesian components of the radiation pattern of the waveguide at a field point  $P(r, \theta, \phi)$  are obtained by integrating the equations (4.44) – (4.49) over the aperture of the waveguide implying the vector summation of field radiated by the array of electric and magnetic dipoles positioned on the radiating aperture of the waveguide.

$$E_x^{WG}(r, \theta, \phi) = \iint_A E_{xT}(x, y, z, r) dx' dy' \quad \dots(4.50)$$

$$E_y^{WG}(r, \theta, \phi) = \iint_A E_{yT}(x, y, z, r) dx' dy' \quad \dots(4.51)$$

$$E_z^{WG}(r, \theta, \phi) = \iint_A E_{zT}(x, y, z, r) dx' dy' \quad \dots(4.52)$$

$$H_x^{WG}(r, \theta, \phi) = \iint_A H_{xT}(x, y, z, r) dx' dy' \quad \dots(4.53)$$

$$H_y^{WG}(r, \theta, \phi) = \iint_A H_{yT}(x, y, z, r) dx' dy' \quad \dots(4.54)$$

$$H_z^{WG}(r, \theta, \phi) = \iint_A H_{zT}(x, y, z, r) dx' dy' \quad \dots(4.55)$$

Functional relationship between the positional coordinates of field point  $P(r, \theta, \phi, x_f, y_f, z_f)$ , the variables  $(x, y, z)$  and source points of Electric and Magnetic dipoles on waveguide aperture

$(\rho', \phi', x', y', z')$  are explicit in equations (4.20) –(4.26) and Figure 4.1 (b). The spherical components of the near field radiation pattern of the waveguide at  $P(r, \theta, \phi)$  can now be written as

$$E_{\theta}^{WG}(r, \theta, \phi) = E_x^{WG} \cos \theta \cos \phi + E_y^{WG} \cos \theta \sin \phi - E_z^{WG} \sin \theta \quad \dots(4.56)$$

$$E_{\phi}^{WG}(r, \theta, \phi) = -E_x^{WG} \sin \phi + E_y^{WG} \cos \phi \quad \dots(4.57)$$

$$H_{\theta}^{WG}(r, \theta, \phi) = H_x^{WG} \cos \theta \cos \phi + H_y^{WG} \cos \theta \sin \phi - H_z^{WG} \sin \theta \quad \dots(4.58)$$

$$H_{\phi}^{WG}(r, \theta, \phi) = -H_x^{WG} \sin \phi + H_y^{WG} \cos \phi \quad \dots(4.59)$$

where  $\phi = 0 - 360^\circ$  and  $\theta$  is  $-180^\circ \leq 0^\circ \leq +180^\circ$

It is pertinent to emphasize that the formulation presented in this section is valid to other antenna configurations as well with the corresponding changes in the expressions of electric field distribution and equivalent currents on aperture (Equations (4.1) to (4.2) and Equations (4.6) to (4.9)).

### 4.3 Simulation Results:

This section discusses simulation results of radiation patterns of circular cylindrical waveguide and conical horn obtained through the analysis presented in the earlier section. The results include the surface contour plots of current distribution over radiating aperture, far-field and near-field radiation patterns of both cylindrical waveguide and conical horn. The discussion in this section also covers the validation studies to substantiate the applicability and appropriateness of the proposed near field analysis of antennas for future system applications such as TWI.

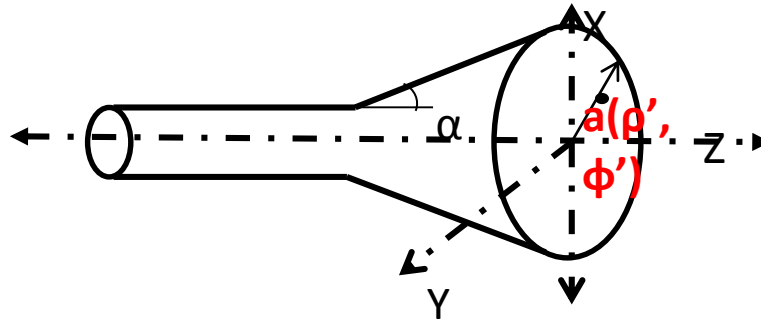
#### 4.3.1 Aperture Current Distribution

The field or current distribution over the aperture of a radiator is a fundamental parameter that determines the radiation characteristics of the antenna. The analysis proposed facilitates to consider both the electric current ‘J’ and magnetic current ‘M’ over the radiating aperture. In this section, the simulated surface contour plots of both the electric and magnetic currents over the radiating aperture are discussed. For the simulation, the operating frequency of 9.375 GHz has been chosen for the dominant mode of circular waveguide and conical horn designed for X-Band frequencies of (8.2-12.4 GHz). For the simulation of the current distribution over the radiating aperture of circular waveguide, equations (4.1) to (4.4) have been invoked. For the case of conical horn, the aperture field distribution of a conical horn given by [Narasimhan M.S. and Rao B.V.,

1971] are used and they are represented by equations (4.61) and (4.62) where L is the axial length of the horn.

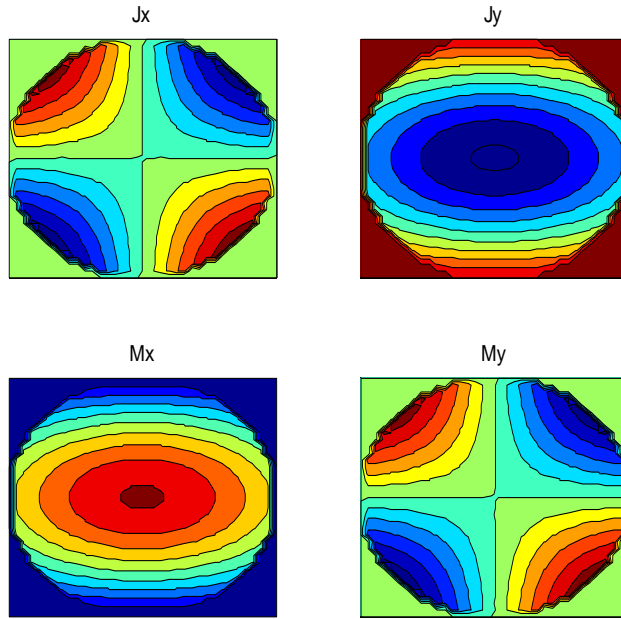
$$E_{\rho}^{mnTE}(\rho', \phi') = \frac{m}{\rho'} J_m \left( \frac{x'_{mn}}{a} \rho' \right) e^{-jk\sqrt{\rho'^2 + L^2}} \sin(m\phi') \quad \dots(4.61)$$

$$E_{\phi}^{mnTE}(\rho', \phi') = \left( \frac{x'_{mn}}{a} \right) J'_m \left( \frac{x'_{mn}}{a} \rho' \right) e^{-jk\sqrt{\rho'^2 + L^2}} \cos(m\phi') \quad \dots(4.62)$$



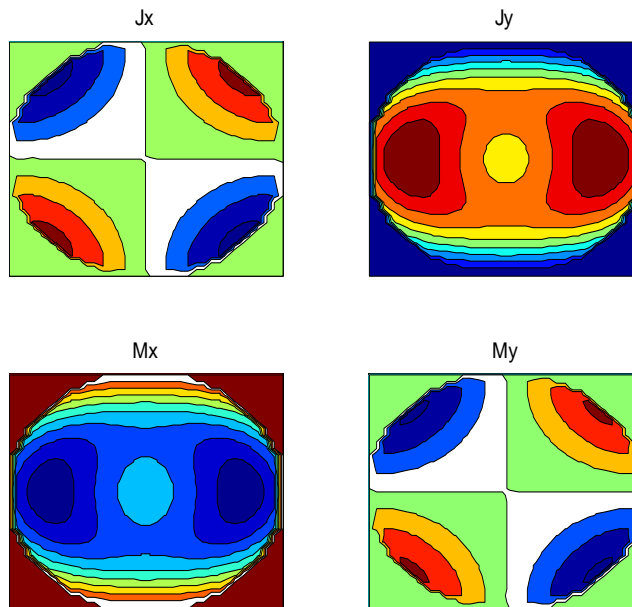
**Figure 4. 2: Conical Horn Antenna**

Figure 4.2 illustrates a geometrical configuration of a conical horn. The radius of aperture 'a' for circular waveguide is a=1.05 cm and for the conical Horn is 4.1cm. The semi flare angle  $\alpha_0 = 21.09^\circ$  and the axial length 'L' is 10.63cms. For the generation of source (excitations) points on the aperture, the step size along both the radial ( $\rho$ ) and azimuthal ( $\phi$ ) directions on the aperture is 36 leading to total number of (36 x 36) points on the radiating aperture of both the circular waveguide and conical horn. The distributions of the electric 'J' and magnetic 'M' current on the aperture of the circular waveguide are illustrated in Figures 4.3 through contour filled images.



**Figure 4. 3: Current Distribution Over Aperture of Circular Waveguide**

The corresponding results of conical horn are shown in Figure 4.4.



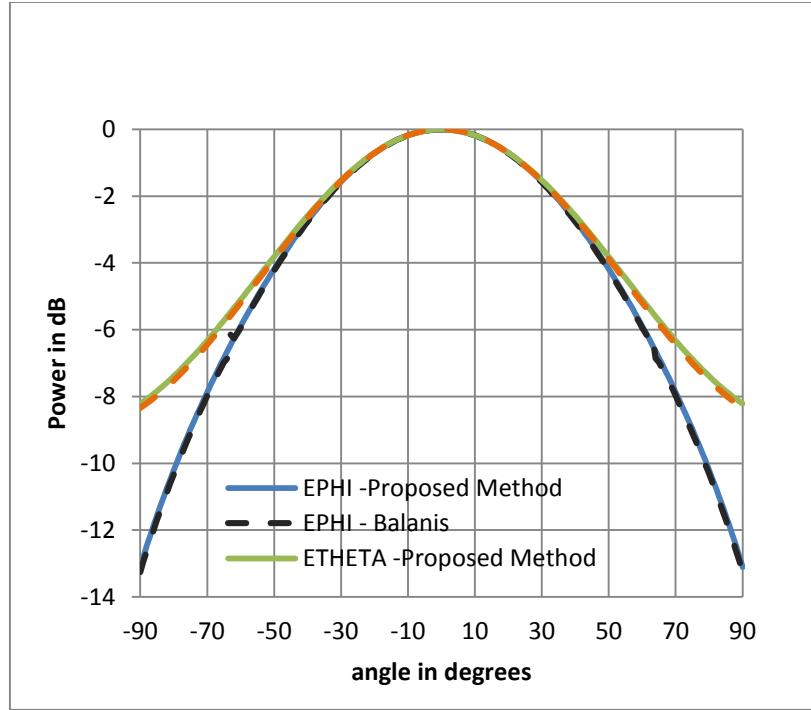
**Figure 4. 4: Current Distribution Over Aperture of Conical Horn**

### 4.3.2 Near-field and Far-field Radiation Patterns

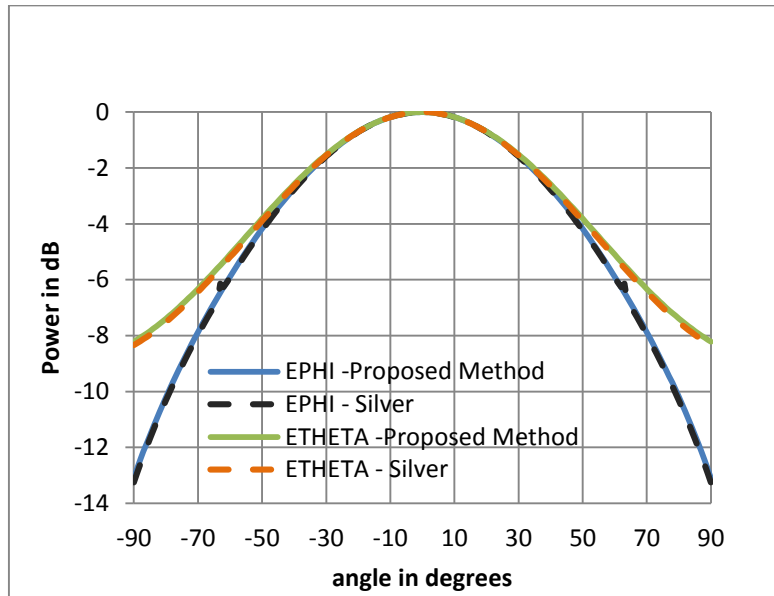
To validate the proposed formulation for the determination of radiation pattern of an antenna at an arbitrary distance covering both the far-field as well as near field, the simulations considered both circular cylindrical waveguide and conical horn as radiating elements.

#### A. Circular Cylindrical Waveguide:

The validation of the proposed near field radiation was initiated taking the note that the proposed analysis can treat the conventional far field radiation pattern as a special case of near field with the radial distance exceeding or far exceeding the conventional far field criterion. For an X-band circular waveguide radiating at a frequency of 9.375 GHz,  $\lambda=3.2\text{cm}$ , the near field distance can be below  $2D^2/\lambda$  ( $< 2.55\text{cm}$ ). Using the proposed approach for the determination of near field of an antenna with  $r=1000\lambda$  which clearly falls into far field of an X band circular waveguide (of radius  $rad=1.05\text{cm}$ ) at 9.375 GHz, the far field radiation patterns ( $E_\theta$  and  $E_\phi$  components) of circular waveguide are computed with the known aperture distribution of the cylindrical waveguide and using equations (4.61) and (4.62) as well as the far field analysis given in (Balanis C.A., 2005). The computed results are shown in Figure 4.5(a). From the results depicted in Figure 4.5(a), it is evident that the results obtained from the two different formulations show excellent correlation and thereby substantiating the proposed formulation for near field radiation pattern. Figure 4.5(b) shows another validation for the radiation patterns through far field analysis given in [Silver S., 1984]. From the results of Figures 4.5(a) and (b), it is again evident that the results on far field radiation patterns of circular waveguide obtained from the different formulations are in excellent correlation with the proposed formulation for near field radiation pattern. It is pertinent to point out that even though equations 4.56 and 4.57 are specifically meant for the near-field radiation patterns of circular waveguides, they are also valid for an observation point located in the far field.

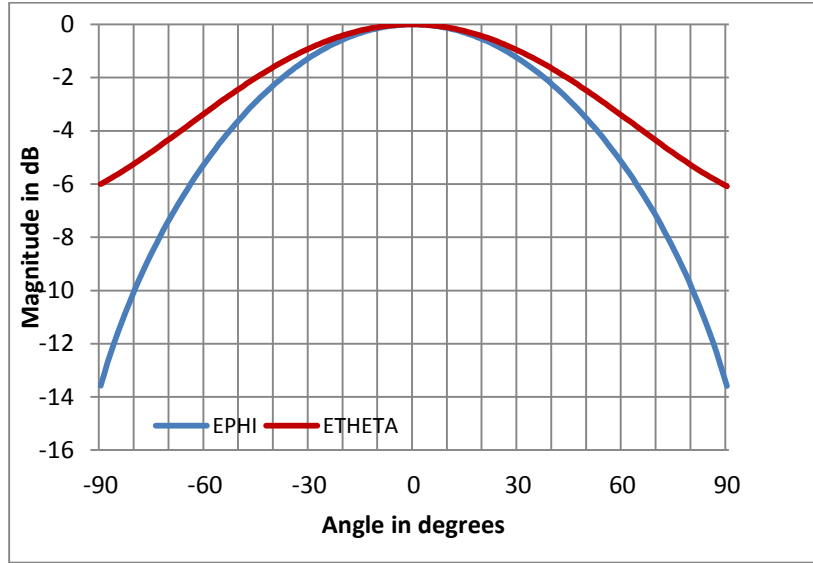


**Figure 4. 5(a): Comparison of Far Field Radiation Patterns of Circular Waveguide obtained from (Balanis C.A., 2005) and proposed Near-field method**

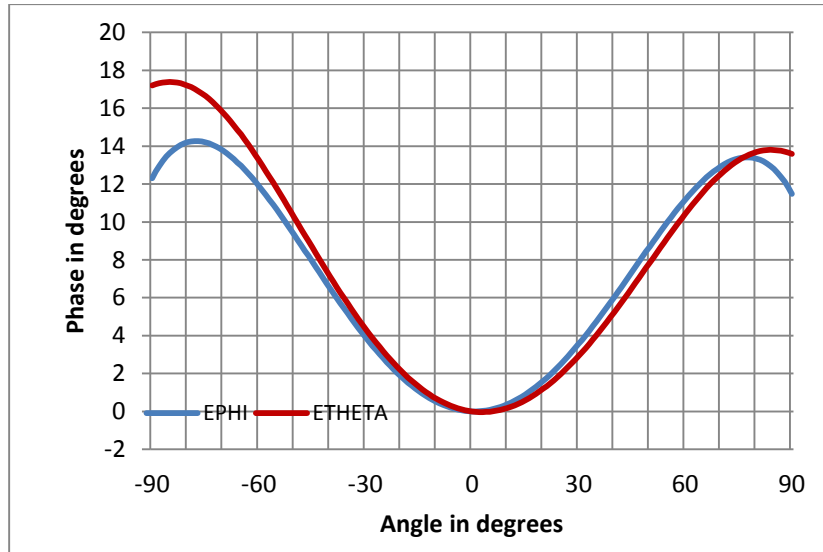


**Figure 4. 5 (b): Comparison of Far Field Radiation Patterns of Circular Waveguide obtained from (Silver S., 1949) and proposed Near-field method**

After substantiating the validity of the simulated far field patterns of circular cylindrical waveguide, the computations of near field radiation (amplitude and phase) patterns of circular waveguide have been carried out for  $r = 0.75\lambda$  at 9.375 GHz and the results are shown in Figures 4.6 (a) and 4.6 (b) respectively.



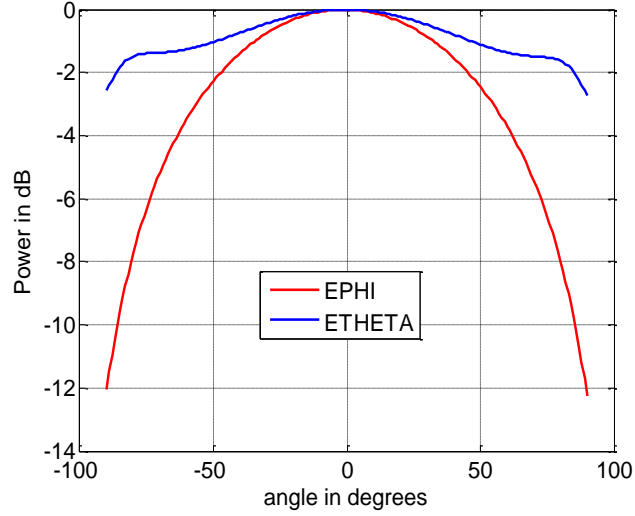
**Figure 4. 6 (a): Amplitude Pattern Patterns of a Circular Waveguide at  $r=0.75\lambda$**



**Figure 4. 6 (b): Phase Pattern of a Circular Waveguide at  $r=0.75\lambda$**

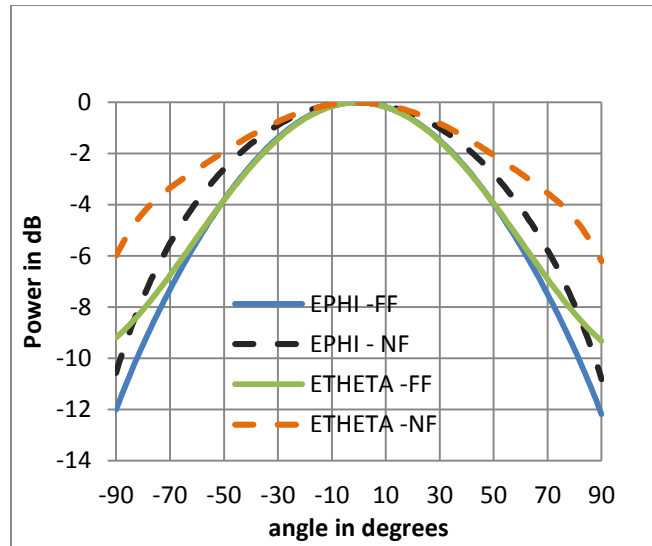
The radiation patterns of circular waveguide at a radial distance  $r = D^2/\lambda$  ( $D=2.1$  cm) and operating at 9.375 GHz are depicted in Figure 4.7.





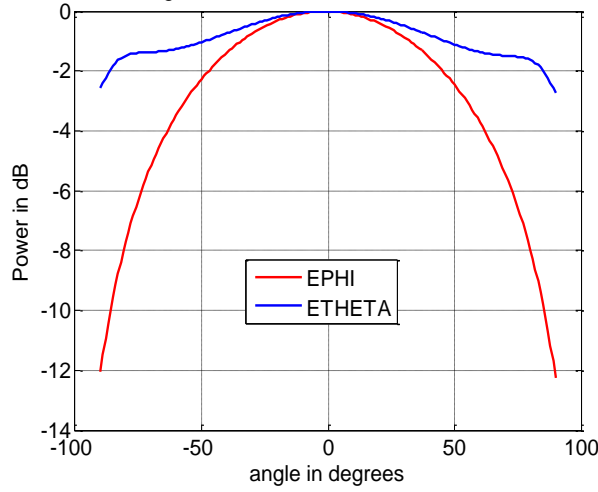
**Figure 4. 7: Radiation Pattern of Circular Waveguide at a distance of  $D^2/\lambda$**

An illustration of difference in normalized conventional far field radiation patterns of circular waveguide and the near field radiation pattern at a distance of  $D^2/\lambda$  is shown in Figure 4.8.

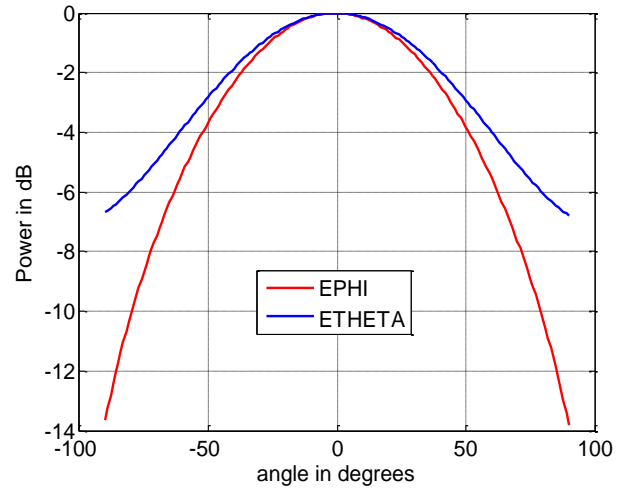


**Figure 4. 8: Comparison Far Field (FF) and Near Field (NF) pattern of Circular Waveguide at  $r= D^2/\lambda$**

The effect of variation in radial distance on the radiation pattern of circular cylindrical waveguide is shown in Figure 4.9. Figures 4.9 (a) and (b) depict the amplitude of radiation pattern of circular waveguide at  $r= D^2/\lambda$  and  $r= 2D^2/\lambda$  respectively.

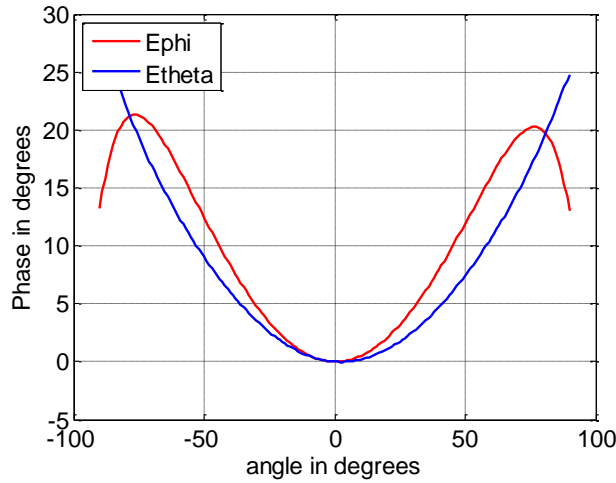


(a)

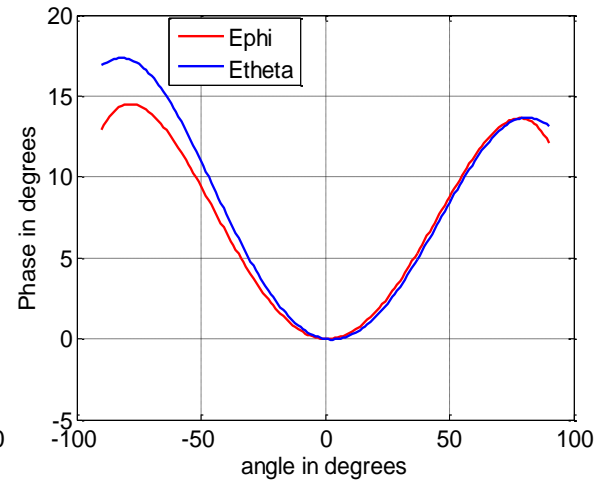


(b)

**Figure 4. 9: Amplitude Radiation Patterns of Circular Waveguide. (a)  $r=D^2/\lambda$ ; (b)  $r=2D^2/\lambda$**   
The phase radiation patterns of circular waveguide at  $r=D^2/\lambda$  and  $r=2D^2/\lambda$  are shown in Figures 4.10 (a) and (b) respectively.



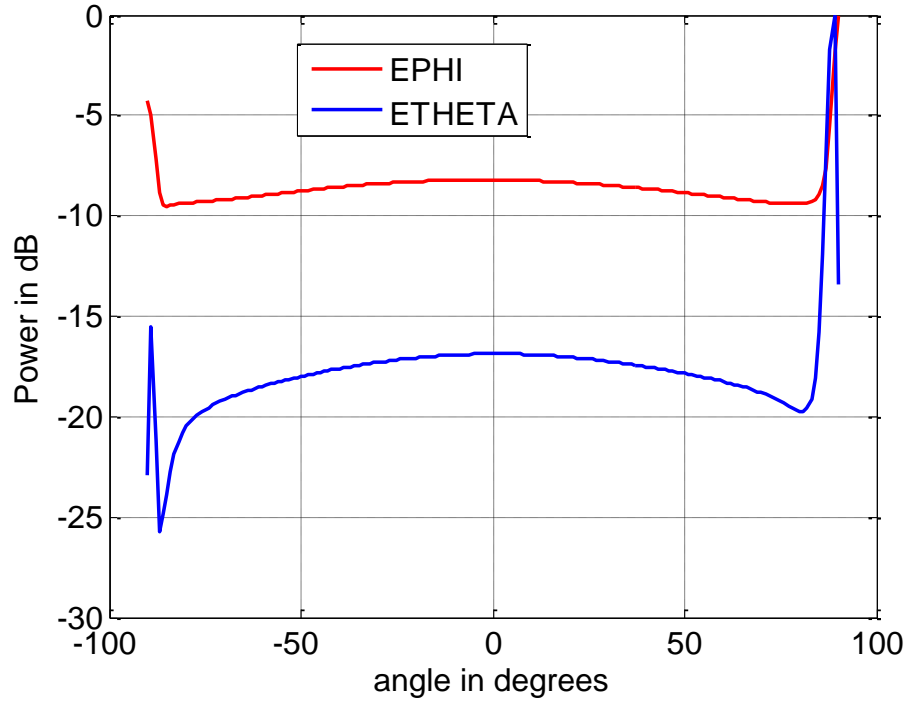
(a)



(b)

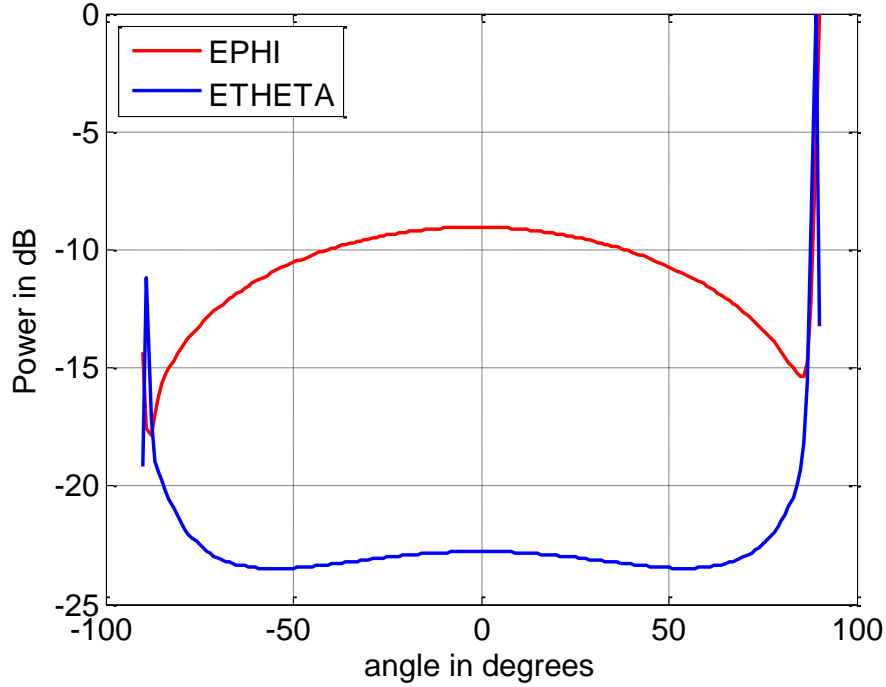
**Figure 4. 10: Phase Radiation Pattern of Circular Waveguide. (a)  $r=D^2/\lambda$  ; (b)  $r=2D^2/\lambda$**   
In the analysis of near field radiation pattern, one of the interesting and curious aspects of observation is to monitor the gradual transformation in the profiles of the radiation pattern with the incremental increase in the radial distance of observation. Simulations were carried out to obtain near-field patterns of an X- band circular waveguide element at distances of  $0.2\lambda$  (0.64cm),  $0.3\lambda$  (0.96cm),  $0.4\lambda$  (1.28cm),  $0.5\lambda$  (1.6cm) and  $0.75\lambda$  (2.4 cm).

Figure 4.11 depicts the radiation patterns of a circular waveguide at a distance ( $r = 0.2\lambda$  or 0.64 cm) which is relatively very close to the radiating aperture of the waveguide.



**Figure 4. 11: Near Field Radiation pattern of Circular Waveguide at  $r = 0.2 \lambda$  (0.64 cm)**

A radial distance of  $0.2 \lambda$  falls within the reactive field region ( $r < 0.62\sqrt{\frac{D^3}{\lambda}} = 0.995$  cm) of waveguide. The radiation patterns of the waveguide at this radial distance follow a rather unconventional profile and are drastically different from the conventional far field radiation patterns of an X- band waveguide. The simulation results of the near field radiation patterns of circular waveguide at  $r=0.3\lambda$  (0.96cm) are shown in Figure 4.12. The results of the Figure 4.12 reveal that the azimuthal component ( $E_\phi$ ) of the radiation pattern appears to exhibit the main lobe profile although with a reduced gain at the bore sight direction. But the  $E_\theta$  component of the radiation pattern of the waveguide does not exhibit broadside feature.

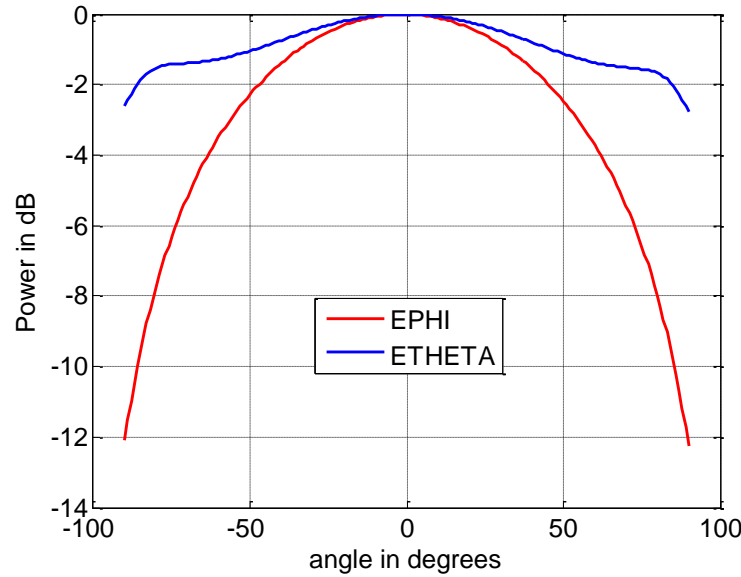


**Figure 4. 12: Radiation Pattern of Circular Waveguide at  $r= 0.3 \lambda$  (0.96 cm)**

The generalised near field analysis of antenna proposed in this thesis is based on the assumption that the field distribution over the radiating aperture is available. In the computation of a radiation pattern of an antenna, it is an implicit assumption that the radiated fields are computed at an observation point which is away from the radiating aperture surface (plane) of the antenna. In all the computations, the observation or field point is always located outside the aperture of the antenna. Therefore the radiation pattern is computed over a plane located at a radial distance which is away from the plane of aperture. In the far field computations, the observation point will never be on the aperture of the antenna. Again in the near field computations, for all the radial distances of measurement which are larger than the radius of the aperture, the field point will not be on the aperture of the antenna. However, for a case with radial near field distance less than the aperture radius of the antenna, for values of ' $\theta$ ' less than  $90^\circ$ , the observation or field point will be outside the aperture plane of the antenna. For  $\theta = \pm 90^\circ$ , the field point of near field computation is located within the aperture of the antenna and the formulation of the near field radiation pattern fails and therefore the obtained results should not be relied upon. The anomaly noticed in Figure 4.11 for  $\theta = \pm 90^\circ$  can be attributed to the above mentioned scenario of a field point located within the radiating aperture of the antenna since the radial distance of  $r=0.2 \lambda$  or 0.64 cm is less than the radius of the cylindrical waveguide at the stated operating frequency of 9.375 GHz. The asymmetry noticed in

Figures 4.11 and 4.12 can be due to the anomaly of the computed values of the field components at  $\theta = \pm 90^\circ$ . As stated, with the failure of the proposed near field analysis to deal with the scenario of the field or observation point located within the radiating aperture of the antenna and the resulting round off errors associated with inconsequential forced erroneous computations despite the failure of the proposed analysis at  $\theta = \pm 90^\circ$ , would have resulted in two different values of amplitude values of the field components of the radiation patterns at  $\theta = 90^\circ$  and  $\theta = -90^\circ$ . Again for the scenario of near field distance smaller than the radius of the radiating aperture, for  $\theta > 90^\circ$ , the observation point will be located within the cylindrical waveguide (since Z co-ordinate of the field point is less than 0) and the proposed near field analysis should not be applied.

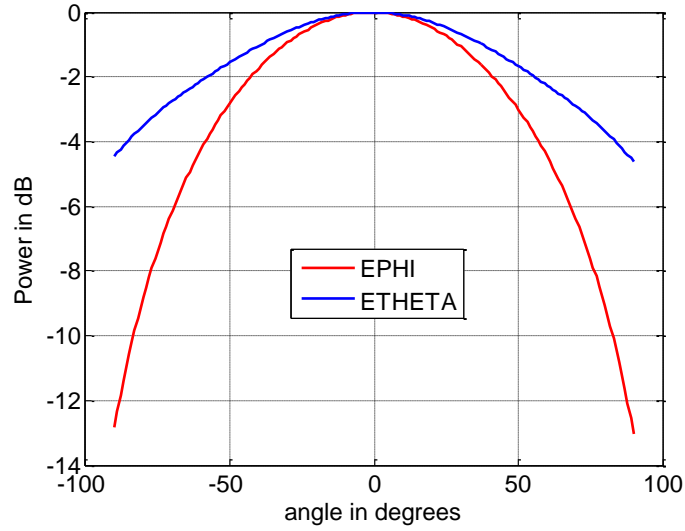
When the near field radial distance is increased to  $r = 0.4\lambda$ , the depicted near field radiation patterns in Figure 4.13 appear to exhibit the broadside radiating features expected out of circular waveguide.



**Figure 4. 13: Radiation Pattern of Circular Waveguide at  $r = 0.4 \lambda$  (1.28 cm)**

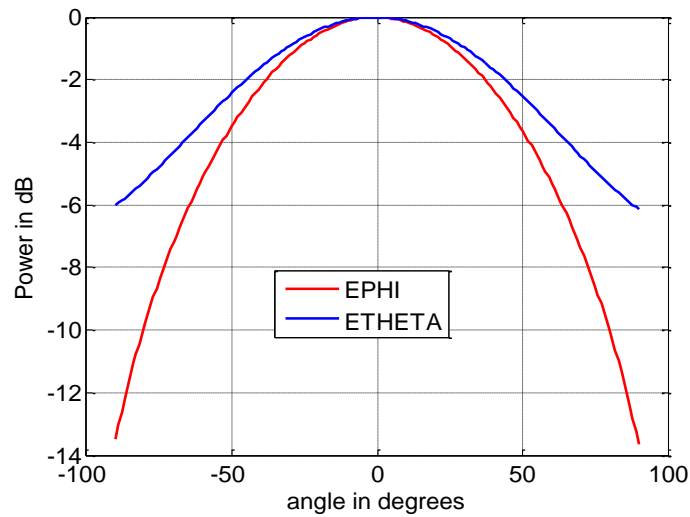
Both  $E_\phi$  and  $E_\theta$  components of the near field radiation pattern shown in Figure 4.13 exhibit clearly defined main lobe with  $E_\theta$  component showing some ripples in the pattern.

At a radial distance of  $r = 0.5 \lambda$  (1.6 cm), both the components of the radiation pattern exhibit smooth profiles of the main lobe and also the ripples in the  $E_\theta$  component vanish (Figure 4.14).

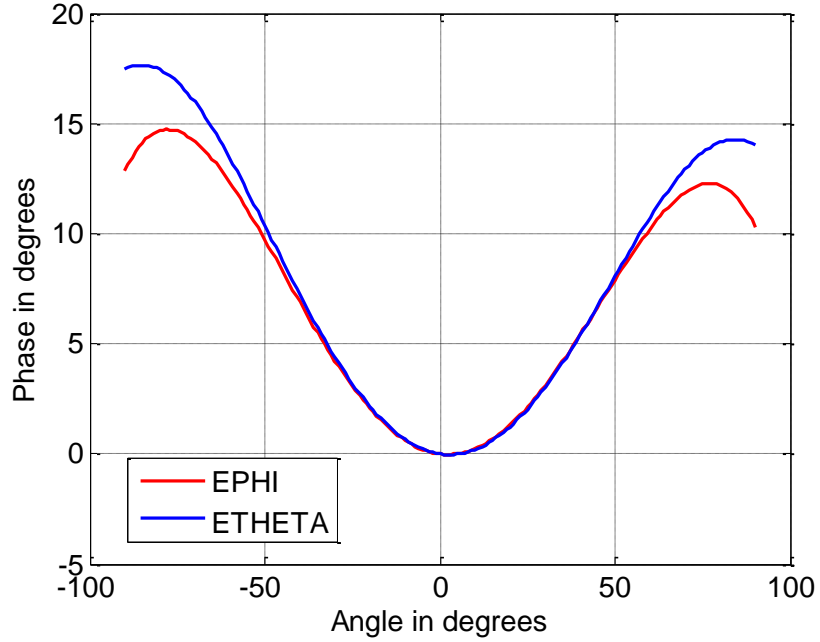


**Figure 4. 14: Radiation Pattern of Circular Waveguide at  $r=0.5 \lambda$  (1.6 cm)**

At a distance  $r= 0.75 \lambda$ , the radiation pattern and phase pattern of circular waveguide (Figures 4.15(a) and (b)) show further improvement in the tapering nature of the  $E_\theta$  component. At  $r= 0.75 \lambda$ , the ratio of radial distance of observation to aperture diameter,  $(r/D) = 0.571$ .



**Figure 4. 15(a): Radiation Pattern of Circular Waveguide at a distance  $r=0.75 \lambda$**



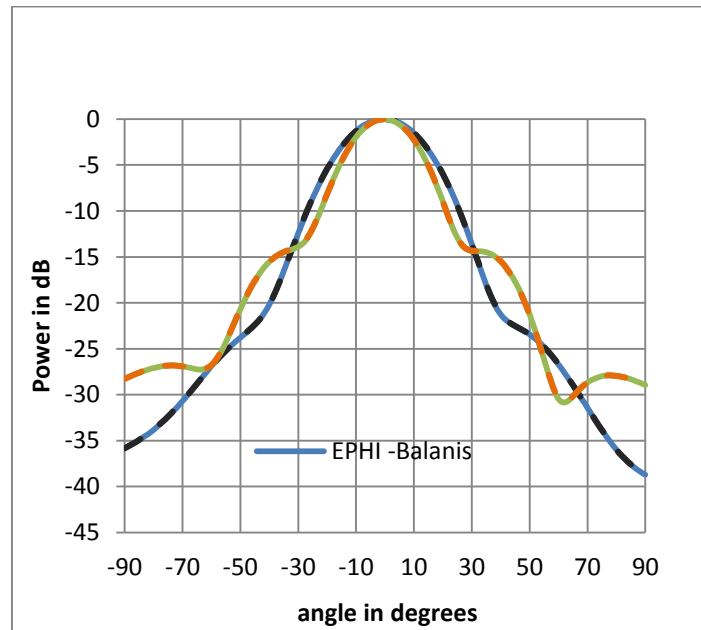
**Figure 4. 15(b): Phase Pattern of Circular Waveguide at a distance  $r=0.75 \lambda$**

**B. Conical Horn:** Conical Horn has been one of the most widely radiating elements in antenna engineering. Apart from the far field analysis, the near field analysis of conical horn has also been a topic of research. In the earlier attempts on near field radiation pattern of Conical horn, UGTD has been widely invoked [Narasimhan M.S. and Rao K.S., 1979; Narasimhan M.S. et. al, 1981]. However, the analyses of the two cited research are restricted to the principal planes only. They cannot be applied to arbitrary plane of observation. In this subsection, the simulation results of near field radiation pattern of conical horn derived through the proposed generalized near field analysis are presented. Unlike the above cited prior work on the near field pattern of conical horn, the analysis proposed in this chapter facilitates the near field computation of conical horn in any arbitrary plane in 3D space which is required in beamsteering scenario covering both azimuthal and elevation angles. From the analytical formulation point of view, the circular cylindrical waveguide configuration can be considered as a limiting case of a conical horn of semi flare angle of zero degree.

The co-ordinate system for near field radiation pattern analysis of a conical horn is shown in Figure 4.2. The analysis for the determination of near field radiation pattern of circular cylindrical waveguide is extended to the case of conical horn without loss of generality. All the equations

developed for the near field radiation pattern analysis of circular waveguide are identically valid to conical horn. The distribution of electric field over the radiating aperture of conical horn are given by Equations (4.61) and (4.62).

As an initial step, the radiation patterns of conical horn with semi flare angle  $\alpha_0 = 21.09^\circ$  and radius=4.1 cm operating at 9.375 GHz is simulated at radial distance  $r=1000 \lambda$ . At this radial distance, the simulation meets and far exceeds the conventional far field distance criterion. In addition, the formulation available in (Balanis C.A., 2005) which is valid only for the far field radiation patterns is also made use of to obtain the far field radiation patterns of conical horn. The results derived through the formulation in (Balanis C.A., 2005) serve as a reference to validate the results obtained through the proposed formulation for the determination of radiation pattern of antenna at any arbitrary distance.

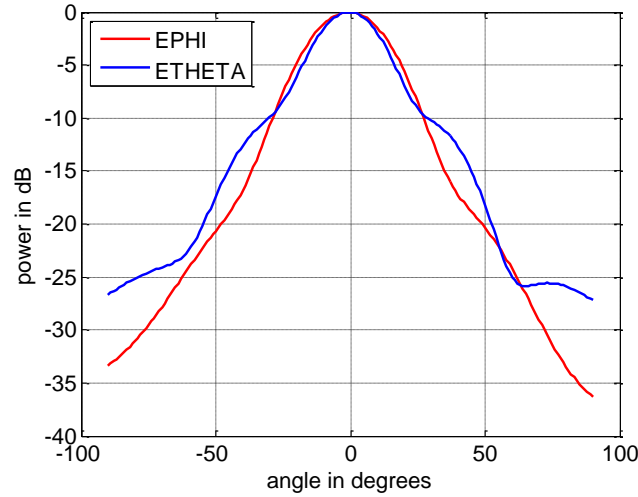


**Figure 4. 16: Comparison of Far Field Radiation Patterns of Conical Horn Antenna obtained from (Balanis C.A., 2005) and proposed Near-Field method**

The results depicted in Figure 4.16 clearly illustrate the excellent correlation between the results obtained through the analysis of (Balanis C.A., 2005) and the new near field formulation proposed in this chapter. For the simulations, conical horn of (radius= 4.1 cm, semi-flare angle  $\alpha_o = 21.09^\circ$ ) was considered with an operating frequency at 9.375 GHz.

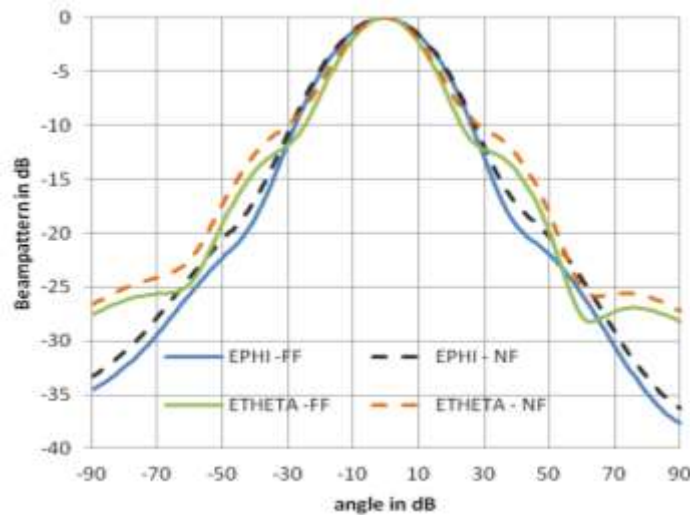


It is pertinent to point out that the analytical formulation proposed in this chapter is valid for any arbitrary distance of observation implying that it is applicable equally well for both near field as well as far-field radiation pattern. The near field radiation patterns of conical horn of semi-flare angle  $\alpha_o = 21.09^\circ$  and radius= 4.1cm at a radial distance of  $D^2/\lambda$  operating at 9.375 GHz are shown in Figure 4.17.



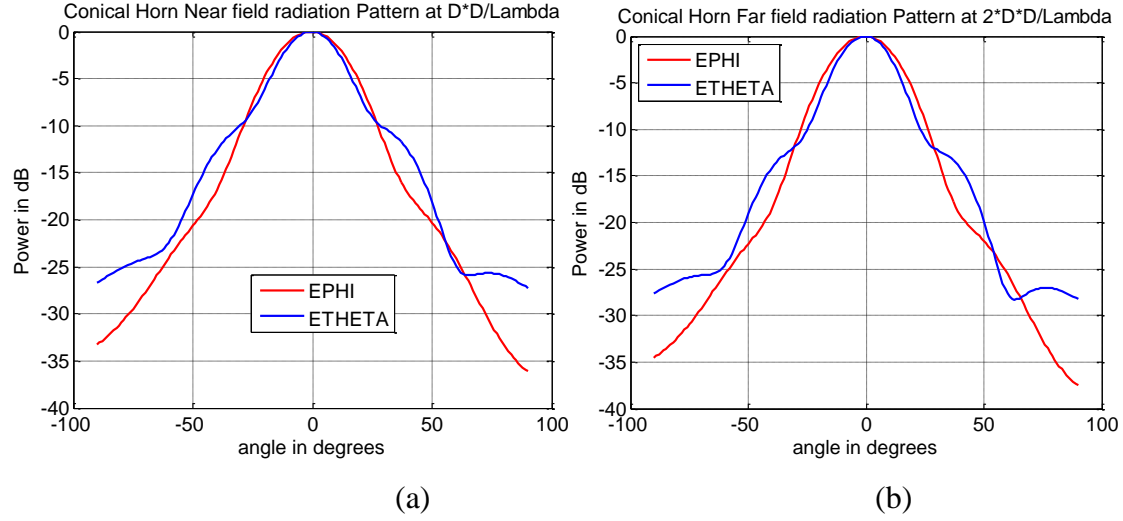
**Figure 4. 17: Near Field Radiation Pattern of Conical Horn at  $r= D^2/\lambda$**

A comparison of radiation patterns of conical horn (semi-flare angle  $\alpha_o = 21.09^\circ$ ) evaluated at radial distances of  $r= D^2/\lambda$  and its far field radiation patterns are illustrated in Figure 4.18.



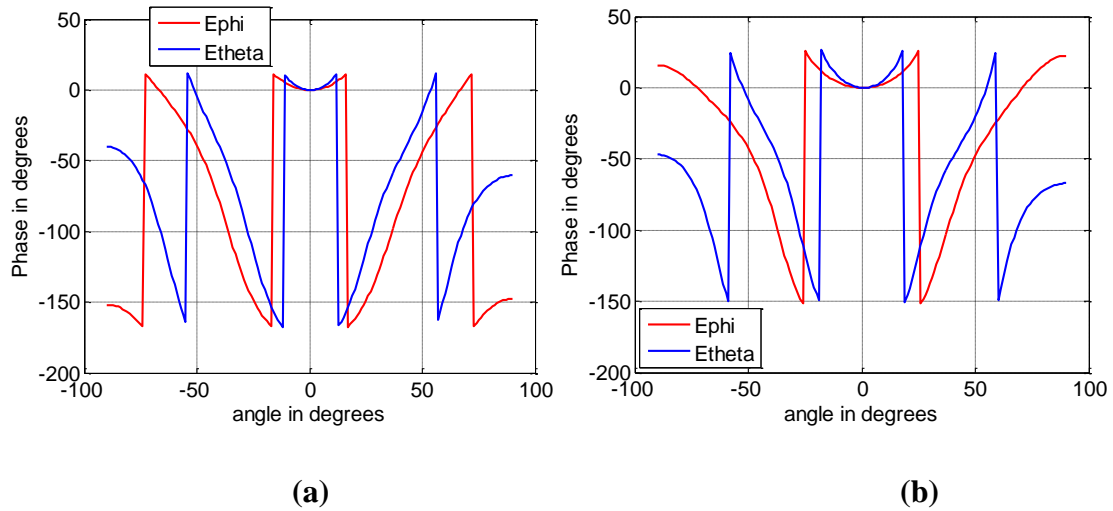
**Figure 4. 18: Comparison of Near-field and Far field Radiation Patterns of Conical Horn; (radius= 4.1 cm; semi-flare angle  $\alpha_o = 21.09^\circ$ )**

The effect of variation in radial distance of observation on the radiation pattern of conical horn is illustrated in Figures 4.19 and 4.20. The near field radiation patterns of conical horn at a radial distance of  $r = D^2/\lambda$  are shown in Figure 4.19 (a). The corresponding radiation patterns at  $r = 2D^2/\lambda$  are depicted in Figure 4.19 (b).



**Figure 4. 19: Comparison of Amplitude Radiation Pattern of Conical Horn: (a)  $r = D^2/\lambda$  (b)  $r = 2D^2/\lambda$ .**

The results of Figures 4.20 (a) and (b) illustrate the phase radiation patterns of the conical horn at radial distances of  $r = D^2/\lambda$  and  $2D^2/\lambda$  respectively.

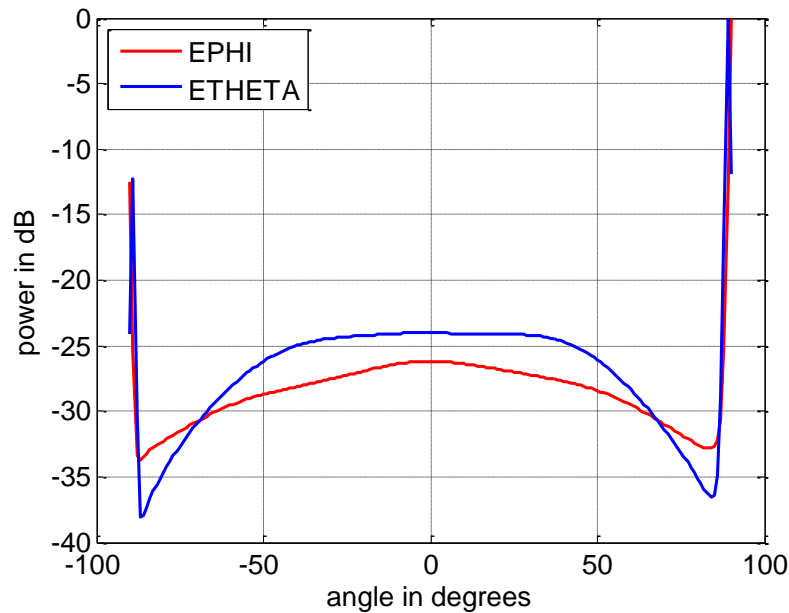


**Figure 4. 20: Comparison of Phase Radiation Pattern of Conical Horn: (a)  $r = D^2/\lambda$  (b)  $r = 2D^2/\lambda$ .**

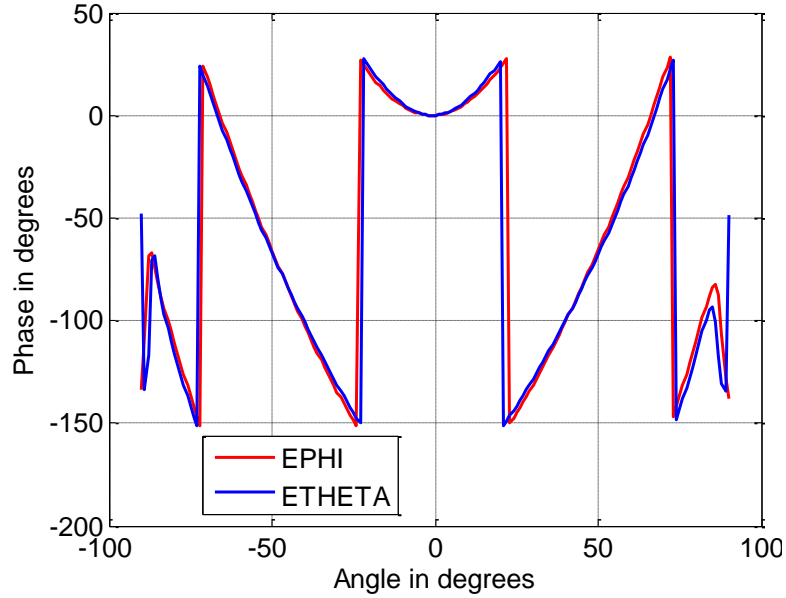
On comparing near-field and far field magnitude and phase plots of Figures 4.19 and 4.20, a clear indication in change of phase and beam widths can be noticed when the radial distance of observation is varied.

The analysis of near field radiation pattern was carried out for conical horn antenna was carried out to observe the gradual transformation in the profiles of the radiation pattern with the incremental increase in the radial distance of observation. Simulations were carried out to obtain near-field patterns of a X- band Conical Horn antenna element at radial distances of  $1\lambda$ ,  $2\lambda$ ,  $3\lambda$ ,  $4\lambda$  and  $10\lambda$ .

For a conical horn antenna operating at 9.375 GHz with a radius of 4.1 cm , a radial distance of  $1\lambda$  falls within the reactive field region ( $r < 0.62\sqrt{\frac{D^3}{\lambda}} = 8.1\text{cm}$ ). The simulation results of the near field radiation and Phase patterns of the conical with semi-flare angle  $\alpha_o = 21.09^\circ$  and radius=4.1 cm at  $r=1\lambda$  are shown in Figure 4.21(a) and (b). The radiation patterns of the conical horn antenna at this radial distance are drastically different from its conventional far field radiation patterns. The results of the Figure 4.21 reveal that both the azimuthal ( $E_\phi$ ) as well elevation ( $E_\theta$ ) components of the radiation patterns do not exhibit broadside feature of a conical horn.

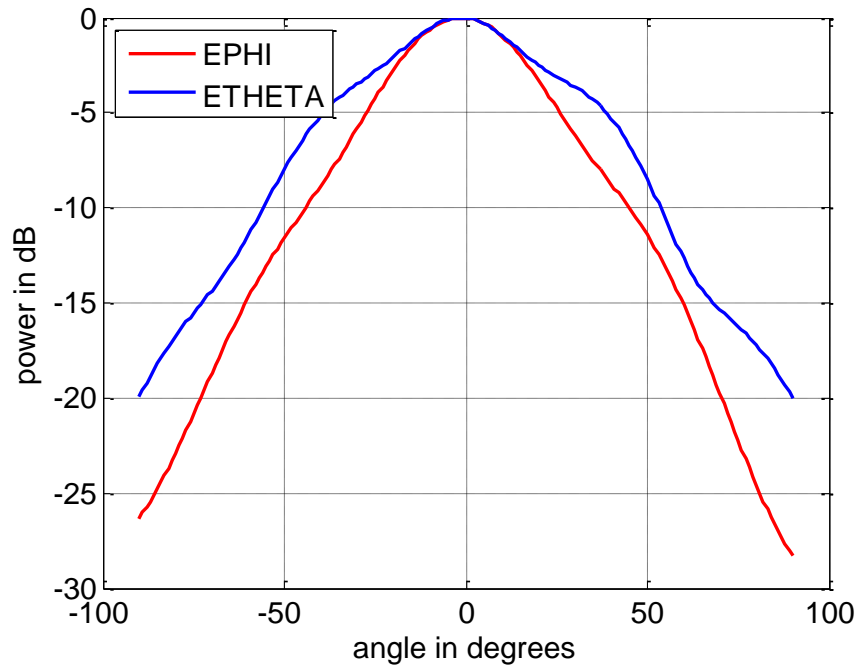


**Figure 4. 21(a): Near Field Radiation pattern of Conical Horn at a distance  $r=1\lambda$  (3.2cm)**



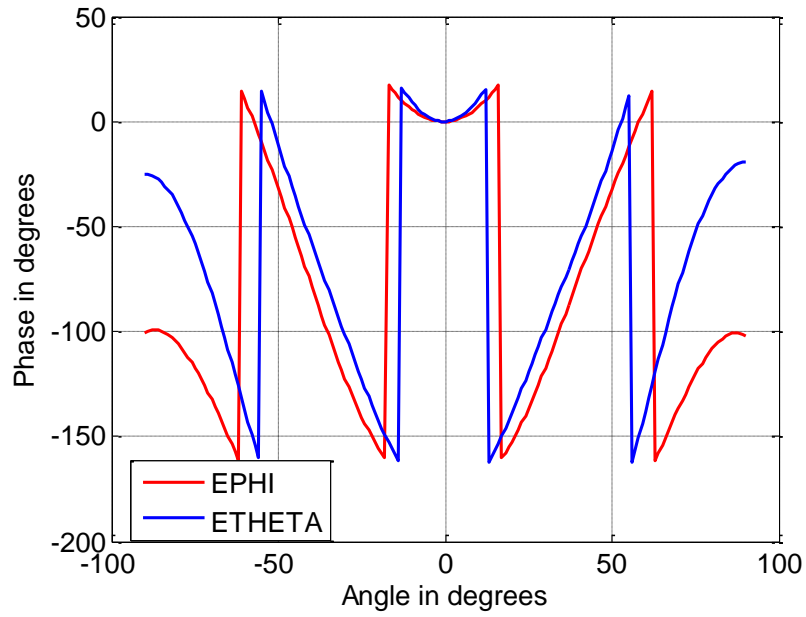
**Figure 4. 21(b): Near Field Phase pattern of Conical Horn at a distance  $r=1\lambda$  (3.2cm)**

When the near field radial distance is increased to  $r=2\lambda$ , the near field radiation patterns appear to exhibit the broadside radiating features expected out of conical horn antenna. Both the  $E_\phi$  and  $E_\theta$  components of the near field radiation and Phase pattern shown in Figure 4.22 (a) and (b) exhibit clearly defined main lobe with  $E_\theta$  component showing some ripples in its pattern. Also, one notices the absence of near-in side lobes of the conical horn. At  $r= 2\lambda$ , the ratio of radial distance of measurement to diameter of radiating aperture,  $(r/D) = 0.781$ .

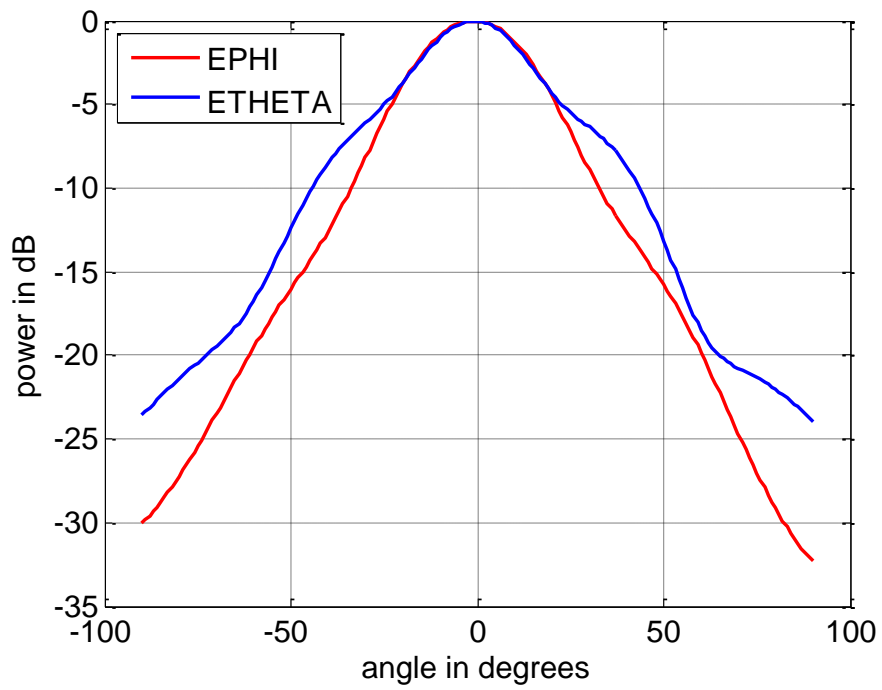


**Figure 4. 22(a): Near Field Radiation pattern of Conical Horn at  $r= 2 \lambda$  (6.4cm)**

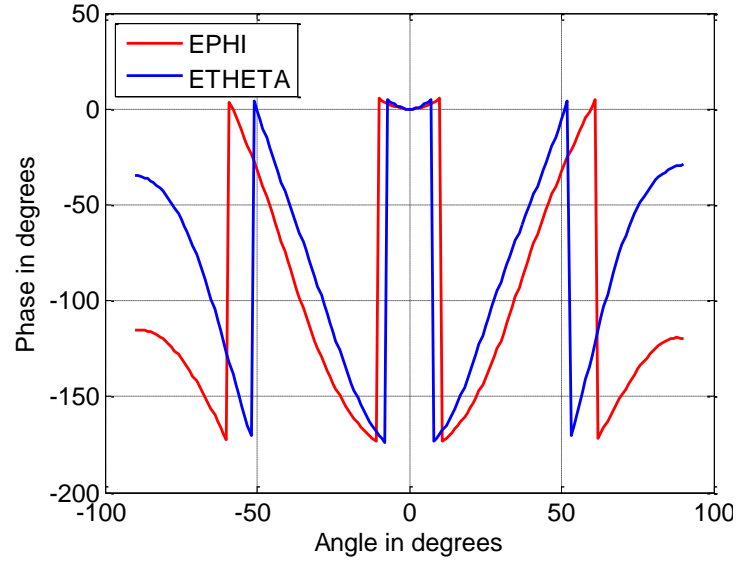
At a radial distance of  $r= 3\lambda$ , both the components of the radiation and Phase pattern exhibit smooth profiles of the main lobe and also the ripples in the  $E_\theta$  component vanish (Figure 4.23). However, the feature of absence of near side lobes continues.



**Figure 4.22(b): Near Field Radiation pattern of Conical Horn at  $r = 2\lambda$  (6.4cm)**

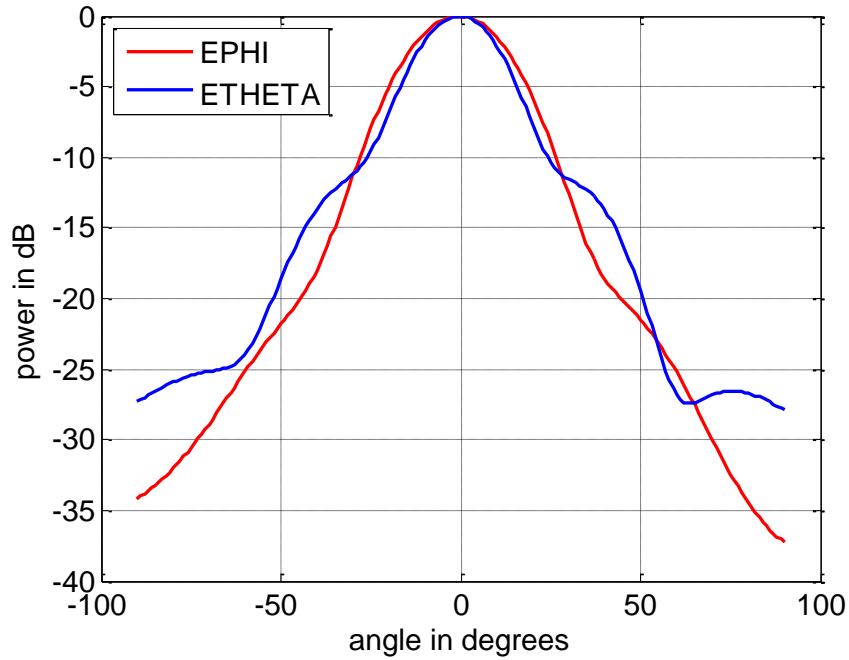


**Figure 4. 23 (a): Near Field Radiation pattern of Conical Horn at a distance  $r = 3\lambda$  (9.6cm)**

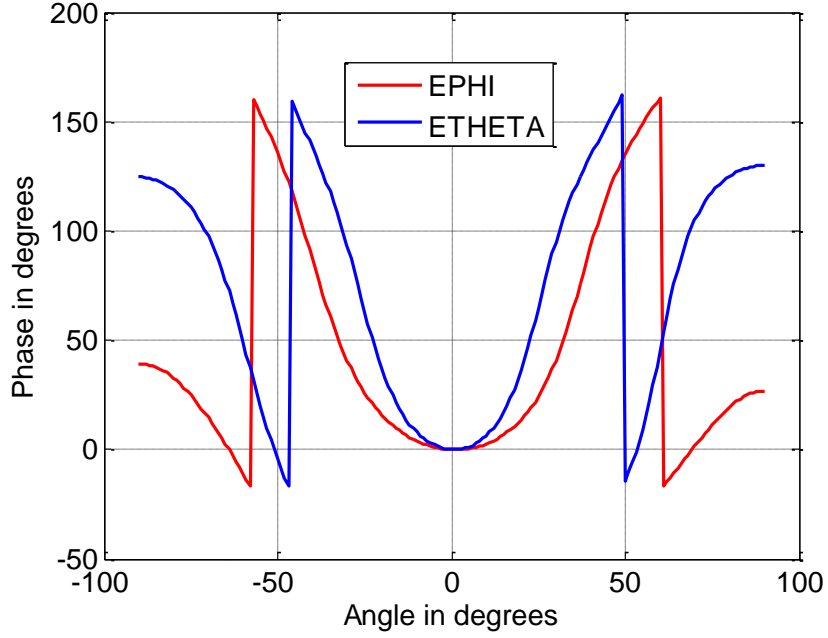


**Figure 4. 23(b): Near Field Phase Pattern of Conical Horn at a distance  $r= 3 \lambda$  (9.6cm)**

At a distance  $r= 10\lambda$ , the radiation and Phase patterns of conical horn (Figure 4.24) show further improvement in the drooping (tapering) nature in the  $E_\theta$  component.



**Figure 4. 24(a): Radiation Pattern of Conical Horn at  $r= 10 \lambda$  (32cm)**



**Figure 4. 24(b): Radiation Pattern of Conical Horn at  $r= 10 \lambda$  (32cm)**

For a conical horn with a radius of aperture of 4.1 cm operating at 9.375 GHz, the radial distance of measurement of  $r= 10 \lambda$  still corresponds to near field distance of observation. Additional results to validate the generalised approach for computation of near field radiation pattern of an antenna proposed in this chapter are presented in Appendix- 2 of this thesis.

#### 4.4 Conclusions

This section summarizes the conclusions that can be derived out of the analysis and simulation results presented in this chapter.

A generalized procedure in the form of an analytical formulation for the determination of radiation pattern of an antenna at any arbitrary distance which covers the near field as well as far field is presented in this chapter. With the prior knowledge of either the current or field distribution on the radiating aperture, the proposed near field analysis is generic and can be applied for wide variety of antenna elements. The underlying principle of the generalized procedure tantamount to considering the radiating aperture as an array of point electric and magnetic dipoles. The radiation pattern of the antenna at any arbitrary point of observation (valid for both near field as well as far field) is obtained by the vector summation of the fields radiated by the array of both electric and magnetic dipoles located on the aperture of the antenna.



The significance of the proposed analysis lies in the derivation of explicit expressions for the co-polar and cross polar components of the radiation pattern of both electric and magnetic dipoles. In addition, in the analysis both the Cartesian as well as spherical polar components of the radiation patterns are emphasized. The spherical polar representation is of direct relevance to conventional antenna engineering analysis of individual radiators and beam forming analysis. The Cartesian representation of the proposed near field analysis is tailor made for initial computations in TWI which is the topic of this thesis.

Keeping in view circular cylindrical waveguide and conical horn as radiating elements for the near field beamforming analysis proposed in this thesis, this chapter has established as well as substantiated the generic and versatile features of proposed novel approach for the determination of near field radiation pattern of these antennas.

To take advantage of the available results through the well-established analytical formulations which are valid exclusively for the far field radiation patterns of antennas, initial simulations of the proposed near field analysis have been carried out with radial distance of observation satisfying the criterion of far field. The simulation results of the proposed near field analysis with the radial distance of observation of  $1000 \lambda$  show excellent correlation with the results derived through analytical formulation of [Balanis C.A., 2005] which is exclusively valid only for the far field.

After substantiating the validity of the proposed analysis for the special case of far field, numerous simulations have been performed to study and analyze the radiation patterns of circular waveguide and conical horn at radial distances of observation lying very close to the radiating aperture. At a distance of  $0.2 \lambda$  from the aperture, the radiation patterns of circular waveguide are vastly/drastically different from the corresponding conventional far field patterns. The broadside radiating feature of the circular waveguide is also absent. As is expected, with the gradual increase in the radial distance of observation, one notices the increasing trend in the radiation patterns of circular waveguides to broadly conform to the profile of conventional far field patterns.

The radiation patterns nearly resemble the corresponding conventional far field patterns at  $r=0.75\lambda$  for circular waveguide and corresponds to  $(r/D) = 0.571$ . For a conical horn with a radius of 4.1 cm, the radiation patterns at  $r=2\lambda$  show defined main lobe and  $r=2\lambda$  is equivalent of  $(r/D)=0.781$ .

The depicted normalized phase patterns of both the circular waveguide and conical horn follow the changes in the profile of the corresponding amplitude patterns. The successful formulation and validation of the approach for the determination of near field radiation pattern of an antenna presented in this chapter is an important step to progress to the next significant analytical formulation involving novel near field beamforming technique to be presented in the next chapter.

## Chapter 5: A Novel Approach For Near Field Beamforming

### 5.1 Introduction

The aim of the thesis is to develop an analytical formulation for the analysis of near field beamforming based TWI. The previous chapter 4 discussed a new analytical formulation to compute both near-field and far-field radiation patterns at equal ease. This chapter presents a novel approach to carry out near-field beamforming using the formulation in Chapter 4 as its foundation. This chapter discusses the mathematical formulation involved in carrying out both the near-field and far-field beamforming

Beamforming has been in use for many years in fields of communication, surveillance, radio and acoustic radars. In beamforming, both amplitude and phase shift (weights) at each element in the antenna array control the directionality of the transmitted or received beam without physical motion of the antenna array. In vast majority of research on array beamforming, the observation point is assumed to be in the far-field of the array implying that the radiation pattern of the beamformer will be considered at a distance of at least  $R = 2D^2/\lambda$  from the array, where R is the distance from the array; D is largest dimension of the array; and  $\lambda$  is operating wavelength. When the observation point is located at a far field distance, the resulting incident wave-front on the test antenna or aperture is planar. The planarity of the incident wave-front on the test antenna simplifies the analyses of antenna as well as beamforming. In many practical situations such as TWI, the observation point can be well within the far-field distance of the array. In such a scenario the far-field assumption in beamforming analysis is not only inappropriate but also inaccurate leading to either the degradation or the distortion of the radiation performance of the beamformer.

The reported research on near field beamforming appears to be rather limited in open literature. Probably, this is in tune with the continued emphasis in Antenna Engineering on the far-field characterization of the antenna radiating elements and arrays. Near-field compensation (Khalil F., 1994) is one of the common methods to achieve near-field beamforming in which a delay correction is used on each antenna array element (sensor) to account for the near-field wave-fronts, which tend to be spherical. Near-field compensation is a first order correction over a limited range of angles. Curvature of the spherical wave-front (because of the near-field) is approximated by a quadratic surface over the array aperture and it ignores the variation of magnitude with distance and angle. It is preferred only for beamforming closer to broad side angle. Another method to

achieve near-field beamforming reported in literature is the near-field/far-field reciprocity (Kennedy R.A. et. al, 1999; Kennedy R.A. et. al, 1998). Near-field/far-field reciprocity described in (Kennedy R.A. et. al, 1999, Kennedy R.A. et. al, 1998) depends on far-field techniques to arrive at near-field problem formulation. The radial reciprocity described in (Kennedy R.A. et. al, 1999) utilizes near-field radiation pattern specification and maps it to an equivalent far-field pattern specification. This method requires 3D or volumetric measurements of near-field pattern of the array at a desired near-field distance. Spherical near-field to far-field transformation is required in this analysis. Then the weights are computed for far-field beamforming and the computed weights are proved to satisfy the near-field specification also.

In this chapter, a technique to achieve near-field/far-field beamforming is proposed which circumvents the earlier stated requirement of 3D near-field radiation pattern measurement of the beamforming array for the computation of weights for beam steering. Unlike in [2], in this chapter the weights for steering of the beam are computed directly for the specified beam pointing angles and near-field distance. This does not require the 3D radiation pattern of the beamforming array. It requires only the radiation pattern of the array in a plane which corresponds to the beam pointing angle  $\varphi_o$ . The arrived formulations for the array factor  $A(\theta, \varphi)$  and beam steering phase factor  $P(\theta_o, \varphi_o)$  essential for beamforming and beam steering are uniformly valid for both near field and far field beamforming scenarios. The developed near field beamforming technique is valid for both linear and planar array antenna configurations. The proposed near-field beamforming analysis requires the determination of near-field radiation patterns of the antenna elements.

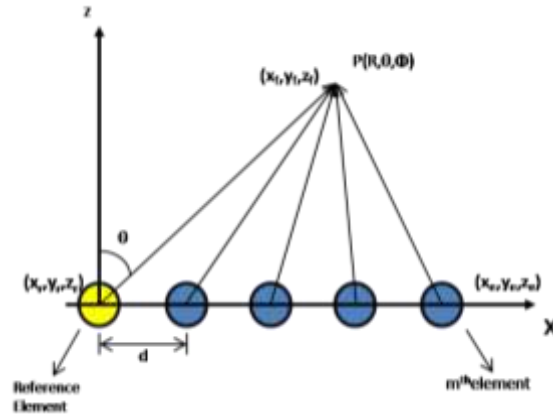
## 5.2 Near Field and Far Field Beamforming

Far-field beamforming methods are well established and one of them is explained clearly in Section 2.4.1. This section provides a novel method of achieving both near-field and far-field digital beamforming. The significant contrast between the far field and near field beamforming can be summarized as follows:

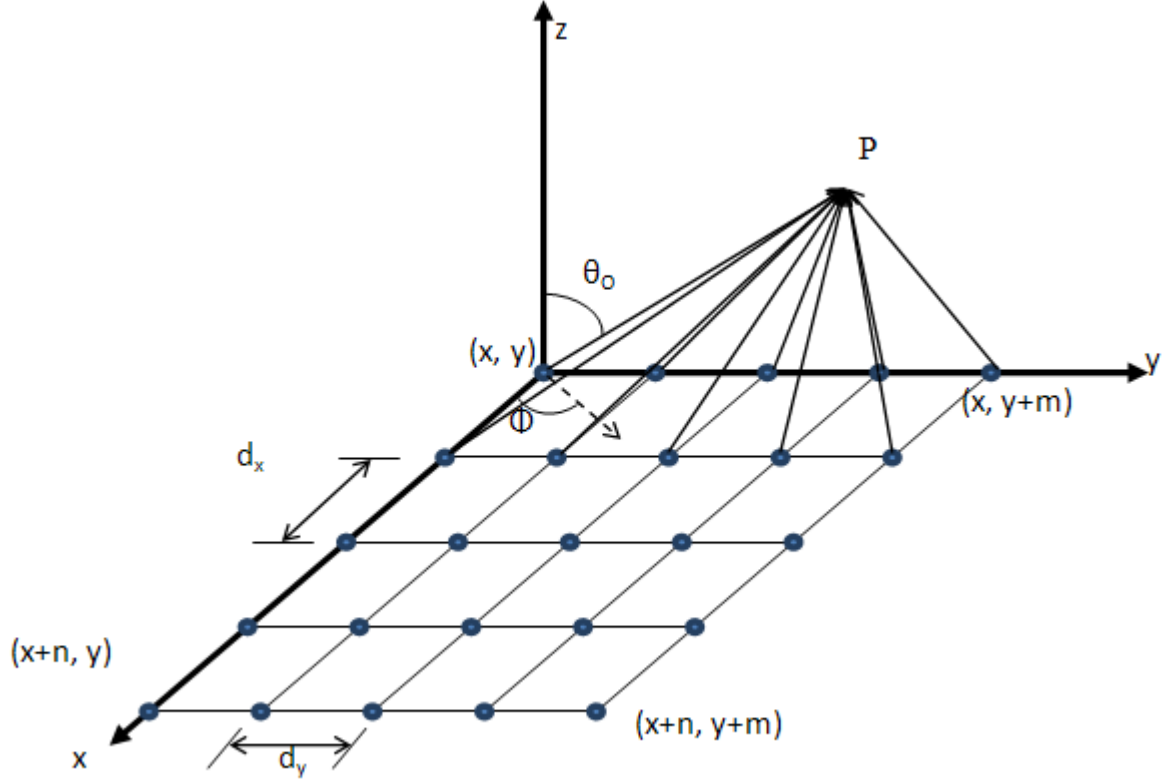
- In near-field beamforming, the rays incident on or radiated from all the elements of the array cannot be assumed to be parallel.

- Unlike in far-field beamforming, the elemental radiation patterns cannot be the same for a given observation point  $P(R, \theta, \varphi)$  since the distances between the array elements and the specified observation point are not equal.
- As a consequence, the spherical polar angles  $\theta$  and  $\varphi$  subtended by various antenna elements at a given observation point P will be different for each elements of the array. Therefore, the elemental radiation pattern of the individual array elements at P cannot be assumed to be the same
- Unlike in far field beamforming scenario, the elemental radiation patterns cannot be factored out of the summation operation in the beamforming analysis.

The novelty of the approach proposed in this chapter and adapted for near-field beamforming is based on the theme that an antenna beamforming analysis developed for near-field technique should be valid for far-field also without loss of generality. A schematic representation of near-field beamforming for linear array is shown in Figure 5.1. A corresponding representation of near field beamformer with a planar array is shown in Figure 5.2.



**Figure 5. 1: Near Field Beamforming Linear Array**



**Figure 5. 2: Near Field Beamforming Planar Array**

Let  $(x_f, y_f, z_f)$  denote the Cartesian coordinates of an observation point P:

$$x_f = R_{NF} \cdot \sin \theta \cdot \cos \varphi \quad \dots(5.1)$$

$$y_f = R_{NF} \cdot \sin \theta \cdot \sin \varphi \quad \dots(5.2)$$

$$z_f = R_{NF} \cdot \cos \theta \quad \dots(5.3)$$

$R_{NF}, \theta$  and  $\varphi$  are the corresponding spherical coordinates of the observation point.  $R_{NF}$  is the distance between the reference element and the observation point  $(x_f, y_f, z_f)$ . Let  $\theta_0$  and  $\varphi_0$  be the intended angular coordinates for beam steering. The resulting Cartesian coordinates of the observation point for the beam steering will then be  $P(x_{fo}, y_{fo}, z_{fo})$ .

where,

$$x_{fo} = R_{NF} \cdot \sin \theta_o \cdot \cos \varphi_o \quad \dots(5.4)$$

$$y_{fo} = R_{NF} \cdot \sin \theta_o \cdot \sin \varphi_o \quad \dots(5.5)$$

$$z_{fo} = R_{NF} \cdot \cos \theta_o \quad \dots(5.6)$$

$\theta_o$  and  $\varphi_o$  are the beam steering angles and  $(R_{NF}, \theta_o, \varphi_o)$  are the corresponding spherical coordinates of the observation point. The array factor  $A_{(q,p)}^{NF}(\theta, \varphi)$  for the near-field beamforming array can be written as

$$A_{(q,p)}^{NF}(\theta, \varphi) = e^{-jk(R_{pq} - R_{11})} \quad \dots(5.7)$$

$$p = 1, 2, 3, \dots, n \quad ; \quad q = 1, 2, 3, \dots, m$$

Where,

$n$  is the number of elements along x-axis of the array

$m$  is the number of elements along y-axis of the array

$R_{pq}$  is the distance between the  $(p,q)^{th}$  element of the array and the observation point

$$P(x_f, y_f, z_f)$$

$R_{11}$  is the distance between the reference element ( $p = 1, q = 1$ ) and the observation point

$$P(x_f, y_f, z_f)$$

$$R_{pq} = \sqrt{(x_f - x_{rp})^2 + (y_f - y_{rq})^2 + (z_f - z_{pq})^2} \quad \dots(5.8)$$

$$R_{11} = \sqrt{(x_f - x_{r1})^2 + (y_f - y_{r1})^2 + (z_f - z_{r1})^2} \quad \dots(5.9)$$

$$x_{rp} = x_1 + (p-1)dx \quad \dots(5.10)$$

$$y_{rq} = y_1 + (q-1)dy \quad \dots(5.11)$$

$$z_{pq} = 0 \quad \dots(5.12)$$

In Figure 5.2, the array is assumed to be in XY plane (  $Z = 0$  plane). Similar to the array factor, the near-field beam steering phase has also been derived and generalized from the existing formulation of far-field beamforming scenario.

The near-field beam steering phase factor is denoted by  $P_{(q,p)}^{NF}(\theta_0, \varphi_0)$ . The near-field beam steering phase factor for the placement of beam at a distance " $R_{NF}$ " from the reference element of the array at an angle  $(\theta_0, \varphi_0)$  measured with respect to the reference element is given by

$$P_{(q,p)}^{NF}(\theta_o, \varphi_o) = e^{+jk(R_{pq}^{BS} - R_{11}^{BS})} \quad \dots(5.13)$$

$$R_{pq}^{BS} = \sqrt{(x_{fo} - x_p)^2 + (y_{fo} - y_q)^2 + (z_{fo} - z_{pq})^2} \quad \dots(5.14)$$

$$R_{11}^{BS} = \sqrt{(x_{fo} - x_1)^2 + (y_{fo} - y_1)^2 + (z_{fo} - z_{11})^2} \quad \dots(5.15)$$

Where  $x_p = x_{rp}$  and  $y_p = y_{rp}$

The expressions for the radiation patterns of near-field beam forming array are given by

$$E_{\theta}^{NF}(R_{NF}, \theta, \varphi, \theta_o, \varphi_o) = \sum_{p=1}^m \sum_{q=1}^n E_{\theta}^{ENF}(R_{pq}, \theta_{pq}, \varphi_{pq}) \cdot A_{(q,p)}^{NF}(\theta_{pq}, \varphi_{pq}) \cdot P_{(q,p)}^{NF}(\theta_o, \varphi_o) \quad \dots(5.16)$$

$$E_{\varphi}^{NF}(R_{NF}, \theta, \varphi, \theta_o, \varphi_o) = \sum_{p=1}^m \sum_{q=1}^n E_{\varphi}^{ENF}(R_{pq}, \theta_{pq}, \varphi_{pq}) \cdot A_{(q,p)}^{NF}(\theta_{pq}, \varphi_{pq}) \cdot P_{(q,p)}^{NF}(\theta_o, \varphi_o) \quad \dots(5.17)$$

Where

$$\theta_{pq} = \cos^{-1} \left( \frac{z_f - z_{11}}{R_{pq}} \right) \quad \dots(5.18)$$

$$\varphi_{pq} = \tan^{-1} \left( \frac{y_f - y_q}{x_f - x_p} \right) \quad \dots(5.19)$$

$E_{\theta}^{ENF}(R_{pq}, \theta_{pq}, \varphi_{pq})$  and  $E_{\varphi}^{ENF}(R_{pq}, \theta_{pq}, \varphi_{pq})$  are the  $\theta$  and  $\varphi$  components of the  $(p,q)^{th}$  element of the array and can be determined using the equations (4.56) and (4.57) of chapter 4 of this thesis.



Specifically when  $\varphi_0 = 0^\circ$ , the resulting radiation pattern corresponds to azimuthal component ( $E_\varphi$ );  $\varphi_0 = 90^\circ$ , the resulting radiation pattern corresponds to elevation component ( $E_\theta$ )

### 5.3 Simulation Results of Near Field and Far Field Beamforming

The concept and mathematical modeling involved in far-field and near-field beamforming are explained in the previous section. With circular waveguide chosen as the desired radiating element, this section presents the beamforming results obtained from simulations carried out for both far-field and near-field using Equations 5.1 - 5.19.

#### 5.3.1 Near Field Beamforming with Linear and Planar Arrays:

Simulation studies have been performed to validate the proposed approach for near field beamforming technique. As was stated earlier while deriving the expressions for array factor and beam steering phase factor required for the realization of near-field beamforming, the derived expressions hold good even for far-field beam steering scenario if  $R_{NF}$  is allowed to approach the conventional far-field distance criterion ( $2D^2/\lambda$ ) or greater.

The total aperture size ( $D_a$ ) of a given array is

$$D_a = N \times D + (N-1) \times dl;$$

where N is the number of elements

D is the diameter of the aperture of antenna element

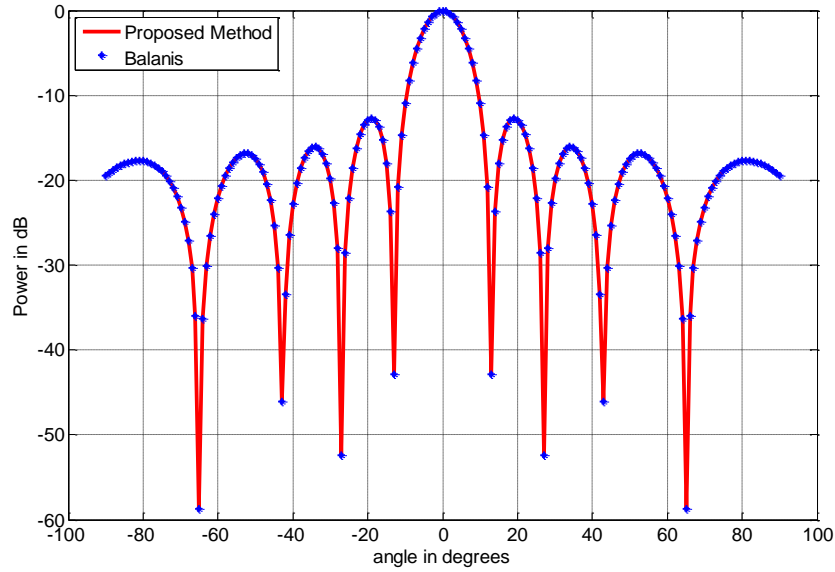
dl is the spacing between the adjacent edges of successive antenna elements

The inter element spacing of the array is  $ds = D + dl$ .

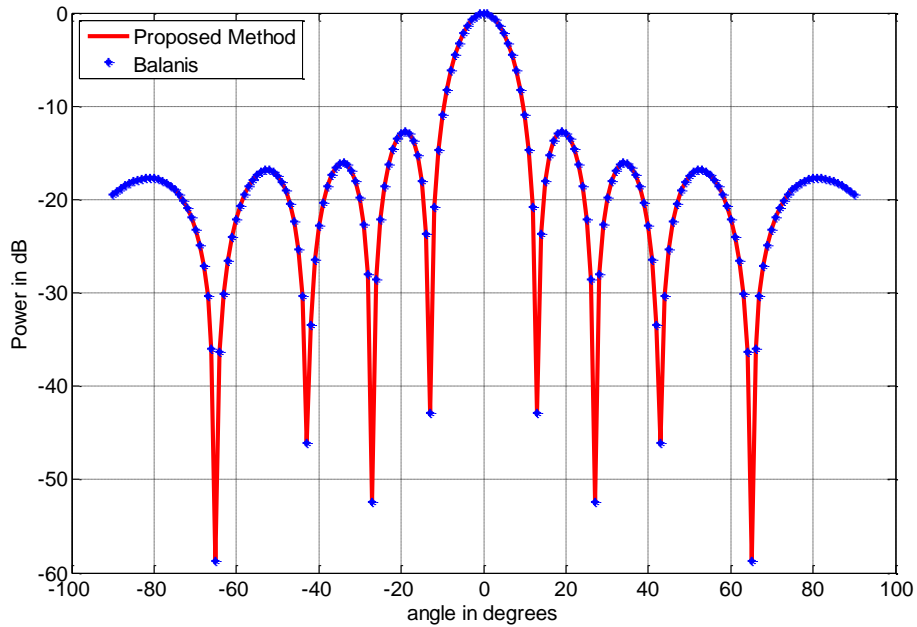
For the simulation, dominant  $TE_{11}$  mode X- band circular cylindrical waveguide operating at 9.375 GHz ( $\lambda = 3.2$  cm) is chosen as the array element. The diameter of the circular waveguide is 2.1 cm. The spacing between the adjacent edges of successive antenna elements 'dl' is chosen as  $\lambda/4$ .

To validate the proposed analysis of near-field beamforming, equations (5.16) and (5.17) have been invoked to compute the radiation patterns of the beamforming array. For the validation studies, 5 element linear array and 5x5 planar array have been considered. The simulation studies carried out using the near-field beamforming technique with  $R_{NF} = 1000\lambda$  (implying that the

observation or field point is at a distance far exceeding the conventional far distance criterion) have yielded the identical results with that derived through the formulation exclusively for the far-field beamforming scenario dealt earlier in chapter 3 as well as in (Balanis C.A., 2005). In Figure 5.3, the results of the simulation with beamforming (5x1) linear array for ( $\varphi_0 = 0^0, \theta_0=0^0$ ) are depicted. The corresponding results pertaining to (5x5) planar array are shown in Figure 5.4.

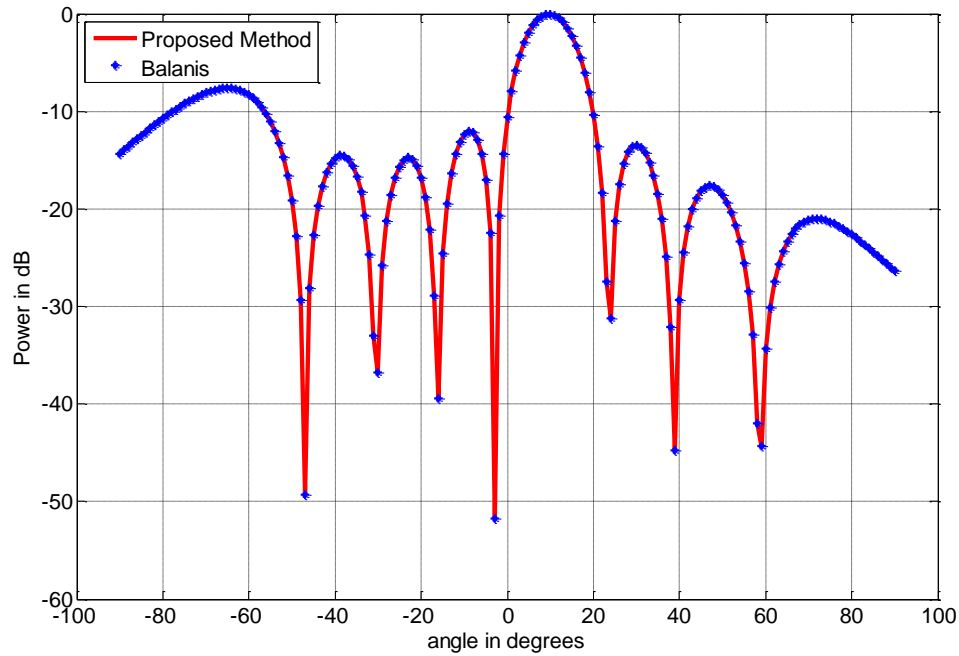


**Figure 5. 3: Far Field Beamforming at ( $\varphi_0 = 0^0, \theta_0=0^0$ ) with (5x1) Linear Array**

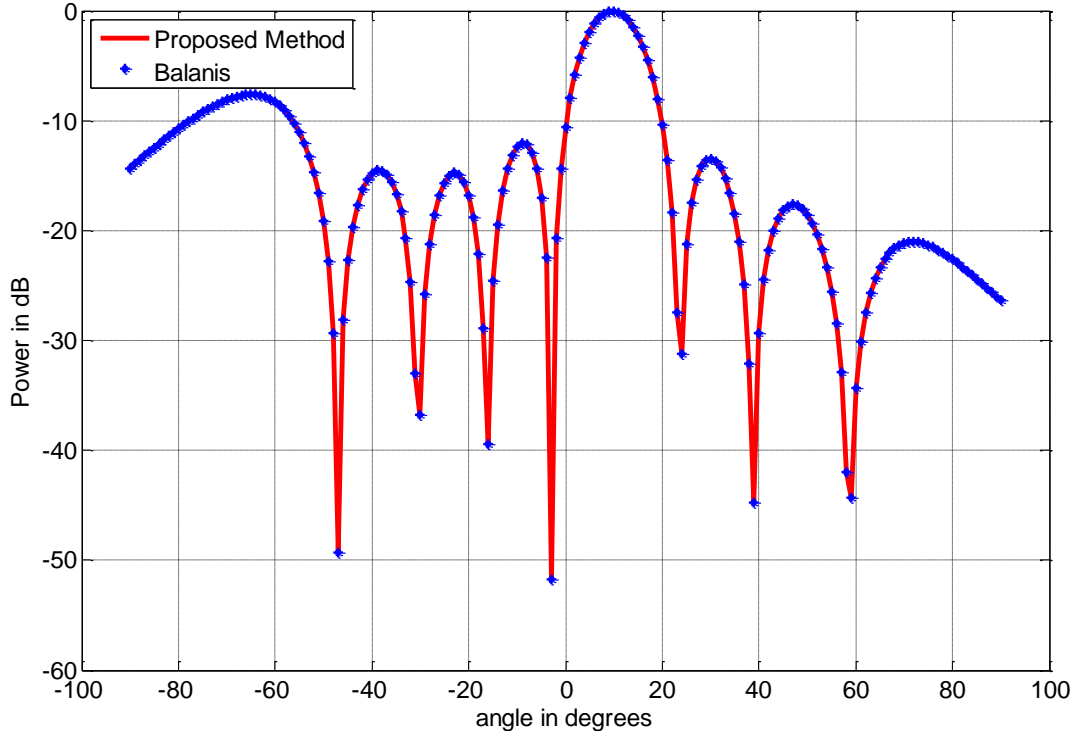


**Figure 5. 4: Far Field Beamforming at ( $\varphi_0 = 0^0, \theta_0=0^0$ ) with (5x5) Planar Array**

The radiation patterns of the beamforming linear and planar arrays for  $(\varphi_0 = 0^\circ, \theta_0 = 10^\circ)$  are shown in Figures 5.5 and 5.6 respectively. The analytical formulations presented in Chapter 4 have been invoked to compute the elemental radiation pattern required for the near field beamforming array. Such a validation study is required and has been emphasized to prove that near-field beamforming technique of this thesis tantamount to modifying the expressions of conventional beam forming to overcome the assumption of planarity of wave-front of electromagnetic rays impinging on the array elements.



**Figure 5. 5: Far Field Beamforming at  $(\varphi_0 = 0^\circ, \theta_0 = 10^\circ)$  with (5x1) Linear Array**

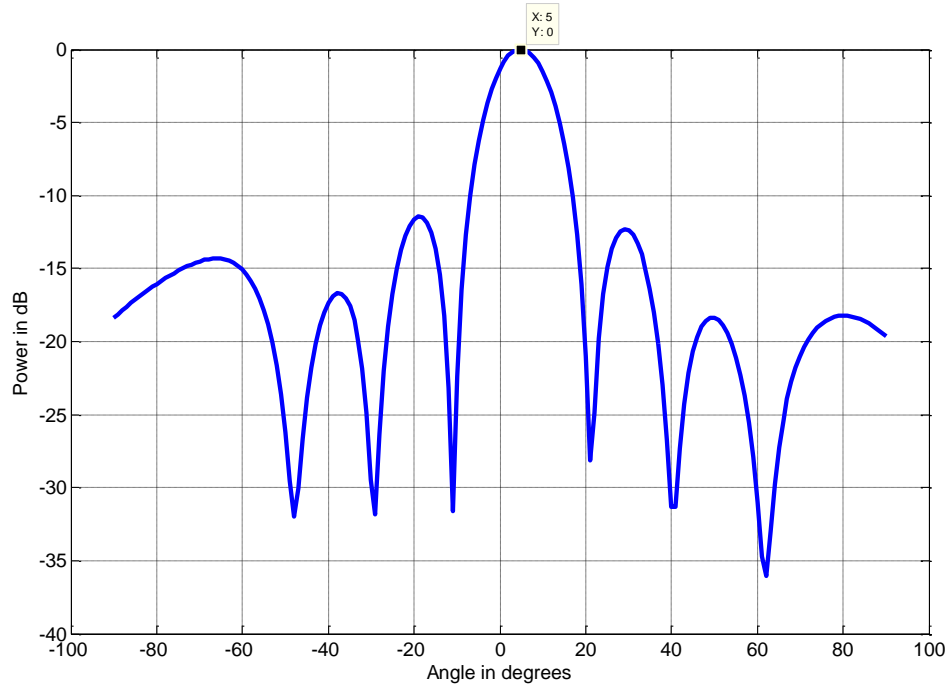


**Figure 5. 6: Far Field Beamforming at ( $\phi_0 = 0^\circ, \theta_0 = 10^\circ$ ) with (5x5) Planar Array**

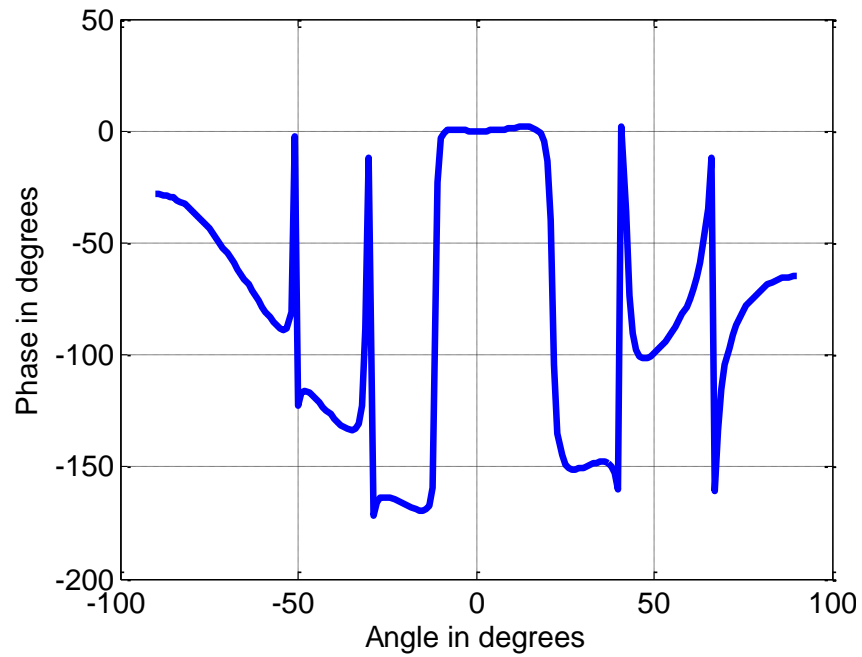
After having established the validation of the proposed near field beamforming technique through an indirect approach by considering the far field scenario as a limiting case of the proposed near field approach, numerous simulation studies have been performed through varying;

- Near field distances
- Range of beam pointing angles
- Configurations of array elements

For a 5-element linear array of circular waveguide, the overall aperture dimension  $D_a = 13.7$  cm. The far-field distance criterion of  $(2D_a^2/\lambda)$  for this configuration is 117.31 cm for  $\lambda = 3.2$ . For  $R_{NF} < 117.51$  cm, the 5 - element linear array of circular waveguide elements will be considered to form or steer the beam in the near field range. The beam steering features of 5 element linear array of circular waveguide was simulated at  $R_{NF} = 3\lambda$  and the results are shown in Figure 5.7.



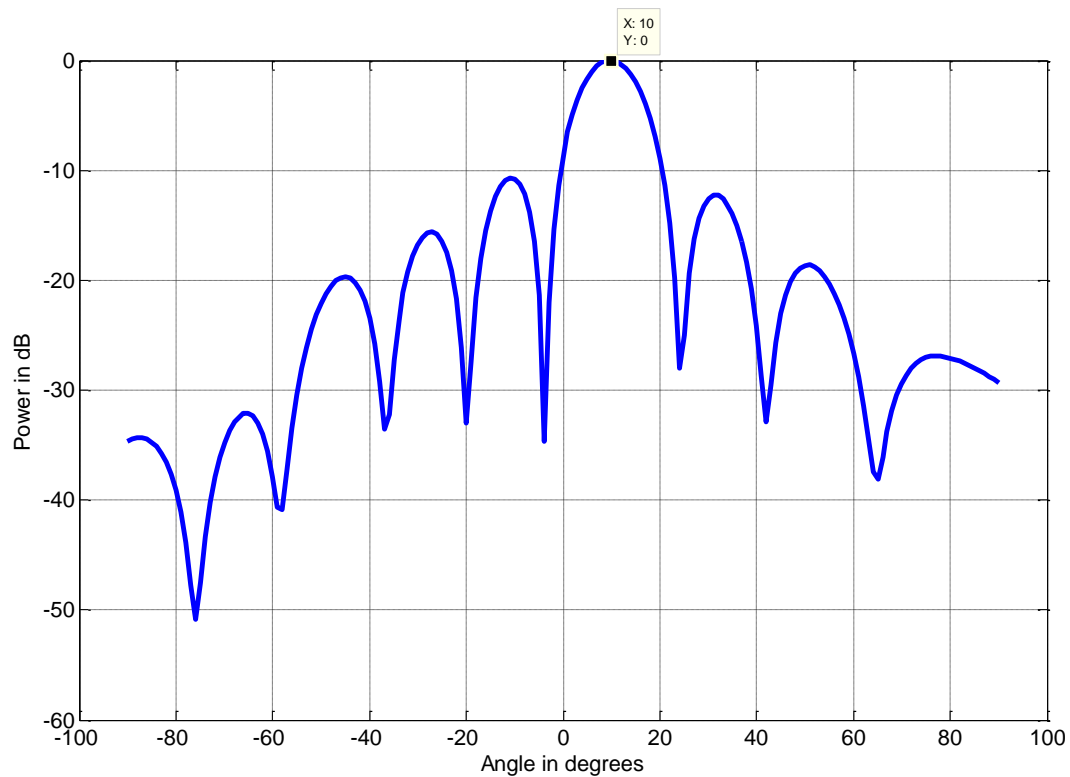
**Figure 5. 7(a): Amplitude Pattern of Near-Field Beamforming with Linear Array of 5 Elements;  $R_{NF} = 3\lambda$  ;  $(\varphi_0=0^\circ, \theta_0=5^\circ)$**



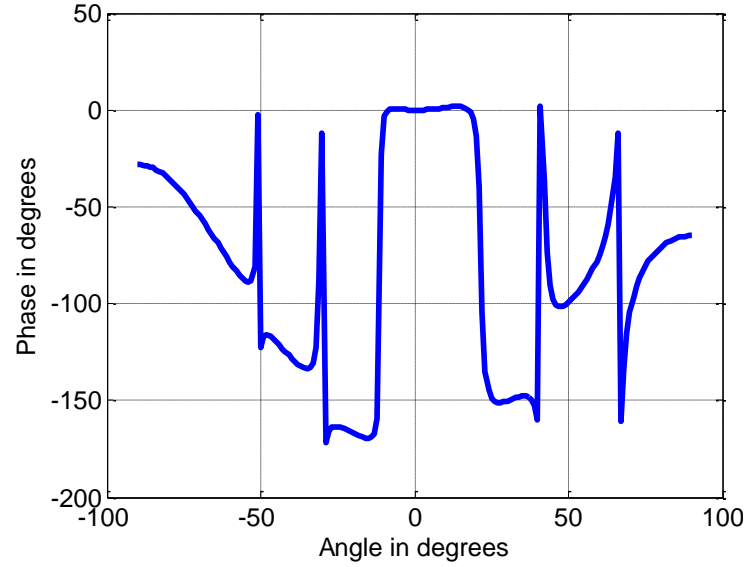
**Figure 5. 7 (b): Phase Pattern of Near-Field Beamforming with Linear Array of 5 Elements;  $R_{NF} = 3\lambda$ ;  $(\varphi_0=0^\circ, \theta_0=5^\circ)$**

The results of Figure 5.7 correspond to the radiation pattern of a linear array evaluated at  $R_{NF} = 3\lambda$ . The amplitude radiation pattern of the 5 element linear array shows the beam steering at  $R_{NF} = 3\lambda$  with  $(\varphi_0=0^\circ, \theta_0=5^\circ)$ . The near field amplitude radiation pattern of the 5 element linear array at  $R_{NF} = 3\lambda$  is shown in Figure 5.7(a). The resulting phase radiation pattern of the 5 element linear array is shown in Figure 5.7(b).

The near field amplitude and phase radiation pattern of 7 element linear array for  $(\varphi_0=0^\circ, \theta_0=10^\circ)$  at  $R_{NF} = 3\lambda$  are shown in Figures 5.8(a) and (b). The results of Figure 5.8(a) clearly reveals the beam steering accomplished by the 7 element at  $\theta_0=10^\circ$ .

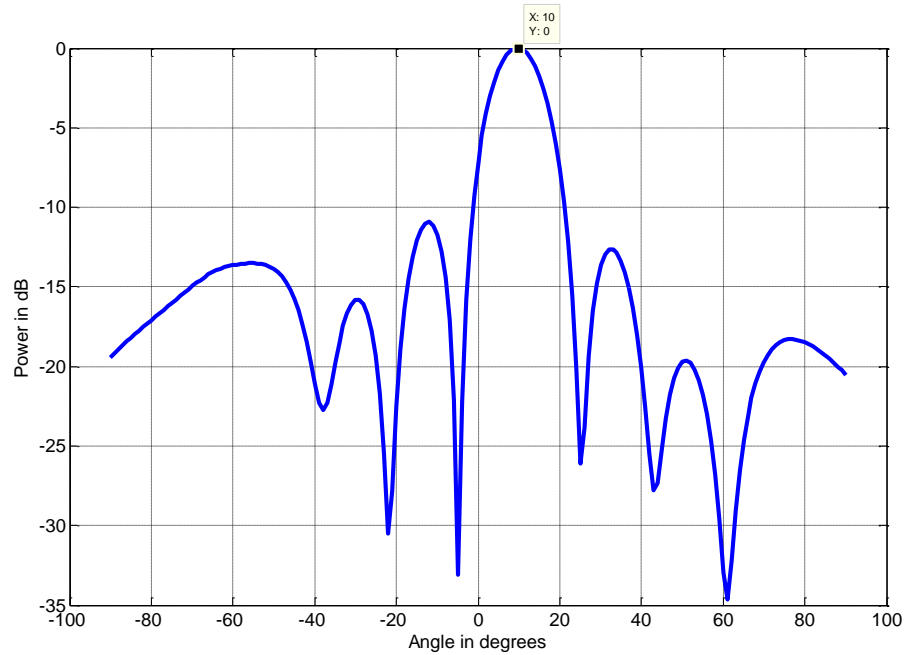


**Figure 5. 8(a): Amplitude Pattern of Near-Field Beamforming with Linear Array of 7 Elements;  $R_{NF} = 3\lambda$  ;  $(\varphi_0=0^\circ, \theta_0=10^\circ)$**

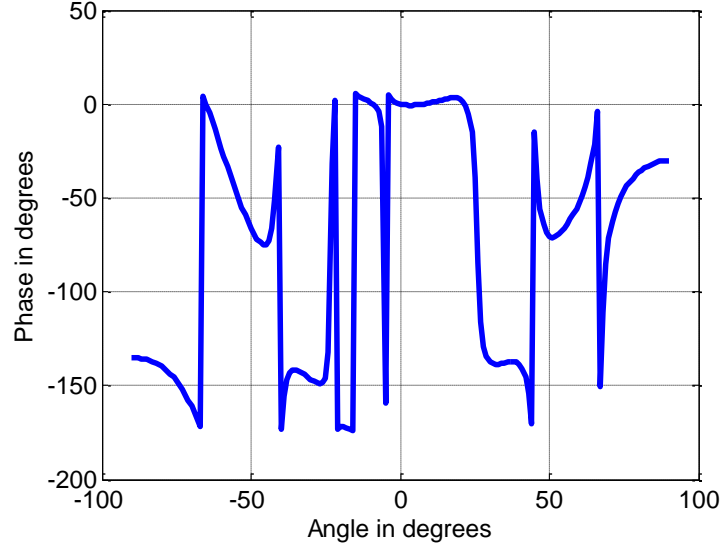


**Figure 5. 8 (b): Phase Pattern of Near-Field Beamforming with Linear Array of 7 Elements;  $R_{NF} = 3\lambda$ ; ( $\varphi_0=0^0, \theta_0=10^0$ )**

Simulation was performed for planar array with 5x5 elements to steer the beam at ( $\varphi_0=0^0, \theta_0=10^0$ );  $R_{NF} = 3\lambda$  and the results are shown in Figure 5.9.

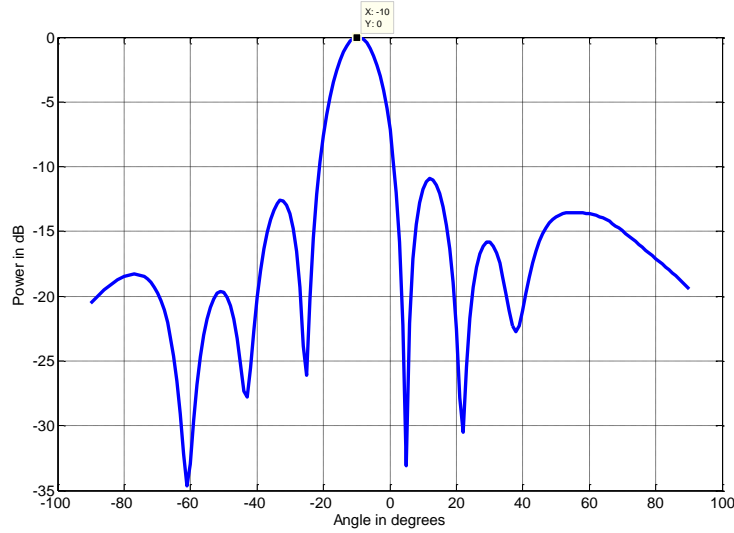


**Figure 5. 9(a): Amplitude Pattern of Near-Field Beamforming with Planar Array of 5x5 elements;  $R_{NF} = 3\lambda$  ; ( $\varphi_0=0^0, \theta_0=10^0$ )**



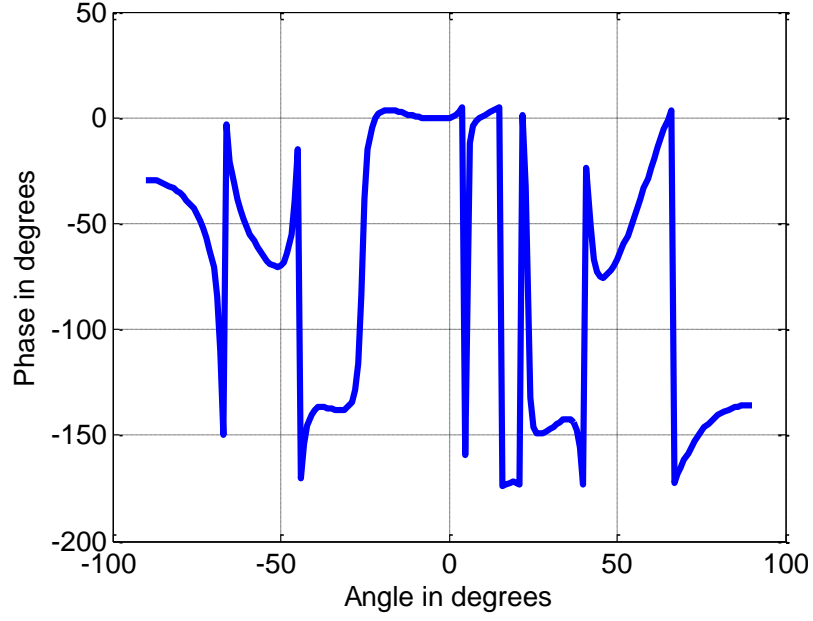
**Figure 5. 9(b): Phase Pattern of Near-Field Beamforming with Planar Array of 5x5 elements;  $R_{NF} = 3\lambda$  ;  $(\varphi_0=0^0, \theta_0=10^0)$**

The near field amplitude and phase radiation patterns depicted in Figures 5.9(a) and (b) clearly reveal the desired beam steering by the planar array thereby substantiating the proposed near field beamforming analysis.



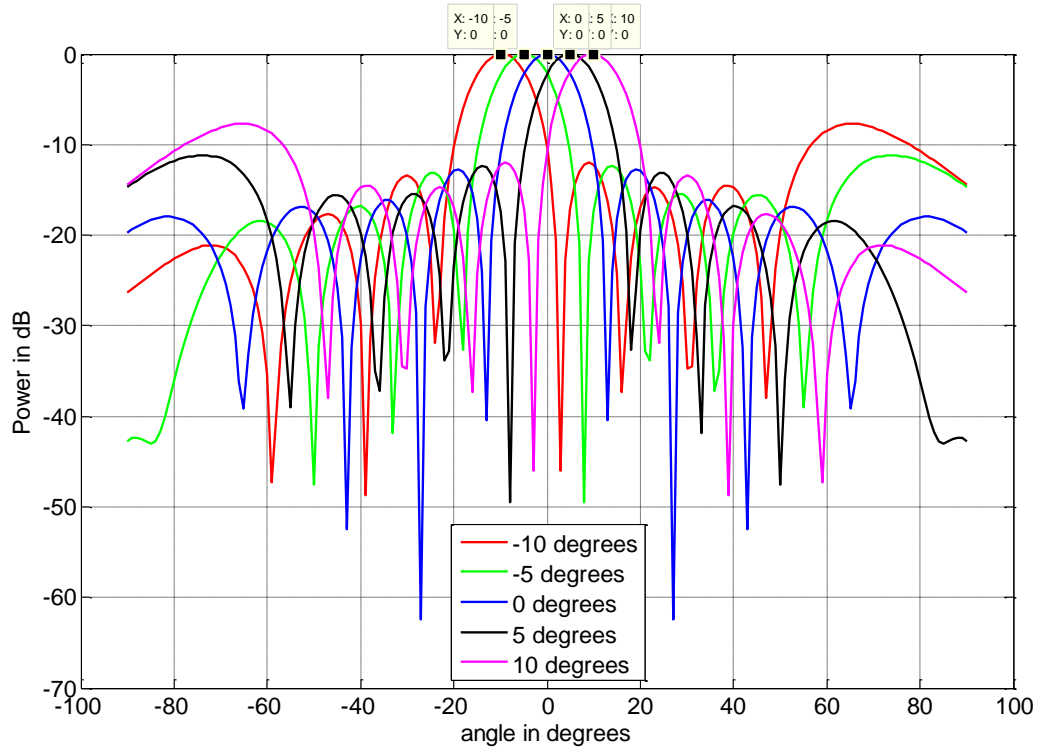
**Figure 5. 10(a): Amplitude Pattern of Near-Field Beamforming with Planar Array of 5x5 Elements;  $R_{NF} = 3\lambda$ ;  $(\varphi_0 = 0^0, \theta_0 = -10^0)$**





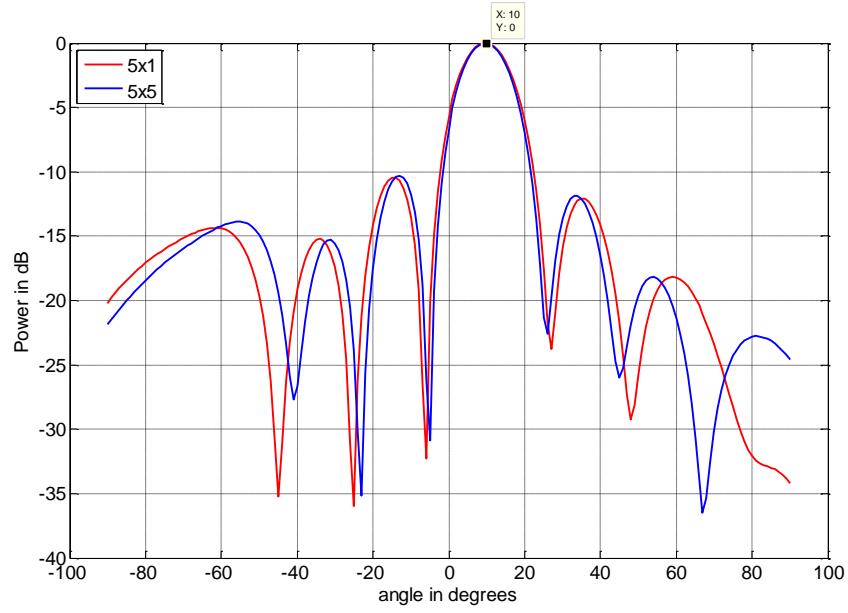
**Figure 5. 10(b): Phase Pattern of Near-Field Beamforming with Planar Array of 5x5 Elements;  $R_{NF} = 3\lambda$ ; ( $\varphi_0 = 0^\circ$ ,  $\theta_0 = -10^\circ$ )**

The results shown in Figure 5.10 correspond to the near field beam steering realized by a (5x5) planar array at  $R_{NF} = 3\lambda$ ; ( $\varphi_0 = 0^\circ$ ,  $\theta_0 = -10^\circ$ ). The results of beamforming by a (5x1) linear array at  $R_{NF} = 100\lambda$  for beamforming angles of  $\theta_0$  varying from  $10^\circ$  to  $-10^\circ$  in steps of  $5^\circ$  in  $\varphi_0 = 0^\circ$  are shown in Figure 5.11.

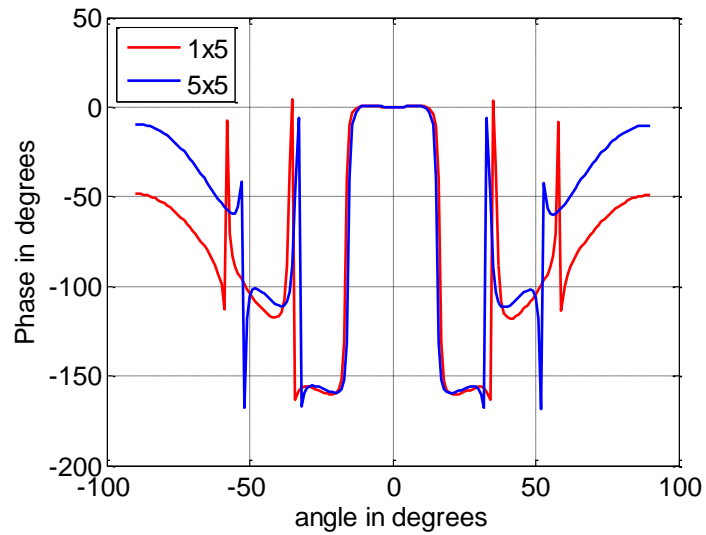


**Figure 5. 11: Far-Field Beamforming with Linear Array of 5 Elements at  $R_{NF} = 100 \lambda$ ;  
 $\theta_0 = -10$  to  $+10$  in steps of 5 degrees;  $\phi_0 = 0^\circ$ .**

Figure 5.12 provides the comparison of near field beamforming with linear array of 5 elements and planar array of 5 x 5 elements at  $R_{NF} = 3\lambda$  with  $\{\phi_0 = 0^\circ, \theta_0 = 10^\circ\}$ . The comparison of amplitude radiation pattern is shown in Figure 5.12 (a). Similarly Figure 5.12(b) depicts the relative comparison of phase radiation pattern between linear array (5x1) and planar array (5x5). The results of Figure 5.12 reveal that both the linear and planar arrays exhibit almost the identical main lobe characteristics and deviations are noticed in the location as well as in amplitude of side lobe levels.



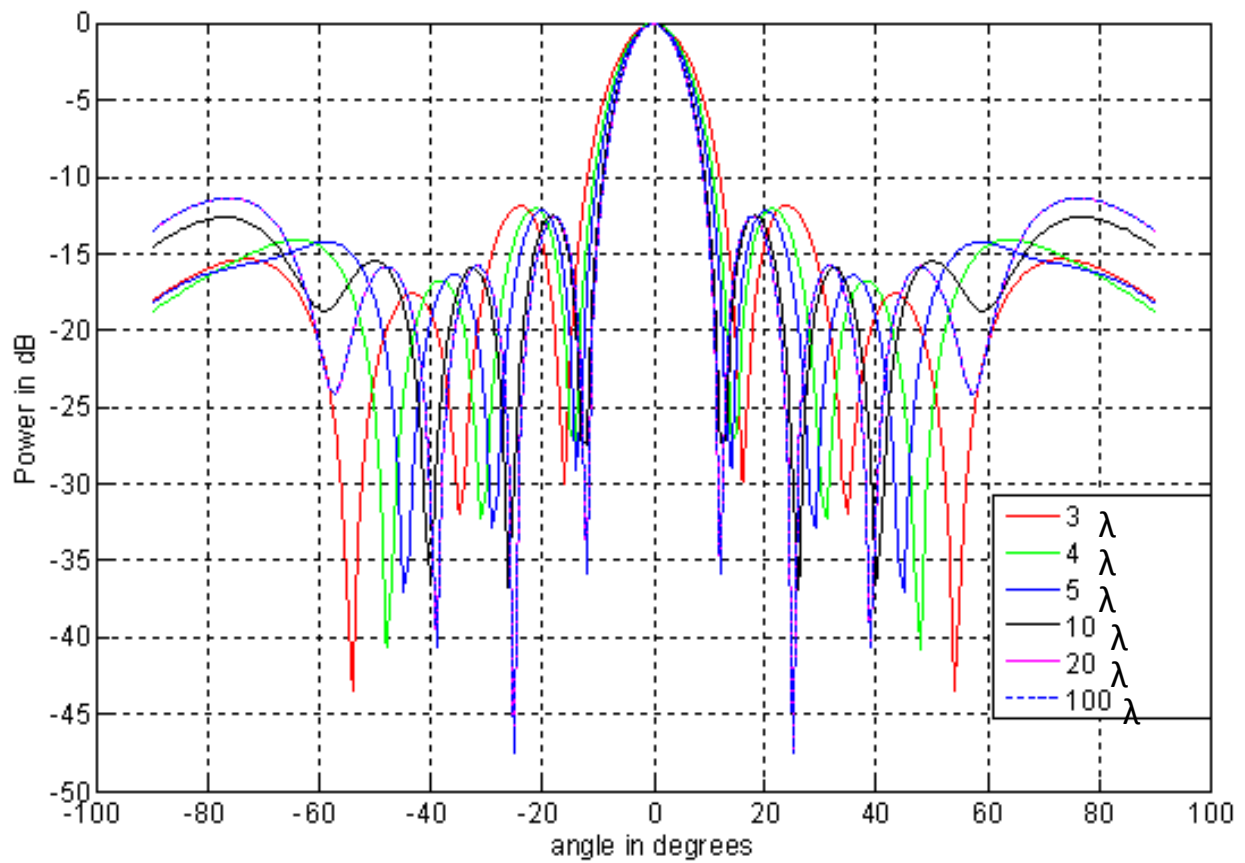
**Figure 5. 12(a): Comparison of Amplitude Pattern of Near-Field Beamformer with (5x1) Linear Array and Planar Array (5 x 5 elements) at  $R_{NF}=3 \lambda$ ; ( $\phi_0=0^\circ$ ,  $\theta_0=10^\circ$ )**



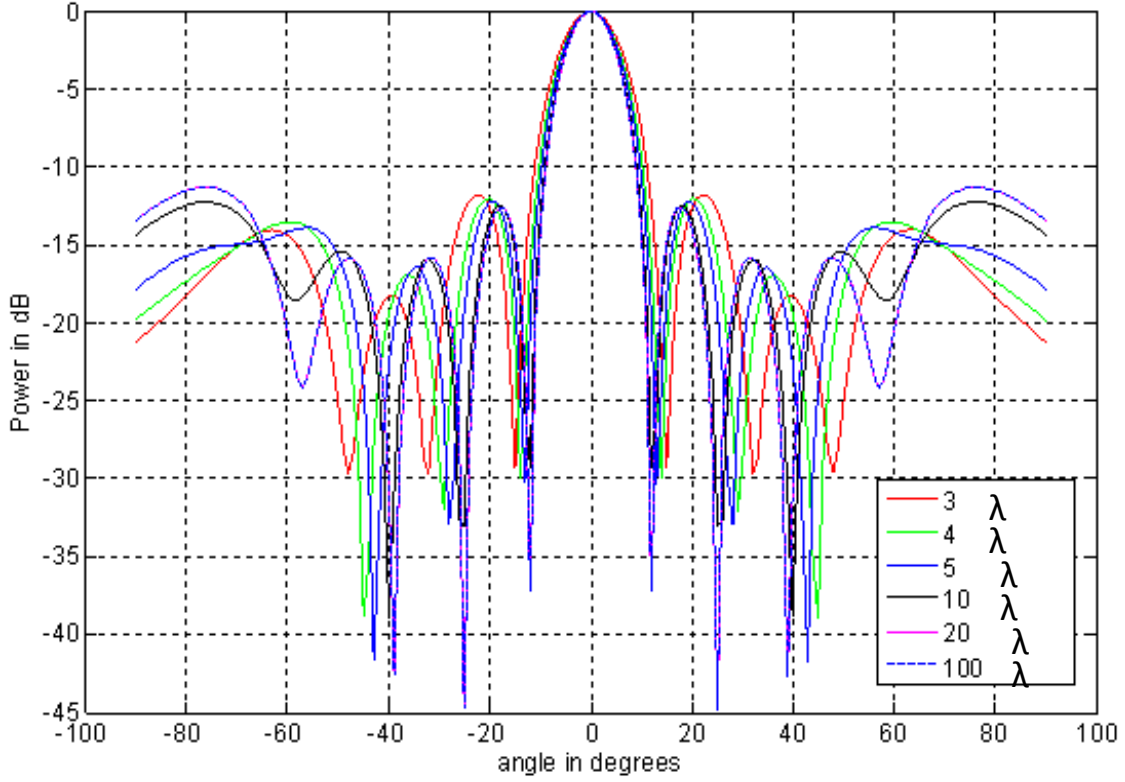
**Figure 5. 12(b): Comparison of Phase Pattern of Near-Field Beamformer with (5x1) Linear Array and Planar Array (5 x 5 elements) at  $R_{NF}=3 \lambda$ ; ( $\phi_0=0^\circ$ ,  $\theta_0=10^\circ$ )**

### 5.3.2 Influence of Near field Radial Distance of Observation on Beamwidth of Near field Beamformer

Simulation studies have been performed to analyze the effect of variation in near field distance of observation on the beamwidth of near field beamformer. While Figure 5.13 illustrates the simulation results on beamwidth pertaining to a near field beamformer with linear array of (5x1) elements for  $(\varphi_0=0^0, \theta_0=0^0)$ , the corresponding results of beamformer with planar array of (5x5) elements are shown in Figure 5.14.



**Figure 5. 13: Variation in Beamwidth of Near Field Beamformer (5x1 linear array) with Change in  $R_{NF}$ ;  $(\varphi_0=0^0, \theta_0=0^0)$**



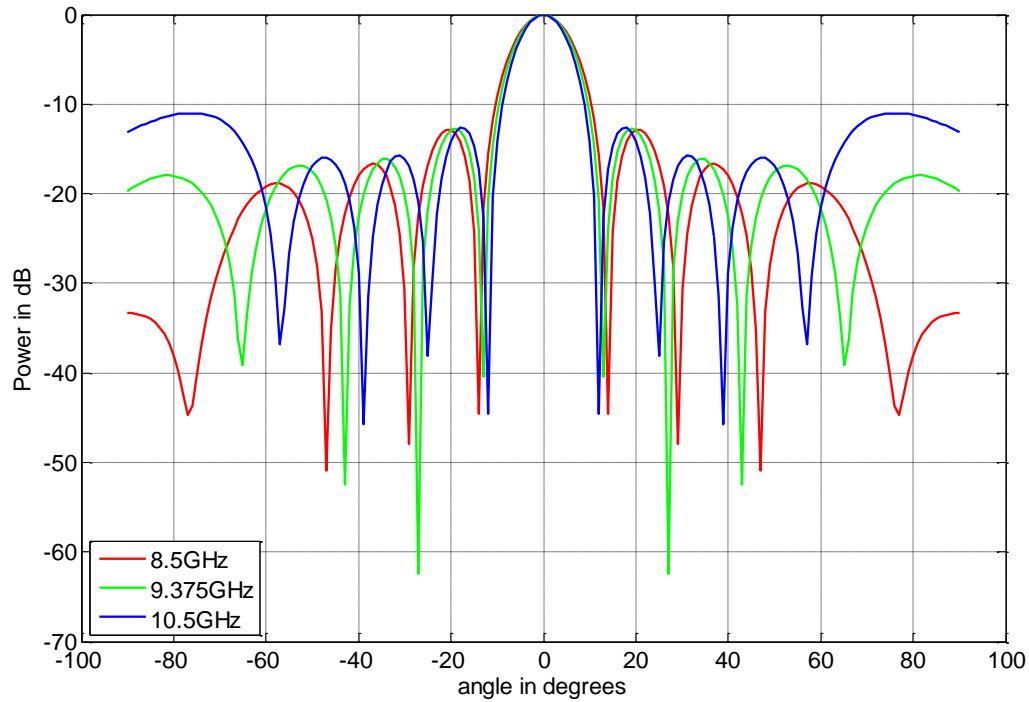
**Figure 5. 14: Variation in Beamwidth of Near field Beamformer (5x5 linear array) with Change in  $R_{NF}$  ; ( $\phi_0=0^0, \theta_0=0^0$ )**

The results of Figures 5.14 and 5.15 indicate that with increasing  $R_{NF}$ , the beamwidth of the radiation pattern reduces indicating that focusing feature of beamforming array can be realized only after certain distance away from the aperture of the array. Such an observation is similar to the one observed in the near field radiation pattern analysis of prime focus paraboloid dealt in [Narasimhan M.S. and Prasad K.M., 1981].

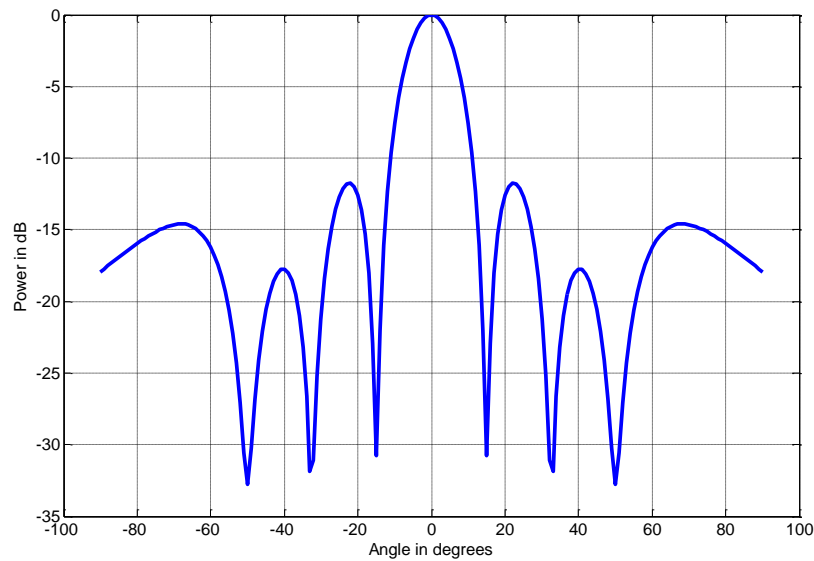
### 5.3.3 Response of Near Field Beamforming Linear array with change in Frequency:

With a linear array of 7 elements, simulation of the radiation characteristics of the near field beamformer was carried out at several spot frequencies in the X- band. The results shown in Figure 5.15 illustrate the effect of change in frequency on the radiation characteristics of the near field beamformer. For the simulation results shown in Figure 5.15, the beam steering angles are ( $\phi_0=0^0, \theta_0=0^0$ ) and  $R_{NF} = 3\lambda$ . As expected, with increase in frequency, the beamwidth of the array

decreases indicating improved gain. One notices the change in the amplitude as well as locations of sidelobes.



**Figure 5. 15: Effect of Change in Frequency on the Radiation Pattern of Near-field Beamformer with (7x1) Linear array ;  $R_{NF}=3 \lambda$  ;  $(\phi_0=0^0, \theta_0=0^0)$**

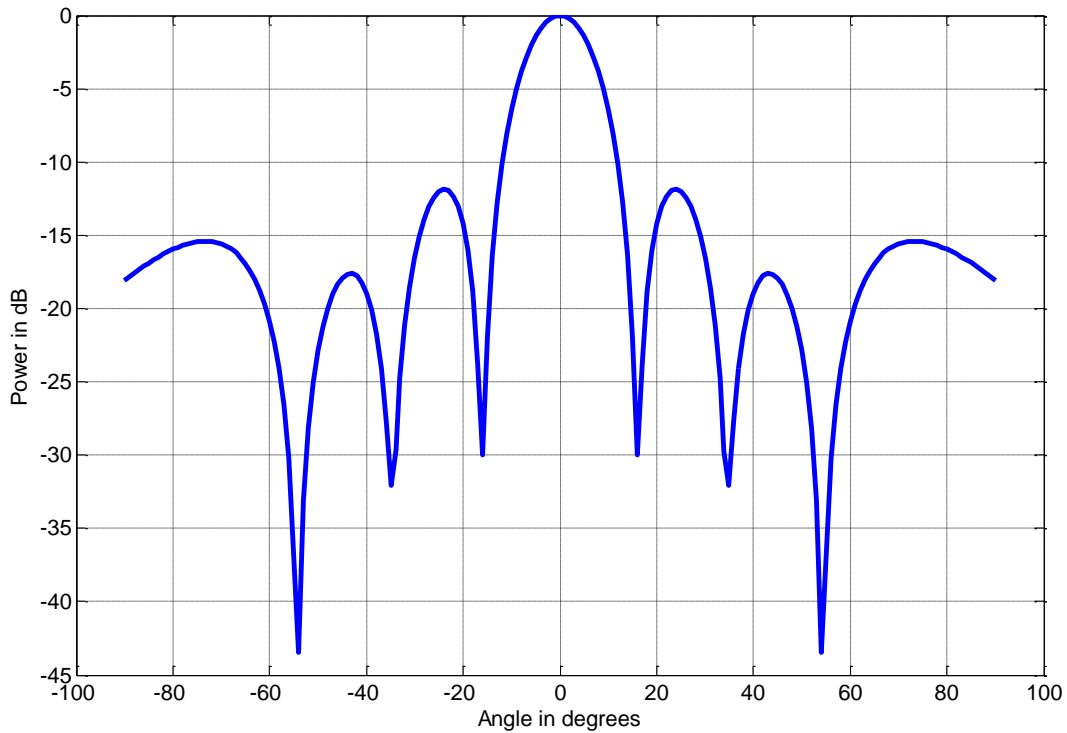


**Figure 5. 16: C – Band Near Field Beamformer with 5 Linear Array (5x1 element) at  $(\phi_0=0^0, \theta_0=0^0)$  ;  $R_{NF} = 3\lambda$ ; 3 dB; Beamwidth =  $14^0$**

When the circular waveguide operating in dominant  $TE_{11}$  mode operating in C band (4-6 GHz) was considered as an array element of a beamformer, the radiation pattern of the near field beamformer operating at 5 GHz at  $R_{NF}=3\lambda$  for  $(\varphi_0=0^\circ, \theta_0=0^\circ)$  is shown in Figure 5.16. The resulting beamwidth of the near field beamformer is  $14^\circ$ .

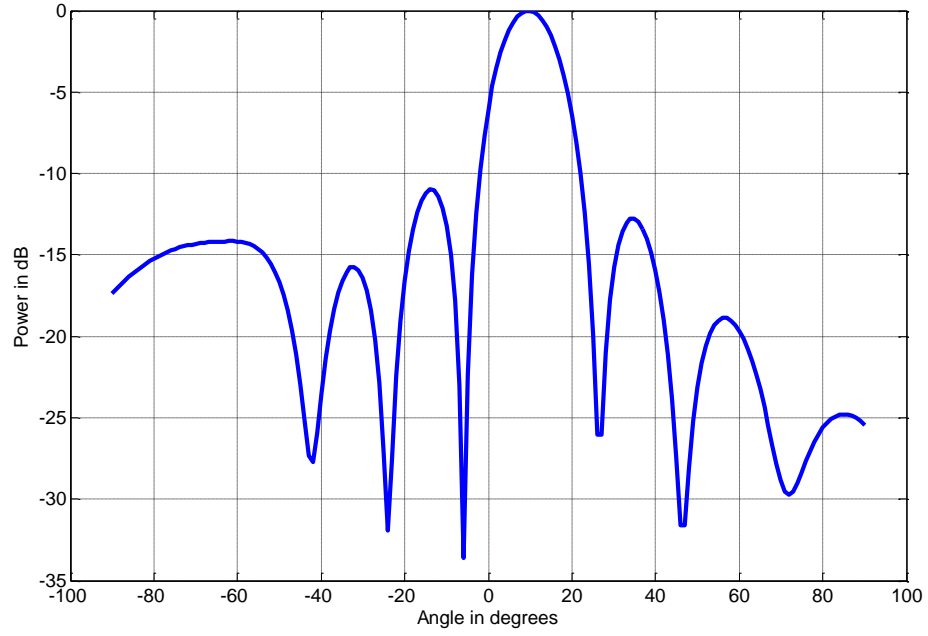
#### 5.3.4 Effect of Beamsteering Angle on the Beamwidth of Near Field Beamformer

Studies have also been carried to observe any variation in the beamwidth of the nearfield beamformer as the array is steered or scanned off the boresight directions. For a linear array of 5 elements, the simulations have shown that for a scan angle variation of  $\theta_0$  from  $-5^\circ$  to  $10^\circ$ , the beamwidth remained unchanged at  $14^\circ$  with  $R_{NF}=3\lambda$  as can be seen from the results shown in Figures 5.17 to 5.19.

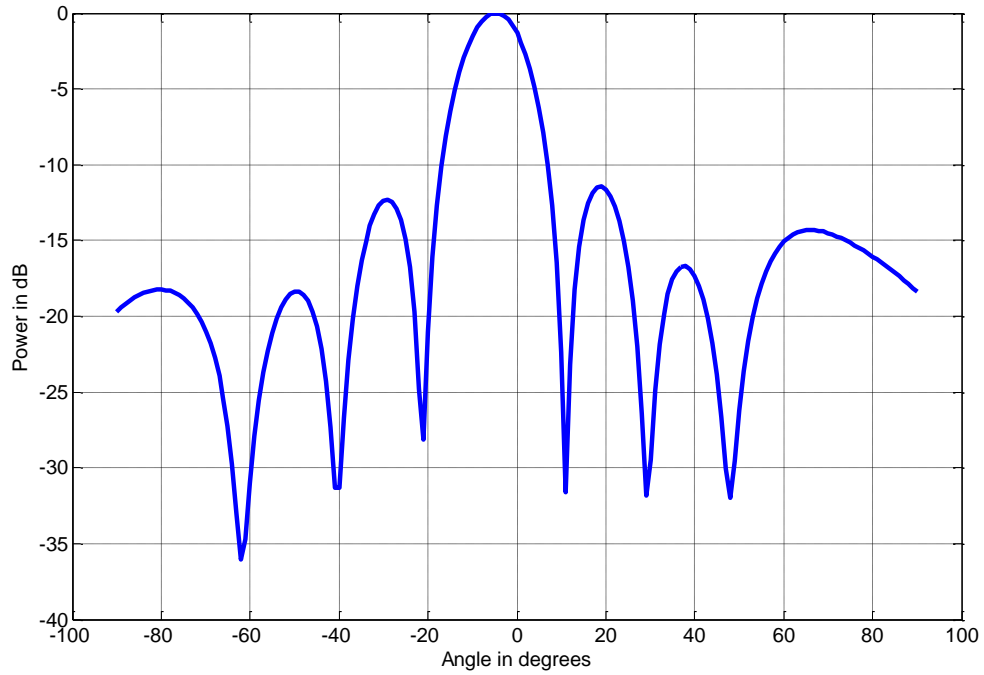


**Figure 5. 17: Near Field Beamformer with 5 Linear Array (5x1 element) at  $(\varphi_0=0^\circ, \theta_0=0^\circ)$  ;  $R_{NF} = 3\lambda$ ; 3 dB Beamwidth=  $14^\circ$**

One can also observe the greater asymmetry in 2<sup>nd</sup> sidelobe levels of the radiation patterns of arrays with beam steered off the boresight directions (Figures 5.17- 5.19).



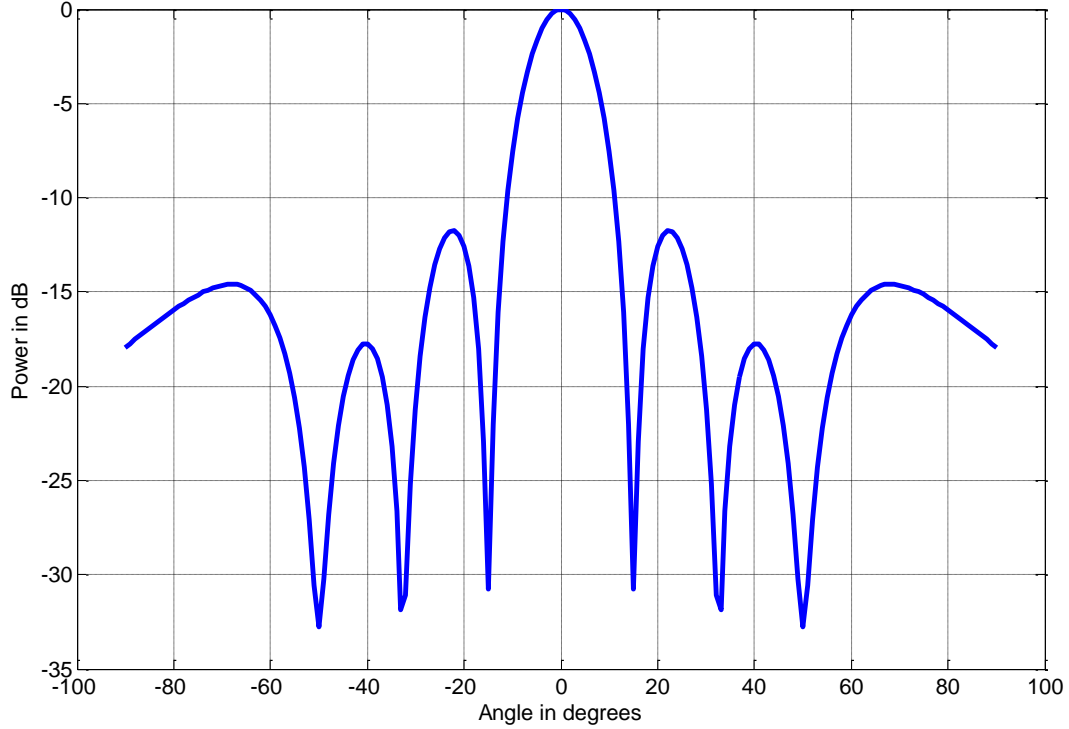
**Figure 5.18: Near Field Beamformer with 5 Linear Array (5x1 element) at  $(\varphi_0=0^\circ, \theta_0=10^\circ)$  ;  $R_{NF} = 3\lambda$ ; 3 dB Beamwidth=  $14^\circ$**



**Figure 5.19: Near Field Beamformer with 5 linear Array (5x1 element) at  $(\varphi_0=0^\circ, \theta_0=-5^\circ)$  ;  $R_{NF} = 3\lambda$ ; 3 dB Beamwidth=  $14^\circ$**



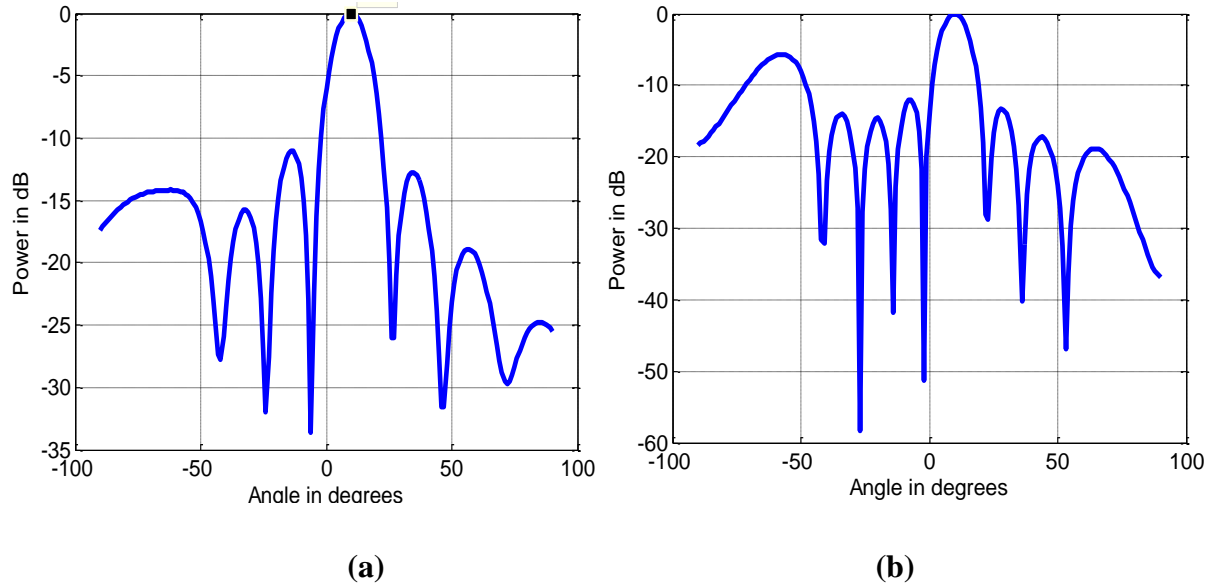
When the circular waveguide operating in dominant  $TE_{11}$  mode operating in C band (4-6 GHz) was considered as an array element of a beamformer, the radiation pattern of the near field beamformer operating at 5GHz at  $R_{NF} = 3\lambda$  for  $(\varphi_0=0^\circ, \theta_0=0^\circ)$  is shown in Figure 5.20. The resulting beamwidth of the near field beamformer is  $14^\circ$ .



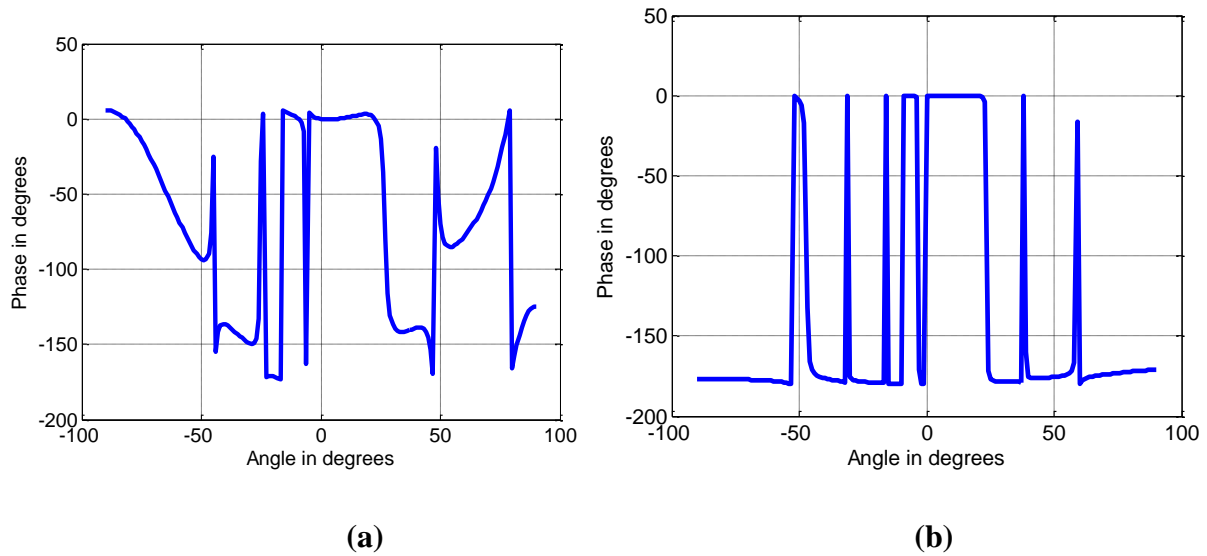
**Figure 5. 20: Near Field Beamformer with 5 Linear Array (5x1 element) at  $(\varphi_0=0^\circ, \theta_0=0^\circ)$  ;  $R_{NF} = 3\lambda$ ; 3 dB; Beamwidth =  $14^\circ$**

### 5.3.5 Comparison of Near Field and Far Field Beamforming Arrays

To illustrate the difference in the radiation pattern of the near field and far field beamformers with linear array (5x1 elements), simulations have been performed for  $(\varphi_0=0^\circ, \theta_0=10^\circ)$  at  $\lambda=3.2$  cm. The amplitude radiation patterns of the beamformer at  $R_{NF} = 3\lambda$  and  $R_{NF} = 100\lambda$  are shown in Figures 5.21 (a) and (b) respectively. The corresponding phase patterns at  $R_{NF} = 3\lambda$  and  $R_{NF} = 100\lambda$  are shown in Figures 5.22 (a) and (b) respectively.

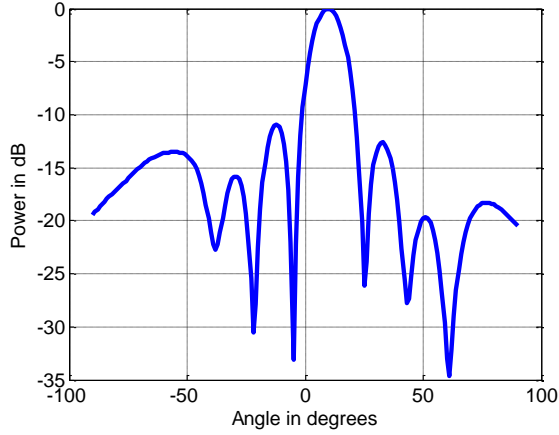


**Figure 5. 21: Comparison of Near and Far Field Amplitude Patterns of Beamformer with (5x1) Linear Array; ( $\phi_0=0^\circ, \theta_0=10^\circ$ ). (a)  $R_{NF}=3\lambda$  (b)  $R_{NF}=100\lambda$**

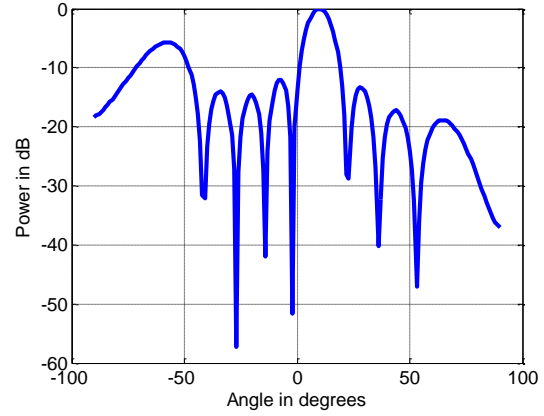


**Figure 5. 22: Comparison of Near and Far Field Phase Patterns of Beamformer with (5x1) Linear Array; ( $\phi_0=0^\circ, \theta_0=10^\circ$ ) (a)  $R_{NF}=3\lambda$  (b)  $R_{NF}=100\lambda$**

A similar comparison of the near field and far field radiation patterns of beamformer with (5x5) planar array is illustrated through Figures 5.23 and 5.24. The amplitude radiation patterns at  $R_{NF}=3\lambda$  and  $R_{NF}=100\lambda$  are shown in Figures 5.23(a) and (b) respectively.



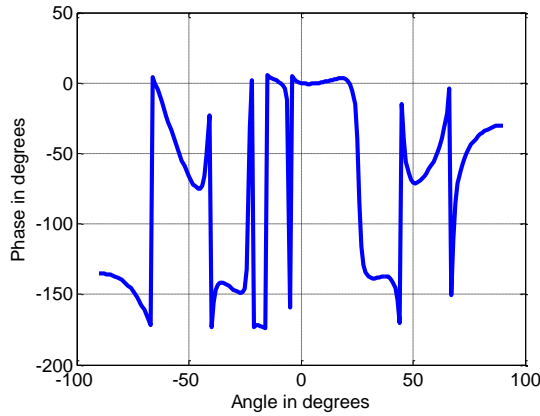
(a)



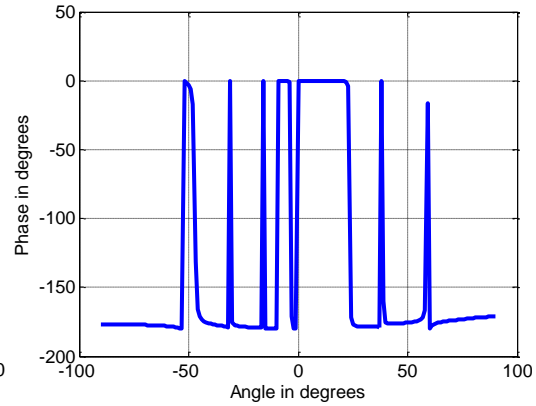
(b)

**Figure 5. 23: Comparison of Near and Far Field Amplitude Patterns of Beamformer with(5x5) Planar Array; ( $\phi_0=0^0, \theta_0=10^0$ ) : (a)  $R_{NF}=3\lambda$  : (b)  $R_{NF}=100\lambda$**

The corresponding phase patterns at  $R_{NF}=3\lambda$  and  $R_{NF}=100\lambda$  are shown in Figure 5.24 (a) and (b) respectively.



(a)



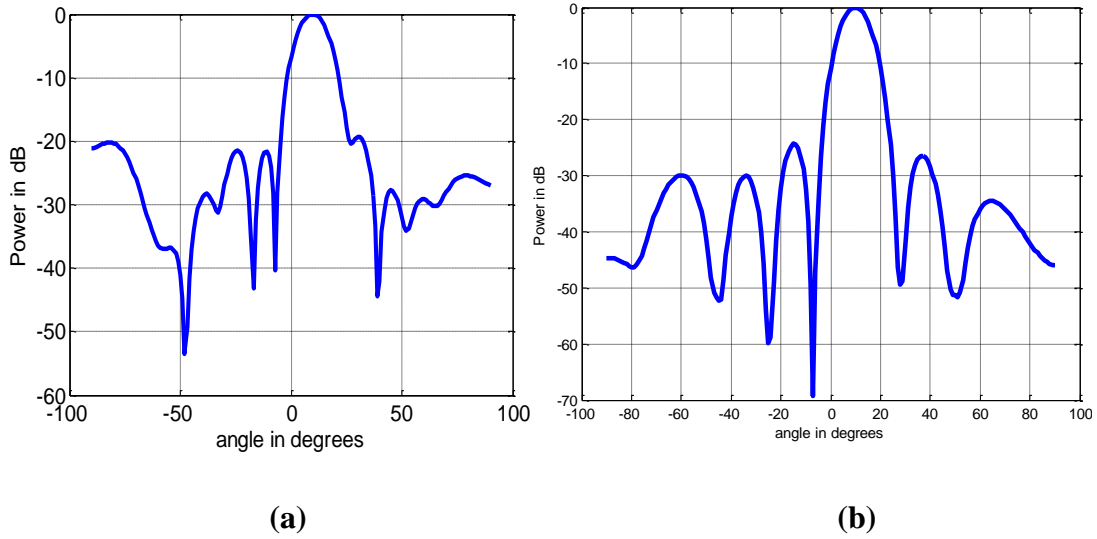
(b)

**Figure 5. 24: Comparison of Near and Far Field Phase Patterns of Beamformer with (5x5) Planar Array; ( $\phi_0=0^0, \theta_0=10^0$ ); (a)  $R_{NF}=3\lambda$  ; (b)  $R_{NF}=100\lambda$**

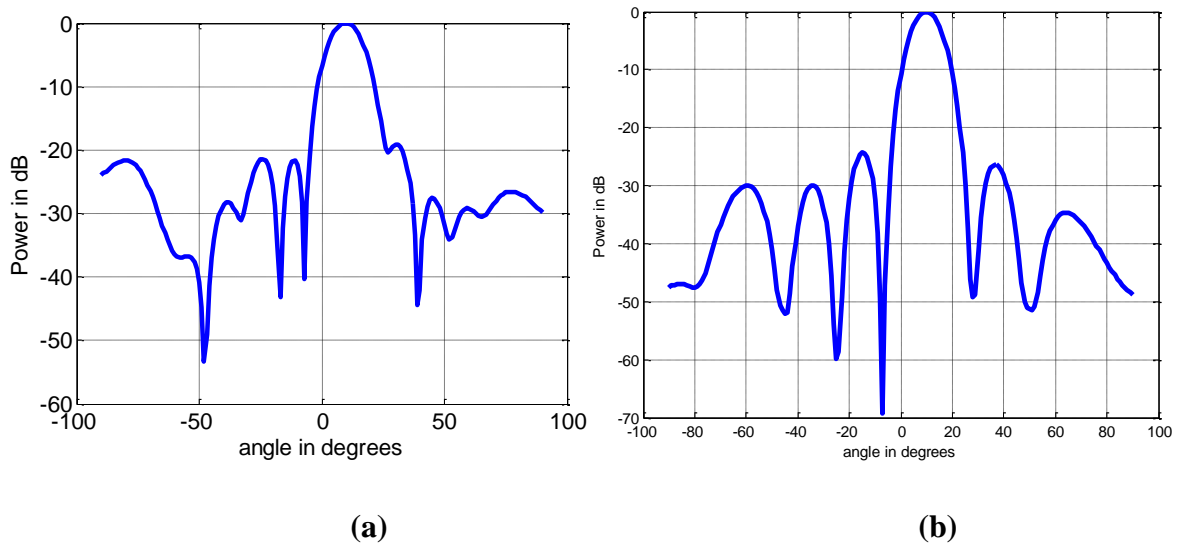
A comparison of the near field and far field radiation patterns of the beamforming arrays reveal that at far field distance of observation, there is a perceptible increase in the asymmetry in the radiation patterns when the beam is steered off the boresight direction.

### 5.3.6 Two dimensional Beamsteering :

To demonstrate the two dimensional beamsteering feature of the proposed near field analysis, simulations have been performed for the computation of radiation patterns of a (5x5) planar array both in the near field ( $R_{NF}=3\lambda$ ) and far field ( $R_{NF}=100\lambda$ ) with ( $\varphi_0=45^\circ$ ,  $\theta_0=10^\circ$ ). The near field beamformer exhibits both the  $E_\varphi$  and  $E_\theta$  components of the radiation pattern. The near field and the far field  $E_\theta$  components of amplitude radiation pattern of the the beamformer are shown in Figures 5.25 (a) and (b) respectively.

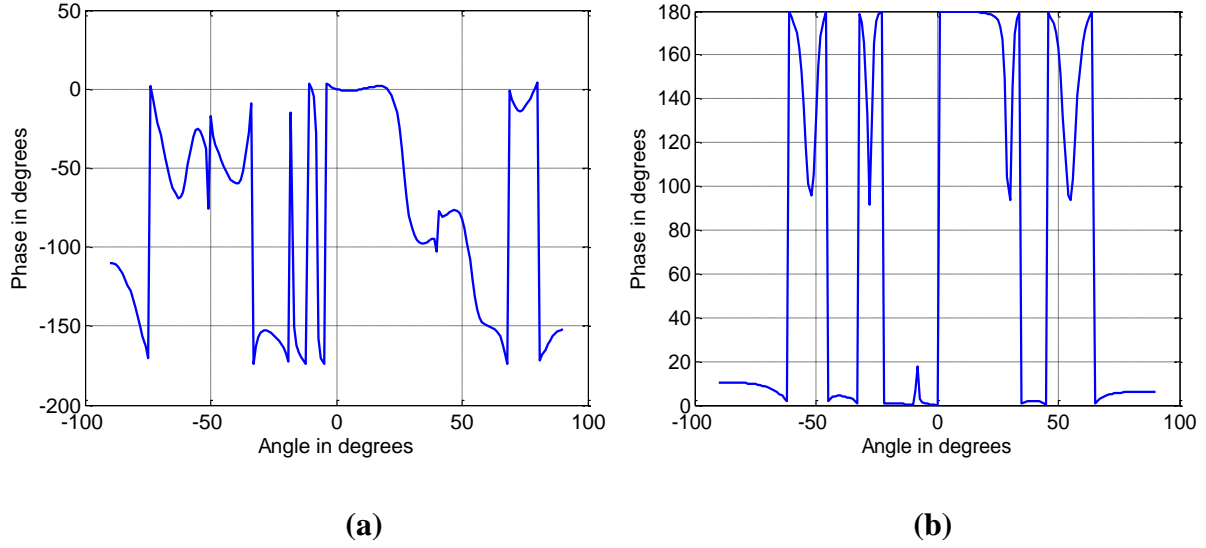


**Figure 5. 25 Comparison of Amplitude Patterns  $E_\theta$  Component of Beamformer with (5x5) Planar array ( $\varphi_0=45^\circ$ ,  $\theta_0=10^\circ$ ) at (a) $R_{NF}=3\lambda$ ; (b)  $R_{NF}=100\lambda$ ;**



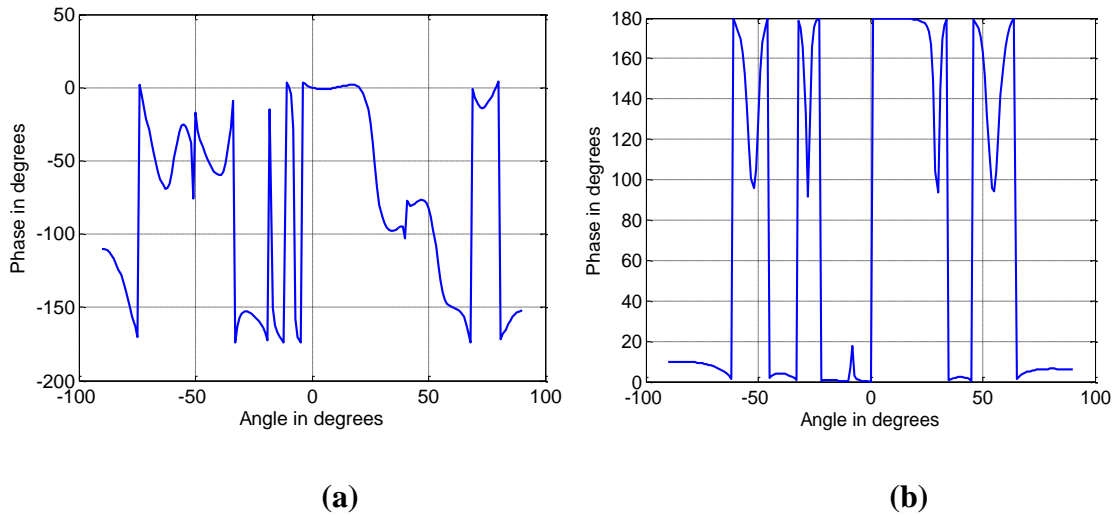
**Figure 5. 26: Comparison of Amplitude Patterns  $E_\varphi$  Component of Beamformer with (5x5) Planar array ( $\varphi_0=45^\circ$ ,  $\theta_0=10^\circ$ ) at (a) $R_{NF}=3\lambda$ ; (b)  $R_{NF}=100\lambda$ ;**

Similarly the corresponding  $E_\phi$  components of the radiation patterns of the beamformer are depicted in Figures 5.26 (a) and (b). The near field and far field phase patterns of  $E_\theta$  component of the beamformer are shown in Figure 5.27.



**Figure 5. 27: Comparison of Phase Patterns of  $E_\theta$  Component of Beamformer with (5x5) Planar array ( $\phi_0=45^\circ$ ,  $\theta_0=10^\circ$ ) at (a)  $R_{NF}=3 \lambda$ ; (b)  $R_{NF}=100\lambda$ ;**

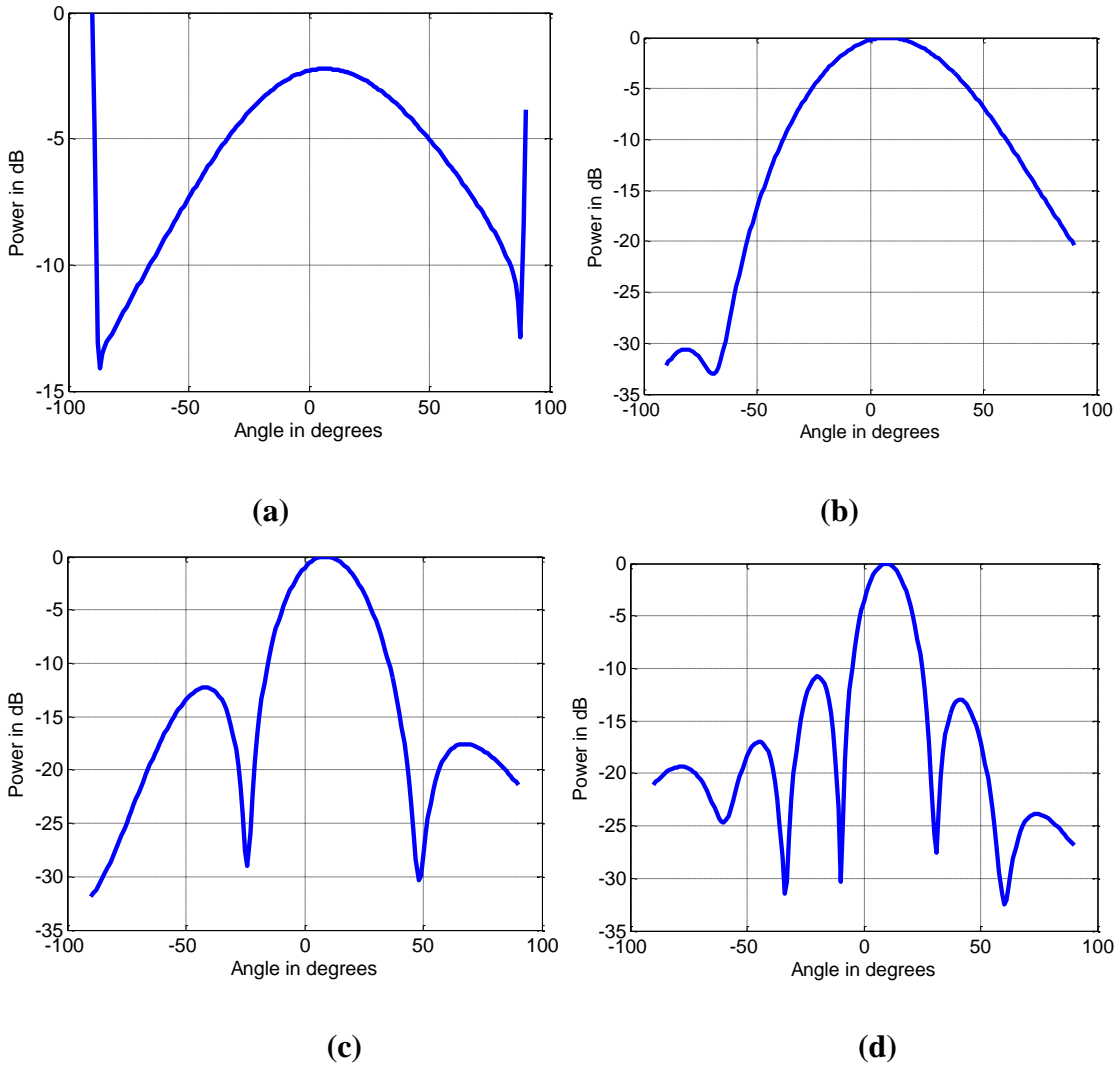
The results shown in Figure 5.28 correspond to the  $E_\phi$  component of the radiation patterns evaluated in both the near field and far field range.



**Figure 5. 28: Comparison of Phase Patterns  $E_\phi$  Component of Beamformer with (5x5) Planar array ( $\phi_0=45^\circ$ ,  $\theta_0=10^\circ$ ) at (a)  $R_{NF}=3 \lambda$ ; (b)  $R_{NF}=100\lambda$ ;**

### 5.3.7 Minimum Distance for Desired Near Field Beamforming:

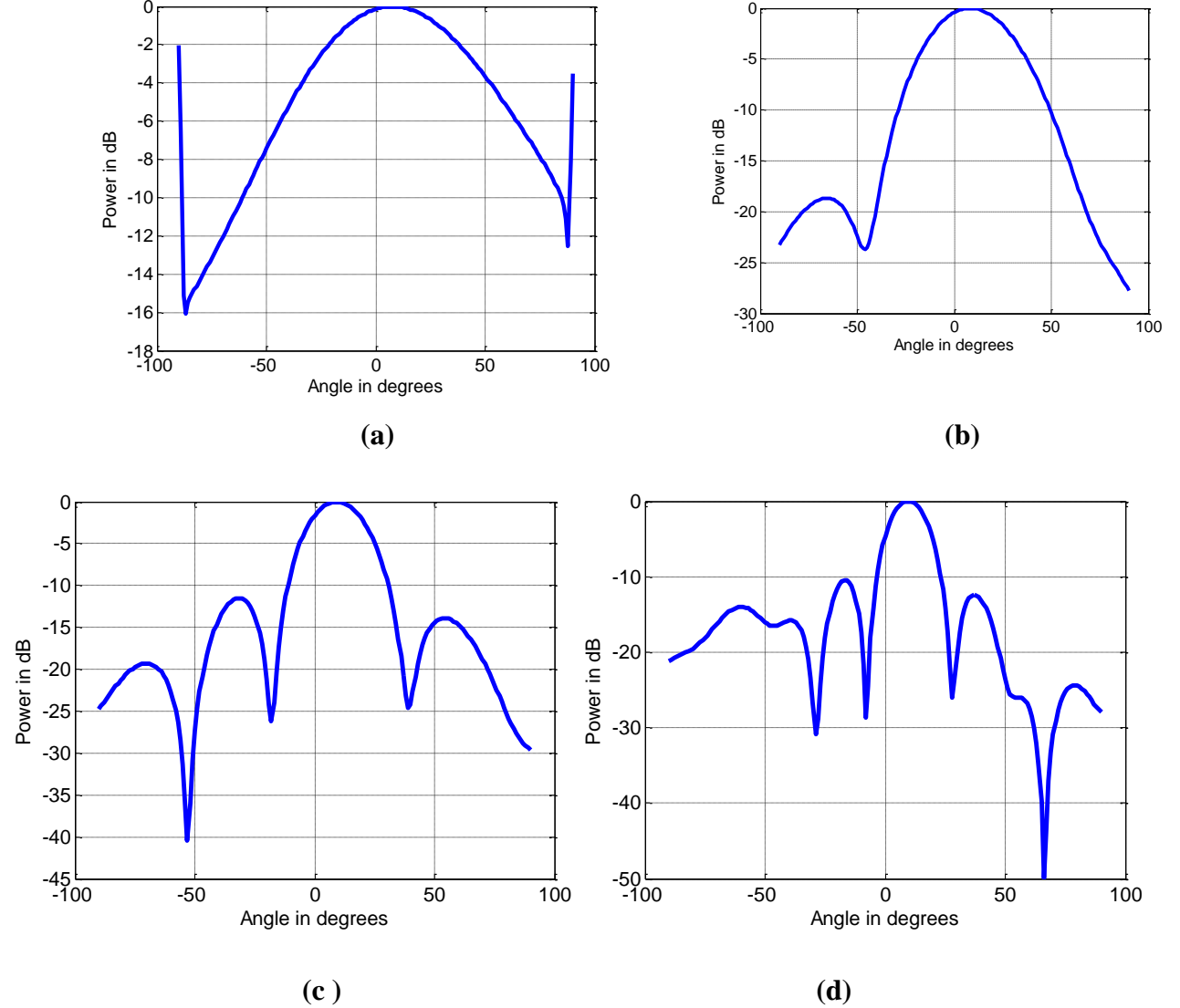
Simulations have been carried out to ascertain the minimum radial distance above which well defined beamformation occurs for a given array configuration. For a (5x1) linear array with desired beamforming angular coordinates of  $(\phi_0=0^\circ, \theta_0=10^\circ)$ , simulation results with the near field beamforming approach indicate beamsteering feature with well defined sidelobes at  $R_{NF}=1 \lambda$ .



**Figure 5. 29: Variation in Radiation Pattern of near field Beamformer with (5x1) Linear array: (a)  $0.3\lambda$  (b)  $0.5\lambda$  (c)  $1\lambda$  (d)  $2\lambda$  at  $(\phi_0=0^\circ, \theta_0=10^\circ)$**

For  $R_{NF} < 1 \lambda$ , the beamsteering is not very effective in view of relatively larger beamwidth.  $R_{NF} = 1 \lambda$  corresponds to ratio of Radial distance to Array Aperture or  $(R_{NF}/D_a) = 0.2334$ . The variation in the radiation pattern of the near field beamforming linear array of (5x1) elements with change in the near field radial distance ' $R_{NF}$ ' is shown in Figure 5.29. Additional but similar simulation

have been carried out for a near field beamformer with (5x5) planar array for smaller values of ' $R_{NF}$ '. Figure 5.30 depicts the variation in radiation pattern of a near field beamformer with (5x5) planar array with change in near field distance of observation.



**Figure 5. 30: Variation in Radiation Pattern of Near Field Beamformer with (5x5) Planar array: (a)  $0.3\lambda$  (b)  $0.5\lambda$  (c)  $1\lambda$  (d)  $2\lambda$  at ( $\varphi_0=0^\circ$ ,  $\theta_0=10^\circ$ )**

The simulation results of the (5X5) planar array with the near field beamforming approach also indicate beam-steering feature with well-defined side lobes at  $R_{NF}=1$

## 5.4 Conclusions

This section summarizes the conclusions and derivable inferences based on the analytical and simulation studies presented in this chapter.

A novel approach for near field beamforming is proposed in this chapter and it is also valid for far field. This feature can be attributed to the following:

1. Computation of beamforming weights directly at the specified arbitrary distance
2. Generalization of near-field array factor and near-field beam steering phase factor to overcome the assumption of planarity of the wave-front impinging on the radiating aperture of the array elements.

Numerous simulation results have been presented to substantiate the validity, versatility and novelty of the proposed approach. Unlike the method of radial reciprocity (Kennedy R.A. et al, 1999), the proposed method does not mandate the requirement of 3D near field data of the beamforming array.

Simulation results derived through proposed near field beamforming technique with radial distance  $R_{NF}$  equal to or greater than conventional far field distance criterion show perfect correlation with the results obtained through alternative formulations in the open literature meant exclusively for far field beamforming or beamsteering technique.

Numerous simulations confirmed that the proposed technique yields reasonably encouraging beamforming results even at a distance of  $R_{NF}=1\lambda$  from the aperture of (5x1) linear or (5x5) planar array. This corresponds to  $(R_{NF}/D_a) = 0.2334$ . However, at distances greater than  $R_{NF}=1\lambda$ , the radiation patterns exhibit more pronounced structure of sidelobes. Below the distance of  $R_{NF}=1\lambda$ , simulation results reveal the radiation pattern featured with less directive main beam.

The significant differences in the radiation patterns of the near field and far field beamformers lie in the beamwidth of the main lobe and the asymmetry in the radiation pattern in case of beamsteering off the boresight direction.



A relative comparison between the radiation performance of X- band and C- band near field beamforming linear array has also been performed to infer the resulting difference in the beamwidth of the array antenna.

Typical simulation studies on the radiation characteristics of planar array to illustrate the realizable two dimensional near field beamsteering have also been presented to validate the concept.

When viewed in totality of the formulations, simulations and discussions presented in this chapter, it is imperative that the primary theme of desired versatility, generality and flexibility expected out of the new analytical formulation for the near field beamforming technique have been substantiated with requisite details and results.

## **Chapter 6: Analysis of Near-Field Beamforming Based TWI System**

### **6.1 Introduction**

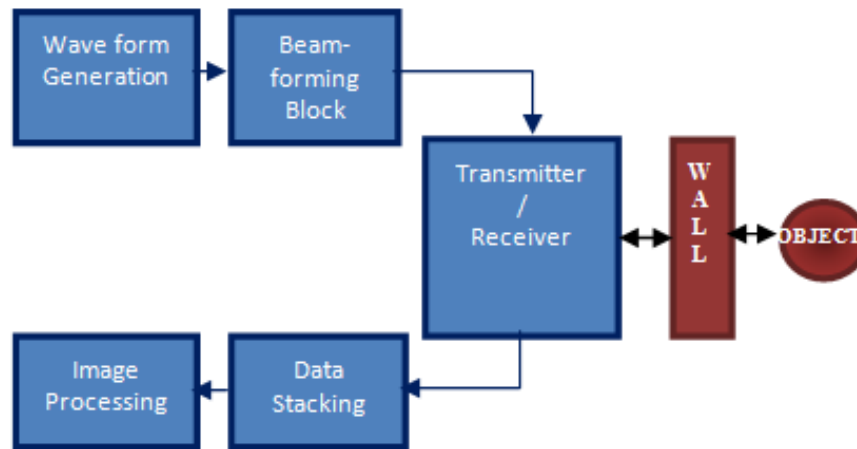
The primary objective of the Through Wall Imaging (TWI) system simulation is to image single or multiple structures behind the wall. This chapter discusses the concepts and mathematical formulations involved in modelling the wall, objects behind the wall and finally provide the methodology to image structures behind the wall using the Near-field beamforming approach. The chapter introduces impedance modelling technique to model 2D and 3D objects of different materials and shapes. It gives a new visualizing methodology which utilizes just the reflected signal amplitude to image structures behind the wall. The chapter discusses the losses involved in the wave propagation and provides the imaging results obtained on simulating several test conditions which involves various targets of different material mediums. It demonstrates reconstruction of flat body (2D) and curved body (3D) objects. The chapter finally presents the total system simulation results obtained from stepped frequency generation and discusses its effectiveness in generating high resolution images of behind the wall scenarios.

### **6.2 Through Wall Imaging System:**

TWI systems are microwave imaging systems that provide high resolution visualization of behind the wall scenarios. They come handy during rescue missions in case of fire, earth quake, avalanche or hostile activity. It can also be used for surveillance and reconnaissance. The idea of TWI system evolved through Ground Penetration Radar (GPR). The working principles of TWI are similar to GPR except that the images are behind the wall rather than the ground (Khalil F., 1994). GPR uses electromagnetic radiation to detect objects of archaeological importance, changes in material, voids and cracks (Kennedy R.A., 1998). Since the late 1990s significant research is being carried out on TWI systems. TWI systems have been proved to work even beyond a single wall from near-range (Baranoski E.J., 2008).

TWI is a cross-disciplinary topic which involves research in electromagnetic propagation, antenna, antenna array design, beamforming, Signal and Image processing among others (Khalil F. *et al*, 1994). GPR and TWI systems generally use Multilateration techniques like Synthetic Aperture Radar (SAR) and Inverse Synthetic Aperture Radar (ISAR) to scan a given area. Multilateration is a process of locating an object by accurately computing the Time Difference Of Arrival (TDOA) of a signal emitted from that object to multiple receivers (sensors). The general idea behind

Multilateration is to correlate range measurements from multiple sensors to specific points in the image (Amin M.G. and Ahmad F., 2013). SAR and ISAR have their own limitations or pre-requisites for imaging – A relative motion between target and radar is a must; consequently stationary objects cannot be imaged.



**Figure 6. 1: Block Diagram of TWI System**

Figure 6.1 shows a TWI system used for imaging an object behind the wall scenario. The TWI system consists of a waveform generation block which generates pulses of constant or a range of continuous frequencies. The way in which the waveforms are generated and associated power differs with every generation technique, such as, sine wave type or impulse type. The sine wave technique has many advantages over the impulse technique but its limitation is that it cannot be put on a monolithic integrated circuit. It can be chosen over other methods because of the ease in modeling of the waveforms, the high bandwidth that can be achieved, stability and appreciable Signal to Noise Ratio (SNR). The waveform generation block is connected to the beamforming block. It in turn is connected to the antenna block which illuminates the wall. Beamforming methodologies differ with the choice of scanning techniques. The scanning can be carried out by SAR or ISAR methods. Any scanning technique however requires an antenna that functions in both in transmit and receive modes. The antenna can be a single element or an array of elements. There can be a single transmitter and single receiver or a single transmitter and multiple receivers or multiple transmitters and multiple receivers. The choice of antenna configuration, its size as well as its performance parameters like the radiation pattern, beam width and frequency of operation play a vital role. These aspects have been covered in chapters 4 and 5.

The transmitted beams propagate and impinge on the target undergoing optical phenomena like reflection, scattering, diffraction and refraction. This in addition to re-radiated field by the target propagated again through the wall and captured at the receiver would lead to loss in the signal strength of the received field and thereby loss/distortion of data. The received fields will be processed using one of the several migration methods like the back projection, back propagation or ISAR imaging methods involving forward and inverse Fourier transforms or one can even use 3D Fourier transforms. The received (scanned) data will be stacked first and will be further processed to generate an image with an acceptable resolution. The image processing methods can involve edge detection, Joint Time Frequency Transform (JTFT), background subtraction or even the fusion techniques (Aftanas M., 2009 ; Schlutz M., 2009).

.

Existing SAR based TWI systems (Aftanas M., 2009) form an image of objects behind the wall. The acquired images from such systems appear as high amplitude blob or a patch to indicate the presence of objects behind the wall. Figure 6.2(a) shows a typical scenario of a flat metal plate placed on a chair and image reconstruction as reported in (Aftanas M., 2009). The reconstructed image in Figure 6.2b shows a high amplitude blob or a patch to indicate the presence of an object or a target behind the wall. In Figure 6.2a, the plate and the chair constitute the object. The results reported in (Aftanas M., 2009) and shown in Figure 6.2(b) do not however provide the shape, contour, structural or material information of the imaged object. The TWI system (Gassler J, 2008) based on SAR techniques needs to be moved physically along the walls at spatial steps and intervals. Such a proposition may tend to be time consuming and not practical in scenarios of natural disasters or hostile situations. From a practical perspective, a TWI system whose functioning does not involve physical motion of the system is highly desirable. An approach for conceptualization, design and simulation validation of a TWI system devoid of its physical motion constitutes the primary objective of this thesis. Towards this, the physical motion of the system to realize the scanning of the radiation pattern of the antenna is fully avoided and instead beamforming technique is proposed to steer the main beam of the radiation pattern of the antenna without physically rotating it.

This item has been removed due to third party copyright. The unabridged version of the thesis can be viewed at the Lanchester Library, Coventry University.

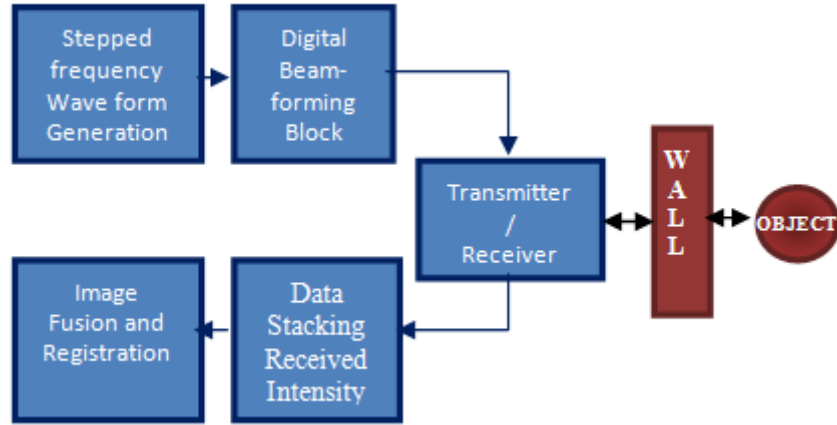
**(a) Scene**

**(b)Reconstructed Image**

**Figure 6. 2: Test Scenario of SAR (Aftanas M., 2009)**

Digital beamforming is a new method that is being pursued apart from the conventional methods for scanning a given space to image the scenario behind/beyond the wall. Generally far-field techniques are used and they are well established. However, they assume that both the wall and the objects behind the wall are at far-field distances (distance between the antenna and wall/object is greater than or equal to  $2D^2 / \lambda$ , where D is the maximum linear dimension of the antenna and  $\lambda$  is the wavelength). Practically walls/objects can be at any distance smaller than  $2D^2 / \lambda$  and such a scenario is categorized as near-field.

In a TWI system, one of the important considerations is the illumination of both the outer wall and the object behind the wall with as many different beam scans as possible to realize almost a complete illumination with higher incident power. With the insistence of multiple scans, in every scan the focus is to place the main beam of the beamforming array to the precise location defined through the near-field distance as well as beam steering angles  $(\varphi_0, \theta_0)$  and not the near-field radiation pattern itself.



**Figure 6. 3: Proposed Block Diagram of TWI System with Step Frequency Waveform**

Stepped frequency has many advantages such as wider dynamic range, higher mean power and lower noise figure. Probably the most important one is the possibility of shaping the power spectral density. This feature allows changing level of the side lobes just by changing the “windowing” function.

This chapter proposes a new methodology of TWI which involves stepped frequency based near-field beamforming technique to scan objects behind the wall and provide the 2D/3D contour of the object. Figure 6.3 depicts the block diagram of the proposed model for TWI system. This chapter provides a complete mathematical model of the proposed TWI system which also involves mathematical analysis involved in modelling the wall, object, the incident and reflected fields from the wall to the object and vice versa. The antenna modelling for TWI applications along with radiation patterns obtained for simulating the transmission and reception of signals through the wall, objects and back to the receiver has been discussed in chapters 4 and 5 of this thesis. This chapter also proposes a new imaging methodology that is computationally less expensive to reconstruct objects behind the wall without invoking inverse transformations.

### 6.3 Wall and Object Modelling

The TWI radar system must illuminate the target behind the wall and image the scenario by utilizing the received ElectroMagnetic (EM) signal. The media through which the EM signals propagate plays an important role as they induce the various optical phenomena like reflection, scattering, attenuation, diffraction and others to the radiating signal from the transmitter or

receiver. It is a known fact that EM waves do not penetrate metal plates or rods but can pass through most of the materials like concrete walls, wood and bricks. Hence for simulations and from practical/realistic conditions modeling of concrete walls which are usually 9 inch thick is considered. However targets behind the wall are considered to be objects or surfaces which are opaque to the incident waves and the reflected waves are assumed to have sufficiently higher amplitude helping in generating images. For the simulations, targets are usually considered to be pure conductors like carbonyl metal, aluminium; some non conductors like glass, graphite are also modeled. The wall and objects behind the wall are modeled considering the various EM properties like conductivity ' $\sigma$ ', permeability ' $\mu$ ' and permittivity ' $\epsilon$ ' of the given medium. Different materials have different values of these properties and as consequence their response to incident EM radiation will also be different. Most imaging devices build images of behind the wall scenario by reconstructing the relative permittivity profile of the structures behind the wall[ Reference} However the simulations carried out do not reconstruct EM properties profile rather the intensity of reflection of waves from the targets is considered. The simulations considered 2D flat plate models and also 3D or curved body structures as objects behind the wall. The 3D structures like the hemispheres and half-cylinders with concave and convex configurations were considered for simulations.

### 6.3.1 Modelling of Wall

In the simulations carried out impedance modelling is considered for simulating wall and object. The electromagnetic properties like permeability, permittivity and conductivity of air are chosen to be  $\mu_a=1$ ,  $\epsilon_a=1$  and  $\sigma_a= 5.5 \times 10^{-15}$  S/m, and for concrete wall the chosen values are  $\mu_w =1$ ,  $\epsilon_w= 9$  and  $\sigma_w=0.1$  Sm<sup>-1</sup>(Asprone et al., 2010) . The permeability of concrete is 1 because it is a non-magnetic medium. The equations (6.1) and (6.2) show that the mathematical modelling of wall can be carried out with known values of  $\mu$ ,  $\epsilon$  and  $\sigma$ ; Equation 6.1 is for the computation for free space wave impedance; while Equation 6.2 demonstrates modelling a conducting medium with conductive, magnetic and dielectric loss.

$$Z_0 = \frac{E}{H} = \sqrt{\frac{\mu_0}{\varepsilon_0}} = 376.731 = 120\pi \quad \dots \quad (6.1)$$

$$Z_0 = \sqrt{\frac{j\omega\mu}{\sigma + j\omega\varepsilon}} = \sqrt{\frac{\mu_0}{\varepsilon_0}} \sqrt{\frac{j}{\frac{\sigma}{\omega\varepsilon_0} + j\varepsilon_r}} \quad \dots \quad (6.2)$$

$$\text{where } \mu = \mu' - j\mu'' \quad \dots \quad (6.3)$$

$$\varepsilon = \varepsilon' - j\varepsilon'' = \varepsilon_0\varepsilon_r - j\frac{\sigma}{\omega} \quad \dots \quad (6.4)$$

$$\varepsilon_0 = 8.854 \times 10^{-12} \text{ F / m}$$

$$\mu_0 = 4\pi \times 10^{-7} \text{ H / m}$$

Using the Equations (6.1) - (6.4) and different values of  $\mu$ ,  $\varepsilon$  and  $\sigma$  for different mediums, walls structures or objects of different materials and thickness can be modelled. In the simulations, the objects that are modelled have material properties of Aluminium, Graphite, Rubber and Borosilicate glass. The assigned values of  $\mu$ ,  $\varepsilon$  and  $\sigma$  derived through (Frazier, 1996) are given in Table 6.1. The concrete wall is modeled as 9 inch thick structure of 1m height and 1m width. The objects behind the wall are also modeled to be of different materials with EM properties as tabulated in Table 6.1. The distance between the wall and radar is considered to be 1.5m while the distance between wall and object is about 0.5m. The radar is considered to have 5 x 5 elements.

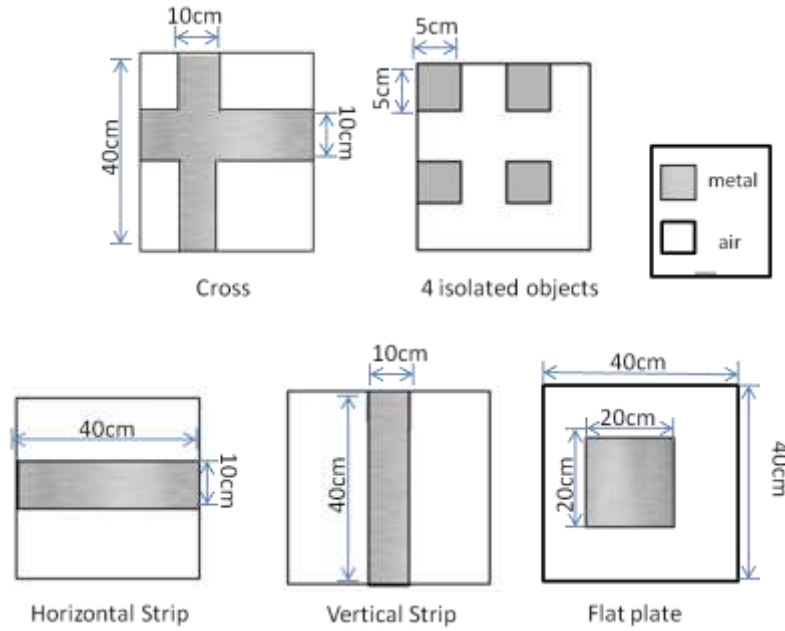
Material	Permeability ( $\mu_r$ )	Permittivity ( $\varepsilon_r$ )	Conductivity ( $\sigma$ ) (Sm <sup>-1</sup> )
<b>Aluminium</b>	1.000022	12	$3.5 \times 10^7$
<b>Graphite</b>	1.0	2.1	$1.276 \times 10^5$
<b>Rubber</b>	1	7	$10^{-4}$
<b>Borosilicate Glass</b>	$4.86 \times 10^{-15}$	11.68	$10^{-11}$

**Table 6. 1: Material Properties**

In order to validate that reflection, scattering, refraction and other optical characteristics cause attenuation in the transmitted power, a simulation for cases of with and without wall were carried out. In presence of a pure reflecting material  $T=0$  and hence all the incident power will be reflecting back leading to magnitude of  $R$  to be unity. The pre assumptions made before carrying out simulations to compute field distribution were that the current distribution  $J$  and  $M$  exist on non-conducting surfaces while only  $J$  exists on conducting surfaces and they are modelled based on basic electromagnetic principles as follows



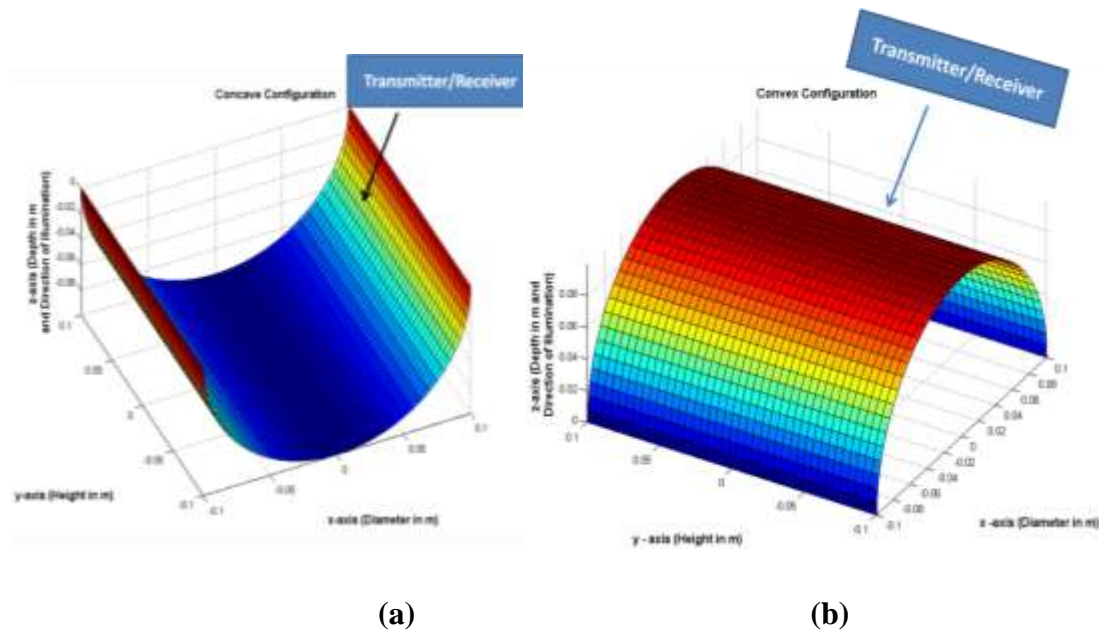
$J = \hat{n} \times H$  and  $M = E \times \hat{n}$  in case of non-conducting surfaces  
 $J = 2\hat{n} \times H$ ; in case of conducting surfaces



**Figure 6. 4: Shapes and Dimension of 2D Flat Plate Objects**

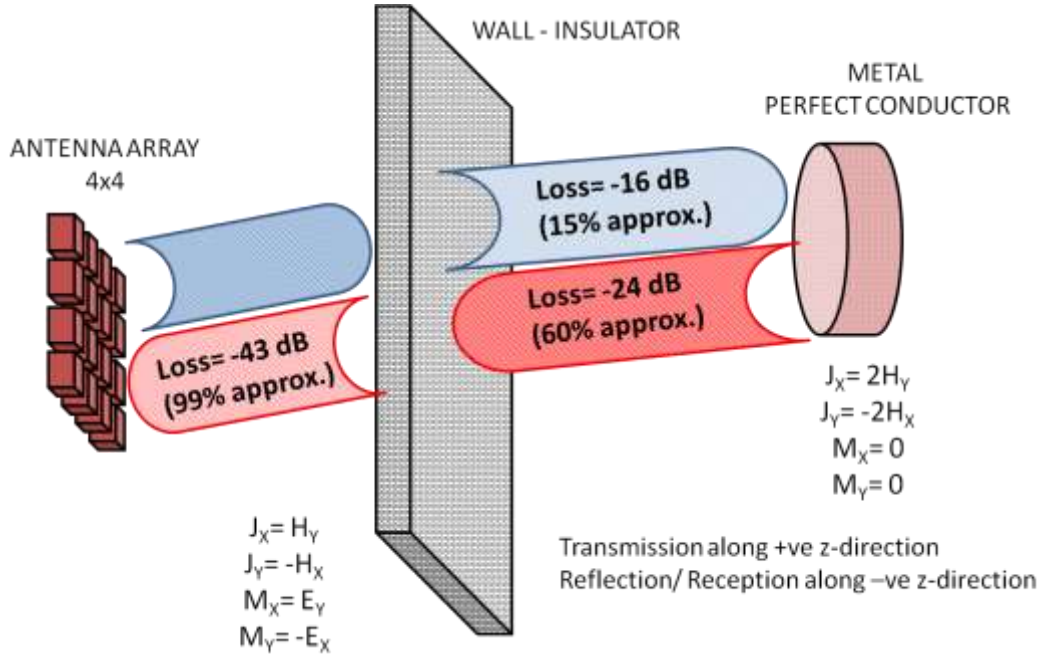
### 6.3.2 Modelling of Objects (Targets):

To have an estimate of total signal loss, the TWI system simulation which includes a concrete wall, a pure conducting object behind the wall was carried out. The object was considered to be a flat metal plate with  $\mu_r=1$ ,  $\epsilon_r=310$  and  $\sigma_a= 5 \times 10^3$  S/m. Simulation were carried for both 2D flat plates and 3D curved bodies. The 2D flat plate objects were modeled in different shapes as shown in Figure 6.4. The 2D flat plates are modeled as a flat square plate, a cross shaped plate, 4 different isolated square plates, horizontally placed metal strip and a vertically placed metal strip. The Figure 6.4 also indicates its respective dimensions. 3D curved bodies considered are a hemisphere and half cylinder with concave and convex configurations as shown in Figure 6.5. The dimensions of the wall considered are 1m (Height) x 1m (Width) x 0.229m (Thickness). The size of the flat plates is 40cm x 40cm. The cylinders are of radius of 20 cm and have a height of 40 cm. The objects are modeled with properties of Graphite (Carbon), Rubber, Borosilicate glass and Aluminium.



**Figure 6. 5 Half Cylinder Models. (a) Concave (b) Convex**

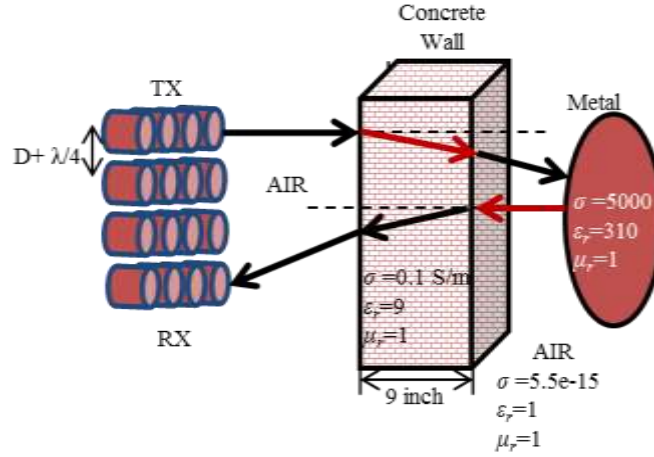
With the above parameters in the simulations, it was observed that the transmission coefficient was 0 and the reflection coefficient was 1 in the presence of pure metal as a wall with  $\mu_w = 1$ ,  $\epsilon_w = \infty$  and  $\sigma_w = 0.1$  S/m. In the absence of the wall the transmission coefficient was 1 and reflection coefficient was 0. Figure 6.6 illustrates the validation and indicates the attenuation of signal at every point through the propagating medium. It indicates that there is about 16dB (15% of transmitted signal power) attenuation in transmitted signal on the back end of the wall and incurs around 24 dB of attenuation (60% of transmitted signal power) after reflection from the target. The total received signal at the receiver after its propagation through the wall is found to have 43dB of attenuation (99% of transmitted signal power) indicating huge data loss and reconstructing images with such minimal information poses a big challenge.



**Figure 6. 6: Signal Transmission Losses in TWI Systems**

#### 6.4 Wave Propagation in Medium

A pictorial representation of the TWI system from wall and object modelling perspectives is depicted in Figure 6.7. Using the 2D beam forming (steering) formulation presented in chapter 5, the outer surface of the wall nearest to the beamforming array antenna will be illuminated by choosing a range of beam steering angular coordinates  $(\theta_0, \varphi_0)$ . Keeping in view the constraints posed by linear and planar array  $\theta_0$  can be realistically varied from  $-60^\circ$  to  $+60^\circ$  and still maintaining the reasonable performance of the array antenna. However, the angular coordinates  $\varphi_0$  can be varied for arbitrary values ranging from 0 to  $360^\circ$  (valid for planar arrays only).



**Figure 6. 7: TWI Scenario**

Every beam steered through the near-field beamforming approach is directed to impinge on the outer surface of the wall and propagates along the z-direction. The incident beam impinged on the outer surface of the wall undergoes both transmission (refraction) and reflection due to change in material property of the wall (from free space to concrete). For obvious reasons, only the field transmitted through the propagation across the wall surface is considered.

The beam incident on the outer surface of the wall undergoes both the refraction and the reflection as a result of change in the material property (from free space to material medium of the wall). The outer surface of the wall means that surface of the wall which is nearer to the radar. It is the field of the refracted ray that illuminates the object behind the wall and the resulting re-radiation from the object towards the inner surface of the wall which carries information or signature of the object under consideration. The field reflected from the outer surface of the wall will not contribute to the information pertaining to the signal emanated from the object behind the wall. The computations on the magnitude of reflection coefficient at several points on the outer surface of the wall reveal that for the concrete wall with the chosen material properties described in sub section 6.3.1 varies from 0.4999 to 0.5001 at a frequency of 9.375 GHz which approximates to a return loss of about – 6 dB. One can still consider the vector summation of the field reflected from various points on the outer surface of the wall to the total field received at all the points of the receive antenna (sensor) array and it will result in an additional computational burden to the already tedious computations involved in the reconstruction of the image of the object behind the

wall. In view of the above listed reasons, the reflections from the outer surface of the wall have not been considered.

Likewise, the field reflected by the inner surface of the wall consequent to the incidence of field re radiated field by the object under test has also not been considered. The inner surface of the wall means that surface of the wall which is nearer to the object behind the wall. The amplitude of the incident field for such a reflection from the inner surface of the wall towards the object will be considerably smaller since the incident field under discussion is a result of the forward refraction from the outer to the inner surface of the wall followed by the propagation of the refracted field through the medium existing between the inner surface of the wall and the object (target). As a consequence, it is reasonable to assume that the amplitude of the field radiated by the object which is incident on the inner surface of the wall will be significantly lower than the amplitude of the signal from the array that directly illuminates the outer surface of the wall. Therefore secondary reflection from the inner surface of the wall towards the object has also not been included in the analysis of reconstruction of the image behind a wall.

However, the analysis of the influence of the field reflected by the outer surface of the wall and the effect of the inclusion of the secondary reflection from the inner surface on the final result of reconstruction of image of the object behind the wall has been listed as a topic for further research.

#### **6.4.1 Computation of Incident Field on the Outer surface of the Wall**

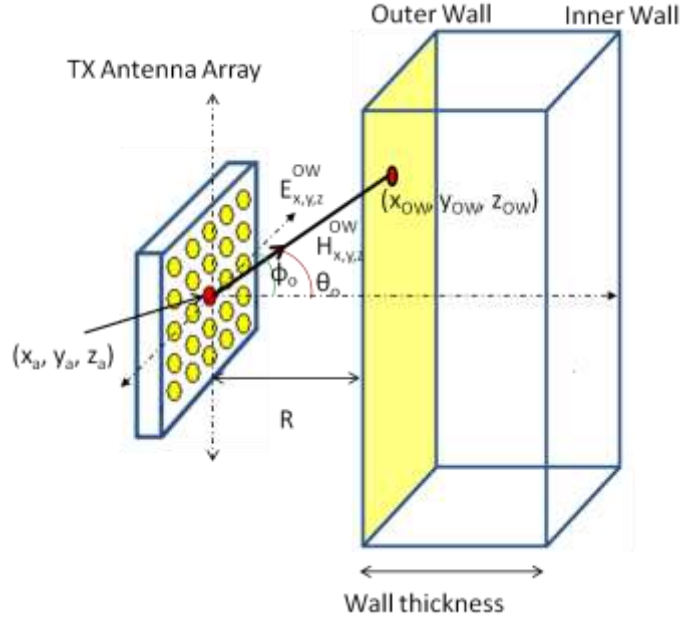
Figure 6.8 demonstrates the computation of incident field on the outer surface of the wall. The term “outer surface” refers to that side of the wall which is not only parallel to the aperture of the Beamforming array but also is facing it directly. The outer surface of the wall is discretized into very fine grids and the co ordinates of a generic point on the outer surface of the wall are denoted by  $(x_{OW}(i, j), y_{OW}(i, j), z_{OW}(i, j))$

Where

$$i=1,2,\dots, m$$

$$j=1,2,\dots, n$$

m and n being the indices of the grid along X- axis and Y –axis respectively.



**Figure 6. 8: Wave Incident on the Outer Surface of Wall**

On the assumption that outer surface of the wall is flat and is located at a distance ‘R’ from the aperture plane of the array, then  $z_{OW}(i,j) = R$ . Since there are  $m \times n$  points on the outer surface of the wall, in a spherical co-ordinate system representation, the position vector of a point on the outer surface can be denoted by  $(r(i, j), \theta(i, j), \phi(i, j))$  with respect to the centre of the array which serves as origin of the coordinate system.

$$r(i, j) = \sqrt{(x_{OW}(i, j))^2 + (y_{OW}(i, j))^2 + (z_{OW}(i, j))^2} \quad \dots(6.5)$$

$$(\theta(i, j)) = \cos^{-1} \left( \frac{(z_{OW}(i, j))}{(r(i, j))} \right) \quad \dots(6.6)$$

$$(\phi(i, j)) = \tan^{-1} \left( \frac{(y_{OW}(i, j))}{(x_{OW}(i, j))} \right) \quad \dots(6.7)$$

Each grid point on the outer surface of the wall corresponds to a particular value of  $\theta$  and  $\phi$ . Each combination of  $\theta$  and  $\phi$  serves as a beam steering or beamforming or beam scan angle  $(\theta_0, \phi_0)$ .

Therefore ( $m \times n = N$ ) number of beam scans are required to ensure that beamforming array directs its main beam to every grid point on the outer surface of the wall at least once. The

individual beam scan or beam steering angles are denoted by  $(\theta_0(I), \varphi_0(I))$ , where I stands I<sup>th</sup> beam scan with I varying from 1 to N.

For a given beam steering angle  $(\theta_0(I), \varphi_0(I))$ , near field radiation patterns  $(E_\theta^{NF}, E_\varphi^{NF})$  incident on all the grid points  $(x_{OW}(i, j), y_{OW}(i, j), z_{OW}(i, j))$  are computed using the equations (5.16) and (5.17) of Chapter 5 with  $RNF=r(i, j)$ ;  $\theta=\theta(i, j)$ ;  $\varphi=\varphi(i, j)$ ;  $\theta_0 = \theta_0(I)$ ;  $\varphi_0=\varphi_0(I)$ . Similarly  $(H_\theta^{NF}, H_\varphi^{NF})$  can also be determined using expressions analogous to equations (5.16) and (5.17). It is pertinent to point out that the near field radiation patterns of individual elements  $(E_\theta^{NF}, E_\varphi^{NF}, H_\theta^{NF}, H_\varphi^{NF})$  can be derived through the equations (4.56) to (4.59) of chapter 4. The Cartesian components of the E and H field incident on any point outer surface of the wall can be obtained as:

$$E_x^{OW}(x_{OW}, y_{OW}, z_{OW}, \theta_0(I), \varphi_0(I)) = E_\theta^{WG} \cos \theta(i, j) \cos \varphi(i, j) - E_\varphi^{WG} \sin \varphi(i, j) \quad \dots(6.8)$$

$$E_y^{OW}(x_{OW}, y_{OW}, z_{OW}, \theta_0(I), \varphi_0(I)) = E_\theta^{WG} \cos \theta(i, j) \sin \varphi(i, j) + E_\varphi^{WG} \cos \varphi(i, j) \quad \dots(6.9)$$

$$E_z^{OW}(x_{OW}, y_{OW}, z_{OW}, \theta_0(I), \varphi_0(I)) = -E_\theta^{WG} \sin \theta(i, j) \quad \dots(6.10)$$

$$H_x^{OW}(x_{OW}, y_{OW}, z_{OW}, \theta_0(I), \varphi_0(I)) = H_\theta^{WG} \cos \theta(i, j) \cos \varphi(i, j) - H_\varphi^{WG} \sin \varphi(i, j) \quad \dots(6.11)$$

$$H_y^{OW}(x_{OW}, y_{OW}, z_{OW}, \theta_0(I), \varphi_0(I)) = H_\theta^{WG} \cos \theta(i, j) \sin \varphi(i, j) + H_\varphi^{WG} \cos \varphi(i, j) \quad \dots(6.12)$$

$$H_z^{OW}(x_{OW}, y_{OW}, z_{OW}, \theta_0(I), \varphi_0(I)) = -H_\theta^{WG} \sin \theta(i, j) \quad \dots(6.13)$$

The incidence angle of the steered beam impinged on a point on the outer surface of the wall is given by (Kraus J.D. and Fleisch D.A., 1999)

$$\theta_{incident}(i, j) = \cos^{-1} \frac{z_{OW}(i, j)}{r(i, j)} \quad \dots(6.14)$$

#### 6.4.2 Wave Propagation through the Wall

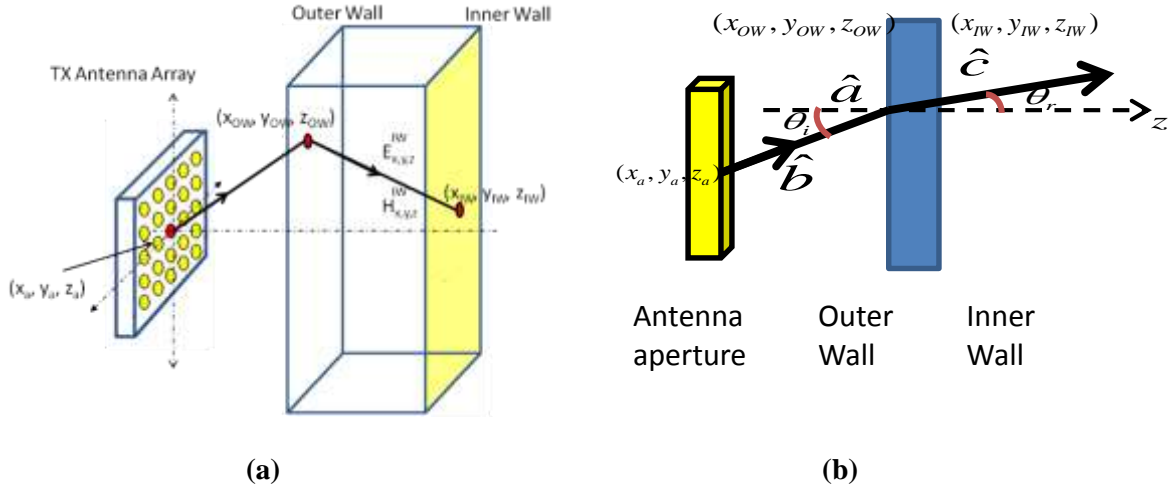
The incident wave with fields  $E_x^{OW}, E_y^{OW}, E_z^{OW}, H_x^{OW}, H_y^{OW}$  and  $H_z^{OW}$  traces a path through the wall undergoing refraction due to change in the refractive index of the mediums and hence it is appropriate to define the transmitted angle using the Snell's law. The propagating signal changes its direction as shown in Figure 6.9. The angle of refraction is calculated by Snell's law and is given by (Kraus J.D. and Fleisch D.A., 1999)

$$\theta_{refracted} = \sin^{-1} \sqrt{\frac{\epsilon_1 \mu_1}{\epsilon_2 \mu_2}} \sin \theta_{incident} \quad \dots(6.15)$$

where  $\theta_{incident}$  is the incident angle

$\mu_1$  and  $\epsilon_1$  are permeability and permittivity of free space

$\mu_2$  and  $\epsilon_2$  are permeability and permittivity of wall



**Figure 6. 9: Wave Propagation Through the Wall**

As illustrated in the Figure 6.9(a), the path traced by the incident wave after its incidence on the outer surface of the wall shows the change in direction. The coordinates of a point of incident ray on the outer surface (closest to Array) and the coordinates of the refracted (transmitted) ray on the inner surface (closer to the target/object) are different. The coordinates of the refracted ray are determined by the well-known criterion in Optics namely the incident ray, the refracted (transmitted) ray and the normal to surface at the point of incidence should lie on the same plane.

$$\hat{a} \cdot \hat{b} \times \hat{c} = 0 \quad \dots(6.16)$$

$$\hat{a} \cdot \hat{b} \times \hat{c} = \begin{vmatrix} 0 & 0 & 1 \\ b_x & b_y & b_z \\ c_x & c_y & c_z \end{vmatrix} = 0 \quad \dots(6.17)$$



$$\hat{a} = \text{Normal} = 0 \cdot \hat{x} + 0 \cdot \hat{y} + 1 \cdot \hat{z} \quad \dots(6.18)$$

$$\hat{b} = \text{Incident ray} = \hat{x}b_x + \hat{y}b_y + \hat{z}b_z \quad \dots(6.19)$$

$$\hat{c} = \text{Refracted ray} = \hat{x}r_{ftx} + \hat{y}r_{fty} + \hat{z}r_{ftz} \quad \dots(6.20)$$

$$\hat{b}_x = (x_{OW} - x_a) \quad \dots(6.21)$$

$$\hat{b}_y = (y_{OW} - y_a) \quad \dots(6.22)$$

$$\hat{b}_z = (z_{OW} - z_a) \dots \quad \dots(6.23)$$

$$r_{ftx} = (x_{IW} - x_{OW}) \quad \dots(6.24)$$

$$r_{fty} = (y_{IW} - y_{OW}) \quad \dots(6.25)$$

$$r_{ftz} = (z_{IW} - z_{OW}) \dots \quad \dots(6.26)$$

where  $(x_a, y_a, z_a)$  are co ordinates of the source;  $(x_{IW}, y_{IW}, z_{IW})$  are co ordinates on the inner surface of the wall from where the refracted ray emerges from the Inner surface of the wall. Alternatively using the ray tracing shown in Figure 6.9(b)  $(x_{IW}, y_{IW})$  are calculated through equations (6.27) and (6.28)

$$x_{IW} = \sqrt{\frac{z_{wall}^2 (x_{OW} - x_a)^2 \tan^2 \theta_i}{(x_{OW} - x_a)^2 + (y_{OW} - y_a)^2}} + y_{OW} \quad \dots(6.27)$$

$$y_{IW} = \sqrt{\frac{z_{wall}^2 (y_{OW} - y_a)^2 \tan^2 \theta_i}{(x_{OW} - x_a)^2 + (y_{OW} - y_a)^2}} + x_{OW} \quad \dots(6.28)$$

$Z_{wall}$  = Wall thickness

$z_{IW}$  = R + Wall thickness

Given a point  $(x_{OW}, y_{OW}, z_{OW})$  on the outer surface of the wall facing the array on which the steered beam is incident, the corresponding point for that beam to propagate through the wall and the point where it emerges out of the inner surface of the wall facing the object can be determined using angle of refraction. It may be of importance to state that the task of tracing the path of refracted ray within the wall has to be carried out for the field incident on the m x n grid points on the outer surface of the wall. Such of those refracted rays whose co ordinates  $(x_{IW}, y_{IW}, z_{IW})$  on

the inner surface of the wall lie outside the boundary of the inner surface of the wall are discarded for further analysis.

To compute the fields propagated through the wall, the transmission coefficient of the wall has been determined using (Kraus J.D. and Fleisch D.A., 1999). For perpendicular polarization, the transmission coefficient is given by

$$\tau_{\perp} = \frac{2Z_2 \cos \theta_{incident}}{Z_2 \cos \theta_{incident} + Z_1 \cos \theta_{refracted}} \quad \dots(6.29)$$

The transmission coefficient for parallel polarization is given by

$$\tau_{\parallel} = \frac{2Z_2 \cos \theta_{incident}}{Z_2 \cos \theta_{refracted} + Z_1 \cos \theta_{incident}} \quad \dots(6.30)$$

where,  $Z_1$  is the wave impedance of free space and  $Z_2$  is the wave impedance of medium of the wall

$$|\tau| = \sqrt{\text{Re}(\tau)^2 + \text{Im}(\tau)^2} \quad \dots(6.31)$$

$$\theta_{\tau} = \frac{\text{Im}(\tau)}{\text{Re}(\tau)}. \quad \dots(6.32)$$

$$r(t) = \frac{\text{thickness of the wall}}{\cos(\theta_t)} \quad \dots(6.33)$$

The z component of the field impinged on the outer surface of the wall is perpendicularly polarized with respect to the wall whose normal is z directed. Also, the x and y components of the field impinged on the outer surface of the wall are parallel polarized with respect to the wall.

The x,y, and z components of the field of the wave propagated through the wall and evaluated at the corresponding exiting point  $(x_{IW}, y_{IW}, z_{IW})$  on the inner surface of the wall are computed using

$$E_x^{IW}(x_{IW}, y_{IW}, z_{IW}, \theta_0(I), \varphi_0(I)) = E_{x,y,z}^{OW} |\tau_{\square}| e^{j\theta_{\tau(\square)}} e^{-jks} \quad \dots(6.34)$$

$$E_y^{IW}(x_{IW}, y_{IW}, z_{IW}, \theta_0(I), \varphi_0(I)) = E_{x,y,z}^{OW} |\tau_{\square}| e^{j\theta_{\tau(\square)}} e^{-jks} \quad \dots(6.35)$$

$$E_z^{IW}(x_{IW}, y_{IW}, z_{IW}, \theta_0(I), \varphi_0(I)) = E_{x,y,z}^{OW} |\tau_{\perp}| e^{j\theta_{\tau(\perp)}} e^{-jks} \quad \dots(6.36)$$

$$H_x^{IW}(x_{IW}, y_{IW}, z_{IW}, \theta_0(I), \varphi_0(I)) = H_{x,y,z}^{OW} |\tau_{\square}| e^{j\theta_{\tau(\square)}} e^{-jks} \quad \dots(6.37)$$

$$H_y^{IW}(x_{IW}, y_{IW}, z_{IW}, \theta_0(I), \varphi_0(I)) = H_{x,y,z}^{OW} |\tau_{\square}| e^{j\theta_{\tau(\square)}} e^{-jks} \quad \dots(6.38)$$

$$H_z^{IW}(x_{IW}, y_{IW}, z_{IW}, \theta_0(I), \varphi_0(I)) = H_{x,y,z}^{OW} |\tau_{\perp}| e^{j\theta_{\tau(\perp)}} e^{-jks} \quad \dots(6.39)$$

$$s = \sqrt{(x_{IW} - x_{OW})^2 + (y_{IW} - y_{OW})^2 + (z_{IW} - z_{OW})^2} \quad \dots(6.40)$$

$$z_{IW} = R + \text{Wall thickness} \quad \dots(6.41)$$

Where

$E_x^{OW}, E_y^{OW}, E_z^{OW}, H_x^{OW}, H_y^{OW}$  and  $H_z^{OW}$  are components of the E and H field incident on a given point on the outer surface of the wall

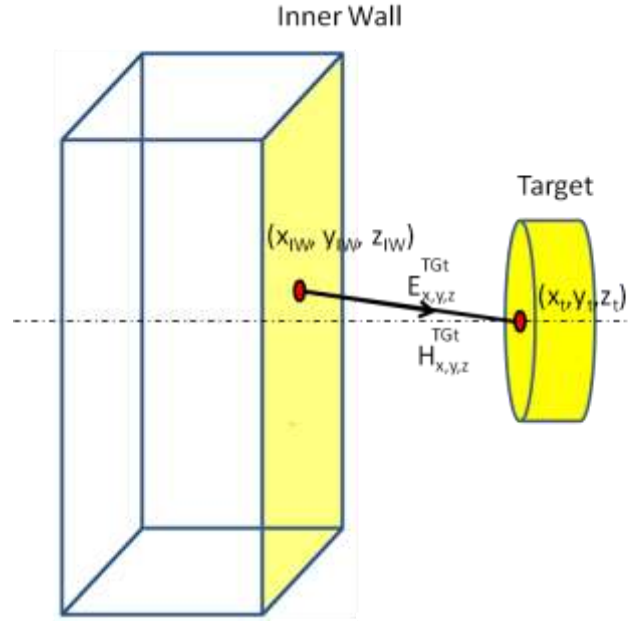
$E_x^{IW}, E_y^{IW}, E_z^{IW}, H_x^{IW}, H_y^{IW}$  and  $H_z^{IW}$  are corresponding components of the E and H field transmitted through the wall and incident on the inner surface of the wall.

$e^{j\theta_{\tau}}$  is the phase decay component due to the transmission coefficient

$e^{-jks}$  is the phase decay due to travel through the path

### 6.4.3 Computation of Field incident on the Target

Figure 6.10 illustrates the computation of field incident on the target. The Cartesian components of the transmitted field evaluated at a point on the inner surface of the wall constitute the incident field impinging on the target or object placed behind the wall.



**Figure 6. 10: Field Incident on the Target**

From the Cartesian components of the refracted (transmitted) field propagated through the wall and evaluated at a point on the inner surface of the wall, one can find the electric and magnetic currents at these points  $(x_{IW}, y_{IW}, z_{IW})$ . Each of these points constitute source points where the equivalent electric current (J) and magnetic current (M) are calculated using the expressions

$$J_{x,y,z}^{IW}(x_{IW}, y_{IW}, z_{IW}) = \hat{n}_{IW} \times H_{x,y,z}^{IW}(x_{IW}, y_{IW}, z_{IW}) \quad \dots(6.42)$$

$$M_{x,y,z}^{IW}(x_{IW}, y_{IW}, z_{IW}) = E_{x,y,z}^{IW}(x_{IW}, y_{IW}, z_{IW}) \times \hat{n}_{IW} \quad \dots(6.43)$$

Where  $\hat{n}$  is the outward normal to the wall (Because of the planarity of wall, the normal is Z-directed).

The current sources  $J_{x,y,z}^{IW}()$  and  $M_{x,y,z}^{IW}()$  can radiate in any direction. They are the primary sources of EM radiation to illuminate the target. One can proceed with the Physical Optics (PO) approach to find the radiated field by  $J_{x,y,z}^{IW}()$  and  $M_{x,y,z}^{IW}()$  at the finely discretized grid points on the target and thus compute radiated fields  $(E_{x,y,z}^{TGT}(), H_{x,y,z}^{TGT}())$  which constitute the field incident on the Target or the incident field on the target. The computation is carried out using the following equations:

$$E_x^{TGT}(x_{IWT}, y_{IWT}, z_{IWT}, r_{IWT}, \theta_0(I), \phi_0(I)) = J_x^{IW}(x_{IW}, y_{IW}, z_{IW})E_{xx}^{ED} + J_y^{IW}(x_{IW}, y_{IW}, z_{IW})E_{xy}^{ED} \\ + M_x^{IW}(x_{IW}, y_{IW}, z_{IW})E_{xx}^{MD} + M_y^{IW}(x_{IW}, y_{IW}, z_{IW})E_{xy}^{MD} \quad \dots(6.44)$$

$$E_y^{TGT}(x_{IWT}, y_{IWT}, z_{IWT}, r_{IWT}, \theta_0(I), \phi_0(I)) = J_x^{IW}(x_{IW}, y_{IW}, z_{IW})E_{yx}^{ED} + J_y^{IW}(x_{IW}, y_{IW}, z_{IW})E_{yy}^{ED} \\ + M_x^{IW}(x_{IW}, y_{IW}, z_{IW})E_{yx}^{MD} + M_y^{IW}(x_{IW}, y_{IW}, z_{IW})E_{yy}^{MD} \quad \dots(6.45)$$

$$E_z^{TGT}(x_{IWT}, y_{IWT}, z_{IWT}, r_{IWT}, \theta_0(I), \phi_0(I)) = J_x^{IW}(x_{IW}, y_{IW}, z_{IW})E_{zx}^{ED} + J_y^{IW}(x_{IW}, y_{IW}, z_{IW})E_{zy}^{ED} \\ + M_x^{IW}(x_{IW}, y_{IW}, z_{IW})E_{zx}^{MD} + M_y^{IW}(x_{IW}, y_{IW}, z_{IW})E_{zy}^{MD} \quad \dots(6.46)$$

$$H_x^{TGT}(x_{IWT}, y_{IWT}, z_{IWT}, r_{IWT}, \theta_0(I), \phi_0(I)) = J_x^{IW}(x_{IW}, y_{IW}, z_{IW})H_{xx}^{ED} + J_y^{IW}(x_{IW}, y_{IW}, z_{IW})H_{xy}^{ED} \\ + M_x^{IW}(x_{IW}, y_{IW}, z_{IW})H_{xx}^{MD} + M_y^{IW}(x_{IW}, y_{IW}, z_{IW})H_{xy}^{MD} \quad \dots(6.47)$$

$$H_y^{TGT}(x_{IWT}, y_{IWT}, z_{IWT}, r_{IWT}, \theta_0(I), \phi_0(I)) = J_x^{IW}(x_{IW}, y_{IW}, z_{IW})H_{yx}^{ED} + J_y^{IW}(x_{IW}, y_{IW}, z_{IW})H_{yy}^{ED} \\ + M_x^{IW}(x_{IW}, y_{IW}, z_{IW})H_{yx}^{MD} + M_y^{IW}(x_{IW}, y_{IW}, z_{IW})H_{yy}^{MD} \quad \dots(6.48)$$

$$H_z^{TGT}(x_{IWT}, y_{IWT}, z_{IWT}, r_{IWT}, \theta_0(I), \phi_0(I)) = J_x^{IW}(x_{IW}, y_{IW}, z_{IW})H_{zx}^{ED} + J_y^{IW}(x_{IW}, y_{IW}, z_{IW})H_{zy}^{ED} \\ + M_x^{IW}(x_{IW}, y_{IW}, z_{IW})H_{zx}^{MD} + M_y^{IW}(x_{IW}, y_{IW}, z_{IW})H_{zy}^{MD} \quad \dots(6.49)$$

where

$$x_{IWT} = x_T - x_{IW}$$

$$y_{IWT} = y_T - y_{IW}$$

$$z_{IWT} = z_T - z_{IW} \quad \dots(6.50)$$

$$r_{IWT} = \sqrt{(x_{IWT}^2 + y_{IWT}^2 + z_{IWT}^2)} \quad \dots(6.51)$$

$$J_{x,y,z}^{TGT}(x_t, y_t, z_t) = \hat{n}_{\text{target}} \times H_{x,y,z}^{TGT}(x_t, y_t, z_t) \quad \dots(6.52)$$

$$M_{x,y,z}^{TGT}(x_t, y_t, z_t) = E_{x,y,z}^{TGT}(x_t, y_t, z_t) \times \hat{n}_{\text{target}} \quad \dots(6.53)$$

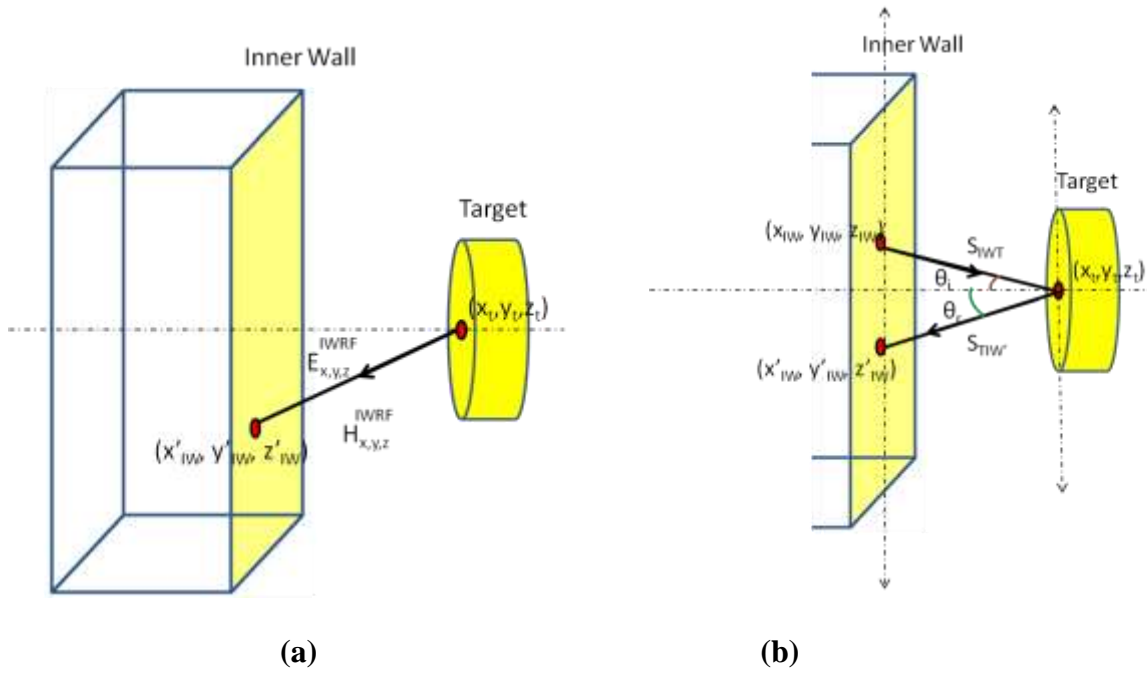
where  $\hat{n}$  is the outward normal to the target. The terms

$$E_{xx}^{ED}(\cdot), E_{yx}^{ED}(\cdot), E_{zx}^{ED}(\cdot), H_{xx}^{ED}(\cdot), H_{yx}^{ED}(\cdot) \text{ and } H_{zx}^{ED}(\cdot)$$

$$E_{xx}^{MD}(\cdot), E_{yx}^{MD}(\cdot), E_{zx}^{MD}(\cdot), H_{xx}^{MD}(\cdot), H_{yx}^{MD}(\cdot) \text{ and } H_{zx}^{MD}(\cdot) \text{ etc., are calculated using the}$$

pertinent equations explained in section 4.2 of Chapter 4 of the thesis.

From the knowledge of  $(E_{x,y,z}^{TGT}(), H_{x,y,z}^{TGT}())$  the equivalent currents  $J_{x,y,z}^{TGT}()$  and  $M_{x,y,z}^{TGT}()$  on the surface of the target can be determined. The E and H fields radiated by  $J_{x,y,z}^{TGT}()$  and  $M_{x,y,z}^{TGT}()$  have to be evaluated on the inner surface of the wall which has to be discretized into fine grids (Similar or identical in size of  $m \times n$  grid points on the outer surface of the wall). The resulting E and H fields on the inner surface of the wall due to current sources  $J_{x,y,z}^{TGT}()$  and  $M_{x,y,z}^{TGT}()$  on the target are denoted by  $(E_{x,y,z}^{IWRF}(), H_{x,y,z}^{IWRF}())$  as shown in Figure 6.11.



**Figure 6. 11: Field Reflected from the Target to the Inner Surface of the Wall**

The computational burden to determine the fields  $(E_{x,y,z}^{IWRF}(), H_{x,y,z}^{IWRF}())$  at closely spaced grid points  $(x'_{IW}, y'_{IW}, z'_{IW})$  on the Inner surface of the wall is prohibitively enormous. To overcome this rather computationally tedious but straight forward approach, a novel scheme which employs the hybrid combination of Geometrical Optics (Ray Technique) and Physical Optics has been arrived at. The proposed hybrid scheme is based on the following significant points.

1. For a given source point  $(x_{IW}, y_{IW}, z_{IW})$  of currents  $J_{x,y,z}^{IW}()$  and  $M_{x,y,z}^{IW}()$  on the inner surface of the wall, Snell's is first applied to search a point of reflection on the target with co ordinates  $(x_t, y_t, z_t)$  such that it results in a reflected ray crossing the inner surface of the wall.
2. If the search is successful and the resulting reflected ray intersects the inner surface of the wall at  $(x'_{IW}, y'_{IW}, z'_{IW})$  then the field components of the incident ray at  $(x_t, y_t, z_t)$  originating from  $(x_{IW}, y_{IW}, z_{IW})$  are computed with the knowledge of  $J_{x,y,z}^{IW}()$  and  $M_{x,y,z}^{IW}()$ .
3. For a given source point  $(x_{IW}, y_{IW}, z_{IW})$ , if the search does not result in a point of reflection on the target  $(x_t, y_t, z_t)$  leading to the reflected ray lying outside the contour of the inner surface of the wall, then the contribution of that point on the target to the reflected field on the inner surface of the wall is discarded.
4. Since the co ordinates of the reflected ray  $(x'_{IW}, y'_{IW}, z'_{IW})$  on the inner surface of the wall corresponding to a source point  $(x_{IW}, y_{IW}, z_{IW})$  are known, the components of the reflected field can be determined employing the concept of reflection coefficient.

The components of the field reflected by a point  $(x_t, y_t, z_t)$  on target (object) at an observation (field) point  $(x'_{IW}, y'_{IW}, z'_{IW})$  are given by

$$E_x^{IWRF} \left( x'_{IW}, y'_{IW}, z'_{IW}, \theta_0(I), \phi_0(I) \right) = E_x^{TGT} \left| \rho_{\square TIW} \right| e^{j\theta_{\rho(\square)}} e^{-jks_r} \quad \dots(6.54)$$

$$E_y^{IWRF} \left( x'_{IW}, y'_{IW}, z'_{IW}, \theta_0(I), \phi_0(I) \right) = E_y^{TGT} \left| \rho_{\square TIW} \right| e^{j\theta_{\rho(\square)}} e^{-jks_r} \quad \dots(6.55)$$

$$E_z^{IWRF} \left( x'_{IW}, y'_{IW}, z'_{IW}, \theta_0(I), \phi_0(I) \right) = E_z^{TGT} \left| \rho_{\perp TIW} \right| e^{j\theta_{\rho(\perp)}} e^{-jks_r} \quad \dots(6.56)$$

$$H_x^{IWRF} \left( x'_{IW}, y'_{IW}, z'_{IW}, \theta_0(I), \phi_0(I) \right) = H_x^{TGT} \left| \rho_{\square TIW} \right| e^{j\theta_{\rho(\square)}} e^{-jks_r} \quad \dots(6.57)$$

$$H_y^{IWRF} \left( x'_{IW}, y'_{IW}, z'_{IW}, \theta_0(I), \phi_0(I) \right) = H_y^{TGT} \left| \rho_{\square TIW} \right| e^{j\theta_{\rho(\square)}} e^{-jks_r} \quad \dots(6.58)$$

$$H_z^{IWRF} \left( x'_{IW}, y'_{IW}, z'_{IW}, \theta_0(I), \phi_0(I) \right) = H_z^{TGT} \left| \rho_{\perp TIW} \right| e^{j\theta_{\rho(\perp)}} e^{-jks_r} \quad \dots(6.59)$$

$$s_r = \sqrt{\left(x'_{IW} - x_t\right)^2 + \left(y'_{IW} - y_t\right)^2 + \left(z'_{IW} - z_t\right)^2} \quad \dots(6.60)$$

To compute the fields reflected by the object, the reflection coefficient of the object has been determined using equations (6.61) and (6.62) (Kraus J.D. and Fleisch D.A., 1999).

$$\rho_{\perp TIW} = \frac{Z_2 \cos \theta_i - Z_1 \cos \theta_r}{Z_2 \cos \theta_i + Z_1 \cos \theta_r} \quad \dots(6.61)$$

$$\rho_{\parallel TIW} = \frac{Z_2 \cos \theta_r - Z_1 \cos \theta_i}{Z_1 \cos \theta_i + Z_2 \cos \theta_r} \quad \dots(6.62)$$

$$|\rho| = \sqrt{\text{Re}(\tau)^2 + \text{Im}(\tau)^2} \quad \dots(6.63)$$

$$\theta_\rho = \frac{\text{Im}(\rho)}{\text{Re}(\rho)}. \quad \dots(6.64)$$

In Equations (6.61-6.62),  $Z_1$  is the wave impedance of free space and  $Z_2$  is the wave impedance of target. The z component of the field incident on the target is perpendicularly polarized with respect to target whose normal is z directed. Also, the x and y components of the field impinged on the target are parallel polarized with respect to the target.

$\theta_i$  and  $\theta_r$  in equation (6.61-6.62) are computed applying Snell's law of reflection and using the co-ordinates of the points on the:

inner wall ( $x_{IW}, y_{IW}, z_{IW}$ )

target ( $x_t, y_t, z_t$ )

inner wall ( $x'_{IW}, y'_{IW}, z'_{IW}$ )

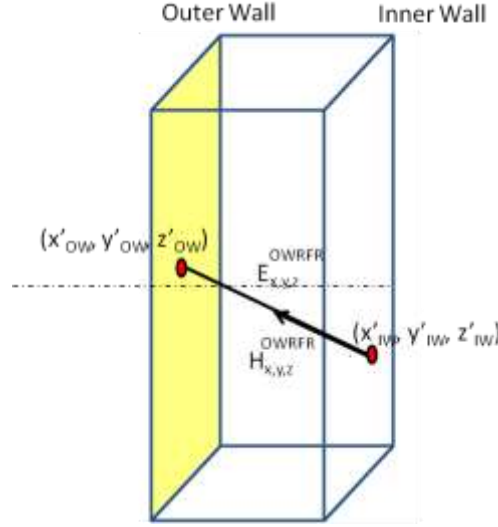
normal at ( $x_t, y_t, z_t$ )

In Figure 6.11 (b)  $S_{IWT}$  is the incident ray and  $S_{TIW}$  is the reflected ray.

#### 6.4.4 Refraction of the Field Reflected by the Target

The E and H fields  $E_{x,y,z}^{IWRf}()$  and  $H_{x,y,z}^{IWRf}()$  reflected by a point ( $x_t, y_t, z_t$ ) on the object and incident on the inner surface of the wall at ( $x'_{IW}, y'_{IW}, z'_{IW}$ ) undergo the refraction and propagate through the wall to emerge out of the outer surface of the wall through a point ( $x'_{OW}, y'_{OW}, z'_{OW}$ ) as shown in Figure 6.12.





**Figure 6. 12: Wave Refracted through the Wall**

The analysis presented in section 6.4.3 can be extended to treat this refraction leading to the wave propagation back towards the beamforming array. The fields  $E_{x,y,z}^{IWRFR}()$  and  $H_{x,y,z}^{IWRFR}()$  upon refraction from a point  $(x'_{IW}, y'_{IW}, z'_{IW})$  on inner surface of the wall to a point  $(x'_{OW}, y'_{OW}, z'_{OW})$  are respectively designated as  $E_{x,y,z}^{IWRFR}()$  and  $H_{x,y,z}^{IWRFR}()$ .

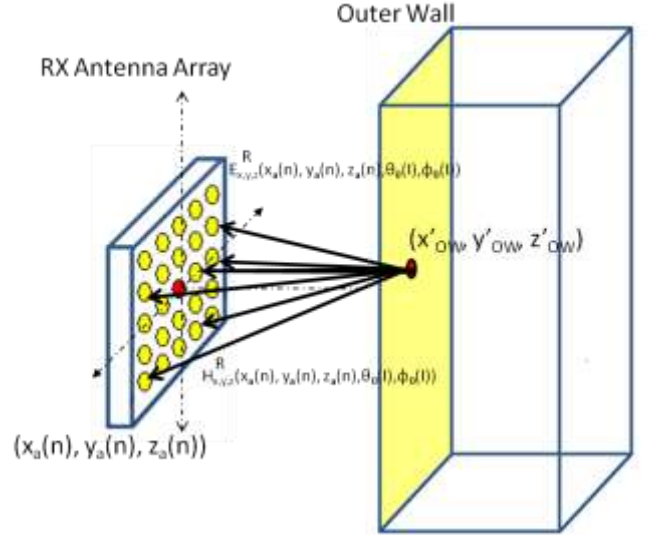
At a point  $(x'_{OW}, y'_{OW}, z'_{OW})$ , the equivalent electric current  $J^R(x'_{OW}, y'_{OW}, z'_{OW})$  and magnetic current  $M^R(x'_{OW}, y'_{OW}, z'_{OW})$  can be calculated.

$$J_{x,y,z}^R(x'_{OW}, y'_{OW}, z'_{OW}) = \hat{n} \times H_{x,y,z}^{IWRFR}(x'_{OW}, y'_{OW}, z'_{OW}) \quad \dots(6.65)$$

$$M_{x,y,z}^R(x'_{OW}, y'_{OW}, z'_{OW}) = E_{x,y,z}^{IWRFR}(x'_{OW}, y'_{OW}, z'_{OW}) \times \hat{n} \quad \dots(6.66)$$

#### 6.4.5 Computation of the Field at the Receiver Array:

The antenna elements arranged in the form of a planar array serve as receive elements. The receiver corresponds to the points on planar array which capture the intensity of the E and H fields needed to form an image. The field at each receiver point relates to a pixel in the image. The centers of radiating aperture of the array elements form an array of field or observation points to capture the E- field and H- fields radiated by the number of current sources  $J^R(x'_{OW}, y'_{OW}, z'_{OW})$  and  $M^R(x'_{OW}, y'_{OW}, z'_{OW})$  located on the outer surface of the wall as shown in Figure 6.13.



**Figure 6. 13: Field Incident on the Receiver**

It is pertinent to point out that the number and the location of current sources  $J^R$  and  $M^R$  on the outer surface of the wall depend upon the:

1. Size thickness and material property of the wall
2. Distance of separation between the aperture of the array and the outer surface of the wall
3. Separation distance between the inner surface of the wall and the target behind the wall
4. Size, shape as well as the material property of the target

The amplitude and Phase of the E- and H- Fields received by the various receive elements or sensors are influenced by the above cited parameters. In addition, the more direct and active parameters that influence the received fields are the Beam steering or Beam forming or Beam scan angles as well as the frequency of operation.

The fields radiated by  $u^{\text{th}}$  current sources  $J^R$  and  $M^R$  located at  $(x'_{OW}(u), y'_{OW}(u), z'_{OW}(u))$  are computed at  $v^{\text{th}}$  receiver with its aperture center located at  $(x_a(v), y_a(v), z_a(v))$

$$\begin{aligned}
E_x^R(x(uv), y(uv), z(uv), r(uv), \theta_0(I), \varphi_0(I)) &= J_x^R(x'_{ow}(u), y'_{ow}(u), z'_{ow}(u))E_{xx}^{ED} \\
&\quad + J_y^R(x'_{ow}(u), y'_{ow}(u), z'_{ow}(u))E_{xy}^{ED} \\
&\quad + M_x^R(x'_{ow}(u), y'_{ow}(u), z'_{ow}(u))E_{xx}^{MD} \\
&\quad + M_y^R(x'_{ow}(u), y'_{ow}(u), z'_{ow}(u))E_{xy}^{MD} \quad \dots(6.67)
\end{aligned}$$

$$\begin{aligned}
E_y^R(x(uv), y(uv), z(uv), r(uv), \theta_0(I), \varphi_0(I)) &= J_x^R(x'_{ow}(u), y'_{ow}(u), z'_{ow}(u))E_{yx}^{ED} \\
&\quad + J_y^R(x'_{ow}(u), y'_{ow}(u), z'_{ow}(u))E_{yy}^{ED} \\
&\quad + M_x^R(x'_{ow}(u), y'_{ow}(u), z'_{ow}(u))E_{yx}^{MD} \\
&\quad + M_y^R(x'_{ow}(u), y'_{ow}(u), z'_{ow}(u))E_{yy}^{MD} \quad \dots(6.68)
\end{aligned}$$

$$\begin{aligned}
E_z^R(x(uv), y(uv), z(uv), r(uv), \theta_0(I), \varphi_0(I)) &= J_x^R(x'_{ow}(u), y'_{ow}(u), z'_{ow}(u))E_{zx}^{ED} \\
&\quad + J_y^R(x'_{ow}(u), y'_{ow}(u), z'_{ow}(u))E_{zy}^{ED} \\
&\quad + M_x^R(x'_{ow}(u), y'_{ow}(u), z'_{ow}(u))E_{zx}^{MD} \\
&\quad + M_y^R(x'_{ow}(u), y'_{ow}(u), z'_{ow}(u))E_{zy}^{MD} \quad \dots(6.69)
\end{aligned}$$

$$\begin{aligned}
H_x^R(x(uv), y(uv), z(uv), r(uv), \theta_0(I), \varphi_0(I)) &= J_x^R(x'_{ow}(u), y'_{ow}(u), z'_{ow}(u))H_{xx}^{ED} \\
&\quad + J_y^R(x'_{ow}(u), y'_{ow}(u), z'_{ow}(u))H_{xy}^{ED} \\
&\quad + M_x^R(x'_{ow}(u), y'_{ow}(u), z'_{ow}(u))H_{xx}^{MD} \\
&\quad + M_y^R(x'_{ow}(u), y'_{ow}(u), z'_{ow}(u))H_{xy}^{MD} \quad \dots(6.70)
\end{aligned}$$

$$\begin{aligned}
H_y^R(x(uv), y(uv), z(uv), r(uv), \theta_0(I), \varphi_0(I)) &= J_x^R(x'_{ow}(u), y'_{ow}(u), z'_{ow}(u))H_{yx}^{ED} \\
&\quad + J_y^R(x'_{ow}(u), y'_{ow}(u), z'_{ow}(u))H_{yy}^{ED} \\
&\quad + M_x^R(x'_{ow}(u), y'_{ow}(u), z'_{ow}(u))H_{yx}^{MD} \\
&\quad + M_y^R(x'_{ow}(u), y'_{ow}(u), z'_{ow}(u))H_{yy}^{MD} \quad \dots(6.71)
\end{aligned}$$

$$\begin{aligned}
H_z^R(x(uv), y(uv), z(uv), r(uv), \theta_0(I), \varphi_0(I)) &= J_x^R(x'_{ow}(u), y'_{ow}(u), z'_{ow}(u))H_{zx}^{ED} \\
&\quad + J_y^R(x'_{ow}(u), y'_{ow}(u), z'_{ow}(u))H_{zy}^{ED} \\
&\quad + M_x^R(x'_{ow}(u), y'_{ow}(u), z'_{ow}(u))H_{zx}^{MD} \\
&\quad + M_y^R(x'_{ow}(u), y'_{ow}(u), z'_{ow}(u))H_{zy}^{MD} \quad \dots(6.72)
\end{aligned}$$

$$x(uv) = x_a(v) - x'_{ow}(u) \quad \dots(6.73)$$

$$y(uv) = y_a(v) - y'_{ow}(u) \quad \dots(6.74)$$

$$z(uv) = z_a(v) - z'_{ow}(u) \quad \dots(6.75)$$

$$r(uv) = \sqrt{x^2(uv) + y^2(uv) + z^2(uv)} \quad \dots(6.76)$$

If there are Q number of current sources on the outer surface of the wall after refraction of the field reflected by the target, then the components of the total E and H field received by the  $j^{\text{th}}$  receive element due to  $I^{\text{th}}$  beam scan or beam steering angle are given by

$$E_{x,y,z}^{TR} (v, \theta_0(I), \varphi_0(I)) = \sum_{u=1}^{u=Q} E_{x,y,z}^R (x(uv), y(uv), z(uv), r(uv), \theta_0(I), \varphi_0(I)) \quad \dots(6.77)$$

$$H_{x,y,z}^{TR} (v, \theta_0(I), \varphi_0(I)) = \sum_{u=1}^{u=Q} H_{x,y,z}^R (x(uv), y(uv), z(uv), r(uv), \theta_0(I), \varphi_0(I)) \quad \dots(6.78)$$

For Imaging the object behind the wall, for every beam scan ( $I=1, 2, \dots, N$ ), there will be data from ‘NR’ number of receive elements ( $v=1.2, \dots, NR$ ) for a given frequency. If ‘NF’ is the total number of frequencies for which data is collected at the receive elements, then for each component of E and H of equation (6.77) and (6.78), in all there will  $N \times NR \times NF$  data available for formation of Image.

## 6.5 Image Processing

In this thesis, an imaging methodology that involves Image fusion and Registration is adopted. The received fields for multiple beam steering angles ( $\theta_0(I), \varphi_0(I)$ ) ( $I=1, \dots, N$ ) are fused using Laplacian Pyramid image fusion technique and it provides a composite image. The elements of the planar array act as both receiver and transmitter of the TWI system. To realize finer illumination of the object behind the wall, the beam steering angles  $\varphi_0(I)$  and  $\theta_0(I)$  are computed at the vertices of very fine grids on the outer surface of the wall. The transmitting beam forming array scans the object behind the wall with all possible combinations of beam steering angles  $\varphi_0(I)$  and  $\theta_0(I)$ . The fields at all the receiver array points corresponding to given values of scanned  $\varphi_0(I)$  and  $\theta_0(I)$  are stacked accordingly. Hence the image reconstructed will be a skewed version of the object. High amplitudes of received (return) signal conclude the presence of an object behind the wall and low amplitudes indicate the absence. Imaging is performed through translation and fusion.

For TWI system, Discrete Fourier Transform (DFT) Registration is best suited for translation since the algorithm works on spatial frequency. Multiple translated images are fused using Laplacian Pyramid Image Fusion to obtain the composite image.

The image registration algorithms highlight the perfect contours of an object behind the wall. These algorithms can be used to correct the skewed version of the Image by reconstructing a

translated version of the actual scene. (Sicairos M.G. *et al*, 2008) suggest that DFT based registration methods are best suited for translation since the algorithm works on spatial frequency of the image which is faster compared to other techniques. The following sections explain both the registration and fusion methods employed for processing the images.

#### **6.5.1 DFT Image Registration**

Image translation is a part of registration and the 2D translation image registration developed by (Sicairos M.G. *et al*, 2008) uses a small fraction of pixels on given image and uses nonlinear optimization. The algorithm uses the spatial frequency of the image to perform registration. The Fourier transform of the image yields better accuracy and faster computation. To carry out translation two consecutive frames obtained for two consecutive beam steering angles are considered. The Fourier transforms of both images (reference frame and next frame) are computed. The spatial frequency of both images is cross-correlated to find the shift in pixels. The peak obtained after cross correlation signifies the amount of translation of points between the two images. The sub pixels are replaced so as to match the original image. The output of Image Registration algorithm is the translated image which later has to be fused with the several stacked frames to get a final composite image highlighting the contours of objects behind the wall. Laplacian Pyramid Image Fusion algorithm is used to obtain the composite image. The algorithmic steps of DFT registration are as follows:

The image translation can be performed with the algorithm steps as follows:

**Step 1:** Obtain Fourier Transform of the reference image

**Step 2:** Cross-correlate the spatial frequency domain

**Step 3:** Identify the peaks which indicate the frequency match

**Step 4:** Estimate the translated pixels from the peak and the center of the image

**Step 5:** Translate the pixels from the next image to the reference image depending on the translated pixels calculated in Step 4

**Step 6:** Repeat step 3 to step 5 to all rows and column of the image (spatial frequencies)

### 6.5.2 Image Fusion

Image Fusion algorithms are used to combine the features of two or more images. An image fusion comparison study carried out in (Sadjadi, 2005) visually shows that Laplacian Pyramid Image Fusion is best suited for images with contrast features. Laplacian pyramid technique is a process to decompose an image into a set of band pass filtered component images, each of which represents different spatial frequency. Laplacian pyramid technique involves a process where a given image frame is downsized to half its original size and is decomposed into a set of Gaussian band pass filtered component images, each of which represents different spatial frequencies. The decomposition is performed by filtering through a band pass filter and shrinking the image to half of its size.

A pyramid is formed by reducing the size of the original image in regular steps. The algorithm further involves inverse pyramid methodology where the decomposed images are up-scaled at each interval; the image is then interpolated to obtain an intermediate result which is again up-scaled and added to the next level of decomposed images. The process is continued until the original size of the image is obtained. The final output is the fused image (Fernández E. C., 2002). For the simulation a pyramid level 'n=3' is assumed based on visual representation obtained from combinations of various trial and error. The flowchart for Laplacian pyramid image fusion is explained through the following:

**Step 1:** A pyramid decomposition level is chosen.

**Step 2:** A Gaussian band pass filter is applied to highlight the features in the images

**Step 3:** The image is decimated to half the dimension of the actual image. (By removing alternate rows and columns)

**Step 4:** The decimated images are up-scaled, interpolated and stored.

**Step 5:** The image is again decimated and the pyramid decomposition level is decreased further

**Step 6:** Steps 2 to 5 are repeated till decomposition level is zero

**Step 7:** The average intensities of the lowest level of decomposition are considered for inverse pyramid transform

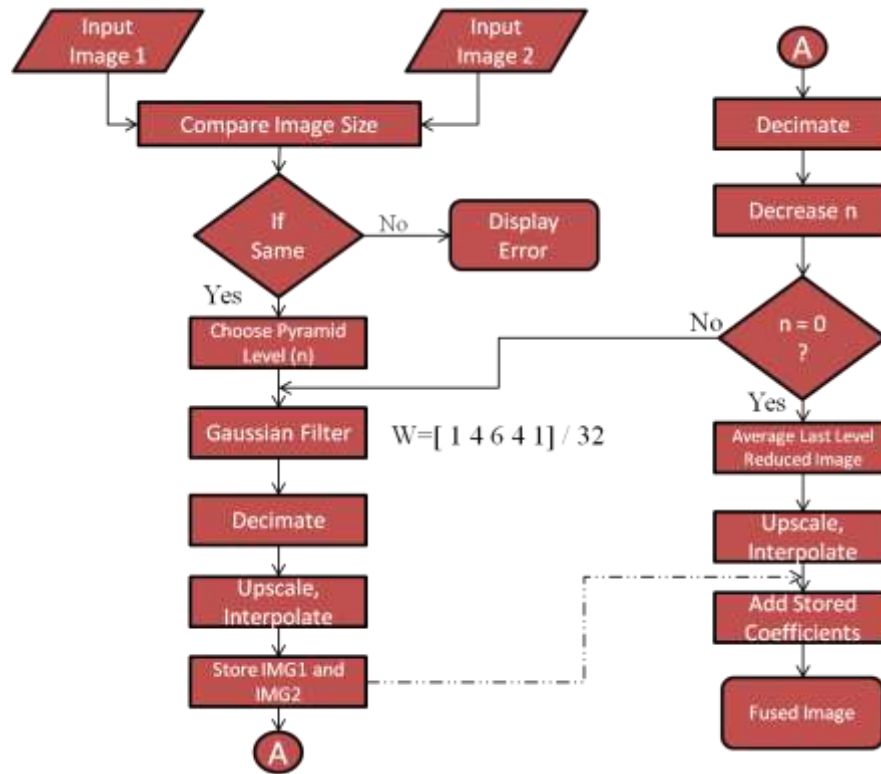
**Step 8:** The last processed image is up-scaled, interpolated and added to the subsequent stored values

Figure 6.14 provides the pictorial representation of the algorithm and Figure 6.15 illustrates the flow chart of the algorithm. The step by step description of the algorithm is also provided.

---

This item has been removed due to third party copyright. The unabridged version of the thesis can be viewed at the Lanchester Library, Coventry University.

**Figure 6. 14: Laplacian Pyramid Image Fusion Technique (Fernández E. C., 2002)**



**Figure 6. 15: Laplacian Pyramid Image Fusion Flowchart**

The flowchart of Figure 6.15 for Laplacian pyramid image fusion is explained in steps as follows:

**Step 1:** Two images of same dimensions have to be considered. If not, the algorithm gives an error

**Step 2:** Apply pyramid decomposition level ( $n=3$ ) in progressive steps of 1

**Step 3:** A Gaussian band pass filter is applied to high light the features in the images

**Step 4:** The image is decimated to half the dimension of the actual image. (*Decimate: Remove alternate rows and columns, and reduce the size by half*)

**Step 5:** The decimated images are up-scaled, interpolated and stored. (*Upscale: Zeros are added to alternate rows and columns, the size of the image is doubled; Interpolation: Average value of intensities of first and the third row or column is put in place of zeros*)

**Step 6:** Decimate the image and decrease the pyramid decomposition level ( $n$ )

**Step 7:** Repeat Step 3 to 6 till  $n=0$



**Step 8:** The average intensities of the lowest level of decomposition is considered for inverse pyramid transform

**Step 9:** The last processed image is up-scaled, interpolated and added to the subsequent stored coefficient values (Matching 'n' values)

## **6.6 Simulation Results of TWI System**

Using the analysis presented in the previous sections pertaining to the proposed near-field beamforming approach for TWI system, simulations have been carried out to substantiate the validity of simple and yet elegant new formulation of two dimensional near-field beamforming technique, the hybrid method of field-ray analysis, the accuracy of near-field radiation patterns from current and magnetic sources (point dipoles), the influence of stepped frequency in TWI system as well as the utility of concurrent applications of digital image processing techniques such as translation and fusion.

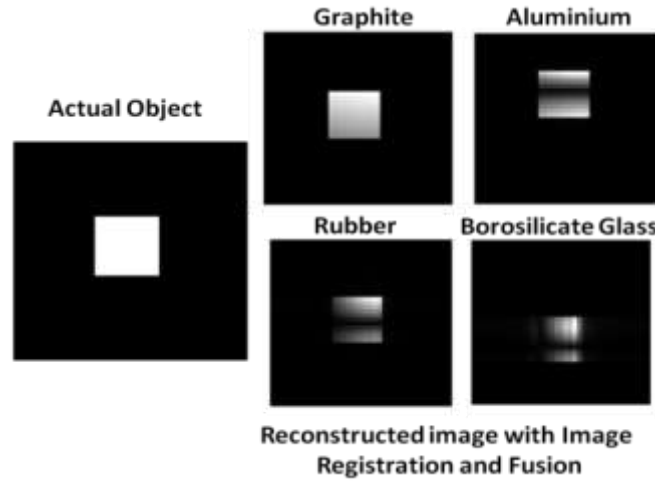
### **6.6.1 Model of Free Space**

As discussed in previous sections, electromagnetic properties of air are chosen to be  $\mu_a = 1$ ,  $\epsilon_a = 1$  and  $\sigma_a = 5.5 \text{ Sm}^{-15}$ , and for concrete wall the chosen values are  $\mu_w = 1$ ,  $\epsilon_w = 9$  and  $\sigma_w = 0.1 \text{ Sm}^{-1}$ . In order to validate the wall modelling, initially wall was also modelled as free space. The simulation results showed that the transmission coefficient was 1 and the reflection coefficient was 0 which is expected since material interface of free space to free space cannot support reflection and hence results in complete transmission. However, when the wall was modelled as a perfect conductor, the simulated results indicated the reflection coefficient to be 1 which is expected since perfect conductor offers a condition for perfect reflection and no transmission.

### **6.6.2 Reconstruction Images of Targets Modelled with different Material**

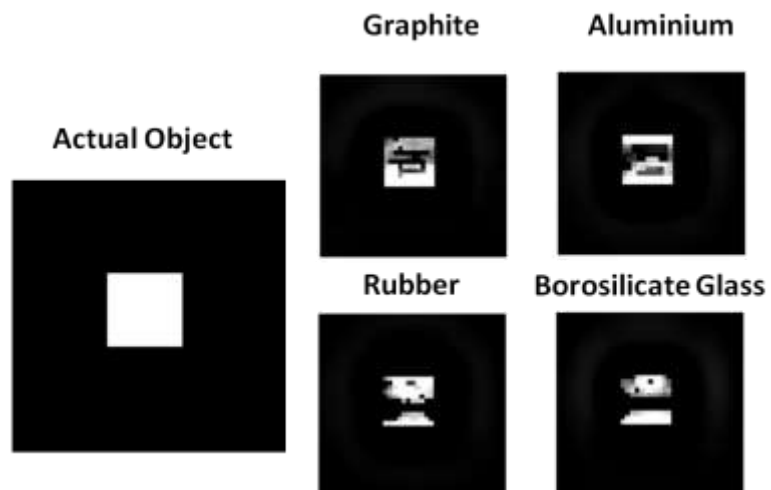
Similar to the wall modelling, the object behind the wall also is modelled with different  $\mu$ ,  $\epsilon$  and  $\sigma$  depending on the type of material. Simulations were carried out for different shapes of the object like a cross, a square and four corner blocks. The distance between the beamforming array and the wall was  $10\lambda$ . The objects were placed  $100\lambda$  away from the wall. The results in Figure 6.16 show the TWI system simulation for an object of square shape. The object was

modelled as graphite (carbon), rubber, borosilicate glass and aluminium. Their properties are as mentioned in Table 6. 4.

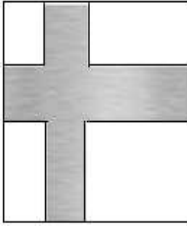



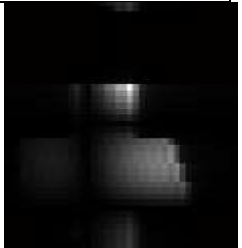

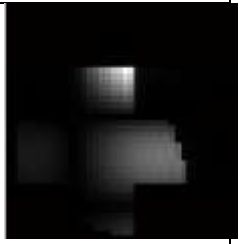



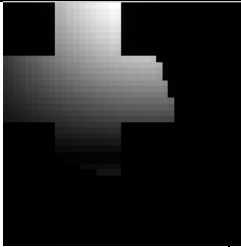
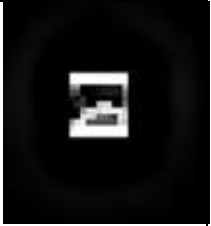
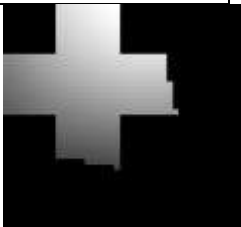
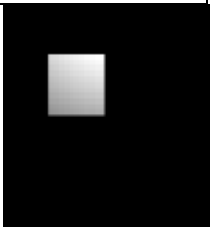
**Figure 6. 16: Reconstructed images obtained through proposed Near-Field Beamforming TWI System**

Since each image reconstructed (for a particular combination of  $\varphi_o(I)$  and  $\theta_o(I)$ ) is a skewed version of the actual object scene, image fusion alone does not help in reconstruction. Figure 6.17 demonstrates the reconstruction of image obtained for objects of different material using image fusion only. It also illustrates the importance of using registration through DFT translation. The results of Image Registration exhibit perfect outline of the shape of the object. It was also found that Image reconstructed is 81% of the actually scene (visual). The simulations carried out using the proposed near-field TWI system included the material properties of the object to treat perfect insulator, perfect conductors and non-perfect conductors. The results indicated that the proposed near-field TWI system can effectively handle the metallic and non-metallic objects behind the wall alike.



**Figure 6. 17: Reconstructed Images obtained through proposed Near-Field Beamforming TWI System using Image Fusion only**

Modelled object		Image Reconstruction	Modelled object		
	Graphite			Graphite	
	Rubber			Rubber	
	Borosilicate Glass			Borosilicate Glass	

	<b>Aluminium</b>			<b>Aluminium</b>	
	<b>Carbonyl Metal</b>			<b>Carbonyl Metal</b>	

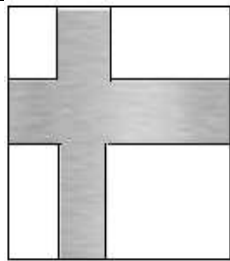

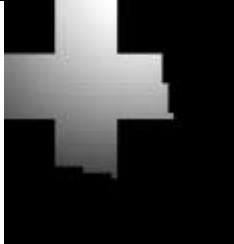


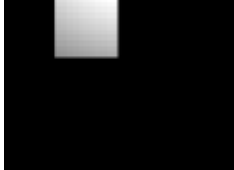
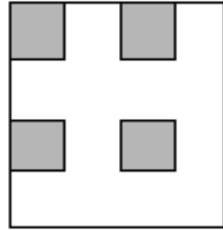
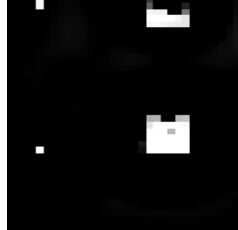
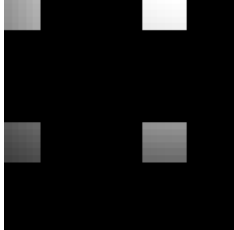
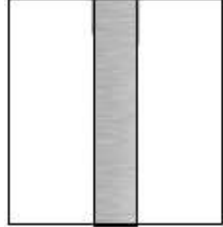
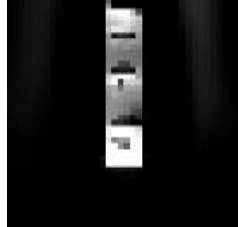
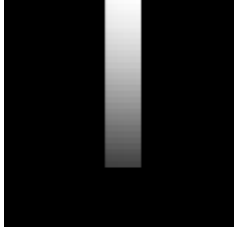
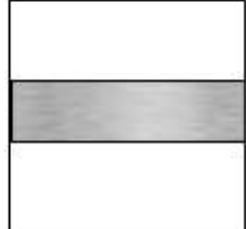
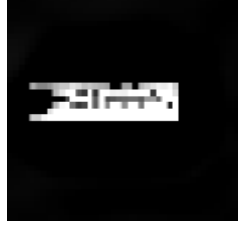
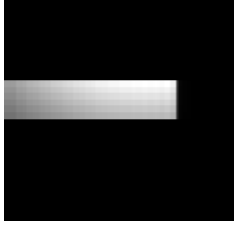
**Table 6. 2: Image Reconstruction of Objects made of Different Materials**

Table 6.3 shows the reconstruction of images of objects made of different materials. The results of table 6.3 also indicates that there is a shift in reconstruction of image of the object which may be due to the difference in reflection angles caused due to change in material properties. Carbonyl metal shows the best reconstruction visually, while the reconstructed image of Rubber and Borosilicate glass is poor. The calculated visual accuracy based on the difference in pixels with the actual scene of the image reconstruction is only 81%.

### 6.6.3 Image Reconstruction with Fusion and Translation

The fields received at the multiple receiver points after backward propagation of the scattered field of the object behind the wall are stored for different incident beam scan angles  $\varphi_o(I)$  and  $\theta_o(I)$ . The received data is subjected to normalization and is further processed using image registration and fusion techniques. On carrying out fusion alone the reconstructed image visually shows data loss and does not really highlight the contours perfectly.

But on subjecting the collected data to translation and then to fusion, a more accurate reconstruction of the imaged object is obtained. Table 6.4 shows the comparison of images obtained from fusion method alone and a combination of fusion and translation algorithms. The Table 6.4 illustrates image reconstruction of all the objects in shown in Figure 6.1.

Modelled object	Image Fusion	Image Fusion and Translation
		
		
		
		
		

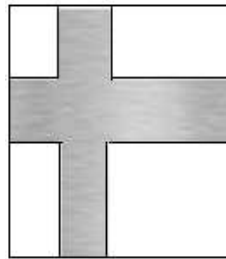
**Table 6. 3: Image Reconstruction using Image Fusion and combination of Fusion and Translation methods**

#### 6.6.4 Stepped Frequency in TWI

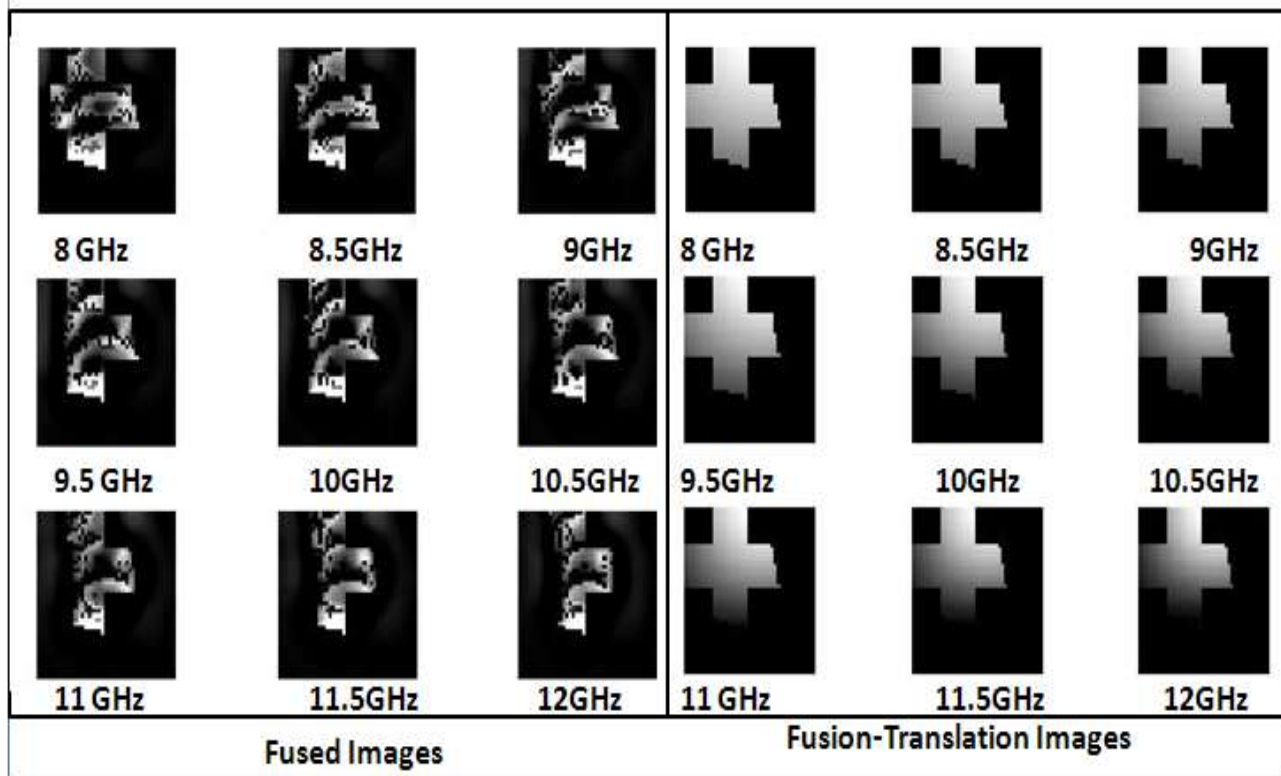
The main aim of the proposed TWI system is to develop high resolution images through stepped frequency illumination of target. With the stepped frequency methodology as explained in Chapter 2, simulations were carried out both in C-Band (4-6 GHz) and X- band ( 8-12 GHz) in steps of

500 MHz. It is a well-known that as frequency increases, penetration depth of radiation through any medium decreases but resolution however remains higher. It implies that images obtained at lower frequencies are of higher quality compared to the ones at higher frequencies. But the stepped frequency imaging generates higher resolution images by fusing the images obtained from all the desired ranges of frequencies. Figure 6.18 illustrates the images obtained from fusion and fusion-translation combination methods for each of the stepped C-band and X-band frequencies. Figure 6.19 shows the fused image of the stepped frequency images (C-Band and X-Band).

Figure 6.19 clearly indicates that at lower frequencies the extent of reconstruction of the imaged object is exceptionally better compared to higher frequencies but fusion of all the images shows a marked improvement in the reconstructed composite image. Table 6.4 provides the Mean Square Error (MSE) and Peak Signal to Noise Ratio (PSNR) of reconstructed composite images for various frequencies used in simulation study. Table 6.4 clearly indicates that MSE of reconstructed image progressively decreases with increase in frequency while its PSNR degrades. It clearly establishes the fact that lower frequencies provide quality image but improved resolution is only due to higher frequencies.



**(a) Input Image**



(b) Reconstructed Images Using Stepped Frequency

Figure 6. 18: Stepped Frequency in Image Reconstruction

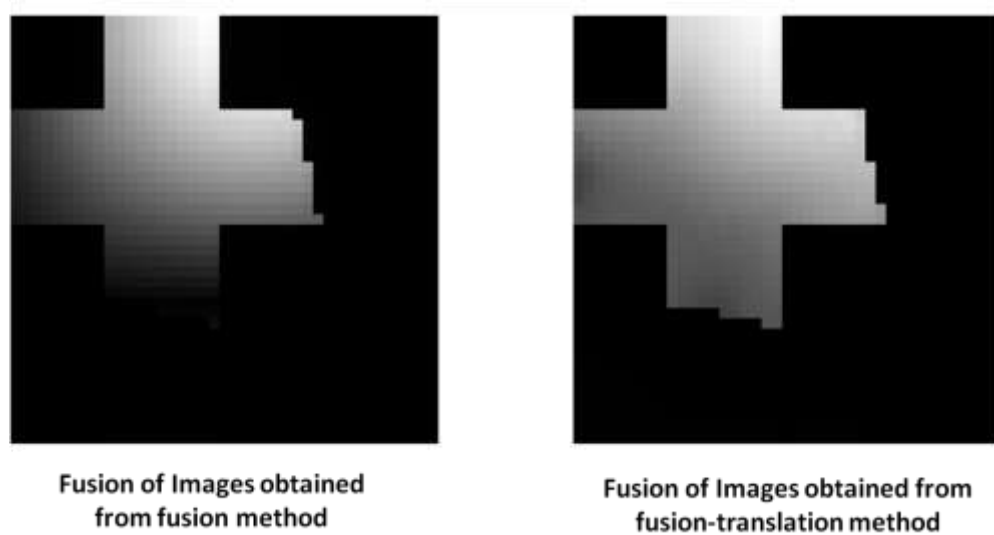


Figure 6. 19: Fused Stepped Frequency Images

Freq. (GHz)	Fused		Fused-Translated	
	MSE	PSNR (dB)	MSE	PSNR (dB)
4	0.1822	55.5246	0.0805	59.0706
4.5	0.2040	55.0349	0.0861	58.7813
5.5	0.2233	54.6414	0.1120	57.6370
6	0.2317	54.4821	0.1754	56.8156
8	0.4866	51.2594	0.1861	55.4341
8.5	0.494	51.1932	0.1933	55.2682
9	0.4993	51.1472	0.2024	55.0683
9.5	0.4984	51.1549	0.2117	54.8729
10	0.4947	51.1872	0.2219	54.6693
10.5	0.5017	51.1262	0.2335	54.4474
11	0.5076	51.0756	0.245	54.2395
11.5	0.5139	51.0216	0.2576	54.021
12	0.5152	51.011	0.2692	53.8293

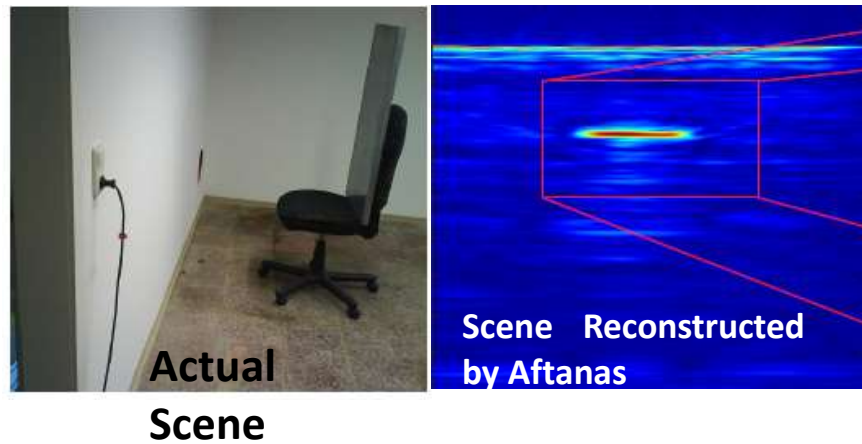
**Table 6. 4: MSE and PSNR of images obtained from X-Band Frequencies**

#### **6.6.5 Comparative Analysis of Results of Proposed TWI and (Aftanas M., 2009)**

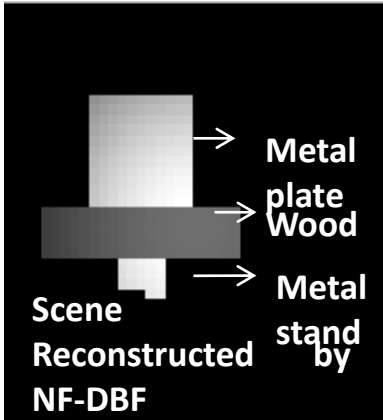
To substantiate the novel feature of the proposed near-field beamforming based TWI system's capability to capture the shape as well as contour of the object behind the wall which hitherto was not possible in (Aftanas M., 2009) which was based on SAR, a scenario discussed in (Aftanas M., 2009) was modelled as an object behind the wall and the simulations were carried out. Figure 6.20



(a) shows a flat metal plate placed on a chair considered to be object behind the wall. For simulation, the chair is assumed to be made of foam with a wooden base and metal stand. The reconstructed image of Figure 6.15(a) using the proposed near-field beamforming TWI technique is shown in Figure 6.20 (b). The corresponding results obtained and published in (Aftanas M., 2009) are shown in Figure 6.20(c). The result of reconstruction of image in Figure 6.20(c) shows a high amplitude blob or a patch to indicate the presence of the plate and the chair. It does not however provide the shape, contour, structural or material information of the imaged structure. From the comparison of results presented in Figure 6.20(b) and Figure 6.20(c), it is evidently clear that the approach proposed in this thesis out performs that invoked in (Aftanas M., 2009). The reconstructed image shown in Figure 6.20 (c) obtained with a combination of fusion-translation algorithms clearly highlights the contours of the structures behind the wall and the materials involved are also differentiated by the varying pixel intensity. The results of Figure 6.20(c) substantiates that the approach proposed in this thesis can detect the contour and the shape of the object behind the wall whereas the earlier method (Aftanas M., 2009) is unable to do so.



(a) Image in (Aftanas, 2010); (b) Reconstructed Image



**(c) Image Reconstructed from proposed NF Beamforming method**

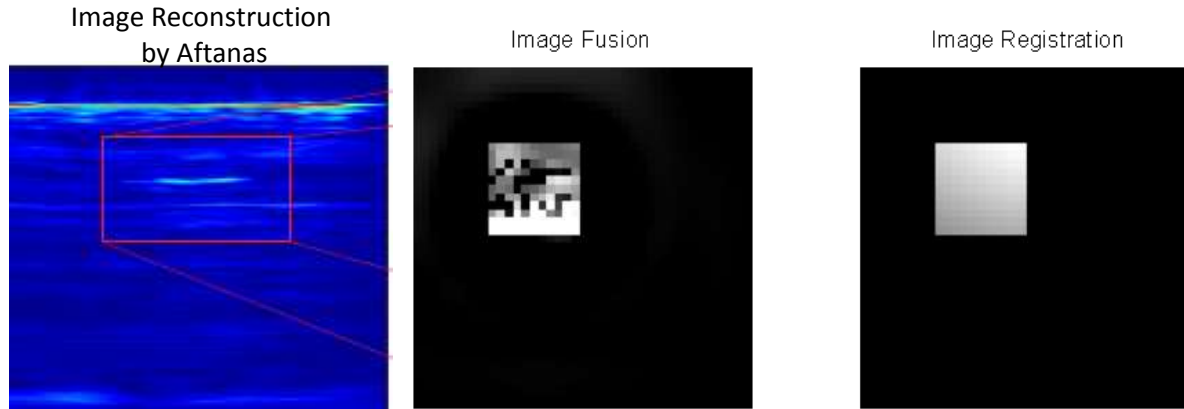
**Figure 6. 20: Comparison of Results of Imaging (Aftanas, 2009)**

Using the same conditions yet another scenario where an aquarium (glass surface) filled with water shown in Figure 6.21 of 20cm x 20 cm x 20 cm placed at a distance of 0.5 m from the wall was simulated. Figure 6.21 shows the comparison of image reconstructed in (Aftanas, 2009) and the proposed method. The TWI technique proposed in this thesis clearly provides the contour of the aquarium and the image reconstructed is due to the reflections from both the glass and water.



**Aquarium behind the Wall**

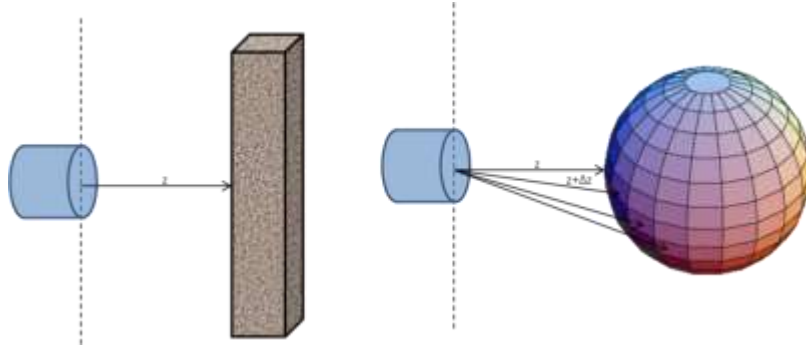
## Water Filled Glass Aquarium behind the wall



**Figure 6. 21: Comparison of Image Reconstruction of Aquarium**

### 6.6.6 Imaging of Curved Body

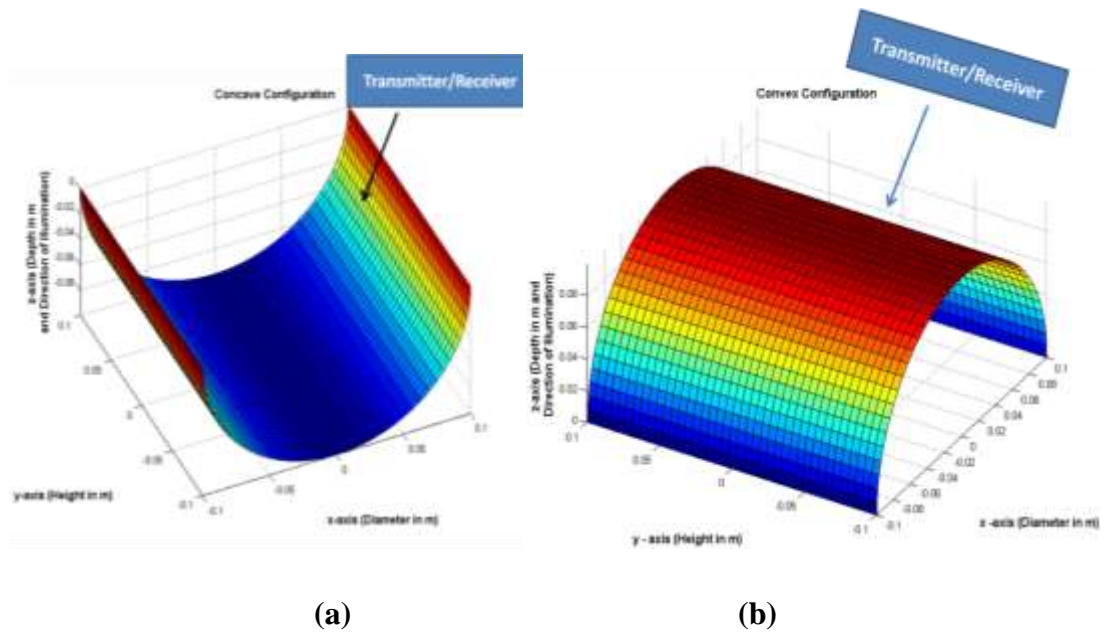
In all the results of the simulation presented in the previous subsections, the chosen surface of objects or the targets behind the wall was a planar and therefore constituted a flat geometrical target. The proposed NF beamforming method for imaging the object behind the wall was extended to treat the case of an object with curvature. The significant difference in the computation of the E and H field lies in that phase of computation which involves the calculation of currents on the target and field scattered back to the inner surface of the wall. Unlike the object with a flat surface for which the normal is  $-Z$  directed, the normal to the curved body continuously changes. Figure 6.22 is a typical depiction of the difference in the way the objects with flat and the curved body are illuminated.



**Figure 6. 22: Comparison of an illumination of a Flat and Curved Body from TWI Perspective**

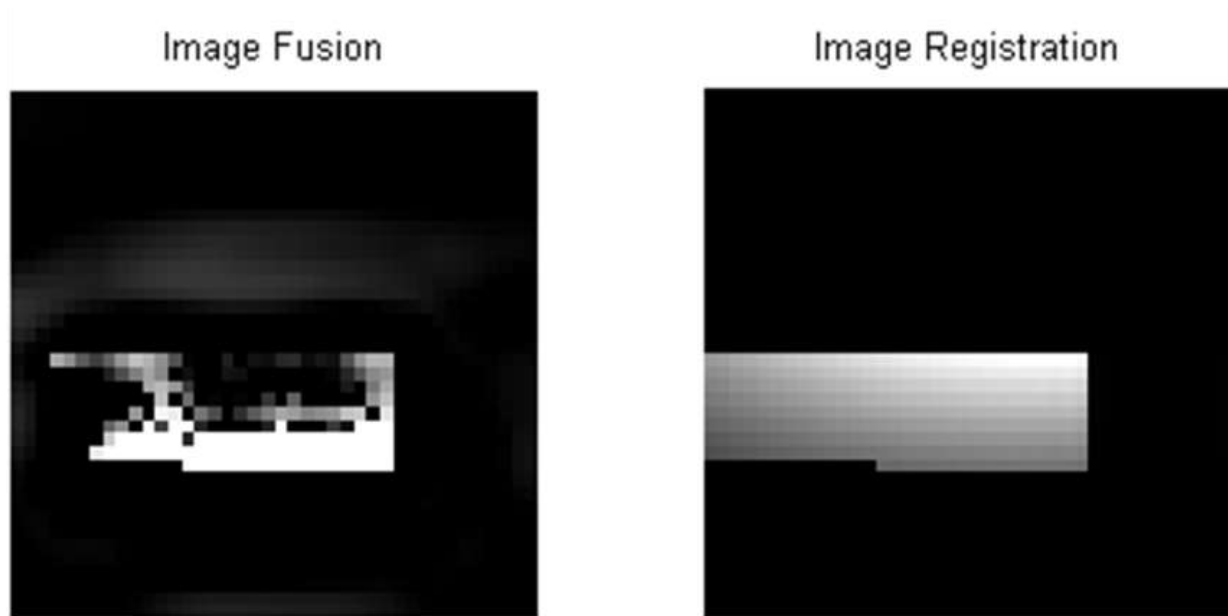
Since the computation of E and H fields in the proposed analysis is based on PO and GO techniques, the diffraction fields are not accounted for. As a consequence, the field scattered by a curved object on the inner surface of the wall can only be accounted by the contribution in the Lit region alone and no contributions from shadow region.

A special case scenario to reconstruct images of curved body surfaces like half cylinders (Figure 6.23) in concave and convex configurations was carried out. A cylinder with radius of 10cm and height of 40 cm was modeled as a typical curved conducting body.

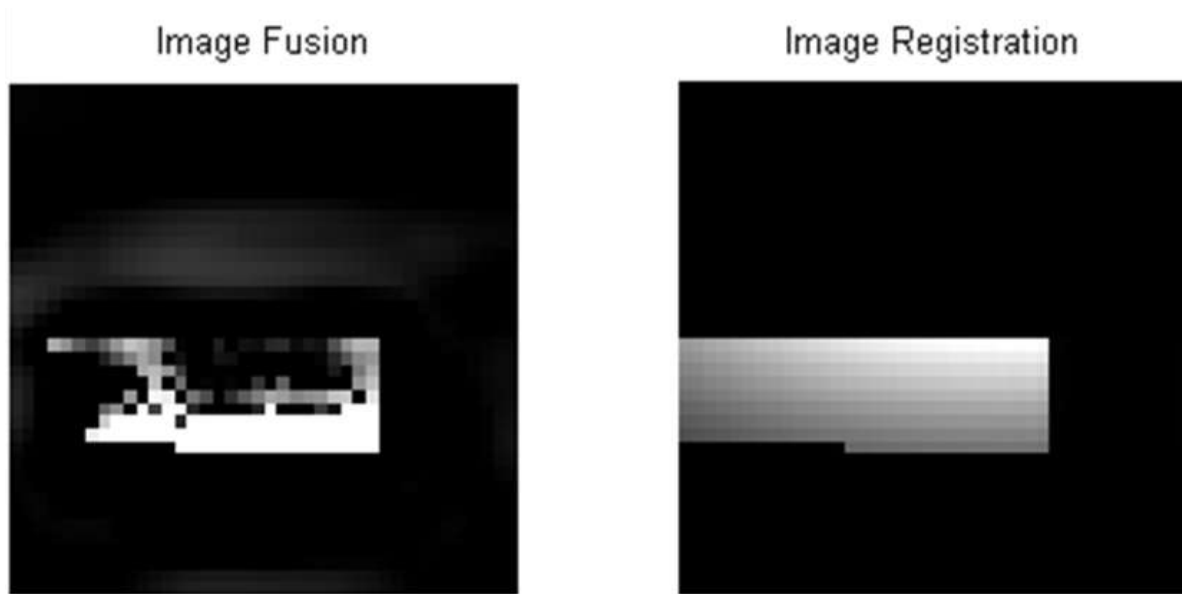


**Figure 6. 23: Half Cylinder Models; (a) Concave; (b) Convex**

Figure 6. 24 illustrates the reconstructed image of the curved object.



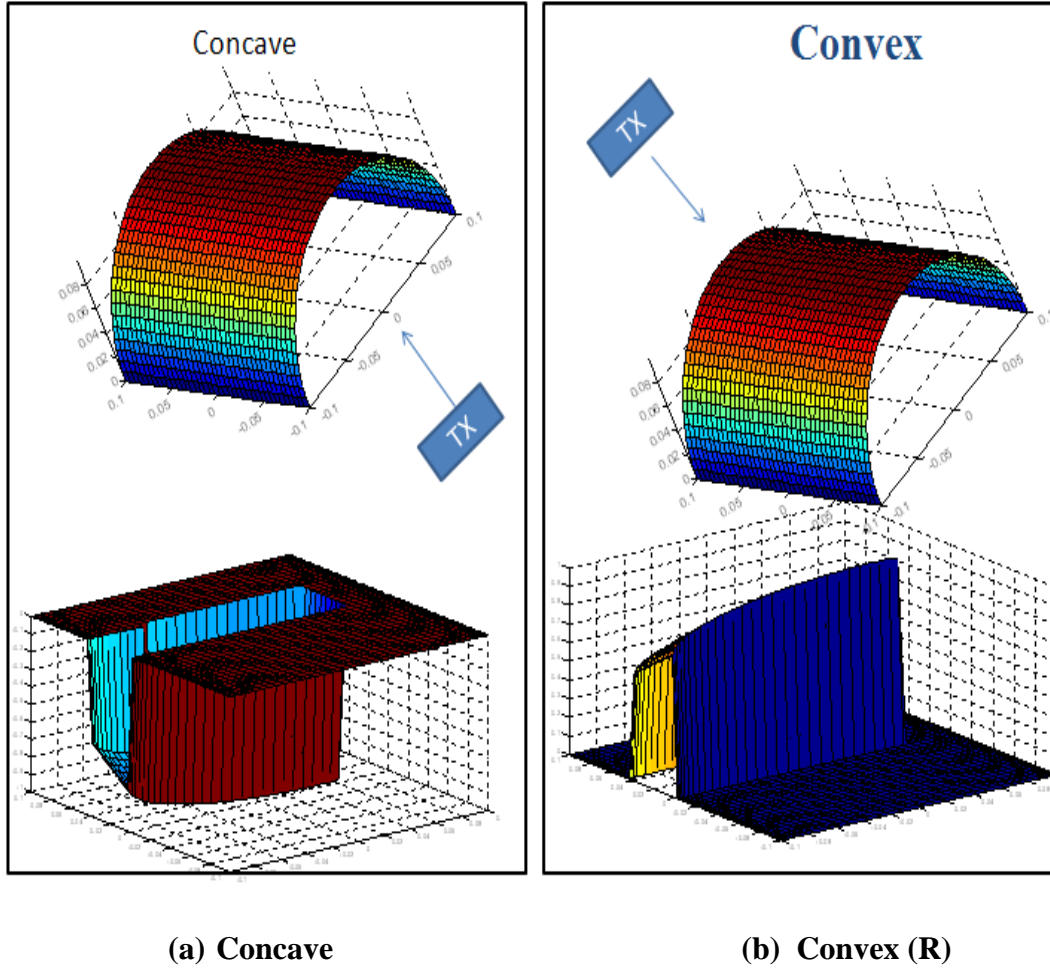
**(a) Concave Cylinder**



(b) Concave Cylinder  
**Figure 6. 24: Reconstructed Image of Half Cylinder Models**

The reconstructed image in Figure 6.24 shows a very small part of the actual target clearly indicating the variation in pixel intensity. The pixel intensities are different for both concave and convex configurations. In modeling and placement of the curved body shown in Figure 6.23, the lit region of the convex cylinder was relatively closer to the aperture of the receiver than the corresponding concave cylinder. As a consequence it is reasonable to expect higher intensity of the scattered field from the convex cylinder than the concave cylinder. This is evident in the results of the reconstructed image the pixel intensity of the imaged convex body is higher compared to concave body.

For the reconstruction of the images of the 3D objects behind the wall, the depth of the object can be perceived through the distribution of the intensity of reflected field (higher the intensity, closer the object to the receiver and vice versa) on a normalized scale. The results in Figure 6.25 clearly demonstrate the satisfactory reconstruction of the shape and contour of the imaged 3D structure using the image intensity as a parameter that varies with the depth of the object (along z axis).



**Figure 6. 25: Reconstructed Lit Region 3D Map of Half Cylinder Models**

## 6.7 Conclusions

This chapter proposed a new approach for the development of TWI system invoking near-field beamforming techniques overcoming the limitations of SAR as well as ISAR based TWI systems. The near-field beamforming technique does not require movement of the antenna array or the objects to reconstruct the image of the object behind the wall. The motion required by the SAR and ISAR has successfully been replaced by near-field beamforming technique involving electronic steering of the main beam of the beamforming antenna array. Unlike the previously reported research work on TWI, the novelty of the proposed TWI system in capturing the shape and contour of the object behind the wall has been demonstrated through extensive simulation studies. Subjecting the received data to translation and then fusion methods showed more accurate reconstruction of the imaged object compared to fusion methods alone. The calculated visual

accuracy based on the difference in pixels with the actual scene of the image reconstruction is 81%.

The advantageous features of adapting the stepped frequency waveform generation as well as the application of image registration in the improvement of reconstructed image have also been demonstrated through numerous case studies. Stepped frequency simulations were carried out for frequencies in C- band (4-6 GHz) and in X- band (8-12 GHz) in steps of 500 MHz. Simulation results reveal that the reconstructed images obtained at lower frequencies are of higher quality compared to the higher frequencies. Mean Square Error (MSE) and Peak Signal to Noise Ratio (PSNR) of reconstructed image clearly indicated that MSE progressively decreases with increase in frequency while its PSNR degrades. The transmission loss due to the wall was observed to be about -16 dB in a typical X band frequency. The signal strength at the receiving point (after forward incidence on the outer surface of the wall + penetration through the wall + incident field on the object behind the wall + scattered field by the object penetrating through the wall + free space propagation back to receiver) was observed to be -43 dB. The simulated results of the reconstructed image of the object behind the wall derived through the proposed near-field beamforming technique show a superior performance over an existing system (Aftanas, 2009) which conclusively establishes the potential utility as well as the novelty of the proposed approach.



## **Chapter 7: Conclusion and Future Work**

This chapter provides a summary of the inferences and technical conclusions derived from the research undertaken in this thesis. Potential scope and academic avenues for further research which emerge as logical extensions of the analytical formulations and simulations of this thesis are also highlighted

### **7.1 Summary**

The thesis proposes a new approach for the development of TWI system invoking near-field beamforming techniques overcoming the limitations of SAR as well as ISAR based TWI systems. The near-field beamforming technique does not require movement of the antenna array or the objects to reconstruct the image of the object behind the wall. The proposed TWI system facilitates the scan of the desired scenario in both azimuth and elevation. In the proposed approach, the motion required by the conventional SAR and ISAR based TWI has successfully been replaced by near-field beamforming technique involving electronic steering of the main beam of the beamforming antenna array. Unlike the existing TWI systems reported in the literature, the simulation model of TWI system of this thesis can treat any distance of separation (far field or near field) between the antenna array and the wall as well as the wall and the object. The thesis provides the design and development of a novel simulation model of a TWI system which uses Stepped Frequency and Near Field - BeamForming (NF-BF) techniques to scan a through the wall scene and reconstruct 2D image of it. The reconstruction of the image of the object behind the wall has been realized through conventional digital image processing techniques which are devoid of inversion techniques which are as explained in section 6.5.

The proposed new approach to image objects behind the wall is built upon the fundamental principles of antennas, wave-propagation, beamforming, signal and image processing. Structures like wall and objects behind the wall were modeled considering electromagnetic properties like permeability, permittivity and conductivity. The objects behind the wall were modeled to be made of Carbonyl metal, Rubber, Graphite, Borosilicate glass and Aluminium. The various optical phenomena like reflection, refraction, scattering and attenuation induced by the medium of wave propagation were incorporated in the simulation model.

The advantageous features of adapting the stepped frequency waveform generation as well as the application of image registration in the improvement of reconstructed image have also been demonstrated through numerous case studies. Simulation results of TWI associated with Stepped Frequency technique showed that images obtained at lower frequencies are of higher quality compared to the one higher frequencies. Fusion of the images obtained from the desired range of frequencies resulted in a high resolution image providing a detailed contour of the shape of the imaged structure. The reconstructed image also indicates the variation in composition of the material of the target by change in pixel intensity. Image reconstruction of curved bodies or 3D surfaces behind the wall was carried out and the simulation results illustrated that the reconstructed image was only due to field contributions from the lit region of the target with no contributions from shadow region. The simulation results also demonstrated the satisfactory reconstruction of the shape and contour of the imaged 3D structure using the image intensity as a parameter that varies with the depth of the object.

The developed simulation model of TWI radar system has planar array of circular waveguides as antenna elements radiating in X- band (8-12GHz) to carryout signal transmission, beamforming, reception and image processing. An evaluation of an estimate of total signal loss a typical TWI system would undergo was carried out and it was found that only 1% of the actual signal transmitted power is received back and the received signal with such an extremely low amplitude is processed to realize the formation of the images. The received signal when subjected to a combination of image translation and fusion methods resulted in improved reconstruction of image of the target/object than possible with fusion method alone. The calculated visual accuracy based on the difference in pixels with the actual scene of the image reconstruction was 81%.

In summary, this thesis is associated with the following original contributions:

- Mathematical and simulation model of near field beamforming based stationary TWI system with Two Dimensional beam steering capability to reconstruct the image of the object including its shape and contour
- Novel near field Beamforming method that overcomes the usual requirement of 3D or volumetric near field radiation patterns of the beamforming array
- New imaging methodology involving fusion and translation methods to develop high resolution images of behind the wall scenarios with the amplitude of received signals

- Generic and versatile new procedure to compute near field radiation patterns of antennas with prior knowledge of its either field or current distribution over the radiating aperture
- Novel scheme which employs the hybrid combination of Geometrical Optics (Ray Technique) and Physical Optics techniques to reduce the computational burden in the wave propagation studies involved in the development of simulation model of TWI system

## **7.2 Conclusions**

This section provides with the observations, derived inferences and reasoned interpretations associated with the research findings in near field analysis of antennas, near field beamforming and mathematical modelling of TWI system.

### **7.2.1 Near Field Analysis of Antennas**

The following are the technical inferences and interpretations associated with near field analysis of antennas

- A generalized procedure for the determination of near field radiation patterns of an antenna at any arbitrary distance is presented and the proposed approach is applicable to wide variety of antenna elements. The proposed procedure has a requirement of prior knowledge of either the current or field distribution on the radiating aperture
- The underlying principle of the generalized procedure tantamount to considering the radiating aperture as an array of point electric and magnetic dipoles. The radiation pattern of the antenna at any arbitrary point of observation (valid for both near field as well as far field) is obtained by the vector summation of the fields radiated by the array of both electric and magnetic dipoles located on the aperture of the antenna.
- The significance of the proposed analysis lies in the derivation of explicit expressions for the co- polar and cross polar components of the radiation pattern of both electric and magnetic dipoles.
- With circular cylindrical waveguide and conical horn as radiating elements in the near field beamforming analysis, the generic and versatile features of proposed novel approach for the determination of near field radiation pattern of these antennas have been substantiated
- The simulation results of the proposed near field analysis with the radial distance of observation of  $1000 \lambda$  show excellent correlation with the results derived through analytical formulation of (Balanis C.A., 2005) which is exclusively valid for the far field

- At a distance of  $0.2 \lambda$  from the aperture, the radiation patterns of circular waveguide are vastly/drastically different from the corresponding conventional far field patterns. The broadside radiating feature of the circular waveguide is also absent
- With the gradual increase in the radial distance of observation, one notices the increasing trend in the radiation patterns of circular waveguides to broadly conform to the profile of conventional far field patterns
- The radiation patterns of circular waveguide at  $r=0.75\lambda$  for (Distance of Observation /Diameter) = 0.571 nearly resemble the corresponding conventional far field patterns
- For a conical horn with a radius of 4.1 cm, the radiation patterns at  $r=2\lambda$  (Distance of Observation /Diameter)=0.781 show defined main lobe

### 7.2.2 Near Field Beamforming Analysis

The following are the technical inferences and interpretations associated with the analysis of near field beamforming

- A novel approach for near field beamforming is proposed that is also valid for far field. This feature can be attributed to the following:
  - Computation of beamforming weights directly at the specified arbitrary near field distance
  - Generalization of near-field array factor and near-field beam steering phase factor to overcome the assumption of planarity of the wave-front impinging on the radiating aperture of the array elements.
- Unlike the method of radial reciprocity (Kennedy R.A. et al, 1999), the proposed method does not mandate the requirement of 3D near field radiation pattern of the beamforming array.
- Simulation results derived through proposed near field beamforming technique with radial distance ' $R_{NF}$ ' equal to or greater than conventional far field distance criterion show perfect correlation with the results obtained through alternative formulations in the open literature meant exclusively for far field beamforming or beamsteering technique.
- Numerous simulations confirmed that the proposed technique yields reasonably encouraging beamforming results even at a distance of  $R_{NF}=1\lambda$  from the aperture of (5x1) linear or (5x5) planar array. This corresponds to  $(R_{NF}/\text{Aperture of Array})=0.2334$

- At distances greater than  $R_{NF}=1\lambda$ , the radiation patterns exhibit more pronounced structure of sidelobes
- Below the distance of  $R_{NF}=1\lambda$ , simulation results reveal the radiation pattern featured with less directive main beam
- The significant differences in the radiation patterns of the near field and far field beamformers lie in the beamwidth of the mainlobe and the asymmetry in the radiation pattern in case of beamsteering off the boresight direction
- Typical simulation studies on the radiation characteristics of planar array to illustrate the realizable two dimensional near field beamsteering have also been presented to validate the concept

### 7.2.3 Mathematical Modelling of TWI

The following are the technical inferences and interpretations associated with mathematical modelling of a TWI system

- This thesis proposed a new approach for the development of TWI system invoking near-field beamforming techniques overcoming the limitations of SAR as well as ISAR based TWI systems
- The near-field beamforming technique does not require movement of the antenna array or the objects to reconstruct the image of the object behind the wall. The motion required by the SAR and ISAR has successfully been replaced by near-field beamforming technique involving electronic steering of the main beam of the beamforming antenna array
- Unlike the previously reported research work on TWI, the novelty of the proposed TWI system in capturing the shape and contour of the object behind the wall has been demonstrated through extensive simulation studies
- Subjecting the received signal (data) to translation and then fusion method showed more accurate reconstruction of the imaged object compared to fusion method alone. The calculated visual accuracy based on the difference in pixels with the actual scene of the image reconstruction is 81%
- The advantageous features of adapting the stepped frequency waveform generation as well as the application of image registration in the improvement of reconstructed image have also been demonstrated through numerous case studies

- Simulation results reveal that the reconstructed images obtained at lower frequencies are of higher quality compared to the one obtained at higher frequencies
- Mean Square Error (MSE) and Peak Signal to Noise Ratio (PSNR) of reconstructed image clearly indicated that MSE progressively decreases with increase in frequency while its PSNR degrades
- The simulated results of the reconstructed image of the object behind the wall derived through the proposed near-field beamforming technique shows a superior performance over an existing system (Aftanas, 2010) which conclusively establishes the potential utility as well as the novelty of the proposed approach

### **7.3 Recommendation for Future Work:**

Suggestions for potential avenues to augment the existing body of knowledge are a significant feature of research philosophy.

TWI is relatively a new and an emerging technology showing prominent promise for rescue and security applications. The analytical formulations and simulation studies of the thesis have clearly proved that the accuracy and precision of reconstructed image of the behind the wall scenario depends on the effectiveness of invoked analysis of electromagnetic wave propagation as well as algorithms of advanced signal and image processing techniques.

Following are the suggestions/recommendations for the further pursuance of the research topic of this thesis.

- The proposed model of TWI did overcome the requirement of motion of the radar(antenna array) and the object for the formation of image thereby circumventing one of the limitations of the SAR/ISAR based TWI system. The thesis has considered only the stationary target. However, an extension of the proposed analysis and simulation to deal with the non-stationary (moving) object can be a next logical step to pursue to enhance the scope of this thesis
- In the presented analysis of the thesis, multiple reflections or the scattering between the target and the surrounding wall have not been considered. An analysis of improvement in

the accuracy and resolution of reconstructed image through the inclusion of the multiple scattering in the analysis will be a significant academic contribution

- The Image processing algorithms in the thesis did consider only the amplitude of the signal at the receiver points. Further analysis and simulation to consider the utility of phase information of the received signal in reconstruction process of the image can be of interest both from system and academic perspective
- Extension of the analysis for the estimation of the distance between the TWI radar and the target as well as the analysis to determine the size of the object behind the wall can be a considerable academic value to the TWI system
- Formulation of an analysis and modelling of a near field beamforming based TWI system has been the principal theme of this thesis. In the formulation as well as in the simulation, practicability of the implementation of the proposed TWI has always been a consideration throughout course of this research study. It will be of great practical utility to undertake an experimental investigation of the same topic to substantiate the novelty and to analyse the efficacy of implementation

## References

- Aftanas M.,2009, Through Wall Imaging with UWB Radar, Ph.D Thesis, Technical University Of Kosice, Slovakia
- Ahmad F., Amin M. G.,Kassam S. A. and Frazer G. J., 2003. A Wideband, Synthetic Aperture Beamformer for Through-The-Wall Imaging, IEEE International Symposium on Phased Array Systems and Technology, pp. 187-192
- Amin M., and Ahmad F.,2008, Multi-location wideband synthetic aperture imaging for urban sensing applications, Journal of the Franklin Institute, Vol. 345, pp. 618–639
- Amin M.G. and Ahmad F., 2013, Through-the-Wall Radar Imaging: Theory and Applications, in Chellappa R. and Theodoridis S. (Eds.), E-reference Signal Processing, Elsevier, Oxford
- Asprone D., Assante D., Chiariello A., Manfredi G., Miano G., Prota A. and Rubinacci G., 2010, Assessment of the Electromagnetic Disturbance of a Glass Fiber Reinforced Composite Fencing Structure, Journal of Composites for Constrution, Vol.14(5),pp.629–635
- Balanis C. A., 2005. Antenna Theory, Analysis and Design, Third Edition, A John Wiley & Sons, Inc., Publication
- Baranoski E.J., 2008, Through Wall Imaging: Historical Perspective And Future Directions, ICASSP, pp. 5173-5176,DARPA, USA.
- Brooker G., 2010, Industry Training Course Material – Sensor Systems, Australian Center for Field Robotics, pp. 303-356
- Camero-Website, 2011, Camero-Step into the known, Tactical Through Wall Imaging Solutions, Website:<http://www.camero-tech.com/about.php> as referred on 26-03-2011.



Daniels D.J., 2004, Ground Penetrating Radar (2nd ed.). Krieger (Institution of Engineering and Technology), pp.1–4.

Debes C., 2010. Advances in Detection and Classification for Through-the-Wall Radar Imaging, Ph.D. Thesis, Technische Universität Darmstadt, Deutschland

DeMartini G.B., Coulombe M.J., Horgan T.M., Soper B.W., Dickinson J.C., Gile R.H. and Nixon W.E., 2013, A 100 GHz Polarimetric Compact Radar Range for Scale-Model Radar Cross Section Measurements, Proceedings of the Antenna Measurements Techniques Association (AMTA), pp. 276-281

Eduardo Fernández-Canga, 2002, Image Fusion, Department of Electronic & Electrical Engineering, Signal and Image Processing group, University of Bath. UK

Frazier L.M., 1996, Surveillance Through Walls and Other Opaque Materials, Proc. IEEE National Radar Conference Electronic Systems, pp. 27-31

Gassler J, 2008, Step into the Unknown, CAMERO- Tactical Through-Wall Imaging Solutions, Website

Harrington R.F., 1961, Time-Harmonic Electromagnetic Fields, McGraw-Hill

Haynes T., 1998. A Primer on Digital Beamforming, Spectrum Signal Processing, <http://www.spectrumsignals.com>

Hunt A.R., 2004. A Wideband Imaging Radar for Through-the-Wall Surveillance, Sensors, and Command, Control, Communications, and Intelligence (C3I) Technologies for Homeland Security and Homeland Defense III. Edited by Carapezza, Edward M. Proceedings of the SPIE, Volume 5403, pp. 590-596

Karakasiliotis A.V., Lazarov A.V., Frangos P.V., Bouladakis G. and Kalognomos G., 2008. Two-Dimensional ISAR Model and Image Reconstruction with Stepped Frequency-Modulated Signal, IET Signal Process., Vol. 2, No. 3, pp. 277–290

Karthikeyan M. and Govind K.R., 1985, Private Communication, Center for Systems and Devices, Indian Institute of Technology, Madras, India

Kennedy, R.A., Ward, D.B. and Abhayapala T.D., 1998, Broadband Near-field Beamforming Using a Radial Beam pattern Transformation , IEEE Transaction on Signal Processing, Vol.46, No.8., pp. 2147-2156

Kennedy, R.A., Ward, D.B. and Abhayapala T.D.,: ‘Near-field Beamforming Using Radial Reciprocity’, IEEE Transaction on Signal Processing, January 1999, Vol.46, No.48., pp. 33-40

Khalil, F., Jullien, J.P. and Gilloire, A., :‘Microphone array for sound pickup in teleconference systems’, J.AudioEngSoc., September 1994, Vol. 42, no.9, pp. 365–371

Kmec M, Herrmann R., and Sachs J. Peyerl, 2006, A Family of M-Sequence based UWB sensors, Proceedings of 51st International Scientific Colloquium

Kraus J.D. and Fleisch D.A., 1999, Electromagnetics with Applications, Fifth Edition, Tata McGraw Hill, New Delhi, pp.169-239

Kucukkilic T., 2006, ISAR Imaging and Motion Compensation , M.S. Thesis, Middle East Technical University

Kumar B. P., “Synthesis of Near-field Patterns of a Class of Two-dimensional Array Antennas”. Ph.D. Thesis, Indian Institute of Technology, Madras, 1992

Leong K.M., 2000, Stepped Frequency Imaging Radar Simulation, MS Thesis, Naval Postgraduate School, Monterey, California, USA

Liu, Abbey C. K. and Insana M. F. ,2004, Linear Approach to Axial Resolution in Elasticity Imaging, IEEE Trans. On Ultrason., Ferroelect., Freq. Contr., Vol. 51, pp. 716–725

Lu T.,Agarwal K., Zhong Y., and Chen X., 2010. Through-Wall Imaging: Application of Subspace-Based Optimization Method, Progress In Electromagnetics Research, PIER 102, pp.351-366

Montebugnoli S., Bianchi G., Cattani A., Ghelfi F., Maccaferri A. and Perini F.,2004, Some Notes on Beamforming, The Medicina IRA-SKA Engineering Group

Narasimhan M.S. and Bobby Philips, 1987, Synthesis of Near-Field Patterns of Arrays, IEEE Transactions on Antenna and Propagation, Vol-35, pp. 212-218

Narasimhan M.S. and Prasad K.M.,1981, GTD analysis of Near Field Patterns of a Prime Focus Symmetric Paraboloidal Reflector Antenna, IEEE Transactions on Antennas and Propagation, Vol. 29, pp. 959 – 961.

Narasimhan M.S. and Rao K.S.,1979, GTD Analysis of the Near-Field Patterns of Conical and Corrugated horns, IEEE Transactions on Antenna and Propagation, Vol.27, pp.705-708

Narasimhan M.S.and Kumar B. P., 1990, A Technique of Synthesizing the Excitation Currents of Planar Arrays or Apertures, IEEE Transactions on Antenna and Propagation, Vol. 38, No. 9, pp.1326 – 1332

Narasimhan M.S. and Kumar B.P., 1990, A Technique of Synthesizing the Excitation Currents of Planar Arrays or Apertures, IEEE Transactions on Antenna and Propagation, Vol. 38, No. 9, pp.1326 – 1332

Narasimhan M.S., Raghavan K. and Ramanujam P., 1982, A Correction to the Available Formula for the GTD Near Field Patterns of Conical Horns, IEEE Transactions on Antenna and Propagation, Vol.30, pp. 1042-1043

Narasimhan M.S. and Rao B.V., 1971, Modes in a Conical Horn: New Approach, Proceedings IEE, Vol. 118, pp. 287-292

Neven W.H.L., Quilter T.J., Weedon R. and Hogendoorn R.A., 2005, Report on Wide Area Multilateration, National Aerospace Laboratory, Eurocontrol

Park J.I. and Kim K.T., 2010, A Comparative Study on ISAR Imaging Algorithms for Radar Target Identification, Progress In Electromagnetics Research, Vol. 108, pp.155-175.

Paulose A., 1994, High Radar Range Resolution with step frequency waveform, MS Thesis, Naval Postgraduate School, Monterey, CA, USA

Peabody J.E., Charvat G.L., Goodwin J. and Tobias M., 2012, Through Wall Imaging Radar, Lincoln Laboratory Journal, Vol. 19 No.1 pp. 62-72

Sadjadi F., 2005. Comparative Image Fusion Analysis, Lockheed Martin Corporation

Schlutz M., 2009. Synthetic Aperture Radar Imaging Simulated in MATLAB, M.S. Thesis, California Polytechnic State University, San Luis Obispo, USA.

Schmidt, R. O. 1986, Multiple Emitter Location and Signal Parameter Estimation. IEEE Transactions on Antennas and Propagation, Vol. 34, No.3, pp. 276-280.

Seng C.H., Bouzerdoum A, Tivive F.H.C. and Amin M., 2010, Fuzzy Logic-Based Image Fusion for Multi-View Through-the-Wall Radar, Digital Image Computing: Techniques and Applications, IEEE Computer Society, pp. 423-428.

Sicairos M.G., Samuel T. T., and Fienup J. R., 2008, Efficient Subpixel Image Registration Algorithms Optics Letters, Vol. 33, No. 2, , Optical Society of America

Silver S., Microwave Antenna Theory and Design, 1<sup>st</sup> Edition, A McGraw Hill Book Company Inc., 1949

Soutsos M.N., Bungey J.H., Millard S.G., Shaw M.R. and Patterson A., 2010, Dielectric Properties of Concrete and their influence on Radar Testing, NDT & E International Volume 34, Issue 6, September 2010, pp. 419–425

Unknown, 2011, Multilateration, Website: <http://en.wikipedia.org/wiki/Multilateration> as referred on 26-03-2011

## **Appendix – 1**

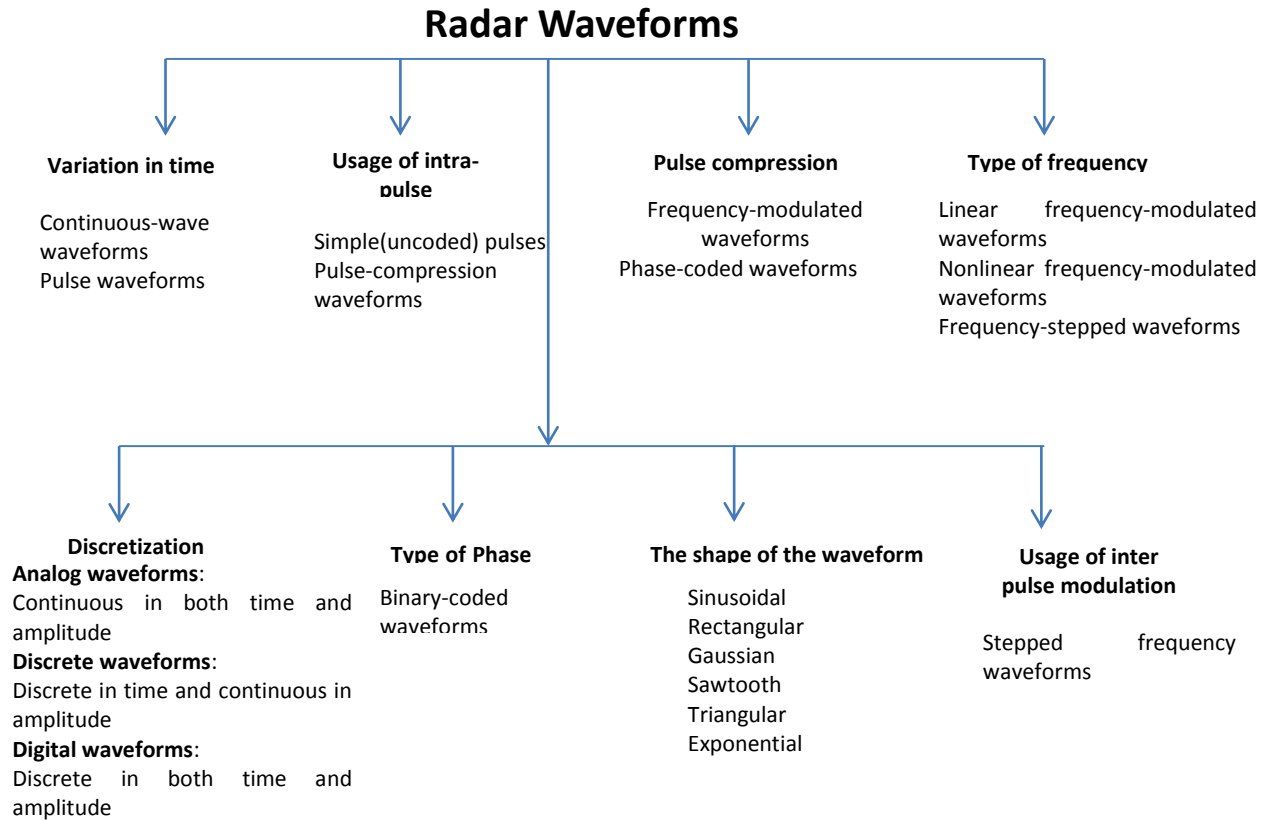
This appendix presents a detailed discussion on the generic principles of different types of waveforms used in Radar systems.

### **A.1 Radar Waveforms:**

Waveform and its processing in a radar system depends on the radar's application since the correct choice of the waveform defines all the main characteristics and properties, including performance of target detection, resolution, measurement, and classification.

Requirements of range, Doppler coverage, accuracy of detection, error fraction, computation complexity, cost of waveform generation and signal-processing systems are the major factors that influence the choice of a waveform. There are various considerations for the choice of a waveforms and accordingly there are different types of waveforms which can be selected. The Figure A1.1 describes the various choices for selection of waveform.

Some of the main characteristics of radar to be considered for desirable performance are operating frequency, pulse repetition frequency, transmitter power, antenna gain and the receiver sensitivity. The performance of radar also depends on characteristics like resolution, target detection, measurement, and classification. Resolution is the ability to separate the signals from adjacent sources. Resolution of radar also involves angular resolution, Doppler resolution, frequency resolution and range resolution. The range resolution is of utmost importance for Through Wall Imaging (TWI) applications. It defines the choice of waveform, method of transmission and signal processing.



**Figure A1.1 Types of Radar Waveforms**

The radar range resolution depends on the bandwidth of the received signal and is written as

$$\rho = \frac{c}{2B} = \frac{c\tau}{2} \quad \dots (A.1.1)$$

where ,  $c$  = Speed of light

$B$  = Bandwidth of the signal

$\tau$  = Pulse width

The bandwidth of a time gated signal is inversely proportional to the pulse duration. Shorter pulses are better for range resolution. The amplitude of the received signal is also proportional to the pulse width (duration) meaning that long pulses are better for signal reception. Hence the

desired signal should combine high energy of long pulse width with the high resolution of a short pulse width.

### **A.1.1 Pulse Compression**

Pulse compression is a technique that forms an important process in the transmission of radar signal. It is a wave shaping process where the desired pulsed signal is frequency or phase modulated in order to help resolve targets which may have overlapping echoes (received target signals). The technique combines high energy of long pulse width with the high resolution of a short pulse width and since each pulse has a unique frequency, the echoes can be completely separated.

Pulse compression is preferred over the high power transmitters as they require high voltage power supplies. They have reliability or safety issues and they are expensive.

Range resolutions are insignificant for signals with fixed frequency continuous wave radars due to the narrow spectrum of the transmitted waveform. Frequency and phase modulations are preferred techniques to modulate the transmitted signal for widening the spectrum and maintaining a good range resolution. The received signals can further be processed with matched filters.

There are a number of techniques to improve range resolution of the radar system. Intra pulse compression techniques are most commonly used and they are applied through either frequency coding or phase coding to each transmitted pulse. The received pulses are processed in a filter matched to the transmitted signal resulting in a compressed pulse. Frequency coding techniques include the common Linear Frequency Modulation (LFM) or chirp method, and discrete coded segments within the pulse. Phase coding techniques include binary phase codes as well as various poly-phase codes.



### **A.1.2 Phase-Coded Pulse Compression**

Phase coded pulse compression techniques use the concept of Binary Phase-Shift Keying (BPSK) modulation. The codes are made of 'm' chips which are in or out of phase with a reference signal as shown in the Figure A1.2.

This item has been removed due to third party copyright. The unabridged version of the thesis can be viewed at the Lanchester Library, Coventry University.

#### **Figure A1.2. Phase Variation of Pulse Code with Reference to Modulating Stream**

**(Brooker G., 2010)**

At the receiver end of the radar, the demodulation is achieved by multiplying the incoming RF signal by a coherent carrier to recover/detect the original BPSK signal with appropriate filtering.

The phase of the received signal will be shifted by an amount dependent on the round trip time and the Doppler velocity. The receiver generally utilizes two processing channels to recover the in-phase signal and the one which recovers the quadrature signal to avoid the degradation of SNR. The signals are then converted to digital signals via ADCs and correlated with the stored binary sequence and then combined. A special case of the stored binary sequences are the Barker codes where the peak of the autocorrelation function is  $N$  (for a code of length  $N$ ) and the magnitude of the maximum peak side lobe is 1.

Barker codes have a limitation that codes with lengths greater than 13 are not found. Barker code sequences are called optimum because they offer zero Doppler shift and the peak to side lobe

ratio is  $\pm n$  after matched filtering (where  $n$  is the number of bits). The Barker code is the only code that has equal side lobes at this low level, but this only applies along the zero-Doppler axis.

The CW phase-coded techniques offer the same performance as other techniques but has limitations when the radar transmits and receives simultaneously. Processing still remains a potential problem as the computationally expensive autocorrelation process is required to extract the range information from the return echo.

### **A.1.3 Pseudo Random Codes Optimal Binary Sequences**

Optimal binary sequence is one whose peak side lobe of the aperiodic autocorrelation function is as minimum as possible for a given code length. Optimal codes are usually computed through computer searches. A longer search time for higher code length  $N$  is a serious limitation of this technique.

Maximal length (M-Sequence) sequences are those that can be obtained from linear feedback shift registers. A typical shift register generator is shown in the Figure A1.3. These have a structure similar to random sequences and therefore possess desirable autocorrelation functions. They are often called Pseudo-Random (PR) or Pseudo-Noise (PN) sequences.

This item has been removed due to third party copyright. The unabridged version of the thesis can be viewed at the Lanchester Library, Coventry University.

### **Figure A1.3 Generation of PN Sequence (Brooker G., 2010)**

The  $N$  stages of the register are pre-loaded with all 1s or a combination of 1s and 0s. The shift register is clocked, and the output at any stage is the binary sequence. When the feedback connections are properly chosen, the output is a sequence of maximal length  $N$  where  $N = 2^n - 1$ , where  $n$  is the number of stages of the shift register. There are a total of  $M$  maximal length

sequences that can be obtained from a generator with  $n$  stages, where  $M$  is given by the following formula:

$$M = \frac{N}{n} \prod \left(1 - \frac{1}{p_i}\right) \quad \dots (A1.2)$$

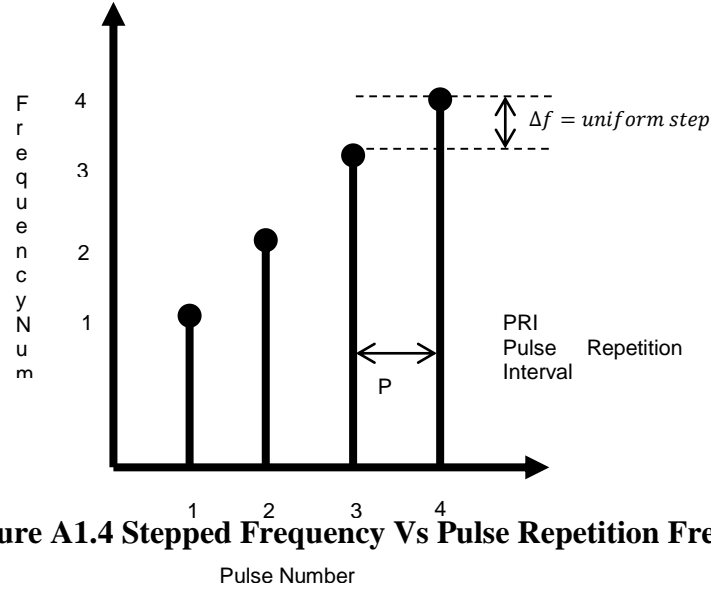
where  $p_i$  are the prime factors of  $N$ . The sequence of length  $N$  determines the bandwidth of the system. This also allows generation of large time-bandwidth products which result in good range resolution from registers having a small number of stages. Table 11.3 in (Brooker, G., 2010) lists the length and number of maximal length sequences obtained from shift registers of various lengths along with the feedback connection required to generate one of the sequences.

With a continuous operation of the shift register, a continuous repeating waveform is generated which can be used for continuous-wave operation. Aperiodic waveforms are obtained if the output of the waveform generator is terminated after one complete sequence, and these are generally used for pulsed-radar applications. The autocorrelation functions of the two cases vary in terms of their side lobe structure.

The M-Sequence or Pseudo Random code or PN sequence involving radar techniques have large power requirements to generate signals of relatively low amplitudes and maintain a desirable SNR. M-sequence techniques can easily be put in form of a monolithic integrated circuit. For high speed applications long binary dividers are used. The only limiting factor is the complex signal processing involved in processing the received data. Most of the GPRs like DEMINE (Belgium), DEMAND (Italy) and a project from QinetiQ (UK) work on the principles of M-Sequence (Sachs J., 2003).

#### **A.1.4 Step Frequency Waveform**

The step frequency waveform is a variation of the common linear FM pulse compression. It can also be called as interpulse variation waveform (Paulose A., 1994). A series of  $N$  coherent pulses are transmitted whose frequencies are progressively increased from pulse to pulse by fixed frequency steps of increment  $\Delta f$  as shown in Figure A1.4. Each pulse has a fixed pulse width  $\tau$ , and the pulses are transmitted at a fixed Pulse Repetition Frequency (PRF).



**Figure A1.4 Stepped Frequency Vs Pulse Repetition Frequency**

The frequency  $f_k$  of the  $k^{\text{th}}$  pulse is given by

$$f_k = f_c + (k-1) \Delta f \quad \dots (A1.3)$$

where  $f_c$  is the carrier frequency

The instantaneous bandwidth of this waveform is approximately equal to the inverse of the pulse width and is much less than the effective bandwidth. The effective bandwidth of the waveform denoted as  $B_{\text{eff}}$  is determined by the product of the number of pulses  $N$  and the frequency step size  $\Delta f$ .

$$B_{\text{eff}} = N \Delta f \quad \dots (A1.4)$$

The range resolution for any waveform is dependent on the effective bandwidth of the waveform. The range resolution of the step frequency waveform in meters is given as

$$\rho = K \frac{c}{2B}$$

$$\rho = K \frac{c}{2N\Delta f} \quad \dots (A1.5)$$

where  $K$  is a constant determined by the weighting window and is  $\geq$  unity

$c$  is the speed of light ( $3 \times 10^8$ ) m/s

From Equation (A1.5), the range resolution can be made finer by either increasing the number of pulses and/or increasing the frequency step size (Paulose A.,1994).

The returns of the  $N$  pulses at different carrier frequencies constitute the frequency spectrum of the reflectivity of the target and are coherently integrated by the inverse FFT to yield the High Resolution Range (HRR) profile. The signal processing transforms the original wide range bins into finer range bins. The HRR profile does not give absolute range position of the target but gives the relative position of each scattering center within the original range bin (Paulose A.,1994) .

The advantage of the step frequency method over other pulse compression techniques is that the range resolution is increased while still maintaining a narrow instantaneous bandwidth. As a result, the analog to digital conversion requirements are less stringent. Moreover, as opposed to the UWB waveform, the range resolution can be achieved by merely adding a stepped frequency synthesizer to a conventional narrowband radar receiver and performing the required signal processing on the received signal.

The step frequency waveform has two primary limitations. Unlike a pulse-Doppler radar, the step frequency radar cannot directly measure the velocity of moving targets based on the Doppler shift. In addition, unlike the case of phase coded pulse compression, the step frequency waveform requires additional time to transmit and receive  $N$  pulses needed to obtain the equivalent wide bandwidth of a single narrow pulse.

## **A.2 Applications of Radar Waveforms**

Ground Penetration Radars (GPRs) use different types of radar waveforms to have optimal range resolution. Because of the simplicity, implementation and economic reasons, Time domain based amplitude modulation is generally preferred over frequency modulated or stepped frequency

methods. However time domain based amplitude modulation is associated with the limitation of significant amount of noise and low conversion efficiency.

Linear Frequency Methods (LFMs) have the limitation of requiring a high performance to maintain linearity across frequency sweep. This is difficult to achieve with the constraints of low cost. Stepped frequency methods are chosen as they have improved receiver performance in terms of dynamic range compared to amplitude modulated methods. Phase coded and Pseudo Random Noise (PN) coded Sequence methods are gaining more prominence. PN coded radars are not affected by interference but their limitation lies in their dynamic range due to the auto-correlation property of the PN code. The limitations of dynamic range restrict the operating range of PN coded radars to 10 miles typically.

Medical Radar applications are generally seen in ultrasound imaging methods. In ultrasonic imaging, the peak acoustic pressure cannot be arbitrarily increased because of patient safety. The pulse compression techniques are employed to adhere to the compliance of FDA's limit of acoustic pressure while improving the SNR compared to conventional systems. Like any other radar system, ultrasound systems can have varied choice of waveform specification depending on the application to improve their range resolution. The choices include interpulse, intrapulse coded signals, the PN and Barker coded signals. (Liu et. al., 2004) used PN sequences to improve depth of focus. There is no one waveform that satisfies all the requirements. Generally FM chirp methods are used in Quantitative Ultrasounds to improve axial resolution. Studies are carried out using pre-enhanced FM chirps along with filtering to provide idealistic ultrasound images.

## Appendix – 2

This appendix presents a comparison of measured near field radiation patterns of a Conical horn with the computed radiation patterns obtained through the generalized procedure for the determination of radiation pattern of antenna proposed in chapter 4 of the thesis.

The procedure adopted in chapter 4 of the thesis for the validation of the proposed generalised procedure for the determination of near field radiation pattern of antenna is rather an indirect approach. The stated indirect approach is meant to imply that the far field is a special case of near field analysis with the radial distance of observation set to satisfy the conventional far field criterion of  $2D^2/\lambda$  where  $D$  and  $\lambda$  denote the size of the antenna and the wavelength respectively. A correlation established between the results on the far field using the proposed near field and an alternative method exclusively valid for the far field analysis, indirectly validates the near field analysis proposed in chapter 4 of this thesis. Accordingly, the obtained far field radiation patterns of the cylindrical waveguide and conical horn using the proposed near field approach have been compared with the corresponding radiation patterns obtained using alternative formulations available in (Silver S., 1949) and (Balanis C.A., 2005). The correlation between the results of far field radiation pattern obtained through the proposed near field approach and the conventional far field approach illustrated in Figure 4.5 has been invoked to justify or indirectly substantiate the validity of the proposed near field formulation.

In addition to the stated indirect approach, additional simulation studies on the near field radiation patterns of conical horn have been performed with the identical geometrical parameters of the horn, the frequency and the near field distance mentioned in (Narasimhan M.S. and Rao K.S., 1979). In Figures A2.1 to A2.2 of this appendix, a comparison of the results on the near field radiation patterns of a conical horn obtained by the proposed near field approach and the corresponding measured results reported in (Narasimhan M.S. and Rao K.S., 1979) is presented. The dimensional parameters of the horn reported in (Narasimhan M.S. and Rao K.S., 1979) are:

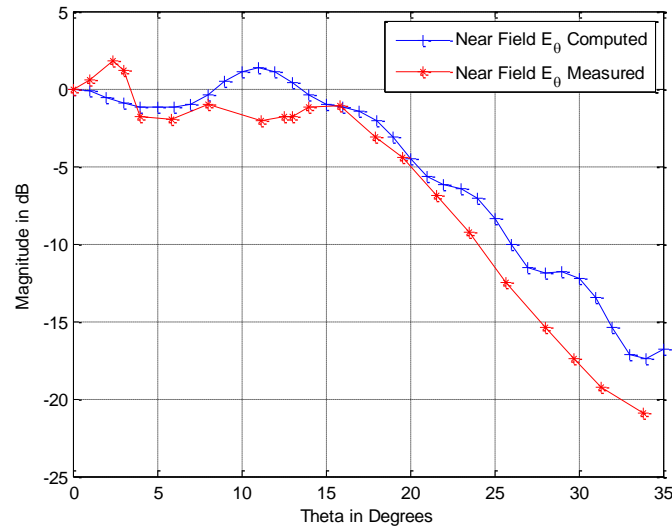
Frequency= 11.17 GHz

Wavelength= 2.685 cm

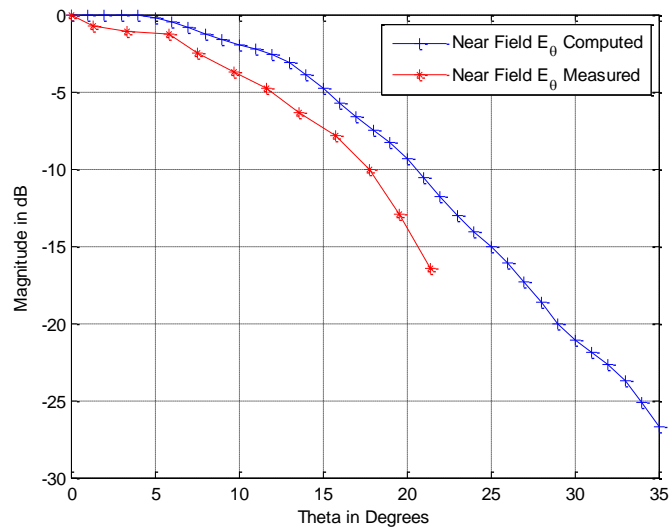
Semi Flare angle =  $25^\circ$

Axial Length of the horn= 32.65 cm

Radius of Aperture of Conical Horn= 15.22 cm



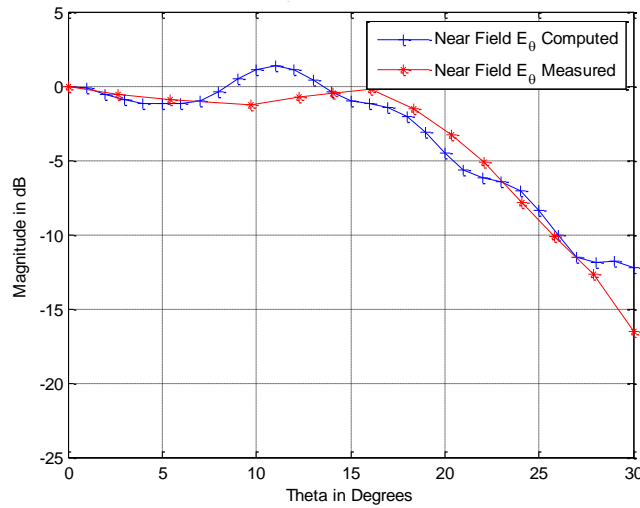
**Figure A2.1(a): Comparison of Near field E-Plane Radiation Pattern of Conical Horn at distance  $r=30.5\text{cm}$ . (Measured results from (Narasimhan M.S. and Rao K.S., 1979))**



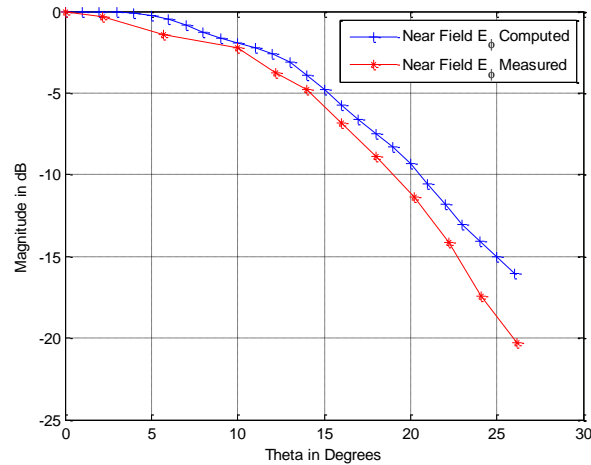
**Figure A2.1(b): Comparison of Near field H-Plane Radiation Pattern of Conical Horn at distance  $r=30.5\text{cm}$ . (Measured results from (Narasimhan M.S. and Rao K.S., 1979))**



In Figures A2.1(a) and A2.1(b), the results correspond to a near field distance of measurement (computation) of 30.5 cm which is within the range of the reactive near field (38.78 cm) . For the results depicted in Figures A2.2(a) and (b), the corresponding near field distance is 91.47 cm which falls outside the range of reactive near field. The conventional minimum far field criterion for this conical horn geometry and frequency is 690.2 cm. The results depicted in Figures A2.1 and A2.2 illustrate the correlation between the measured results of (Narasimhan M.S. and Rao K.S., 1979) and the computed results obtained through the near field analysis proposed in chapter 4 of this thesis.



**Figure A2.2(a): Comparison of Near field E-Plane Radiation Pattern of Conical Horn at distance  $r=91.47\text{cm}$ . (Measured results from (Narasimhan M.S. and Rao K.S., 1979))**



**Figure A2.2(b): Comparison of Near field H-Plane Radiation Pattern of Conical Horn at distance  $r=91.47\text{cm}$ . (Measured results from (Narasimhan M.S. and Rao K.S., 1979))**

In both Figures A2.1 and A2.2, there is a better correlation in the near field radiation pattern in the E- plane ( $E_\theta$  component) compared to that of H- plane ( $E_\phi$  component). The results of the Figure A2.2 illustrate an improved correlation between the two results as the distance of near field measurement is increased from 30.5 cm to 91.47 cm, which is outside the range of the reactive near field of the conical horn at the given frequency of measurement. A similar comparative study could not be carried out for the circular cylindrical waveguide due to the non- availability of the measured data of near field radiation patterns.

It is well known that the interaction between the mounting fixtures that support the test antenna and the transmit antenna as well as accuracy of alignment of axes of antennas have pronounced effects in the near field measurements. The resolution of the measurement setup and the precision of alignment of axes of the two antennas have not been explicitly mentioned in the above referenced paper. A satisfactory agreement between the two results at a near field distance which is outside the reactive near field validates the proposed generalized analysis for the determination of near field radiation pattern of antennas.

### Appendix – 3

The following research publications are associated with this thesis.

Serial No.	Title	Journal
1	A Simple Approach For Near Field Beamforming	International Journal on Communications Antenna and Propagation (IRECAP), 4(3), pp. 64-76, 2014.
2	A Generalized Approach for Computation of Near Field Radiation Pattern of an Antenna	International Journal on Antenna and Propagation (IRECAP) (Hindawi Publications Corporation), <a href="http://dx.doi.org/10.1155/2014/958148">http://dx.doi.org/10.1155/2014/958148</a> , 2014
3	Mathematical Model and Wave Propagation Analysis of a Through Wall Imaging System using Near-field Beamforming	IEEE Transactions on Image Processing (Under Review)

## Appendix – 4

# **LOW RISK RESEARCH ETHICS APPROVAL**

## Low Risk Research Ethics Approval Checklist

### Applicant Details

Name <b>PREETHAM SHANKPAL</b>	E-mail <b>preetham@msrsas.org</b>
Department	Date <b>10.05.2011</b>
Course <b>Ph.D</b>	Title of Project

### Project Details

**MODELLING AND SIMULATION STUDIES ON NEAR FIELD  
BEAMFORMING BASED THROUGH WALL IMAGING SYSTEM**

Summary of the project in jargon-free language and in not more than 120 words:

- Research Objectives
- Research Design (e.g. Experimental, Desk-based, Theoretical etc)
- Methods of Data Collection

### Participants in your research

1. Will the project involve human participants?	Yes	No <input checked="" type="checkbox"/>
---	-----	--

If you answered **Yes** to this questions, this may **not** be a low risk project.

- If you are a student, please discuss your project with your Supervisor.
- If you are a member of staff, please discuss your project with your Faculty Research Ethics Leader or use the Medium to High Risk Ethical Approval or NHS or Medical Approval Routes.

### Risk to Participants

2. Will the project involve human patients/clients, health professionals, and/or patient (client) data and/or health professional data?	Yes	No <input checked="" type="checkbox"/>
3. Will any invasive physical procedure, including collecting tissue or other samples, be used in the research?	Yes	No <input checked="" type="checkbox"/>
4. Is there a risk of physical discomfort to those taking part?	Yes	No
5. Is there a risk of psychological or emotional distress to those taking part?	Yes	No <input checked="" type="checkbox"/>
6. Is there a risk of challenging the deeply held beliefs of those taking part?	Yes	No <input checked="" type="checkbox"/>
7. Is there a risk that previous, current or proposed criminal or illegal acts will be revealed by those taking part?	Yes	No <input checked="" type="checkbox"/>
8. Will the project involve giving any form of professional, medical or legal advice, either directly or indirectly to those taking part?	Yes	No <input checked="" type="checkbox"/>

If you answered **Yes** to **any** of these questions, this may **not** be a low risk project.

- If you are a student, please discuss your project with your Supervisor.
- If you are a member of staff, please discuss your project with your Faculty Research Ethics Leader or use the Medium to High Risk Ethical Approval or NHS or Medical Approval Routes.



**Risk to Researcher**

9. Will this project put you or others at risk of physical harm, injury or death?	Yes	No ✓
10. Will project put you or others at risk of abduction, physical, mental or sexual abuse?	Yes	No ✓
11. Will this project involve participating in acts that may cause psychological or emotional distress to you or to others?	Yes	No ✓
12. Will this project involve observing acts which may cause psychological or emotional distress to you or to others?	Yes	No ✓
13. Will this project involve reading about, listening to or viewing materials that may cause psychological or emotional distress to you or to others?	Yes	No ✓
14. Will this project involve you disclosing personal data to the participants other than your name and the University as your contact and e-mail address?	Yes	No ✓
15. Will this project involve you in unsupervised private discussion with people who are not already known to you?	Yes	No ✓
16. Will this project potentially place you in the situation where you may receive unwelcome media attention?	Yes	No ✓
17. Could the topic or results of this project be seen as illegal or attract the attention of the security services or other agencies?	Yes	No ✓
18. Could the topic or results of this project be viewed as controversial by anyone?	Yes	No ✓

If you answered **Yes** to **any** of these questions, this is **not** a low risk project. Please:

- If you are a student, discuss your project with your Supervisor.
- If you are a member of staff, discuss your project with your Faculty Research Ethics Leader or use the Medium to High Risk Ethical Approval route.

**Informed Consent of the Participant**

19. Are any of the participants under the age of 18?	Yes	No ✓
20. Are any of the participants unable mentally or physically to give consent?	Yes	No ✓
21. Do you intend to observe the activities of individuals or groups without their knowledge and/or informed consent from each participant (or from his or her parent or guardian)?	Yes	No ✓

If you answered **Yes** to **any** of these questions, this may **not** be a low risk project. Please:

- If you are a student, discuss your project with your Supervisor.
- If you are a member of staff, discuss your project with your Faculty Research Ethics Leader or use the Medium to High Risk Ethical Approval route.

**Participant Confidentiality and Data Protection**

22. Will the project involve collecting data and information from human participants who will be identifiable in the final report?	Yes	No <input checked="" type="checkbox"/>
23. Will information not already in the public domain about specific individuals or institutions be identifiable through data published or otherwise made available?	Yes	No <input checked="" type="checkbox"/>
24. Do you intend to record, photograph or film individuals or groups without their knowledge or informed consent?	Yes	No <input checked="" type="checkbox"/>
25. Do you intend to use the confidential information, knowledge or trade secrets gathered for any purpose other than this research project?	Yes	No <input checked="" type="checkbox"/>

If you answered **Yes** to **any** of these questions, this may **not** be a low risk project:

- If you are a student, discuss your project with your Supervisor.
- If you are a member of staff, discuss your project with your Faculty Research Ethics Leader or use the Medium to High Risk Ethical Approval or NHS or Medical Approval routes.

**Gatekeeper Risk**

26. Will this project involve collecting data outside University buildings?	Yes	No <input checked="" type="checkbox"/>
27. Do you intend to collect data in shopping centres or other public places?	Yes	No <input checked="" type="checkbox"/>
28. Do you intend to gather data within nurseries, schools or colleges?	Yes	No <input checked="" type="checkbox"/>
29. Do you intend to gather data within National Health Service premises?	Yes	No <input checked="" type="checkbox"/>

If you answered **Yes** to **any** of these questions, this is **not** a low risk project. Please:

- If you are a student, discuss your project with your Supervisor.
- If you are a member of staff, discuss your project with your Faculty Research Ethics Leader or use the Medium to High Risk Ethical Approval or NHS or Medical Approval routes.

**Other Ethical Issues**

30. Is there any other risk or issue not covered above that may pose a risk to you or any of the participants?	Yes	No <input checked="" type="checkbox"/>
31. Will any activity associated with this project put you or the participants at an ethical, moral or legal risk?	Yes	No <input checked="" type="checkbox"/>

If you answered **Yes** to these questions, this may **not** be a low risk project. Please:

- If you are a student, discuss your project with your Supervisor.
- If you are a member of staff, discuss your project with your Faculty Research Ethics Leader.



### Principal Investigator Certification

If you answered **No** to all of the above questions, then you have described a low risk project. Please complete the following declaration to certify your project and keep a copy for your record as you may be asked for this at any time.

#### Agreed restrictions to project to allow Principal Investigator Certification

Please identify any restrictions to the project, agreed with your Supervisor or Faculty Research Ethics Leader to allow you to sign the Principal Investigator Certification declaration.

Participant Information Leaflet attached

Informed Consent Forms attached.

### Principal Investigator's Declaration

Please ensure that you

- Tick all the boxes below and sign this checklist
- Students must get their Supervisor to countersign this declaration

I believe that this project <b>does not require research ethics approval</b> . I have completed the checklist and kept a copy for my own records. I realise I may be asked to provide a copy of this checklist at any time.	
I confirm that I have answered all relevant questions in this checklist honestly.	
I confirm that I will carry out the project in the ways described in this checklist. I will immediately suspend research and request a new ethical approval if the project subsequently changes the information I have given in this checklist.	

### Signatures

If you submit this checklist and any attachments by e-mail, you should type your name in the signature space. An email attachment sent from your University mailbox will be assumed to have been signed electronically.

#### Principal Investigator

Signed Preeti (Principal Investigator or Student)

Date 10-07-2011

Students storing this checklist electronically must append to it an email from your Supervisor confirming that they are prepared to make the declaration above and to countersign this checklist. This email will be taken as an electronic countersignature.

#### Student's Supervisor

Countersigned Key (Supervisor)

Date 19-07-2011

I have read this checklist and confirm that it covers all the ethical issues raised by this project fully and frankly. I also confirm that these issues have been discussed with the student and will continue to be reviewed in the course of supervision.